Tracing the Evolution of Local Universe Galaxies by Kinematical Studies of H I

Dissertation
zur
Erlangung des Doktorgrades (Dr. rer. nat.)
der
Mathematisch-Naturwissenschaftlichen Fakultät
der
Rheinischen Friedrich-Wilhelms-Universität Bonn

vorgelegt von

Milan den Heijer

aus
Vlissingen

Bonn
September 2014

Angefertigt mit Genehmigung der Mathematisch-Naturwissenschaftlichen Fakultät der
Rheinischen Friedrich-Wilhelms-Universität Bonn

1. Gutachter	P.D. Dr. Jürgen Kerp
2. Gutachter	Prof. Dr. Pavel Kroupa
3. Gutachter	Prof. Dr. Jochen Dingfelder
4. Gutachterin	P.D. Dr. Petra Friederichs

Tag der Promotion:	18. Dezember, 2014
Erscheinungsjahr:	2015

Contents

Abstract

This work studies the neutral gas in external galaxies using the neutral atomic hydrogen (H I) line to investigate the kinematics of the gas component. This thesis consists of three parts, one part focusses on early-type galaxies (ETGs), one part on spiral galaxies, and one part on the systematic effects which are inherent to the applied methods.

The first part of this work studies the Tully-Fisher Relation (TFR, Tully & Fisher 1977) for ETGs. This work applies the TFR to study physical properties of ETGs. To this end, the asymptotic rotation velocities for a subset of the ATLAS^{3D} ensemble of ETGs have been derived using velocity fields. These velocities are complemented by K-band magnitudes from the 2MASS survey as well as stellar mass-to-light ratios from the ATLAS^{3D} project. It is found that the K-band TFR reveals a high scatter. If instead the baryonic TFR is constructed, the scatter is substantially reduced. Furthermore, the H I TFR appears to be largely consistent with the carbon monoxide (CO) TFR for the ATLAS^{3D} sample. This implies that the CO line, which is detectable out to larger redshifts, can also be used to study the TFR and thus can in principle be used to study the redshift evolution of galaxies. Finally, the ETG TFR has been compared to that of spiral galaxies. The K-band TFR for ETGs is found to be systematically below the one for spiral galaxies. It is also found that if the average $\mathcal{M}_\star/L_K$ of spirals is approx. 0.3 $\mathcal{M}_\odot/L_\odot$, the baryonic TFR for ETGs and spirals is identical.

The second chapter studies a sample of spiral galaxies from the "Bluedisk" ensemble. The goal is to gain insight into the dominating mechanism by which galaxies are supplied with gas to form stars in the local universe. Concerning this, there are two hypotheses: firstly, the accretion of cold gas from the external environment. Secondly, condensation of gas via cooling of a hot coronae of ionised gas as predicted in a dark matter scenario. The "Bluedisk" sample consists of a sample of 48 galaxies, half of which are selected using optical properties to be particularly gas rich, and the other half to have normal gas content. The data is investigated for signatures of cold gas accretion, i.e., warps, lopsidedness etc. Moreover, the velocity fields of both of the subsamples are used to search for asymmetries, which could point at enhanced accretion of gas. The result is that there are no signs of enhanced episodic gas accretion from the environment. This is in line with the earlier results from the "Bluedisk" survey, focussing on the morphological aspects of the galaxies.

The final chapter studies a selection of systematic effects in the analysis of H I data. Firstly, the effect of Milky Way (MW) contamination on the kinematics of the short-spacing correction (SSC) data set is investigated. In this case, the MW emission causes errors in the flux measurements. Based on NGC 2403 data, it has been shown that also the kinematics cannot be analysed if the velocity field is used. Instead, the data cube has to be analysed to obtain a good description of the data. Secondly, the influence of distance on velocity fields is studied, as this is relevant for both of the preceding chapters. It is found that only for the most nearby spiral galaxies with distances of roughly 20 Mpc, radial profiles of the most important kinematical quantities; the rotation curve, the disk geometry, and even non-circular motions, can be measured. If one studies galaxies at larger distances, only global kinematical properties can be extracted. Finally, it is shown that the vertical density and velocity structure of a galaxy can have an impact on the deduced parameters from a velocity field.

Chapter 1

Introduction

The neutral atomic hydrogen (H I) line has an important place in radio astronomy. Since hydrogen is the most abundant element in the universe, the H I line is one of the most important tracers for the interstellar medium (ISM). This line results from a hyperfine transition of neutral hydrogen at 21.1 cm or a frequency of 1.41 GHz and although it is a forbidden transition, due to the large abundance it can be measured. Therefore, it became an important tool to study the ISM (e.g. velocity structure, morphology). In the nearby universe, it can be observed in the radio regime, either by a single-dish telescope or an interferometer. One of the most important discoveries based on this line is the fact that the rotation curves do not show a Keplerian drop, but remain flat instead (Shostak & Rogstad, 1973; Bosma, 1978), which can be interpreted as a signature of dark matter (e.g. van Albada et al. 1985), or alternatively, the need to modify the laws of gravity (Milgrom, 1983c). Where single-dish instruments have a poor angular resolution, interferometric arrays are usually used to map the H I distribution in galaxies. The work presented in this thesis focusses on the latter and aims to use the H I line to study the kinematics of galaxies in order to learn about evolutionary properties of these objects. In particular, the kinematics of different types of galaxies is investigated to learn about evolutionary properties of early-type galaxies (ETGs) (Chap. 2). Moreover, it is unknown how spiral galaxies acquire gas to form stars. The second objective is therefore to search for signatures that could point to accretion of neutral gas which fuels the formation of stars (Chap. 3).

The Tully-Fisher Relation (TFR, Tully & Fisher 1977) is a relation between the width of the H I line and the brightness of galaxies, and has been widely used to determine distances to galaxies (e.g. Sakai et al. 2000). The line width measures the maximum rotation velocity of a galaxy. Since hydrogen gas is present in galaxies out to large radii, often extending far beyond the stellar disk, the H I line has been used extensively in building the TFR. The fundamental relation underpinning the TFR is widely considered to be the baryonic TFR (McGaugh et al., 2000), which relates asymptotic rotation velocity and baryonic mass. Apart from studying the TFR to derive distances, it is often used as a constraint on models of galaxy formation (van den Bosch, 2000), and efforts have been undertaken to investigate the physical origin of this particular relation (Steinmetz & Navarro, 1999). Moreover, galaxy evolution can be studied using the TFR by comparing the TFR for different morphological classes of galaxies. Of particular interest is the TFR for ETGs. This has been studied in the past for S0 (lenticular) galaxies (Bedregal et al., 2006), which are a type of galaxies intermediate between spiral galaxies and elliptical galaxies. This thesis aims to build the TFR for ETGs. Since these types of galaxies are usually gas poor and are not dominated by rotation, a study of their TFR has been difficult. However, the neutral atomic hydrogen (H I) observations of the galaxies from the ATLAS^{3D} sample (Cappellari et al., 2011a), presented in Serra et al. (2012), have shown that there are many ETGs which contain atomic gas. Using this data, it is investigated whether a TFR exists for these galaxies and how it compares to the TFR of spiral galaxies.

In the second part of this Ph. D. thesis, the focus is on the kinematics of spiral galaxies. Observed star formation rates of nearby spiral galaxies are found to be lower than the predictions of the replenishment of their gas supplies (Maller & Bullock, 2004; Richter, 2012). This raises questions about the origin of this gas. Commonly, one distinguishes between the scenarios of episodic gas accretion from the environment (Sancisi et al., 2008), and the continuous replenishment of gas from the cooling of the shock-heated corona expected to be associated to each galaxy (White & Rees, 1978). It is, however, not clear which is the dominating mechanism. This chapter studies gas accretion for a sample of 48 spiral galaxies. Catinella et al. (2010) establish a scaling relation, which uses optical properties to predict the gas content of galaxies. Wang et al. (2013) use this relation along with data from the Sloan Digital Sky Survey (SDSS, Abazajian et al. 2009) to identify a sample of 48 galaxies. Half of these galaxies contain a (predicted) excess amount of H I gas, and the other half have a normal (predicted) gas content. These galaxies are similar in all other aspects (inclination, redshift, stellar mass etc.). They are studied to search for phenomena such as warps and lopsidedness, which are commonly interpreted as signatures of gas accretion. As opposed to existing studies, which focus on such phenomena in great detail for very well resolved galaxies in the Local Volume (e.g. Sancisi et al. 2008; Heald et al. 2011), this chapter attempts a more statistical approach to investigate accretion in galaxies, which are located at larger distances (of the order of 120 Mpc). Observations at such distances are required, such that the selection criteria are fulfilled. These galaxies are, however, only moderately resolved. This study can thus be considered as prototypical for future interferometric surveys such as ASKAP (Johnston et al., 2007), for which many galaxies will be surveyed at such distances.

The final part of this thesis deals with various systematical effects in the analysis of H I kinematics. In particular with analyses of velocity fields. These are a derivative product of data cubes, which are three dimensional representations of the observation (right-ascension, declination and frequency). Especially for galaxies located at large distances, degrading spatial resolution dominates the resulting data products. Moreover, interferometric observations of nearby galaxies fail to measure the diffuse gas component. Single-dish observations have to be incorporated into the measurement set to recover the complete gas distribution of the galaxy. The effect of such a short-spacing correction (SSC) on the kinematics is investigated in this chapter. Also the role of accretion is emphasised in this chapter; it is described in detail how accretion can be inferred from H I data and also the limits of such analyses are investigated.

This dissertation is structured as follows: Chap. 2 presents an analysis of the TFR for ETGs. The sample consists of ETGs from the ATLAS^{3D} sample (Cappellari et al., 2011a), which contains 260 ETGs. This TFR is compared to existing TFRs for ETGs and spiral galaxies from literature. Chap. 3 is devoted to a study of the origin of the gas used to fuel star formation in spiral galaxies using the H I data from the “Bluedisk” ensemble (Wang et al., 2013). Consequently, Chap. 4 presents a reflection of several systematics comprised in the analysis of the H I kinematics. It connects to both of its preceding chapters, especially to Chap. 3, and it reflects on how future surveys with the main objective to study gas accretion can be designed, and how the kinematical information can be extracted. Finally, Chap. 5 summarises the results and contemplates on their implications.

Chapter 2

The Tully-Fisher relation for early-type galaxies

Abstract

In this chapter, a study of the neutral atomic hydrogen (H I) K-band and baryonic Tully-Fisher Relation (TFR, Tully & Fisher 1977) of a sample of 16 early-type galaxies (ETGs) from the ATLAS^{3D} survey is presented. This analysis is based on Westerbork Synthesis Radio Telescope (WSRT) H I observations, IR photometry, and stellar $\mathcal{M}/L$ ratios from star-formation histories and dynamical models from literature. The H I circular velocity is derived using tilted-ring modelling of the velocity field or the full H I data cube. It is found that the baryonic TFR is significantly tighter than the "classical" TFR, which is in this case analysed using the K-band. Variations of stellar $\mathcal{M}/L$ ratio within the sample are therefore important. Furthermore, no significant offset is found between the H I and carbon monoxide (CO) K-band TFRs. This indicates that the molecular gas, albeit confined to smaller radii than the H I, has typically reached or is close to the flat part of the rotation curve of ETGs. It is established that the baryonic TFRs of ETGs and spirals are compatible provided that the average $\mathcal{M}_\star/L_K$ of spirals is $\approx 0.3\,\mathcal{M}_\odot/L_\odot$, in line with recent determinations based on dynamics and stellar population models.

This chapter is structured as follows: in Sec. 2.1, an introduction of the TFR is presented. In Sec. 2.2, the theoretical context and terminology of this area of research is discussed. This encompasses the observables of the TFR, different versions of the TFR, and a short overview of the types of galaxies that exists and the variation of the TFR between these types. Moreover, it describes the physical background of the TFR. Section 2.3 describes the ATLAS^{3D} project and portrays the sample selection procedure. Section 2.5 presents the results of the TFR based on K-band luminosities and Sec. 2.6 shows the results of the analysis of the baryonic TFR of the sample. The final section (2.7) presents a discussion of the results.

2.1 Introduction

The TFR (Tully & Fisher, 1977) is an empirical scaling relationship between the line width of the H I line and the optical luminosity for spiral galaxies. In general, empirical scaling relationships are crucial to the understanding of many processes in astrophysics and other natural sciences. Examples for scaling relations in astrophysics are the relation between the mass of a supermassive black hole and the velocity dispersion of the stars in the bulge of the host galaxy (Merritt, 2000), as well as the fundamental plane (e.g. Djorgovski & Davis 1987; Dressler et al. 1987), which is a relation between three quantities in elliptical galaxies: effective radius, surface brightness and velocity dispersion. Common to many scaling relations is that the variables are manifestations of underlying, complex processes. The fundamental plane for example can be considered as a manifestation of the virial theorem expressed in observable quantities.

Scaling relations, the TFR in particular, have multiple applications. The TFR is well known for its application in estimating distances to galaxies in the local universe. The reason for this is that the observed brightness of a galaxy depends on its distance whereas the line width, usually measured as W_{20} (the width of the H I line at 20% of its peak intensity), is independent of distance. This is, however, not the only relevant application. Another important aspect of the TFR is its use in models of galaxy formation: since the TFR is known to be a relation with very little scatter, it can be used as a constraint for these models, or the model parameters can be tuned such that the model reproduces the TFR (see e.g. White & Frenk 1991; Kauffmann et al. 1993; van den Bosch 2000). A third application of the TFR, the one central to this chapter, is its role in the investigation of differences between (morphological) types of galaxies to study galaxy evolution. Spiral galaxies are gas-rich, actively star forming galaxies which are supported by rotation. ETGs are galaxies which are old red galaxies largely devoid of gas which are supported by pressure, and are possibly the decedents of spiral galaxies. The TFR can be used to investigate this open question in the evolution of galaxies.

2.2 Theoretical background

In this section, a theoretical foundation for the TFR is provided and an overview of the current status of research on the TFR is given. In Sec. 2.2.1, the observables are defined and several forms of the TFR are discussed. Sec. 2.2.2, provides a discussion of the physics behind the TFR. Sec. 2.2.3 gives an overview of the different galaxy morphologies and the current status of the TFR morphological type dependence.

2.2.1 Observables and different versions of the TFR

In this section, the observables are discussed by which the TFR is constituted. The classical TFR is a correlation between the logarithms of the width of the H I line and the optical luminosity, originally measured in the blue (B) band. However, since its initial description, many corrections have been applied to the measurement of these quantities. This reduced the scatter and solved breaks in the relation making the TFR compatible for a wide range of galaxies. The most recent and possibly most fundamental form of the TFR is the baryonic TFR, which relates the two physical parameters: rotation velocity and baryonic mass.

2.2.1.1 “Classical” TFR

The “classical” TFR as first used by Tully & Fisher (1977), is based on photometric information of the B (blue)-band. The corresponding velocity tracer is the H I line width of the integrated spectrum, measured 20% of the peak flux, W_{20} or ΔV using the notation of Tully & Fisher (1977). The line width is closely related to the rotation velocity of a galaxy through the (non-relativistic) Doppler effect, which relates the broadening of an emission line to the motion relative to the observer:

$$\frac{\Delta\lambda}{\lambda_r} = \frac{v_{\mathrm{los}}}{c}, \tag{2.1}$$

where $\Delta\lambda$ is the shift of the line relative to its rest wavelength, λ_r, and $v_{\rm los}$ is the directly observable component of the velocity vector (the component along the line of sight)[1]. The difference between the line-of-sight velocity of the receding side of the galaxy and the one of the approaching side of the galaxy traces the line-of-sight component of the rotation velocity of the galaxy. This quantity has to be corrected for the galaxy inclination according to $1/\sin i$, where i is the angle between the line of sight and the normal of the plane of the galaxy. This is often corrected using the following expression (Holmberg, 1958):

$$\cos i = \sqrt{\frac{q^2 - q_0^2}{1 - q_0^2}}, \tag{2.2}$$

where $q = b/a$ is the observed axis ratio of the optical image of the galaxy (b is the semi-minor axis length and a the semi-major axis length) and q_0 is the intrinsic axis ratio (which is observed as the axis ratio of a galaxy when viewed edge-on). This correction takes the bulge components of galaxies into account. Only the latest type of spiral galaxies (Sc) are nearly flat disks, the earlier the type, the larger the bulge fraction and the larger the intrinsic axis ratio. For simplicity, usually a fixed value around 0.2 is chosen for all morphological types (Tully & Pierce, 2000). Following Tully & Fisher (1977), the quantity originally plotted on the abscissa is therefore the H I profile adjusted to an edge-on orientation:

$$\Delta V(0) = \frac{\Delta V}{\sin i} = \Delta V \cdot \sqrt{\frac{1 - q^2}{1 - q_0^2}}. \tag{2.3}$$

In the subsequent research on the TFR, other empirical corrections were made to the quantity on the abscissa such as broadening due to instrumental effects and due to turbulent gas motions (see e.g. Giovanelli et al. 1997). Moreover, a cosmological correction has to be applied since the profiles are broadened by a factor of $1 + z$.

More recent work such as Verheijen (2001), showed that for the line-width-based TFR, galaxies with rising rotation curves are offset towards lower velocities. An example for this are the low surface brightness galaxies, which are defined by having a surface brightness fainter than 23 mag arcsec^{-2}. Moreover, galaxies with rotation curves that reach a maximum in the optical regime and converge to a lower asymptotic value, are offset towards higher velocities. If instead of the H I line width, the asymptotic velocity, $v_{\rm asymp}$, is used to build the TFR, this offset largely vanishes.

On the ordinate, which traces the optical intensity, the largest differences between the TFRs found in literature concerns the band in which the stellar light is measured. In the early research on the TFR, magnitudes in the blue (B) band were used. Aaronson et al. (1979) firstly used H-band (1.5 to 1.8 μm, in the near infrared) photometry and found a tighter (less scatter) and also steeper TFR. The motivation for measuring the stellar luminosity at longer wavelengths was that blue light is more strongly affected by extinction in the observed galaxy and the Milky Way (MW) (Verheijen, 2001), requiring large corrections to the observed magnitudes (for a quantitative description see e.g. Giovanelli et al. 1995; Tully et al. 1998). Thus, by switching to the infrared TFR, large systematic uncertainties were avoided. Another reason why the infrared TFR is generally preferred over the TFR based on shorter wavelengths is that the slope of the TFR rises for increasing wavelengths, see e.g. Tully & Pierce 2000 (T&P00,

---

[1] In the spectra, only the radial motion (along the line-of-sight) is observable. The symbol $v_{\rm los}$ is used as opposed to $v_{\rm rad}$, which is used to designate the radial velocity of gas in the plane of the galaxy

hereafter). This is seen as favourable since it is closer to the expected slope of the TFR (see Sec. 2.2.2). Over the years, multicolour infrared TFRs have been studied where the focus of this research was to minimise scatter in the TFR to improve the accuracy of the TFR as a distance tool (see e.g. Malhotra et al. 1996; Pierce & Tully 1988; Sakai et al. 2000). More recent work, such as presented in Noordermeer & Verheijen 2007 (NV07, hereafter), prefer the K_s-band ($2.15\mu m$) TFR, since it is less sensitive to recent bursts of star formation.

2.2.1.2 Baryonic TFR

Freeman (1999) pointed out the existence of galaxies (DDO 154 and NGC 2915) that deviate by two magnitudes from the TFR. He noted that in these galaxies, the mass in H I is about one order of magnitude larger than the mass in the form of stars and also that if the H I mass is converted into stars with a mass-to-light ratio $\Upsilon_\star$ of 1, these galaxies follow the B-band TFR. Walker (1999) firstly defined a "pseudo Tully-Fisher relation" between halo circular speed and visible mass. He found the scatter in this relation to be smaller than in the "classical" TFR and that the relation holds also for gas-rich dwarf galaxies. McGaugh et al. (2000) investigated the TFR for a large range of circular velocities ($30 \leq v_{\rm rot} \leq 300$ km s^{-1}), and found a discrepancy for the low mass end ($v_{\rm rot} \leq 90$ km s^{-1}). Plotting the rotation velocity versus the visible mass, which consists of stellar mass and gas mass, puts all the galaxies from his sample on the same relation described by $\mathcal{M}_d \propto v_{\rm rot}^4$, where $\mathcal{M}_d$ is the baryonic mass of the disk, and called the baryonic TFR. Studies such as Gurovich et al. (2004) and NV07 showed the improvement of the baryonic TFR over the "classical" TFR. The latter found a break in the K-band TFR on the high mass end, where galaxies with $v_{\rm rot} \geq 200$ km s^{-1} deviate systematically to the right of the relation and thus are rotating "too fast". This issue could be resolved by switching to the baryonic TFR. The baryonic TFR is commonly found to have a slope with a value around 4 (see e.g. Catinella et al. 2012). To summarise, the baryonic TFR solves several breaks in the "classical" TFR (at the low- and high mass end) and the baryonic TFR seems to have no intrinsic scatter (see e.g. Verheijen 2001). Therefore, it appears that the baryonic TFR is the most fundamental form of the TFR.

Generally, it is important to realise that a TFR describes the relation between the galaxy's light and its (dynamical) mass (through $v_{\rm rot}$), which are in most cases directly *measurable*. The underlying relation, however, seems to be that of the baryonic TFR, which is not directly measurable (except in gas-dominated galaxies), but has to be inferred by assuming/modelling stellar mass-to-light ratios. Studying the baryonic formulation thus provides possibilities to learn about the mass-to-light ratios of galaxies and even about the initial-mass function (IMF).

2.2.2 Physical motivation

From basic principles, a simple expression for the TFR can be derived as follows: the total mass $\mathcal{M}$ within scale length r varies as:

$$\mathcal{M} \propto v_{\rm asymp}^2 r, \tag{2.4}$$

where $v_{\rm asymp}$ is the asymptotic rotation velocity. The luminosity, L, varies as:

$$L \propto \Sigma_0 r^2, \tag{2.5}$$

where Σ_0 is the (constant) mean surface brightness. Combining these gives:

$$v_{\text{asymp}}^4 \propto \frac{\mathcal{M}^2 \Sigma_0}{L}, \tag{2.6}$$

or in the form of a TFR:

$$L \propto \frac{v_{\text{asymp}}^4}{\Sigma_0 (\mathcal{M}/L)^2}. \tag{2.7}$$

Thus, for a universal mass-to-light ratio and a constant mean surface brightness, the empirical form of the TFR seems to be recovered. As pointed out by Zwaan et al. (1995), this consideration also takes the low-surface brightness galaxies into account, which have a lower Σ_0 than normal spirals. For these galaxies, they suggest that the mass surface density $\Sigma_0 = r^2/\mathcal{M}$ controls the luminosity evolution of a galaxy such that the product $\Sigma_0 \cdot (\frac{\mathcal{M}}{L})^2$ is kept constant. This equation therefore seems to provide a reasonable and simple explanation for the existence of a TFR. The physics behind the TFR is, however, most likely more complicated. One reason for this lies in the scales of the light and the dynamical mass distribution (see e.g. Strauss & Willick 1995). The light is confined to regions where the optical disk resides, but the rotation velocity stays constant until many disk scale lengths. Thus, in a dark matter framework, the luminous mass is confined to the centre of the galaxy, whereas the dark matter plays a role at much larger radii. The fact that these components are tightly linked through the TFR points at a complex connection between dark and luminous matter.

In the framework of modified gravity, e.g. Modified Newtonian Dynamics (MOND, Milgrom 1983c,a,b), the (baryonic) TFR follows naturally. This theory postulates that Newton's second law has to be modified for the regimes of low accelerations, hence:

$$\mathcal{M}\mu(a/a_0)\vec{a} = -\vec{\nabla}\Phi_g, \tag{2.8}$$

where $\mathcal{M}$ is the mass, $\vec{a}$ the acceleration, Φ_g the gravitational potential and $\mu(a/a_0)$ an interpolation function between the regimes. This function assures that for low accelerations, the effective acceleration converges to $a \rightarrow \sqrt{g_N a_0}$, since $\mu(a/a_0)\vec{a} = \vec{g_N}$, where g_N is the acceleration computed on the basis of the observed baryonic mass using Newton's laws. Centrifugal equilibrium yields the following expression:

$$a_0 G \mathcal{M} = v_{\text{asymp}}^4. \tag{2.9}$$

Since in MOND, dark matter does not play a dynamical role on galactic scales, $\mathcal{M}$, in the following denoted as $\mathcal{M}_{\text{bar}} = \mathcal{M}_\star + \mathcal{M}_{\text{gas}}$, the sum of the stellar- and gas mass is in this case all observed (baryonic) matter, therefore:

$$\mathcal{M}_{\text{bar}} \propto v_{\text{asymp}}^4. \tag{2.10}$$

In a cold dark matter framework such as ΛCDM, no clear predictions on the TFR are made. In these models, the TFR is rather used as a constraint by which the models have to abide as mentioned in the introduction to this chapter. To explain the observed TFR from ΛCDM principles, several assumptions are needed. Basic considerations of the equivalence between mass and circular velocity (e.g. Mo et al. 1998; Steinmetz & Navarro 1999) lead to the following relation:

$$\mathcal{M}_{\rm vir} = 2.33 \times 10^5 \left(\frac{v_{\rm vir}}{\rm km\,s,^{-1}}\right)^3 \left[\frac{H_0}{H(z)}\right] h^{-1}\mathcal{M}_\odot, \tag{2.11}$$

where $\mathcal{M}_{\rm vir}$ is the total mass inclosed within the viral radius, $v^3_{\rm vir}$ is the rotation velocity at that point, $H_0 = 100\,h\,{\rm km\,s^{-1}}$ is the current Hubble constant and $H(z)$ is the value of the Hubble constant at redshift z. Although this expression seems to be very close to a TFR, there are several problems with it. Two of them are shortly described here:

- The variables are not observables: they refer to the *total* mass and the rotation velocity at the *virial* radius, $R_{\rm vir}$. The quantities one can observe are the circular velocity out to several effective radii and the baryonic mass of the system (under the assumption of a stellar mass-to-light ratio). McGaugh (2012) points out that one needs to introduce factors f_d (fraction of baryons that contribute to the observed mass) f_b (cosmic baryon fraction) and f_v (ratio of measurable rotation velocity to rotation velocity at the viral radius), $\mathcal{M}_b = f_d f_b \mathcal{M}_{\rm vir}$, and $v_f = f_v v_{\rm fir}$ to relate the variables to observable quantities. The velocity at the virial radius is generally not equal to the asymptotic rotation velocity, but their ratio depends on the concentration parameter (see e.g. Bullock et al. 2001), defined as $c_{\rm vir} = \frac{R_{\rm vir}}{r_s}$, where r_s is the disk's scale length. $f_b = 0.17$ is relatively well constrained (Komatsu et al., 2009), but as McGaugh (2012) mentions, models with $f_V = f_d = 1$ do not match the data so these parameters have to be tuned. This is usually done by defining a feedback parameter $\log\epsilon = 3\log f_V - log f_d$ that removes baryons from the disk.

- In a ΛCDM cosmology, scatter is expected from f_d, f_V, the halo concentration and triaxiality and variations of the formation histories (see e.g. Eisenstein & Loeb 1996; Desmond 2012; McGaugh 2012). This expected scatter is much larger than the observed scatter. The observed intrinsic scatter seems to be consistent with naught (Verheijen, 2001).

From these points, it becomes clear that in a cold dark matter theory, the TFR does not follow naturally. Instead, many parameters have to be introduced to reproduce this relation. Moreover, the absence of intrinsic scatter in the baryonic TFR cannot be explained. The consequence of this is that the TFR cannot be used to falsify this theory as opposed to the situation with MOND.

2.2.3 Morphological type dependence of the Tully-Fisher relation

Galaxies can be classified into different categories depending on their appearance. The Hubble sequence mainly distinguishes between four types of galaxies located from left to right in the Hubble tuning fork (Hubble, 1926): elliptical galaxies (E), lenticular galaxies (S0), spiral galaxies (S) and irregular (Irr) galaxies. In this diagram, the first two are called “early-type” galaxies (ETGs) and the latter two are designated as “late-type” galaxies (LTGs). This terminology is, however, slightly confusing: the terms “late-type” and “early-type” are not connected to galaxy evolution, hence, ellipticals do not evolve into spirals. Ellipticals are divided into types E0, E1, ..., E7 in order of increasing ellipticity. Spirals are subdivided into Sa, Sb and Sc in decreasing order according to the size of the bulge and the tightness of the winding of the spiral arms. The presence of a bar in the case of spirals and lenticulars is designated by a “B”. Besides the morphological feature of spiral arms, late type galaxies (in particular spiral galaxies) are characterised by the following properties: presence of a rotationally supported disk, blue in colour, gas-rich, ongoing star-formation. ETGs (in particular ellipticals) are morphologically characterised by smooth elliptical isophotes (lines of constant brightness). Furthermore, they can be generally characterised by: pressure support (little rotation), random motion of stars, red colour, (neutral) gas-poor, and quiescent in star-formation. Lenticular galaxies are an intermediate class between spirals and ellipticals. They lack spiral arms, they have a thin rotating disk and a larger bulge-to-disk ratio than spiral galaxies. Results of the ATLAS^{3D} project, introduced in Cappellari et al. 2011a (C11, hereafter), however, suggests an alternative classification of galaxies based on (stellar) kinematics (Cappellari et al., 2011b). Instead of using the optical appearance (morphology) of the galaxies, they propose a classification which essentially distinguishes between fast- and slowly rotating galaxies through integral field kinematics, thus preferring a categorisation based on intrinsic properties rather than appearance. The fast rotating ETGs are classified parallel to the spiral galaxies, as spiral galaxies without pronounced spiral arms. The slow rotating ETGs constitute a separate sequence, constituted of galaxies with little rotation and thus being dominated by a bulge component.

There have been attempts to investigate whether the parameters of the "classical" TFR (slope, offset and scatter), in particular the offset, vary with galaxy morphological type in the case of spiral galaxies. Roberts (1978) found that for a given absolute magnitude, late-type spirals have a systematically smaller global H I line width compared to early-type spirals. Similarly, Russell (2004) and Shen et al. (2009) find that late-type spirals are more luminous for a given rotation velocity than early-type spirals. However, this difference seems to decrease when near infrared instead of optical photometry is used, as found by e.g. Aaronson & Mould (1983) and NV07. Assuming that the baryonic TFR is the underlying relation, possible differences in the classical TFR could come either from differences in stellar populations via the stellar mass-to-light ratio, $\Upsilon_\star$, a different mass distribution, or both. The fact that in the case of spiral galaxies, the type dependence of the TFR disappears for longer wavelengths and the scatter is minimal, suggests that there is Tho difference in the baryonic TFR between the galaxies, and that longer wavelengths better trace the stellar masses of galaxies.

More recently, the focus has been on studying the TFR for ETGs, especially S0s. The study of the TFR for these types of galaxies is particularly interesting since ETGs and LTGs are expected to be linked in their evolution. The TFR has been used to study the hypothesis of passive evolution (e.g. Ziegler et al. 2001; Jaffé et al. 2014); this is the scenario in which spiral galaxies use up all their gas, cease to form stars and evolve into ETGs. It is therefore conjugate to the merger scenario, in which most of then evolution is brought about via mergers. Studies performed by Bedregal et al. (2006) and Williams et al. (2010) etc. find that the ("classical") TFR of S0 galaxies is below the relation for spiral galaxies. If one assumes that the dynamical mass does not change and therefore v_{rot} remains constant. This would mean that for a constant rotation velocity, these galaxies are less luminous than spiral galaxies. This is in principle consistent with a fading scenario. The problem associated to studying the TFR for ETGs is that they (especially Es) are often gas poor. Therefore, the gravitational potential, which is traced by the H I line at large radius through v_{rot} can in most cased not be determined. The work presented here studies ETGs in which H I gas has been detected and uses this data to construct a TFR for these galaxies. The sample is presented in the next section.

2.3 Data

This work examines the Tully-Fisher relationship for ETGs for the galaxies from the ATLAS^{3D} sample (see C11). This project is one of the most detailed and largest-scale studies of this type of galaxies. This project focusses on ETGs with a multi-wavelength survey combined with theoretical modelling. The survey resulted in spatially resolved, two-dimensional kinematics from H I, CO, and several ionised gas tracers, yielding information on the kinematics of these galaxies over a large range of radii allowing detailed modelling of the full dynamics of these galaxies. One of the largest advances of this project is the usage of integral field spectroscopy with the SAURON instrument (Bacon et al., 2001; de Zeeuw et al., 2002), allowing a detailed mapping of the stellar kinematics. The ATLAS^{3D} sample consists of a volume limited survey of 260 E and S0 galaxies at multiple wavelengths with distance $D < 42$ Mpc and brighter than $M_K = -21.5$ mag.

This work is based on data from the ATLAS^{3D} H I survey of ETGs carried out with the WSRT performed by Serra et al. (2012). This survey targeted a subsample of 166 morphologically-selected ETGs. These are all galaxies in the larger, volume-limited ATLAS^{3D} sample which are observable with the WSRT ($\delta \geq 10°$), where delta is the declination of the source. Serra et al. (2012) describes the detection of H I in 53 ETGs. In particular, 34 objects host H I on rotating disks or rings with radii varying from a few to tens of kpc (classes D and d in that paper). These systems exhibit relatively regular H I kinematics and are therefore the starting point of this TFR study. The data has been processed using a method based on the Multichannel Image Reconstruction, Image Analysis and Display (MIRIAD, Sault et al. 1995) software package and is described in Serra et al. (2012).

The interacting galaxies, the galaxies with strong non-circular motions and the galaxies in which the H I component is not very extended were excluded from the sample. Thus, this sample of 34 objects is refined by excluding galaxies with signs of interaction (NGC 3619, NGC 5103, NGC 5173), galaxies with complex H I kinematics (e.g., strong warps or non-circular motions; NGC 2594, NGC 2764, NGC 4036, NGC 5631, UGC 03960, UGC 09519), and galaxies whose H I disk is smaller than or comparable to the stellar body (NGC 3032, NGC 3182, NGC 3414, NGC 3489, NGC 3499, NGC 4150, NGC 4710, NGC 5422, NGC 5866, UGC 05408). This leaves 15 galaxies. The sample is expanded with NGC 2974, which kinematics are studied in detail by Weijmans et al. (2008). In order to construct a TFR, the H I circular velocity value for these 16 galaxies needs to be determined. For NGC 2685 and NGC 2974 the results of Józsa et al. (2009) and Weijmans et al. (2008) were taken. For NGC 2824, kinematical data has been kindly provided by T. Oosterloo (T. Oosterloo, priv. comm., 2013). For the remaining 13 galaxies, the methods are described in Sec. 2.4. Since the finite resolution of the observations gives rise to beam smearing (see e.g. Sec 3.4.2) in the inner regions of the velocity fields, no complete rotation curves can be derived for the galaxies. Instead, the focus is on measuring the rotation velocity at a large radius, since this is the relevant quantity for the TFR.

To construct the K-band TFR, the absolute magnitude values listed in C11 for all galaxies in this sample are taken. These luminosities were derived from 2MASS (Skrutskie et al., 2006) apparent magnitudes. Details on the photometry and on the distance estimates of all galaxies can be found in C11. It is assumed that the main uncertainties in the K-band magnitudes are caused by distance uncertainties. The distance uncertainty is assumed to be based on the deviation of redshift distances from the NED-D redshift independent distances[2] as described in C11. This deviation is used as an average distance uncertainty for all galaxies and is converted

---

[2] http://nedwww.ipac.caltech.edu/Library/Distances/

into an uncertainty in K-band magnitude. The dispersion in distance is approximately 21 percent, which causes an uncertainty in magnitudes of 0.41 mag.

2.4 Methods

This section gives a description of the methods by which the asymptotic rotation velocities are derived. The velocity fields of galaxies are two-dimensional representations of the projected (line-of-sight) velocity distributions of the galaxies. The most important parameter for the derivation of the asymptotic rotation velocity is the inclination angle of the galaxy. If the inclination is estimated incorrectly, the magnitude by which the estimated rotation velocity deviates from the true rotation velocity strongly depends on the value of the inclination. The rotation velocity, $v_{\rm rot}$, is related to the observed line-of-sight velocity component, $v_{\rm los}$, by

$$v_{\rm rot} = \frac{v_{\rm los}}{\sin i}, \tag{2.12}$$

or, if $q = b/a = \cos i$, where a is the length of the semi-major and b the length of the semi-minor axis:

$$v_{\rm rot} = \frac{v_{\rm los}}{\sqrt{(1-q^2)}}. \tag{2.13}$$

Propagating the uncertainty in inclination (Δq), the uncertainty in rotation velocity ($\Delta v_{\rm rot}$) can be described by:

$$\Delta v_{\rm rot} = v_{\rm los}\left(\frac{q}{(1-q^2)^{3/2}}\right)\Delta q, \tag{2.14}$$

which is plotted in Fig. 2.1 for $v_{\rm los} = 150$ km s^{-1} and $\Delta i = 2°$. In this figure it is apparent that for low inclination angles (below 40°, face-on), a small uncertainty in inclination propagates into a large uncertainty in $v_{\rm rot}$ and for an increasingly edge-on viewing angle the correct knowledge of the inclination angle becomes decreasingly important for an accurate estimation of the rotation velocity.

An important aspect of the TFR is which quantity should be used along the horizontal (velocity) axis. Historically, the TFR has been constructed using the width of the H I spectrum. However, more recent studies tend to use directly the circular velocity, which can be estimated using a variety of methods including H I, CO and Hα resolved rotation curves (e.g., Verheijen 2001; Davis et al. 2011; McGaugh et al. 2001), planetary nebulae (Cortesi et al., 2013) or dynamical modelling (Williams et al., 2009). These different methods may result in estimates of the circular velocity at different points along the rotation curve, and recent analyses have indeed highlighted the importance of the rotation curve shape for TFR studies (see NV07).

To estimate the H I circular velocity, the starting points are the moment-1 velocity fields produced by the WSRT data reduction pipeline based on the MIRIAD software package described in Serra et al. (2012), shown in Figs. A.1, A.2 and A.3 in the appendix. However, velocity fields do not always represent the H I kinematics accurately, in particular for objects with a projected size small enough to suffer from beam smearing (see e.g. Begeman 1987; Teuben 2002). A more in depth discussion of this topic is also presented in Chap. 4. For these objects, the H I data cube is analysed directly. The analysis methods of velocity fields and H I cubes are discussed in Secs. 2.4.1 and 2.4.2, respectively. Table 2.1 lists the resulting circular velocities of

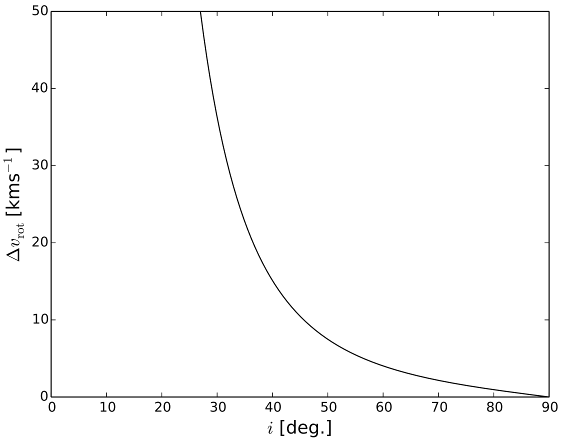

Figure 2.1: Inclination uncertainty versus uncertainty in rotation velocity. This curve is based on Eq. 2.14, with $v_{\rm los} = 150$ km s^{-1} and $\Delta i = 2°$.

all galaxies in this sample. As mentioned in Sec. 2.3, given the size of the H I beam[3] relative to the extent of the galaxies, one is not able to derive full resolved rotation curves. To construct the TFR, therefore the focus is on deriving a single rotation velocity at a large radius. The radii at which these velocities are determined range from 8 to 28 kpc (15 kpc on average) or $R/R_{\rm eff}$ from 3.4 to 13.7 (7.3 on average).

2.4.1 Velocity field analysis

For each galaxy, the H I rotation velocity at large radius is derived by fitting tilted-ring models to the velocity field using the `rotcur` (Begeman 1987) task in the Groningen Image Processing System (GIPSY, van der Hulst et al. 1992) software package. This task performs a least-square fit to the velocity field by modelling the galaxy as a set of rings with increasing radius. It varies the following parameters of each ring: centre, systemic velocity, inclination, position angle and rotation velocity. As starting parameters for the fitting, the inclination is based on the axis ratio of the H I column density map. The position angle, rotation amplitude and systemic velocity are estimated by using position-velocity (xv) diagrams along the major axis of the H I distribution. In the fitting, the following strategy was used: firstly, only the coordinates of the centre were varied for all rings together and then fixed for the rest of the fitting procedure. Secondly, all the parameters were fitted except for the centre and the systemic velocity, they have fixed values for all rings. Finally, the inclination, position angle and rotation velocity ($v_{\rm rot}$) were extracted for each ring, where the spacing between rings is equal to the H I beam size.

The uncertainty in the rotation velocity is largely determined by the uncertainty in the inclination as discussed before. It is therefore important to estimate the latter. To be able to assess the accuracy of the best-fitting parameters a refined strategy has been pursued. Firstly,

---

[3] The beam is an ellipse spanned by the full width at half maximum (FWHM) of the primary lobe of the antenna pattern (the ellipticity depends on the declination of the source), and thus characterises the resolution of the observation

higher order harmonic terms were fitted to the velocity field:

$$v(R,\theta) = v_{\rm sys} + \sum_{k=1}^{fitdeg} c_k(R)\cos k\theta + s_k(R)\sin k\theta, \tag{2.15}$$

where $v_{\rm vsys}$ is the systemic velocity, $c_k(R)$ and $s_k(R)$ are the harmonic amplitudes of order k and θ is the azimuthal angle in the plane of the galaxy. This harmonic decomposition was performed until the fourth order (*fitdeg*=4). This fit was performed using the routine `reswri` from the GIPSY (Schoenmakers et al., 1997) software package. Following Franx et al. (1994), these coefficients can be considered as a diagnostic tool for the rotation velocities based on a tilted-ring fit. They find that an uncertainty in the inclination angle can be directly related to the c_3-term in Equation (2.15) according to:

$$\cos(\theta) = (1 - \frac{\delta q}{4q})\cos(\hat{\theta}) - \frac{\delta q}{4q}\cos(3\hat{\theta}), \tag{2.16}$$

where θ is the correct azimuthal angle, $\hat{\theta}$ the incorrect one caused by an uncertainty in a tilted-ring parameter, $q = \cos(i)$ and $\hat{q} = \cos(i + \delta i) = q + \delta q$. Equation (2.16) demonstrates that an uncertainty in inclination angle gives rise to a non-zero c_3 coefficient, which is given by $-\frac{\delta q}{4q}$. This observation is utilised by minimising the c_3-term by varying the inclination. Additionally, s_1 and s_3 can be interpreted as indicators of non-circular motions. This is taken advantage of by choosing the radius along which $v_{\rm rot}$ is determined, since a high proportion of non-circular motions would cause the measured rotation amplitude to be ambiguous, rings with high s_1 and s_3 are considered to yield unreliable rotation velocities.

Summarising this method, firstly a regular tilted-ring model is fitted to the velocity field to estimate the rings' centre, systemic velocity, position angle, and inclination as described above. These values are then used as input for the harmonic decomposition, which is run multiple times by varying each time the inclination of the corresponding model velocity field in steps of 1 deg. Hence, the function $c_3(i)$ is derived to determine the uncertainty in inclination.

This technique is illustrated by showing its application to the H I velocity field of NGC 3941. This galaxy hosts an H I ring which is well resolved by the WSRT observations, as shown in Fig. 2.2, which also shows the H I velocity field. The best-fitting parameters resulting from a tilted-ring fit are i = 57 deg and $v_{\rm rot}$ = 148 km s^{-1}. Figure 2.3 shows the value of c_3 as a function of inclination offset from the best fitting inclination of 57 deg. This harmonic coefficient has its minimum at the best-fitting inclination. The task `reswri` returns an uncertainty σ_{c3} in c_3. The uncertainty in i is defined as the interval Δi within which c_3 is equal to its minimum value within one σ_{c3}. The horizontal line in Fig. 2.3 represents this definition and, in this case, returns an uncertainty in i of ±1 deg. This result can now be used to estimate the uncertainty in the rotation velocity. In this case, running `rotcur` again at fixed inclinations 56 deg and 58 deg., respectively, and solving for the rotation velocity, yields an uncertainty of ±3 km s^{-1} in the latter. In fact, in cases like this, a conservative estimate of ±8 km s^{-1} has been assigned to the $v_{\rm rot}$ uncertainty, corresponding to about half the channel width (Serra et al., 2012).

In the case of NGC 2974, a similar method has been used by Weijmans et al. (2008): also in this case, a harmonic decomposition of the velocity fields has been performed to constrain the galaxy kinematics.

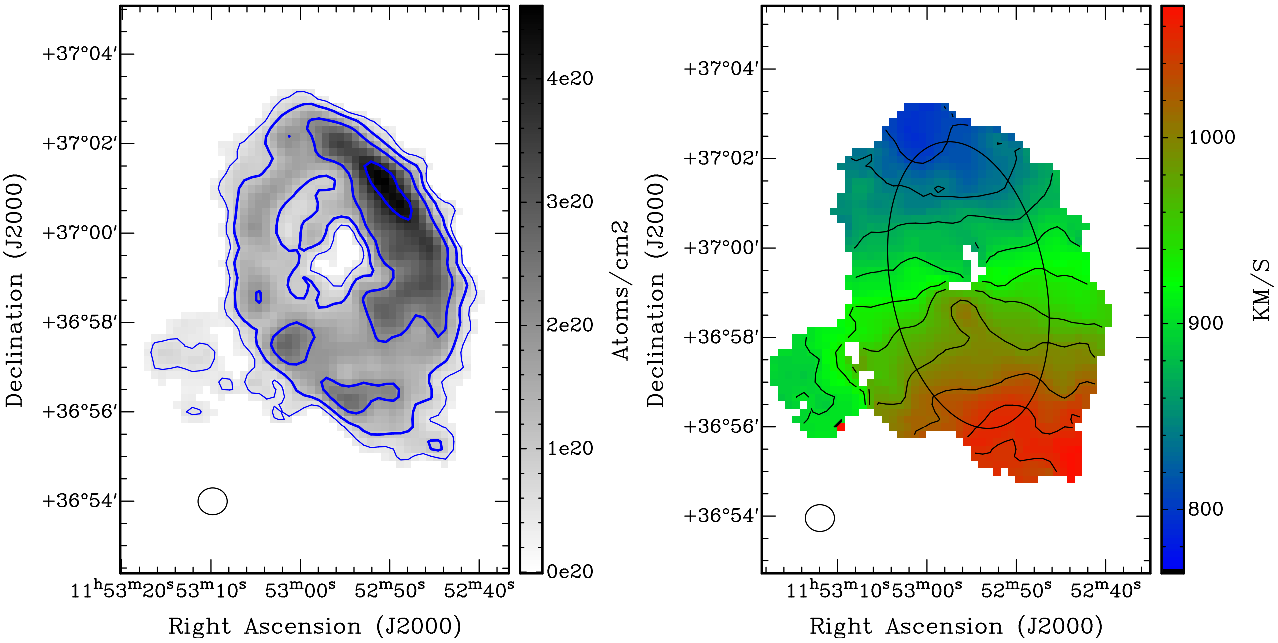

Figure 2.2: *Left*: NGC 3941 column density map. The contours are 0.5, 1, 2, 4×10^{20} cm^{-2}. *Right*: First-moment velocity field. The contours range from 780 to 1080 km s^{-1} with 30 km s^{-1} steps. The overlaid ellipse describes the model geometry (kinematic centre, position angle, inclination and radius) and ellipse on the bottom-left the beam.

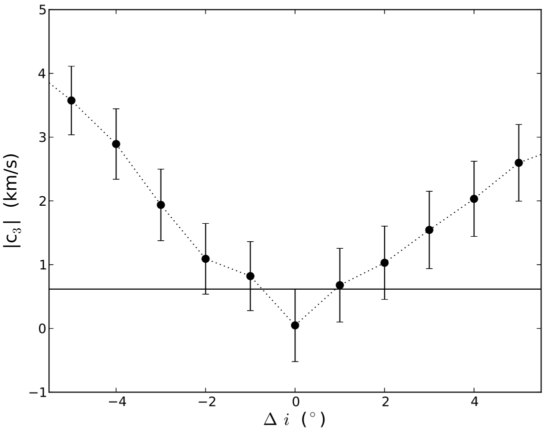

Figure 2.3: NGC 3941 inclination angle offset versus c_3-amplitude. The horizontal line describes the $c_3(\text{bestfit}) + \Delta c_3(\text{bestfit})$, where Δc_3 is the $1-\sigma$ uncertainty of the c_3-term. Since the minimum occurs at the best-fitting inclination angle, and any offset from the best-fitting inclination gives rise to a c_3 amplitude, the inclination can be confidently constrained.

2.4.2 Model data cubes

For poorly-resolved galaxies, where beam smearing persists even in the outer regions (NGC 3838) and for NGC 4203, which has a strong warp, a model is constructed of the full H I data cube instead of using the velocity field. In these cases, therefore a tilted-ring fit using the Tilted Ring Fitting Code (TiRiFiC, Józsa et al. 2007) software is performed [4]. The goal of this is not to construct a perfectly matching kinematical model of the galaxy, but rather to construct simple models to constrain the inclination and rotation amplitude of the galaxy for the outermost point of the rotation curve. Since the TiRiFiC opitimiser searches χ^2 local minima, accurate initial guess values are required for the parametrs. In this work, the starting values for the fit are chosen analogous to Sec. 2.4.1. After setting the initial parameters, the next step consists in fixing some parameters and fitting only a few parameters at a time. This procedure is done iteratively until a stable solution emerges. For simplicity, and considering the limited scope of the fitting (i.e., to derive the outermost value of the rotation velocity instead of the full rotation curve), the position angle and inclination are fitted as being constant with radius if no strong warp is present. In the case of NGC 4203, however, the warp is very pronounced. In this case, the warp is modelled with one step in inclination and position angle: the inclination is found to be 35° in the centre and 30° in the outer part, whereas the position angle is found to be 176° in the centre and 215° in the outer part.

As discussed before, the inclination is the largest source of uncertainty in the rotation velocity. Although the velocity fields do not allow for a direct derivation of the tilted-ring parameters for poorly resolved galaxies, they can be used to estimate the uncertainties on the inclination angle derived from the data cube and therefore the uncertainty in the rotation velocity. In practice, the uncertainty in $v_{\rm rot}$ is constrained by deriving a set of model velocity fields using the GIPSY-task `velfi` with inclinations offset from the best-fitting inclination angle. By inspecting the iso-velocity[5] contours of these velocity fields, a confidence interval for the inclination is estimated and from this the uncertainty in $v_{\rm rot}$.

This method is illustrated by showing its application to NGC 3838. The H I in NGC 3838 is faint and not well resolved by the WSRT beam, causing a large uncertainty in the intensity-weighted velocity. Fig. 2.4 shows the column density map. The ring as reported on in Serra et al. (2012) is not resolved along the minor axis and therefore a basic `rotcur` tilted-ring fit and a harmonic decomposition of the velocity field will not yield any reliable results. In this case a best fitting inclination and rotation velocity are found of 66 deg and 159 km s^{-1}, respectively. The uncertainty in the latter value is estimated by building a number of H I velocity fields for a range of inclination values around the best-fitting one (changing the inclination in steps of 1 deg). It is estimated by eye what the acceptable range of inclination is, which in this case is ±8 deg. Finally, again a model data cube is generated with a fixed inclination at the boundaries of this interval and obtain an uncertainty in the rotation velocity of ±16 km s^{-1}. A diagnostic in the case of the rotation velocities derived from the data cube is performed by a comparison between the xv diagrams of the model with the one from the data. Fig. 2.5 shows a comparison of the observed xv diagram with the one based on the model.

The methods by which NGC 2685 (Józsa et al., 2009) has been analysed are comparable to the data-cube-based method discussed here. Therefore, these data can be very well compared to the data in this chapter. The same is the case for NGC 2824 (T. Oosterloo, priv. comm., 2013), and therefore, also this galaxy is included in the sample.

---

[4] http://www.astron.nl/ jozsa/tirific/

[5] Iso-velocity contours are lines of constant line-of-sight velocity

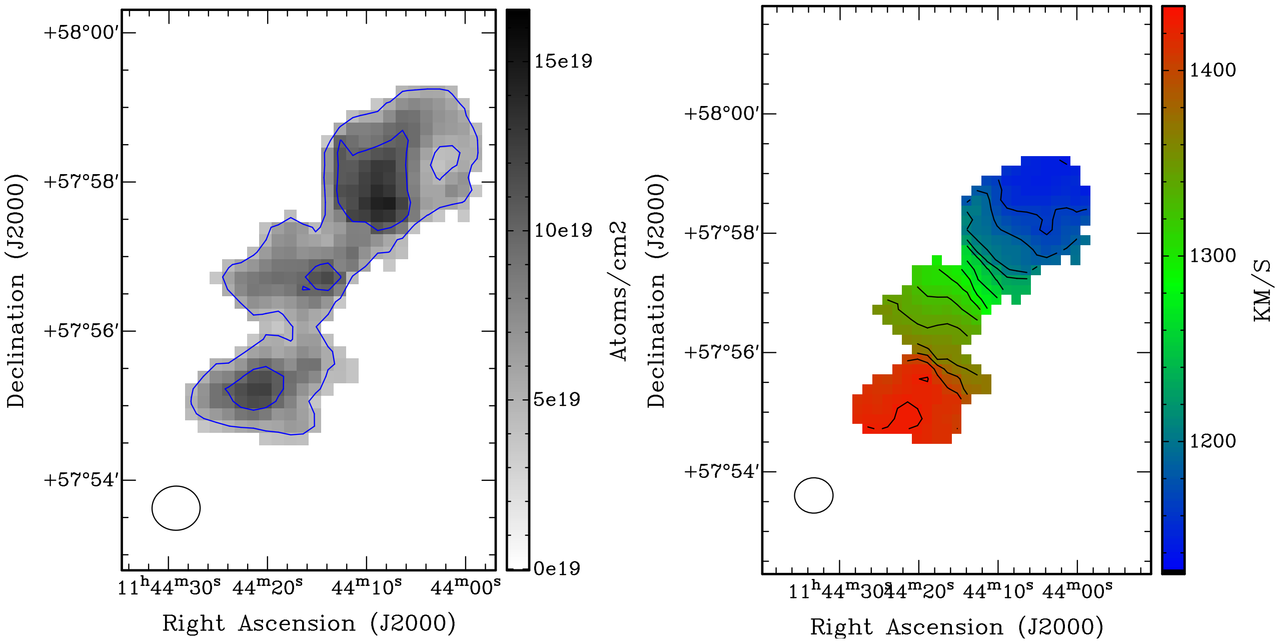

Figure 2.4: *Left*: NGC 3838 column density map. The contours are 5, 10×10^{19} cm^{-2}. *Right*: First-moment velocity field. The contours range from 1100 to 1450 km s^{-1} in steps of 20 km s^{-1}. The ellipse on the bottom-left describes the beam shape.

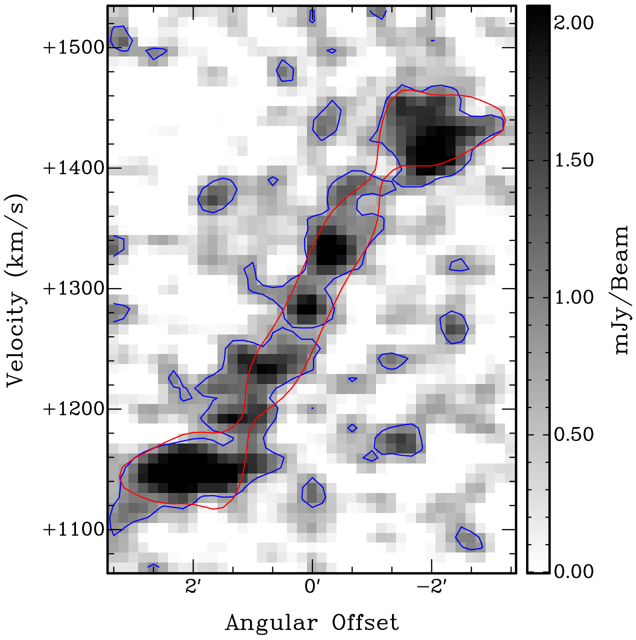

Figure 2.5: NGC 3838 xv diagram. The blue contour corresponds to the observation and the red contour to the model. In both cases, the countour level is at 0.8 mJy, which is approximately the $2\sigma_{\rm rms}$ -level of the data cube.

ID (1)	D (Mpc) (2)	v/c (3)	i (Deg.) (4)	Δi (Deg.) (5)	$v_{\rm rot}$ (km s^{-1}) (6)	Radius (arcsec) (7)	$\log_{10}\mathcal{M}_{H\,I}$ ($\mathcal{M}_\odot$) (8)	$\log_{10}L_{\rm r}$ ($L_\odot$) (9)	$\mathcal{M}/L_{\rm r}^{\rm JAM}$ ($\mathcal{M}_\odot/L_\odot$) (10)	$\mathcal{M}/L_{\rm r}^{\rm SFH}$ ($\mathcal{M}_\odot/L_\odot$) (11)
NGC 2685	16.7	c	65	4	144 ± 10	320	9.33	9.860	2.851	4.169
NGC 2824	40.7	c	65	8	162 ± 10	40	7.59	9.890	4.246	2.203
NGC 2859	27	v	35	5	215 ± 41	115	8.46	10.404	3.698	5.395
NGC 2974	20.9	v	60	2	310 ± 10	130	8.74	10.150	9.572	6.124
NGC 3522	25.5	v	41	2	121 ± 8	85	8.47	9.6	5.070	4.446
NGC 3626	19.5	v	54	1	169 ± 8	120	8.94	10.100	2.735	1.824
NGC 3838	23.5	c	66	8	159 ± 14	150	8.38	9.770	3.882	4.943
NGC 3941	11.9	v	57	1	148 ± 8	195	8.73	9.940	2.512	4.932
NGC 3945	23.2	v	57	-5 +1	237 ± 13	130	8.85	10.390	4.246	5.754
NGC 3998	13.7	v	66	2	246 ± 20	195	8.45	9.970	9.354	6.577
NGC 4203	14.7	c	30	3	197 ± 35	195	9.15	10.070	3.443	6.714
NGC 4262	15.4	v	67	-8 +1	198 ± 10	120	8.69	9.730	5.662	6.053
NGC 4278	15.6	v	45	-2 +5	256 ± 26	150	8.80	10.250	6.745	7.015
NGC 5582	27.7	v	50	2	258 ± 10	210	9.65	10.140	5.272	5.649
NGC 6798	37.5	v	52	2	190 ± 8	150	9.38	10.030	4.571	4.831
UGC 06176	40.1	v	47	-2 + 6	144 ± 14	60	9.02	9.750	4.842	2.128
NGC 7457	12.9	pn	62	-	136	-	< 6.61	9.736	3.034	2.851
NGC 2768	21.8	pn	73	-	316	-	7.81	10.601	8.570	5.916
NGC 1023	11.1	pn	74	-	274	-	9.29	10.287	3.404	6.714
NGC 3489	11.7	pn	61	-	171	-	6.87	9.927	1.820	2.477
NGC 3384	11.3	pn	70	-	196	-	7.25	10.091	2.972	5.297

Table 2.1: Data of the H I K-band and baryonic TFR. The top half are the galaxies analysed in this work, plus NGC 2685 taken from Józsa et al. (2009), NGC 2824 (T. Oosterloo, priv. comm., 2013), and NGC 2974 taken from Weijmans et al. (2008). The bottom half are the data from Cortesi et al. (2013). *Notes*: Column (1): the name is the principal designation from LEDA, see e.g. C11. Column (2): galaxy distance D as listed in C11. Column (3): c indicates that the rotation amplitude is based on a data cube, whereas v indicates a velocity-field-based rotation velocity, and pn indicates the planetary nebulae spectra from Cortesi et al. (2013). Column (4) and (5): inclination angle (i) and uncertainty (Δi). Column (6): rotation velocity ($v_{\rm rot}$). Column (7): Radius at which the rotation velocity has been deterimined. Column (8): H I mass ($\mathcal{M}_{H\,I}$), see Serra et al. (2012). Column (9): SDSS r-band luminosity ($L_{\rm r}$, see Cappellari et al. 2013b). Column (10): r-band stellar mass-to-light ratios from stellar dynamics ($\mathcal{M}/L_{\rm r}^{\rm JAM}$, see Cappellari et al. 2013b) and Column (11): r-band mass-to-light ratios from star formation histories ($\mathcal{M}/L_{\rm r}^{\rm SFH}$, see Cappellari et al. 2013a).

2.5 The H I K-band TFR of ETGs

In this section, the K-band ($\lambda = 2.159\,\mu$m) TFR of ETGs is presented and compared to the one derived using CO kinematics from Davis et al. (2011), who present a TFR derived from the CO kinematics for the galaxies in the ATLAS$^{\rm 3D}$ sample. Finally, the results are compared to the TFR of spirals. The relevant data for the K-band and baryonic TFR (see Sec. 2.6) are summarised in Table 2.1. Figure 2.6 shows the distribution of ETGs on the $M_{\rm K}$-vs.-$\log W$ plane, where $M_{\rm K}$ is the absolute magnitude in K-band and $W = 2v_{\rm rot}$, and is thus corrected for the galaxy's inclination. Also the data from Cortesi et al. (2013) is shown. Their galaxies are also part of the ATLAS$^{\rm 3D}$ sample and the rotational velocity is estimated on the basis of planetary nebulae kinematics at large radius, and therefore are of comparable accuracy to velocities derived in this chapter. The TFR,

$$M_{\mathrm{K}} = a\left[\log_{10}\frac{W}{\mathrm{km\ s^{-1}}} - 2.6\right] + b, \tag{2.17}$$

is fitted to the data (not including the Cortesi et al. 2013 data) by performing a weighted least-square fit of the inverse relation using the `MPFITEXY` package by Williams et al. 2010 (WBC10, hereafter), which depends on the `MPFIT`-package (Markwardt 2009). The resulting best-fitting coefficients are shown in Table 2.2. The table also contains information on the scatter σ_{tot} around the best-fitting relation.

The black dot-dashed line in Fig. 2.6 shows the inverse-fit TFR. Slope and offset cannot be well constrained when fitted simultaneously. Therefore, offsets and scatter will be compared by fixing the slope to reference TFRs from literature. The correlation ρ between the points is only moderate: the un-weighted correlation coefficient is 0.74.

2.5.1 Comparison to the CO K-band TFR

In this section, the H I K-band TFR of ETGs is compared to the "hybrid" CO relation from Davis et al. (2011), which is based on the largest sample of available galaxies, assuming that the CO rotation curve has reached its flat part. The potential offset between the H I and the CO TFR is investigated by fitting a new relation to the H I data, this time keeping the slope fixed to the CO value. The resulting intercept is given in Table 2.2 and indicates no significant offset -23.3 ± 0.2 versus -23.1 ± 0.1 for the H I and CO TFR, respectively. The corresponding TFR is represented by the red line in Fig. 2.6. The lack of a significant offset means that the molecular gas used as a dynamical tracer in Davis et al. (2011) has typically reached the flat part of the rotation curve which is traced by the H I data, as also found in Davis et al. (2013).

Here it is calculated how much the circular velocity is allowed to fall for the H I TFR to remain compatible with the CO TFR. In the case that the H I TFR falls below -23 mag (the CO TFR offset plus its uncertainty), it is considered to be no longer consistent with the CO TFR. Therefore, it is found that a velocity drop of 9 per cent is allowed.

2.5.2 Comparison to the K-band TFR for spirals

Davis et al. (2011) also report an offset from the spiral TFR from T&P00. The latter TFR is a TFR for a large sample of spiral galaxies over several bands, including the K-band. The H I TFR is consistent with the CO TFR. This result is therefore another confirmation that the ETG TFR is offset from the TFR for spirals (see also Sec. 2.5.1). The offset is, however, somewhat smaller than the offset found in Davis et al. (2011): they found an offset of 0.93 mag with respect to the spiral TFR of T&P00, who found a TFR of $M_K = -8.78(\log W - 2.6) - 24.02$. The offset found in this chapter is therefore 0.7 mag, when the slope is fixed to the slope from T&P00 (see Table 2.2). This is about 0.2 mag smaller.

Below, the K-band TFR for ETGs is compared to an established K-band TFRs for spirals from literature. In particular, it will be studied if it can be confirmed that the K-band ETG TFR derived from neutral hydrogen is offset towards higher velocities (or lower luminosities) as found by other studies (e.g. Bedregal et al. 2006 or Davis et al. 2011), as discussed in the above.

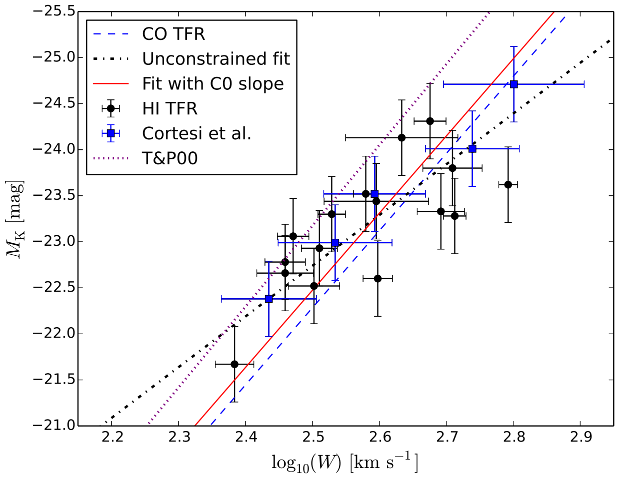

Figure 2.6: H I K-band TFR for 16 galaxies (black circles) and the TFR from Cortesi et al. (2013) (blue squares). The CO Tully-Fisher relation (dashed blue line) is taken from Davis et al. (2011). The solid red line is the fit to the H I TFR with the slope fixed to the CO TFR and the dashed-dotted black line is the unconstrained fit to the H I TFR. The purple dotted line is the T&P00 K-band TFR.

2.5.2.1 Comparison to WBC10

In the above, it has been shown that an offset of about 0.7 mag exists with respect to the T&P00 relation, slightly smaller than the offset found in Davis et al. (2011). Here, these results are compared to the results from WBC10, who studied an ensemble of 14 S0 and 14 spiral galaxies. Their S0 TFR is only 0.5 mag below the spiral TFR. They attribute their offset, which is smaller than the offset found in earlier studies (e.g. Bedregal et al. 2006), to be due to different velocity measures. A fit to the galaxies fixing the slope to the WBC10 slope, reveals a 0.25 mag offset from their sample of spirals, which is best described by $M_K = (-9.17 \pm 0.87)(\log W - 2.6) + (-23.57 \pm 0.12)$. Therefore, the offset of the TFR from this work with respect to the WBC10 sample of spiral galaxies is smaller than the offset with respect to the T&P00 TFR.

2.5.2.2 Comparison to NV07

NV07 study the K-band TFR of massive spiral galaxies using H I line widths and resolved rotation curves, from which the asymptotic rotation velocity is derived. The method by which the circular velocity has been determined compared to the work of T&P00 and WBC10 is therefore most similar compared to the method as described in Sec. 2.4. NV07 find a K-band TFR of the form: $M_K = (-9.64 \pm 0.25)(M_K - 2.6) + (-23.95 \pm 0.04)$. Compared to the fit to the H I TFR data with the slope fixed to the NV07 slope (see Table 2.2), an offset of roughly 0.6 mag is established. WBC10 emphasise that when comparing zero-point offsets for different TFRs, it is important that similar velocity tracers are used. Therefore, the offset between the NV07 TFR and the TFR from this chapter can be considered as the most meaningful ones.

This work seems to confirm the zero-point offset of the K-band ETG TFR with respect to the TFR for spirals as found in the CO TFR from Davis et al. (2011) and WBC10. In Davis et al. (2011), it is suggested that a simple fading mechanism (see e.g. Dressler 1980),

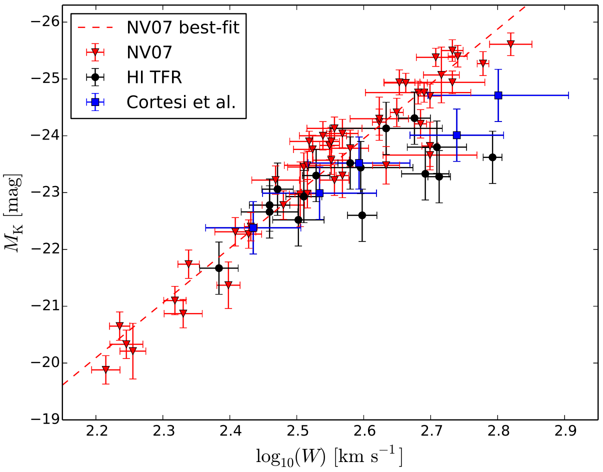

Figure 2.7: NV07 K-band TFR. The red triangles are the NV07 data based on the asymptotic rotation velocities, the dashed red line the best fit to these data points, the blue circles the Cortesi et al. (2013) data and the black circles the data points from this work.

combined with low levels of residual star formation (as implied by the presence of molecular gas) would explain this offset. WBC10 remark that a difference in size between ETGs and spirals could provide an alternative explanations for the offset. Their work showed that the offset between their S0 TFR and spiral TFR is also present in the dynamical mass TFR: $\log v_{\rm rot}$ versus $\log \mathcal{M}_{\rm dyn}$, where $\mathcal{M}_{\rm dyn}$ is the dynamical mass. Dynamical mass scales as $R \cdot v_{\rm rot}^2$, where R is some characteristic radius. If ETGs were more concentrated, the offset in the TFR could be explained by a difference in the mass distribution between ETGs and spirals.

NV07 found that, in particular for their K-band TFR based on H I line widths, there is a subset of galaxies rotating 'too fast' (or equivalently, are 'too dim'), causing a 'kink' in the relation. Figure 2.7 shows the NV07 K-band TFR compared to the K-band TFR from the ATLAS$^{\rm 3D}$ galaxies. Interestingly, this large offset in the TFR for galaxies with $v_{\rm rot} \gtrsim 200$ km s^{-1} ($\log W \gtrsim 2.6$) seems also present in the sample from this work and persists in the Cortesi et al. (2013) sample. NV07 established that by using the asymptotic circular velocity as a velocity tracer and by replacing the K-band luminosity with the baryonic mass, the change in slope can be largely removed. They used a constant $(\mathcal{M}/L)_K = 0.8$ to convert their luminosities into stellar masses and then the gas mass was added to this stellar mass. This $\mathcal{M}/L$ value corresponds to a maximum-disk scenario, hence the largest possible $\mathcal{M}/L$ to maximise the contribution of the disk to the rotation curve. This will be studied in detail in Sec. 2.6.

2.6 Baryonic TFR and the $\mathrm{M}_\star/\mathrm{L}_\mathrm{K}$ ratio of ETGs

As mentioned in the introduction, the TFR is an empirical relation between circular velocity and luminosity, which may result from a relation between more fundamental galaxy properties. Some authors have investigated the existence of a baryonic TFR, where total baryonic mass replaces luminosity, see e.g. McGaugh et al. (2000) and McGaugh 2012 (McG12, hereafter). Some authors consider the baryonic TFR to be the underlying fundamental relation since it has less scatter than the "classical" TFR and removes changes in slope (see e.g. Gurovich et al.

	a	b	σ_tot	ρ
K-band, unc.	-4.67 ± 0.99	-23.25 ± 0.12	0.43	0.74
K-band	-8.38 (CO)	-23.31 ± 0.17	0.67	0.74
K-band	-8.78 (T&P00)	-23.32 ± 0.18	0.69	0.74
K-band	-9.13 (WBC10)	-23.32 ± 0.19	0.72	0.74
K-band	-9.64 (NV07)	-23.33 ± 0.20	0.77	0.74
H I BTFR (JAM), unc.	2.38 ± 0.25	10.71 ± 0.03	0.24	0.94
H I BTFR (SFH), unc.	2.51 ± 0.42	10.71 ± 0.05	0.47	0.80
H I BTFR (JAM)	3.36 (NV07)	10.72 ± 0.04	0.39	0.94
H I BTFR (SFH)	3.36 (NV07)	10.72 ± 0.06	0.57	0.80
CO BTFR (JAM), unc.	3.71 ± 0.34	10.61 ± 0.04	0.43	0.91
CO BTFR (SFH), unc.	3.96 ± 0.39	10.54 ± 0.05	0.44	0.93
CO BTFR (JAM)	3.36 (NV07)	10.61 ± 0.04	0.42	0.91
CO BTFR (SFH)	3.36 (NV07)	10.55 ± 0.05	0.46	0.93
H I BTFR (JAM)	3.8 (McG12)	10.73 ± 0.05	0.50	0.94
H I BTFR (Salpeter)	3.8 (McG12)	10.73 ± 0.07	0.65	0.80
H I BTFR (Kroupa)	3.8 (McG12)	10.55 ± 0.07	0.65	0.80
CO BTFR (JAM)	3.8 (McG12)	10.61 ± 0.04	0.41	0.91
CO BTFR (SFH)	3.8 (McG12)	10.55 ± 0.05	0.46	0.93

Table 2.2: (Inverse fit) Parameters of the H I K-band and baryonic TFR from Secs. 2.5 and 2.6, for the first 16 galaxies in Table 2.1, hence, not the Cortesi et al. (2013) data. *Notes*: The rows in the table present the best-fitting parameters: slope (a), offset (b), scatter (σ_tot), and correlation coefficient (ρ). The K-band TFR is shown on the top half and the JAM and SFH baryonic TFR (referred to as BTFR) on the bottom half. The slopes without uncertainties correspond to the cases where the slope has been fixed to some reference TFR (see text for details). The scatter in the baryonic TFR has been converted into magnitudes by multiplying by 2.5. BTFR (Salpeter) and BTFR (Kroupa) stand for the baryonic TFR based on a Salpeter and Kroupa IMF, respectively.

2004; Begum et al. 2008, NV07, Zaritsky et al. 2014). Here, the baryonic TFR of ETGs is studied.

The baryonic mass ($\mathcal{M}_\mathrm{bar}$) is calculated as the sum of the cold gas mass and the stellar mass. The former is taken as the H I mass given in Serra et al. (2012) multiplied by a factor of 1.4 to take into account for the presence of helium and metals. Moreover, for completeness the mass of the molecular component from Young et al. (2011) is added to the gas mass.

Stellar masses are calculated using r-band luminosities from Cappellari et al. (2013b) and multiplying them with a mass-to-light ratio $\mathcal{M}/L_\mathrm{r}$. Two different derivations of this ratio are considered: first, the mass-to-light ratios resulting from Jeans Anisotropic Multi-Gaussian Expansion (JAM, Cappellari 2008) modelling of stellar kinematics. These values have been derived for the full ATLAS$^\mathrm{3D}$ sample by Cappellari et al. (2013b), and here the results from the self-consistent JAM models (model A) are used from that paper. The second mass-to-light ratios taken from literature are based on the star formation historys (SFHs) derived using a Salpeter IMF (Cappellari et al., 2013a).

In the sample used in this work, the stellar mass is the dominant contribution to the baryonic mass; the H I to stellar mass fraction ranges from roughly 0.1 to 8 per cent (2.2 per cent on average). The quantities used to build the baryonic TFR are shown in Table 2.1.

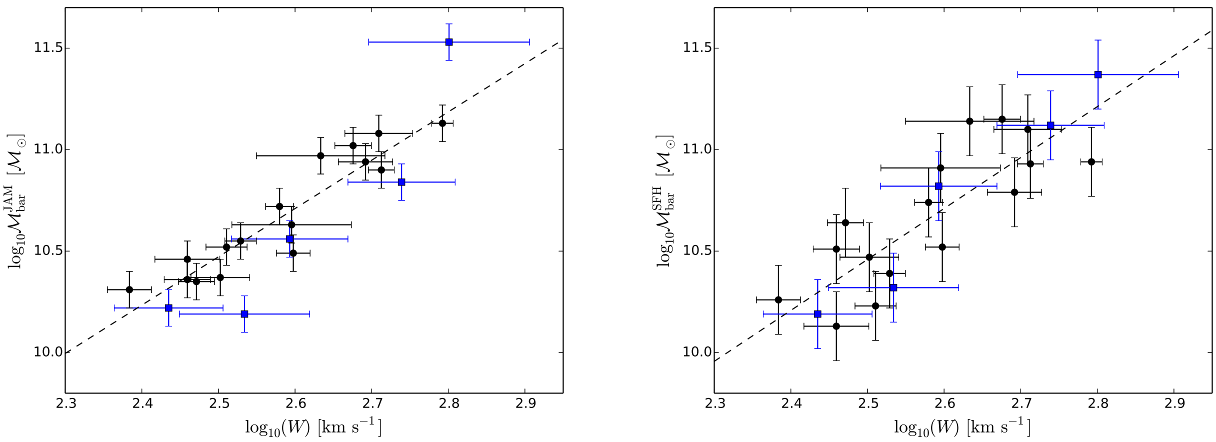

Figure 2.8: JAM (left) and SFH (right) baryonic TFRs. The line is the best-fitting line for all the data points, with no constraints on the parameters. The black circles are the H I TFR data points from this work and the blue squares are from Cortesi et al. (2013).

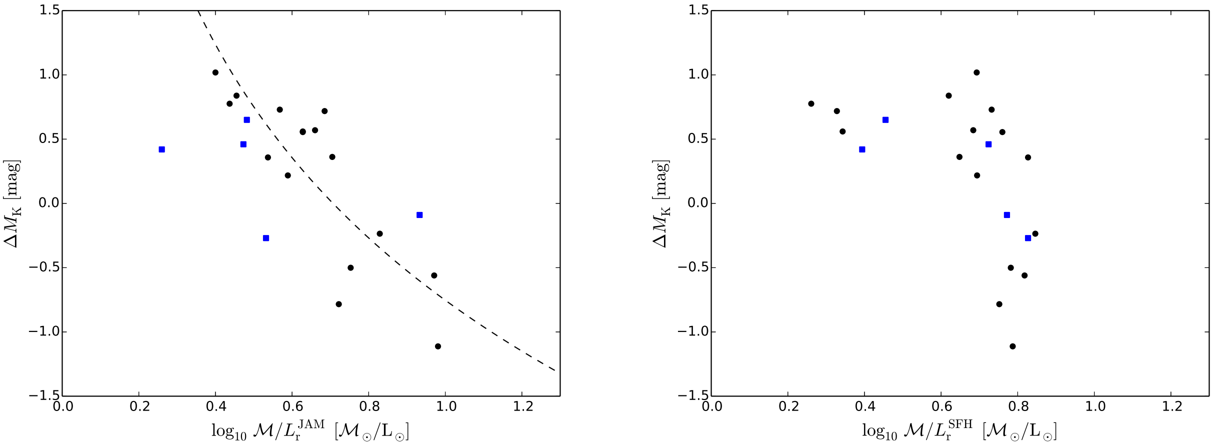

Figure 2.9: Residual magnitudes with respect to the CO TFR from Davis et al. (2011) compared to the $\mathcal{M}/L_\star^{\rm JAM}$ (left) and $\mathcal{M}/L_\star^{\rm SFH}$ (right). The black circles are the H I TFR data points from this work and the blue squares are from Cortesi et al. (2013). The line in the left panel describes the case in which all galaxies have the same $\mathcal{M}/L$ and only distance uncertainties cause a deviation from the CO TFR.

Figure 2.8 shows the JAM and SFH baryonic TFRs. It is assumed that the main source of uncertainty in the baryonic mass ($\mathcal{M}_\mathrm{bar}$) is the estimated distance. Uncertainties in $\mathcal{M}_\star/L_\mathrm{r}$ are neglected. An uncertainty of 0.41 mag is taken for M_K (see Sec. 2.3). Given that $\mathcal{M}_\star/L_\mathrm{r}^{SFH}$ is independent of distance, whereas $\mathcal{M}_\star/L_\mathrm{r}^{JAM}$ has a $1/D$ distance dependence, the uncertainties on the SFH masses vary as D^2, whereas the uncertainties on the JAM masses vary linearly with D. Therefore, typical uncertainties of ~ 0.17 dex in $\log \mathcal{M}_\mathrm{SFH}$ and ~ 0.09 dex in $\log \mathcal{M}_\mathrm{JAM}$ are assumed. The dashed lines in Fig. 2.8 represent the best-fitting, unconstrained baryonic TFRs.

The fits are performed as in Sec. 2.5 (inverse relation) by simply replacing M_K with $\log \mathcal{M}_\mathrm{bar}$ in Eq. 2.17. The coefficients of the fit are given in Table 2.2.

2.6.1 Comparison of the baryonic TFR to the K-band TFR

From Fig. 2.6 it appears that the scatter around the ETG K-band TFR is large. This is confirmed by the numbers in Table 2.2. It is significantly larger than the scatter found by NV07 or by WBC10 which is 0.36 mag and 0.39 mag, respectively. Here it is established that the H I baryonic TFR (in particular based on $\mathcal{M}_\star/L_\mathrm{r}^\mathrm{JAM}$) is significantly tighter than the K-band relation (see Table 2.2). It is noted that due to the limited number of data points, the fit parameters (slope, zero-point offset and scatter) are not well determined in the fits where both slope and zero-point offset are free parameters. The corresponding statements regarding offsets and scatter are therefore based on fit results where the slope is fixed to some established baryonic TFR slope (see Table 2.2).

The fact that the scatter in the TFR is reduced when replacing L_K with $\mathcal{M}_\mathrm{bar}$ (which is nearly the same as $M_\star$ for this sample) suggests that $\mathcal{M}_\star/L_\mathrm{r}$ variations across the sample contribute significantly to the large scatter and low correlation in the “classical” TFR (Fig. 2.6). This is demonstrated in Fig. 2.9, which shows the relation between $\mathcal{M}_\star/L_\mathrm{r}$ (both JAM and SFH) and the residual from a reference TFR, which in this case is taken to be the “hybrid” CO TFR of Davis et al. (2011). As expected, the residuals correlate well with $M_\star/L_\mathrm{r}$. This is more evident for the JAM values, which is logical, since the JAM baryonic TFR is tighter than the SFH relation (Fig. 2.8).

Assuming that ETGs follow a baryonic TFR with low intrinsic scatter, this result would naively imply that the JAM $\mathcal{M}_\star/L_\mathrm{r}$ values are more accurate than the SFH ones. There at least two possible explanations for this:

- First, the correlation between ΔM_K and $\mathcal{M}_\star/L_\mathrm{r}^\mathrm{JAM}$ (which in turn determines the scatter in the JAM baryonic TFR) might be at least in part due to distance uncertainties. To understand this effect it should be noted that the uncertainty in mass, derived from JAM modelling, scales linearly with D (Cappellari, 2008) while L_r is proportional to D^2. If ETGs follow a baryonic TFR and have the same $\mathcal{M}_\star/L_\mathrm{r}$, in the left panel of Fig. 2.9 they would move along the dashed line in the presence of distance uncertainties. Since this line describes the trend well, it can be concluded that the contribution of distance uncertainties to the observed scatter can only be explained if the intrinsic scatter in the JAM baryonic TFR is small. However, since also the SFH $\mathcal{M}_\star/L$ show a trend with the magnitude residual, distance uncertainties cannot be the full explanation for the lower scatter in the baryonic TFR.

- Second, the JAM and SFH $\mathcal{M}_\star/L_\mathrm{r}$ differ in a systematic way, which has been shown to be due to systematic variations of the IMF (Cappellari et al., 2012). Therefore, at least part of the reason, why the JAM based baryonic TFR is a tighter relation than the

K-band TFR and the baryonic TFR derived from stellar populations (SFH), is due to a varying IMF for ETGs.

2.6.2 Comparison to high mass spiral galaxies

NV07 also study the H I baryonic TFR of spiral galaxies, as discussed in Sec. 2.5.2.2. They find a “kink” in their K-band TFR which is largely removed by constructing the baryonic TFR instead. They use a fixed $\mathcal{M}_\star/L_\mathrm{K} = 0.8\ \mathcal{M}_\odot/L_\odot$ for all galaxies in their sample. This ratio is consistent with the maximum-disk scenario[6]. NV07 find a baryonic TFR with an intercept of 10.88 ± 0.02 and a slope of 3.36 ± 0.10 based on their asymptotic rotation velocities, which are derived in a way comparable to this work. The baryonic TFRs are then fitted with a slope fixed to the NV07 value of 3.36 which results in intercepts of 10.71 ± 0.03 (JAM) and 10.71 ± 0.05 (SFH) respectively. From this fit, an offset is established between the spirals and the ETGs also in the baryonic TFR. Assuming that spirals and ETGs follow the same baryonic TFR, there must be an error either in the $\mathcal{M}/L$s as used in this work, the $\mathcal{M}/L$ assumed by NV07, or in both, since a different $\mathcal{M}/L$ causes an up- or downward shift in the baryonic TFR.

Figure 2.10 shows again the baryonic TFR of ETGs. The dashed line represents the baryonic TFR of spirals inferred by NV07 with the assumption of $\mathcal{M}_{\star/}L_\mathrm{K} = 0.8\ \mathcal{M}_\odot/L_\odot$. The black circles and blue squares are the data points from this work and the data points from Cortesi et al. (2013), respectively, based on $\mathcal{M}_\star/L_\mathrm{r}^\mathrm{JAM}$. The red triangles are the NV07 data points computed using a lower mass-to-light ratio of $\mathcal{M}_\star/L_\mathrm{K} = 0.32\ \mathcal{M}_\odot/L_\odot$. Spirals and ETGs follow the same baryonic TFR if $\mathcal{M}_\star/L_\mathrm{K} = 0.32$ is assumed for the spirals. Therefore, the $\mathcal{M}_\star/L_\mathrm{K}$ values adopted by NV07 are systematically too high to make the baryonic TFR of their spirals compatible to the ETGs in this work.

Such an offset can thus in principle be reduced or removed by assuming a different $\mathcal{M}_\star/L_\mathrm{K}$ within reasonable limits. In particular, based on integral-field spectroscopic observations of the DiskMass sample, some authors (Bershady et al., 2010; Martinsson et al., 2013) find that a mean value of $0.32\ \mathcal{M}_\odot/L_\odot$ for spirals is the most appropriate mass-to-light ratio for their sample of galaxies. Figure 2.10 shows that such a value makes the NV07 galaxies better compatible to the ATLAS$^\mathrm{3D}$ H I sample.

The works of Maraston (2005) and Tonini et al. (2009) agree with the assumptions of such a sub-maximal $\mathcal{M}_\star/L_\mathrm{K}$ is. They study the effect of thermally pulsating asymptotic giant branch (TP-AGB) stars on the stellar mass-luminosity relation. When TP-AGB stars not taken into account, the $\mathcal{M}/L_\mathrm{K}$ is overestimated, since a higher stellar mass is needed to produce the same K-band luminosity. Therefore, including TP-AGB stars in stellar population models results in a lower $\mathcal{M}/L_\mathrm{K}$. In order to get $\mathcal{M}/L_\mathrm{K} = 0.32$, the stellar mass-luminosity relation needs to be offset by ≈ 1 mag (a factor of 2.5 in $\mathcal{M}/L_\mathrm{K}$), which is in agreement with the results of Tonini et al. (2009, 2010).

2.6.3 Comparison to the CO baryonic TFR

After having established in Sec. 2.5.1 that the CO- and the H I-based ATLAS$^\mathrm{3D}$ K-band TFRs are compatible, the baryonic TFR based on the CO data from Davis et al. (2011) is compared to the baryonic TFR from this work. Since these galaxies are part of the ATLAS$^\mathrm{3D}$ sample, $\mathcal{M}/L_\mathrm{r}$ values, r-band luminosities and H I masses are available for most galaxies (see Serra

---

[6] In rotation curve decompositions, the mass-to-light ratio is a free parameter. The maximum-disk scenario refers to a scenario in which this mass-to-light ratio is tuned, such that its contribution of the disk to the gravitational potential, and thus to the rotation velocity, is at a maximum.

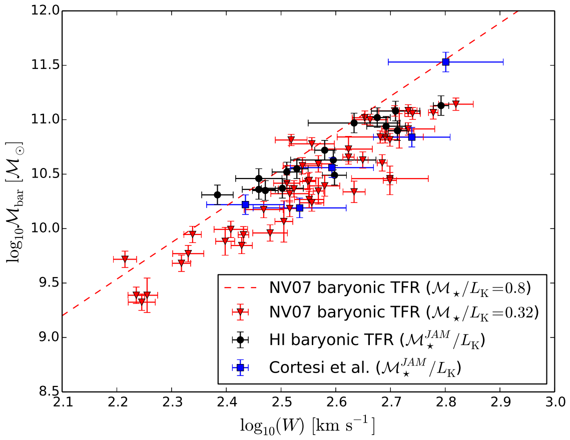

Figure 2.10: Baryonic TFRs. The red triangles are the NV07 data points, calculated using an $\mathcal{M}/L_\mathrm{K} = 0.32$ instead of 0.8. The black circles are the galaxies from this work, using the JAM mass-to-light ratios, and the blue squares the Cortesi et al. (2013) data points. The line describes the NV07 baryonic TFR with $\mathcal{M}/L_\mathrm{K} = 0.8$.

et al. 2012; Cappellari et al. 2013b,a). The “hybrid” sample as defined in Davis et al. (2011) is studied. Only NGC 4292 is not included in the ATLAS$^\mathrm{3D}$ sample and for PGC 058114 there is no $\mathcal{M}_\star/L_\mathrm{r}$ value available. These two galaxies are not included here. Since in the WSRT H I survey (see Serra et al. 2012), only galaxies above a declination of $\delta > 10°$ have been observed, no H I masses can be assigned to 7 of these galaxies and therefore, these galaxies are excluded from the comparison as well. This leaves 19 galaxies for which the CO baryonic TFR from Davis et al. (2011) can be compared to the H I baryonic TFR.

A line is fitted to the data points CO data points. The best-fitting parameters are listed in Table 2.2. It is found that the JAM- and SFH-based CO baryonic TFRs are identical within the uncertainties and that the scatter is about 0.4 mag in the unconstrained fit. In Davis et al. (2011), the authors found a scatter of 0.54 mag in the K-band TFR fitting both the slope and the zero-point offset. Thus, the CO baryonic TFR based on $\mathcal{M}/L_\mathrm{r}$ from stellar dynamics (scatter of 0.42 mag) as well as the one based on stellar populations (scatter of 0.46 mag) show a lower scatter than the K-band TFR. It thus follows that for the H I TFR, as well as for the CO TFR, the baryonic TFR is the tighter relation compared to the K-band TFR.

Moreover, to compare zero-point offsets of the H I baryonic TFRs to the CO baryonic TFRs, an additional fit is performed fixing the slope to 3.8 (see Sec. 2.6.4 and McG12). This value is also close to the slope derived by e.g. Catinella et al. (2012) or Zaritsky et al. (2014). Alternatively, the slope is fixed to the NV07 value of 3.36 and the zero-point offset is determined (see Table 2.2). A comparison of the CO baryonic TFR with the baryonic TFR from this work and Cortesi et al. (2013) is shown in Fig. 2.11 and Table 2.2. As seen in the K-band TFR, the CO baryonic TFR lies slightly below the H I baryonic TFR, although with weak statistical significance.

If this baryonic TFR is compared to that of the spirals, in particular to NV07, offsets of 0.68 mag and 0.83 mag are found for the JAM and SFH baryonic TFRs, respectively. These offsets go in the same direction as in the K-band TFR, hence, the ETGs TFR is below that of the spirals. The offset of the CO K-band TFR for ETGs from the spirals found in Davis et al. (2011) is about a full magnitude. Therefore, the baryonic TFR does somewhat decrease

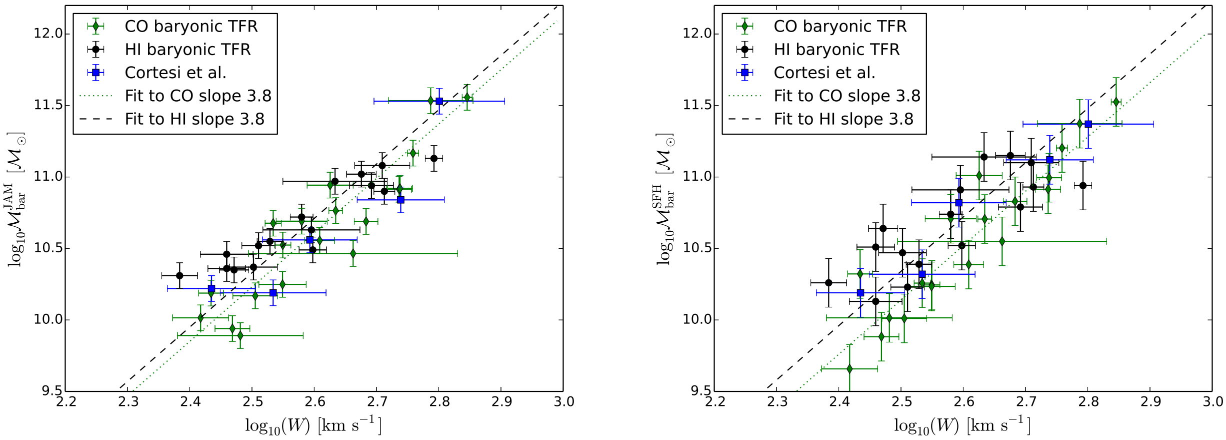

Figure 2.11: JAM (left panel) and SFH (right panel) baryonic TFRs for the galaxies from Davis et al. (2011) (green diamonds), the H I baryonic TFR (black circles) and the Cortesi et al. (2013) baryonic TFR (blue squares). The black dashed line describes the best-fitting zero-point offset with a slope fixed to 3.8 to the H I baryonic TFR data. The dotted line is the same fit applied to the CO baryonic TFR data.

the offset with respect to the spirals as found in e.g. Davis et al. (2011). Analogous to the H I baryonic TFR, also the CO baryonic TFR is better defined when based on $\mathcal{M}/L_{\rm r}$ from stellar dynamics rather than stellar populations.

2.6.4 Comparison to the full range baryonic TFR

The next step is to explore how the results compare to a baryonic TFR for gas-rich galaxies at the low-mass end. The data is compared with the baryonic TFR presented by McG12. In that paper, the author studied the baryonic TFR of a sample of especially gas-rich galaxies ($\mathcal{M}_{\rm gas} > \mathcal{M}_\star$), to minimise the influence of the mass-to-light ratios which can be biased due to the usually necessary assumptions on the IMF. This baryonic TFR has a slope of 3.8 ± 0.2 and spans a range of rotation velocities from 17 km s^{-1} to 149 km s^{-1}.

Figure 2.12 shows a plot of these data points compared to the baryonic TFR data from this work and the Cortesi et al. (2013) data points. In McG12, the stellar masses are estimated using a Kroupa IMF (Kroupa, 2001), whereas the ATLAS$^{\rm 3D}$ SFH-based baryonic masses are derived using a Salpeter IMF (Salpeter, 1955). Therefore, the stellar masses are corrected by multiplying the SFH-based mass-to-light ratios with a factor of 0.65, which accounts for the difference in mass between the Salpeter and the Kroupa estimation of the mass (Cappellari et al., 2012).

Figure 2.12 and Table 2.2 compare the JAM and SFH baryonic TFRs to the McG12 relation. McG12 finds $\log_{10}\mathcal{M} = \log_{10} A + \log_{10} v_{\rm rot}^x$, where $\log_{10} A = 2.01 \pm 0.41$ and $x = 3.82 \pm 0.22$ or equivalently: $\log_{10}\mathcal{M} = 3.82(\log_{10} W - 2.6) + 10.79$. There seems to be an offset of the JAM and SFH relations with respect to the McG12 baryonic TFR. Due to the large uncertainty in the zero-point offset of the McG12 baryonic TFR, however, this offset is not strongly statistically significant. From the figure, however, the offset appears to be larger at the high mass end. Both the baryonic TFR from stellar dynamics, as well as the baryonic TFR from star formation histories show indications of an offset from the McG12 relation. Moreover, the effect of $\mathcal{M}/L$ on the masses of the McG12 galaxies is minimised due to the composition of the sample (gas rich galaxies). Therefore, these offsets can have two causes:

- Systematical differences in $\mathcal{M}/L$ for this work's ETGs and the McG12 sample. Cappellari et al. (2012) showed that there are systematical differences in the $\mathcal{M}/L$ if one estimates $\mathcal{M}/L$ from stellar populations (SFH) or from stellar dynamics (JAM). Therefore, a systematical difference can be expected in their TFRs when comparing this chapter's sample to the McG12 sample. This is most clearly visible in the left panel of Fig. 2.12, since under the assumption of a universal IMF and a universal baryonic TFR, there are large differences between the ETGs from this work and the McG12 galaxies.
- Different mass distributions in the galaxies in this chapter's sample and the McG12 galaxies could play a role in the comparison of the TFRs. As briefly pointed out in Sec. 2.5.2.2, smaller sizes of ETGs could provide an explanation for the offset from the baryonic TFR for spirals. This can be suspected from the right panel of Fig. 2.12: $\mathcal{M}/L$ effects are minimised since both masses are derived using the same IMF (Kroupa). The JAM-based baryonic TFR has a lower scatter than the SFH-based relation. Moreover, the McG12 relation is not strongly affected by the assumed IMF, since these galaxies are gas-dominated. The fact that the right plot still shows an offset, which increases for higher masses, could indicate that $\mathcal{M}/L$ effects are not the only cause for the offset from the McG12 relation. In addition, there could be a difference in mass distributions between the samples.

Therefore, it can be concluded that $\mathcal{M}/L$ effects have to play a role, since the baryonic TFR shows less scatter than the K-band TFR, making a non-universal $\mathcal{M}/L$ essential for the construction of a baryonic TFR. However, on the other hand, the intrinsic mass distribution also appears to be important.

2.7 Discussion

The H I K-band and baryonic TFR of a sample of 16 ETGs from of the ATLAS^{3D} project are studied. For galaxies that are sufficiently well resolved, the velocity fields in the outskirts are studied using a harmonic analysis to find the best-fitting v_{rot}. In three other cases, the full data cube is modelled in order to derive the kinematical information of the galaxy, and in three further cases existing kinematical data is used. These circular velocities as well as 2MASS K-band luminosities are used to construct the "classical" TFR. Moreover, using stellar mass-to-light ratios and gas masses from the ATLAS^{3D} project, the baryonic TFR is constructed. In the case of the baryonic TFR, it is distinguished between mass-to-light ratios from stellar kinematics and from star formation histories. The following results are derived:

1. The "classical" TFR ($\log(W)$ vs. M_{K}) shows a large scatter. This scatter is found to be of the order of 0.7 mag.
2. The "classical" TFR found in this work is consistent within uncertainties with the CO relation for the ATLAS^{3D} sample (Davis et al., 2011). This suggests that the rotation curve stays flat from the region where the CO is located out to many effective radii. Hence, no evidence of a drop in circular velocity has been found. As discussed in Davis et al. (2011), it also gives rise to the possibility to use the CO TFR to study the TFR

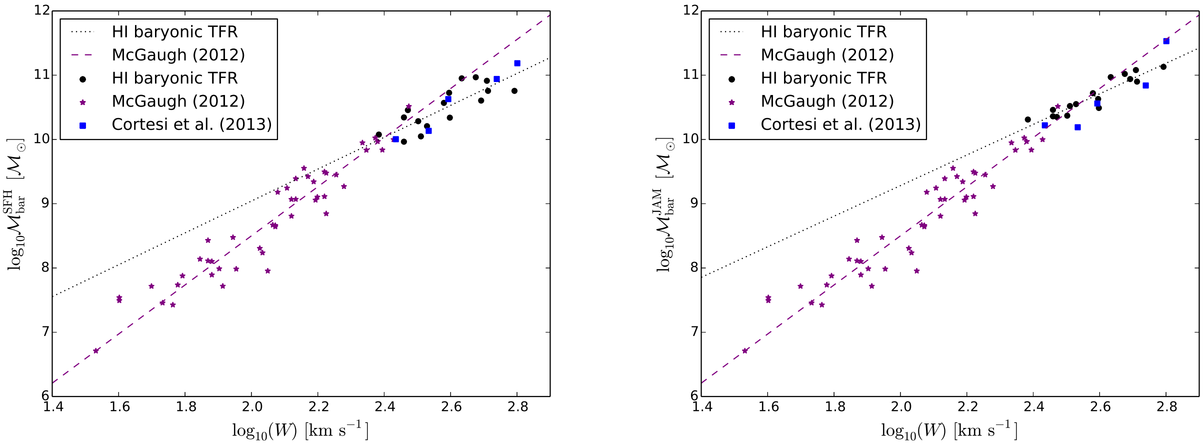

Figure 2.12: The baryonic TFR from McG12 compared to the baryonic TFR from this work based on SFH (left) and JAM (right) r-band mass-to-light ratios. The black circles are the galaxies studied in this work, the purple stars are the McG12 galaxies and the blue squares are the Cortesi et al. (2013) data points. The purple dashed line is the baryonic TFR from McG12 and the dotted black line is the fit to the H I baryonic TFR from this work.

at higher redshifts. Telescopes such as the Atacama Large Milimeter Array (ALMA) could be used to target galaxies at high redshift. This will enable the investigation of the redshift evolution of ETGs.

3. The baryonic TFR fits the data better, especially when using the mass-to-light ratios based on JAM models of stellar kinematics. Two factors play a role in this: (i) variations of the IMF for ETGs, and (ii) the different dependence on distance uncertainties. In the latter case, the low scatter in the JAM-based baryonic TFR can be for a large part explained by distance uncertainties, implying the intrinsic scatter in the baryonic TFR is very low for this sample of ETGs. If distance uncertainties would be the only factor responsible for the scatter of the K-band TFR, $\Delta D/D$ would have to be about 92 per cent to explain the full spread in the K-band TFR residuals of about 2 mag as shown in Fig. 2.9. Given the limits on distance uncertainties from C11, it is therefore concluded that distance uncertainties play a role, but are not the only factor explaining the low scatter in the JAM baryonic TFR relative to the scatter in the K-band TFR.

4. The JAM baryonic TFR lies below the baryonic TFR as found by NV07. Assuming that spirals and ETGs follow the same baryonic TFR, apart from a difference in the mass distribution in ETGs and spiral galaxies, an explanation can be that NV07 assumed an incorrect $\mathcal{M}/L$. Assuming a lower $\mathcal{M}/L$, as found in recent dynamical and stellar population models, makes the baryonic TFR of this work's sample entirely consistent with the baryonic TFR for the NV07 spiral galaxies. A lower $\mathcal{M}/L$ implies that the contribution of the disk to the observed rotation curve in the inner disk is not maximal. Hence, dark matter plays a dynamical role in the inner parts of the galaxies, i.e. disks are submaximal. This is in line with recent findings of the DiskMass-Survey (Martinsson et al., 2013). Another indication for this is that the TFR for low- and for high surface brightness galaxies is identical, which implies that $\mathcal{M}/L$ for high surface brightness

galaxies is lower (see e.g. Zwaan et al. 1995).

5. There are hints for an offset of the JAM-based baryonic TFR of this work's sample galaxies with respect to the baryonic TFR from McG12, presented for low-mass spiral and irregular galaxies. This possible discrepancy could be caused by errors in the assumptions of the star formation history models, i.e., the IMF varies from galaxy to galaxy as has been shown by Cappellari et al. (2012). Alternatively, a difference in the mass distributions between the McG12 sample galaxies and the ATLAS^{3D} ETGs could explain the offset.

w

Chapter 3

Gas accretion in nearby H I-rich spiral galaxies

The contents of this chapter with the exception of Sec. 3.5, The H I Tully-Fisher relation for high mass gas-rich galaxies, have been submitted to Astronomische Nachrichten/Astronomical Notes (AN) on July 15th, 2014. The title of the paper is *“A study of the kinematics of unusually* H I*-rich galaxies”* . The paper’s authors are: Milan den Heijer, Gyula I. G. Józsa, Jürgen Kerp, Paolo Serra, Thijs van der Hulst, Guinevere Kauffmann, Jing Wang, Frank Bigiel, Jarle Brinchmann, David Carton, Diane Cormier and Mei-Ling Huang.

Abstract

How galaxies obtain their gas supplies to form stars is an unsolved question in galaxy evolution. Most of the research so far has focussed on very nearby galaxies situated within the Local Volume (e.g. Heald et al. 2011). This, however, severely limits the parameter space of the galaxies that can be studied (morphology, geometrical orientation, stellar mass etc.). Thus, in order to draw conclusions on how star formation of galaxies is fuelled, one has to expand their parameters space. This can only be realised by studying galaxies at larger distances, which is the aim of this chapter. The subject of study in this chapter is the neutral atomic hydrogen (H I) kinematics of the “Bluedisk” ensemble of 48 galaxies selected from the Sloan Digital Sky Survey (SDSS, Abazajian et al. 2009) and observed at 21 cm with the Westerbork Synthesis Radio Telescope (WSRT). Half of the sample consists of galaxies with a high H I mass fraction predicted from optical properties, the other half of the sample are galaxies with a “normal” predicted gas fraction.

By studying the H I velocity fields of these galaxies, it is investigated whether there are indications of ongoing gas accretion: i.e. global asymmetries and signatures such as warping and kinematical lopsidedness. In addition, the K-band (“classical”) Tully-Fisher relation, and the baryonic Tully-Fisher relations are compared for both groups. As a result, no enhanced kinematical asymmetries between the H I-rich sample and the control sample galaxies are found, indicating no significant difference in kinematical signatures such as warping and lopsidedness. Furthermore, no indications are found for a difference in position angle and systemic velocity offset with respect to the optical images between the sub-samples. No clear evidence for enhanced global asymmetry of the H I-excess galaxies in comparison to the control sample galaxies is established. This result implies that at the redshift of the sample ($z \approx 0.025$), the amount of accreted cold gas is insufficient to be detected by the WSRT using the employed methods. Since the observed number of Lyman-α clouds varies according to $\frac{dN}{dz} = (\frac{dN}{dz})_0 (1+z)^\gamma$, where $\gamma \approx 2$ (Rauch, 1998), this means that one has to consider galaxies at a higher redshift to observe cold accretion. The Square Kilometer Array (SKA), which will have a much higher angular resolution (about 1 arcsec, see Huynh & Lazio 2013), will be able to investigate cold accretion at higher redshifts.

Finally, the baryonic Tully-Fisher relation does not show a clear difference between the samples and reveals a comparable scatter for the K-band Tully-Fisher relation.

This chapter is structured as follows: Sec. 3.1 reflects on the contemporary view of accretion of gas in galaxies and introduces the "Bluedisk" survey. Sec. 3.2 introduces the data products used in this chapter. Sec. 3.3 presents a visual inspection of the data, whereas Sec. 3.4 uses quantitative tools to describe this ensemble of galaxies. Finally, Sec. 3.5 discusses the Tully-Fisher relation for this ensemble of galaxies and 3.6 summarises the results and presents an outlook.

3.1 Introduction

In this section, the current view on gas accretion is discussed and the "Bluedisk" survey is introduced. This section is structured as follows: Sec. 3.1.1 provides an overview of the existing research on cold gas accretion in nearby galaxies and motivates the design a new survey to advance the current state of research and Sec. 3.1.2 provides details of the "Bluedisk" survey, such as the sample selection scheme and the results achieved.

3.1.1 Gas accretion in nearby galaxies

One of the main unsolved problems in galaxy evolution theories is how galaxies accrete cold gas and fuel their continuing star formation activity: observed accretion rates of cold gas are lower than the rates that follow from the cooling and cloud fragmenting of gas predicted by ΛCDM models (e.g. Maller & Bullock 2004, Richter 2012). Moreover, the star formation rates vary between one (Robitaille & Whitney, 2010) to a few stellar masses per year (Misiriotis et al., 2006) in the Milky Way (MW), which is often found to be higher for external galaxies (Kennicutt, 1998). The typical gas of a disk galaxy is, however, around $10^9\,\mathcal{M}_\odot$ (Fraternali & Tomassetti, 2012). Therefore, without replenishment, star formation cannot be sustained much longer than a few Gyrs. Moreover, the "G-dwarf problem" (see e.g. McWilliam 1997) presents evidence that external gas has to be accreted over time. G-dwarfs are stars with lifetimes of the order of the age of the galaxy. Therefore, all these stars ever formed should still be visible. However, a deficit of such stars is observed. This implies that an increase of the amount of gas over time is required rather than a closed-box scenario in which all the gas is initially present in the disk.

The H I line plays a key role in the study of this type of gas accretion, since it traces the neutral gas component in- and around galaxies (see Sancisi et al. 2008 for a review).

In the current paradigm of galaxy formation and evolution, there are two scenarios by which galaxies acquire their supply of cold gas required for star formation:

The first scenario is the steady and/or episodic accretion of cold gas from the external environment (Tosi, 1988). The main evidence for this scenario is that many galaxies are surrounded by gas-rich dwarfs, H I cloud complexes and H I tails and host extra-planar gas (Sancisi et al., 2008). Moreover, most galaxies have warped H I disks and are kinematically/morphologically lopsided, indicating tidal interaction with massive companions or accretion of small companions. Steady or episodic accretion of cold gas could be responsible for the observed asymmetries. The work of Sancisi et al. (2008) presents a landmark in this area of research; the authors sum up the observed evidence of cold accretion resulting from H I observations of the MW and nearby galaxies. As proof for ongoing accretion they quote: i) the presence of gas-rich dwarfs or H I cloud complexes, tails and filaments, ii) extra planar gas (intermediate- and high velocity clouds), iii) warps in spiral galaxies, iv) morphological and kinematical lopsidedness of disk galaxies. They infer that the typical accretion rate of a spiral galaxy is found to be of the order 0.2 $\mathcal{M}_\odot$ yr^{-1}, whereas typical star formation rates (SFRs), are commonly found to be much higher (see e.g. Heesen et al. 2014). In order to explain the observed SFRs of spiral galaxies, Sancisi et al. (2008) therefore infer an additional accretion channel: the smooth infall of gas from the intergalactic medium (IGM).

The other possible mechanism by which galaxies constantly can acquire their gas is thought to be through the cooling of the hot corona of shock-heated gas (White & Rees, 1978). In CDM, galaxies form through hierarchical merging. The gas falls into the dark halo potential wells and is shock heated to the halo's virial temperature. This gas then loses its energy by thermal (X-ray) radiation and is no longer supported by thermal pressure, after which it condenses onto the disk as cold gas, serving as material for star formation. Empirical evidence is, however, scarce: only in the case of the most massive spiral galaxies, diffuse X-ray emission has been detected (see. e.g. Anderson et al. 2013). It is also suspected that the MW contains such a halo (Gupta et al., 2012). Besides the inconclusive evidence for the existence of such halos, the derived cooling-rates are found to be too low to explain the observed star-formation rates (Anderson et al., 2013), and also the masses are too low to constantly fuel the star formation. Recent models based on supernova driven circulation of gas in the galactic halo (see Marasco et al. 2012; Marinacci et al. 2012), however, suggest accretion rates of $\approx 2\mathcal{M}_\odot$ yr^{-1}. This rate would agree with the observed star formation rates without requiring constant replenishment from the intergalactic medium.

Therefore, it is not clear which is the dominating mechanism by which galaxies obtain their gas supplies. Recent and ongoing efforts to study this problem are sensitive H I interferometric surveys such as the Hydrogen Accretion in Local Galaxies Survey (HALOGAS, Heald et al. 2011) survey. Such surveys, however, have not yet presented conclusive evidence for the existence of large quantities of rotationally lagging, extra-planar gas, interpreted by some authors as a signature of ongoing accretion of cold gas onto the disk. However, in the HALOGAS survey, the 22 observed objects are in the Local Volume. This is a sphere of about 10 Mpc, and contains of the order 500 galaxies (Karachentsev et al., 2008) of different morphologies, hence, only a subset of these contain the prerequisites to study their neutral gas kinematics (e.g. extended H I disk, optimal inclination, not located in the plane of the MW etc.). Thus, possible accretion mechanisms can be studied in detail, but not for large number of galaxies and a large variety of properties. Therefore, to enlarge the galaxy parameter space, one has to study a larger number of galaxies and thus move to larger distances as is done in the "Bluedisk" project.

The galaxies in the "Bluedisk" sample are at a mean distance of 120 Mpc, a distance at which many thousands of galaxies will be surveyed with new instruments such as the Australian Square Kilometre Array Pathfinder (ASKAP, Johnston et al. 2007) and Apertif (Verheijen et al., 2009). Studying galaxies at such distances increases the range of different galactic environments and offers significantly more possibilities for data selection. For this work, the choice of larger distances than usually employed for structural H I studies is inevitable: within both the coverage of the SDSS and the reach of the WSRT, only 123 suitable H I-rich candidates were identified within a redshift range of $0.01 < z < 0.03$ (Wang et al., 2013). At these distances, however, angular resolution effects (see e.g. Teuben 2002) begin to limit conventional analyses. Given the large number of moderately resolved H I observations expected in the near future, it is an interesting question how well velocity fields are suited for a kinematical analysis of such observations. A detailed analysis of the systematical effects inherent to observations of galaxies at larger distances as well as other systematical effects are presented in Ch. 4.4.1.

3.1.2 The "Bluedisk" survey

Catinella et al. (2010) established a tight correlation, a fundamental plane between the atomic gas contents, UV-/optical colours and stellar surface mass densities based on a sample of ∼1000 galaxies. This plane (see Fig. 12 of Catinella et al. 2010) can thus be used to predict the atomic gas content based on stellar properties: the stellar surface mass density and the NUV-r colour. Part of their sample, however, is displaced from this plane, showing an increased atomic gas content compared to what would be expected on the basis of their colours and densities alone. Extending the parametrisation of Catinella et al. (2010), Li et al. (2012) were successful to predict the excess H I by including stellar mass and colour gradient as predictors for the H I mass. In particular, galaxies with a strong colour gradient towards their outskirts show an H I excess with respect to the plane as defined by Catinella et al. (2010). This, together with the observation that the ionised gas in these outer disks is metal-poor (Moran et al., 2012) and evidence for a correlation of increased star formation activities in the past 2 Gyr with atomic gas mass (Huang et al., 2013) may indicate ongoing gas accretion in these gas-rich galaxies.

This work uses H I data from the "Bluedisk" H I survey carried out with the WSRT. This is a survey of 48 galaxies with photometric and spectroscopic data available from the SDSS and the Galaxy Evolution Explorer (GALEX) imaging survey. The sample has stellar masses ranging between $10^{10}\,\mathcal{M}_\odot$ to $10^{11}\,\mathcal{M}_\odot$, lying in a redshift range between 0.01 and 0.03 and is chosen to have high quality UV images from the GALEX satellite. The photometrically determined (using the above-mentioned relation) H I mass-to-stellar mass ratio, $\mathcal{M}_{HI}/\mathcal{M}_\star$ of 25 "H I-rich galaxies" is chosen to exceed the value defined by the "fundamental plane" by a factor of larger than 4. A control sample of similar size is chosen to have a normal up to high $\mathcal{M}_{HI}/\mathcal{M}_\star$, that is a factor of 1-1.5 higher than found for the fundamental plane. Originally, observations of 50 galaxies had been scheduled. However, observations of 2 galaxies of the control sample are missing from the data set: one galaxy (number 34) has not been detected and another galaxy (number 41) has not been observed. For further details about the sample selection, observational setup, data reduction and a first interpretation of the H I column density distributions see Wang et al. (2013).

The most important results of the "Bluedisk" project (Wang et al., 2013) are:

- The H I-rich galaxies lie on the same H I mass versus H I size relation as the "normal" spirals.
- The H I-rich galaxies do have significantly larger H I to optical extents. Hence, the galaxies with an excess of H I gas have a gas disk that is larger compared to the size of the optical disk.
- The morphological distribution of the galaxies with an excess H I content appears to be more clumpy.
- The authors did not find any indication that the H I-rich galaxies are more morphologically disturbed than the 'normal' spirals. These results can be interpreted as a counterindication for a scenario in which the majority of galaxies are refuelled by mergers. Instead, they are more compatible with a scenario in which residual hot X-ray gas is being refuelled from the IGM and condenses onto the disk (White & Rees, 1978).

Wang et al. (2014) analyse the radial H I profiles for the "Bluedisk" sample. They find that these profiles are very homogeneous in the outer ranges of the galaxies. Moreover, they find that in about half of the H I-rich galaxies, most of the excess gas is located outside of the stellar disk. In the other half of the H I-rich sample, the excess gas is more confined to the centre. The authors also compare their observations to hydrodynamical simulations and semi-analytical models and find that these reproduce their findings. Moreover, in the semi-analytical models, the homogeneous outer H I surface brightness profiles are caused by the assumption that inflowing gas is distributed exponentially.

3.2 Data

The details of the data reduction are presented in Wang et al. (2013). In summary, the data were reduced by using a Python pipeline introduced by Serra et al. (2012), which itself employs a set of Multichannel Image Reconstruction, Image Analysis and Display (MIRIAD, Sault et al. 1995) tasks. Under different weighting schemes, the primary data products per observation are a set of data cubes at differing spatial resolution and sensitivity with a velocity resolution of 24.8 km s^{-1}. In a second step, a source finder defines masks encompassing regions of emission in the data cubes, which are used to determine descriptive parameters and - in combination with the unmasked data - further data products, such as column-density maps, and velocity fields. Here, the calculation of the velocity fields is described.

The starting point for this study of the H I kinematics are the masked data cubes with a robust weighting of 0.4 and no tapering, since they show a favourable combination of sensitivity and angular resolution to study their kinematics. From these data cubes, first-moment maps were derived, which are intensity-weighted velocity maps. First moment maps, however, are strongly affected by beam smearing (see e.g. Begeman 1987; Teuben 2002; Józsa et al. 2007 and Sec. 3.4.1) caused by the finite resolution of the observations. Beam-smearing causes the first-moment velocity fields not to be an accurate representation of the galaxy kinematics, and therefore another approach has been taken to calculate velocity fields. In this approach, h_3 Gauss-Hermite polynomials are fitted to the line of sight velocity distributions (LOSVDs), following van der Marel & Franx (1993) and de Blok et al. (2008). The script used to perform these fits is based on a script provided by T. Oosterloo (priv. comm., 2013). The fits are performed on the unmasked data cubes, which are convolved such that the resulting data cubes have a circular point spread function. This is necessary, since galaxies at lower declinations are observed with a more elliptically shaped beam. Only pixels with column densities exceeding the detection threshold in the (masked) column density map as shown in Wang et al. (2013) are taken into account in the fit. Moreover, as starting values for the fits, the values of the moment-1 velocity fields are taken. To further reduce the impact of the noise, fitted amplitudes below twice the noise level of the data cube are discarded.

To provide an example, the first moment velocity field and the resulting Gauss-Hermite velocity field are compared in Fig. 3.1. The first moment velocity field has been masked using detection thresholds from the column density maps in Wang et al. (2013). The first-moment map in this figure shows more distortions compared to the Gauss-Hermite velocity field, making a tilted-ring fitting approach troublesome. One of the reasons for this is that noise has a larger effect on these maps, since the intensity-weighted mean velocity is very sensitive to the noise peaks. This effect is visible as strongly curved contours and an irregular behaviour of the first moment velocity field. The reduced beam smearing in the Gauss-Hermite velocity field can be recognised by the smaller separation between the iso-velocity contours[1] in the centre of the map.

---

[1] Iso-velocity contours are lines of constant line-of-sight velocity

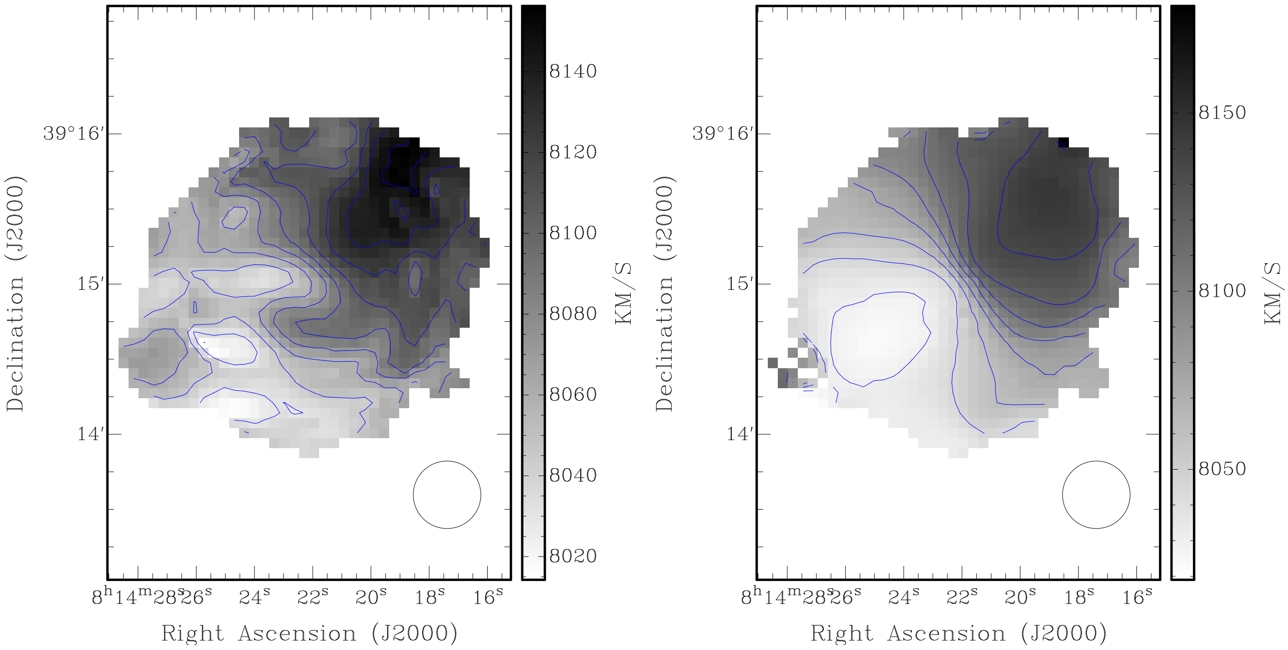

Figure 3.1: *Left*: moment-1 velocity field. *Right*: Gauss-Hermite velocity field. The velocities shown are barycentric line-of-sight velocities in the radio velocity definition. The separation of the contours is 15 km s^{-1}. The circle on the bottom-right corner indicates the size of the beam, which is roughly 27 arcsec in this case.

3.3 Qualitative analysis of asymmetries

In this section, the results of a qualitative analysis of the kinematics of the H I data based on an inspection of the data cubes, position-velocity (xv) diagrams, and velocity fields are provided. The aim is to investigate if one can identify obvious kinematical differences between the H I-rich galaxies and the control galaxies. In particular, it is investigated by inspection if galaxies in the H I-rich sample show more features such as warping of the disk, kinematical lopsidedness, and non-circular motions compared to those of the control sample. The galaxies in the H I-rich sample are by selection H I-rich compared to the galaxies in the control sample and with that, since they follow the H I-mass-size relation (Broeils & Rhee, 1997), larger. The data cubes of the H I-rich galaxies therefore contain a larger number of independent data points. This is expected to affect the quantitative analysis of the kinematics. Moreover, to some extent, such resolution effects can be spotted by eye more accurately than via quantitative analysis of the data. For example, warps can be identified from radial profiles of the inclination and the position angle[2], however, for galaxies at these distances such profiles cannot be extracted (see Sec. 4.4.1). On the other hand, such warps are more easily identified using a visual analysis of the data cube, velocity field, and xv diagram. With a visual inspection, the aim is to make sure that obvious biases influencing the analysis are taken into account.

In the following, data cubes, iso-velocity contours and xv diagrams for each individual galaxy

---

[2] The position angle is the angle between the major axis of the receding side of the galaxy and the north of the coordinate system (through east).

are inspected to search for features that indicate non-circular motions, warping, lopsidedness, H I tails, or complexes and indications for ongoing interactions. Kinematical lopsidedness, generally a deviation from circular orbits, is most effectively indicated if the rotation curve of the receding side of the galaxy differs from the rotation curve of the approaching side (Swaters et al., 1999). This can be observed most directly by comparing the iso-velocity contours of both sides of the galaxies in combination with the xv diagrams along the kinematical major axes.

A varying position angle of the major axis and inclination with radius point to the presence of warping of the disk, where one usually distinguishes between S-, U- and L-shaped warps. U- and S warps can be seen in the velocity field and confirmed by inspection of the data cube. On the contrary, it is difficult to distinguish between L-shaped warps and kinematical lopsidedness (see e.g. van Eymeren et al. 2011), thus both are categorised as kinematical lopsidedness. The presence of non-circular motions is derived by searching for wiggles in the iso-velocity contours (see e.g. Bosma 1981). Furthermore, it is noted that to minimise systematic biases by beam smearing, the edges and the centre of the velocity fields are not analysed in this inspection. Finally, it is pointed out that selection effects play a role in this analysis: warps are easier to identify if the angular momentum axis tilts perpendicular to the line-of-sight (Józsa, 2005). Table 3.1 lists the results and the velocity fields are shown in Figs. B.1 and B.2 in the appendix. The xv diagrams along the major axis, representing the radially projected rotation curve are shown in Figs. B.3 and B.4 in the appendix.

Based on the 25 H I-excess galaxies and 23 control sample galaxies in Table 3.1, 12 of the galaxies from the H I-rich- and 9 of the control sample galaxies show curvature of the velocity field contours. Moreover, 19 of the H I-rich galaxies show signatures of warping, compared to only 11 galaxies in the control sample. The number of the H I-rich galaxies showing features of lopsidedness (kinematical and/or morphological) is 10, which is 12 in the case of the control sample galaxies. Furthermore, the number of galaxies that show a nearby H I tail or cloud complex is 17 for the H I-rich-, and 6 for the control sample. Finally, if a galaxy is defined to be asymmetric as a galaxy that is warped asymmetrically and/or lopsided (kinematically and/or morphologically), asymmetries in 13 H I-rich- and 14 control sample galaxies can be established.

The only difference found is that the H I-rich galaxies have a slightly higher frequency of obvious warping and a higher occurrence of H I tails and cloud complexes. The difference regarding warps is nevertheless not very large and strongly biased, since the H I-rich galaxies have more extended H I disks. Therefore, the warps are more easily identified than in the control sample galaxies (see also García-Ruiz et al. 2002). Both reasons make this observed difference just weakly significant.

In Wang et al. (2013), the galaxies 7, 13, 29, 31 and 46 were found likely to be interacting based on the optical images. Inspection of the H I kinematics confirms this and adds galaxies 15 and 48 to the list. In these cases, the H I kinematical structure shows clear signs of two very nearby, positionally partly overlapping galaxies in the data cube. Therefore, in 3 H I-rich galaxies it is expected that an interaction is taking place compared to 4 cases in the control sample.

3.4 Quantitative analysis of asymmetries

In this section, quantitative approaches are presented aimed to test whether the extremely gas-rich galaxies have kinematical properties that distinguish them from the control sample and

ID	Curved contours	Warp S/U/A	Tail/ complex	Kin. lops.	Morph. lops.	Int.	$V_{\rm sys}$ km s^{-1}	$V_{\rm rot}$ km s^{-1}	Γ deg.
(1)	(2)	(3)	(4)	(5)	(6)	(7)	(8)	(9)	(10)
1	0	0	0	0	0	0	8308 ±1	102 ± 1	311 ± 9
2	0	S	0	0	0	0	7348 ± 5	178 ± 1	19 ± 3
3	1	S	1	0	0	0	8768 ± 6	189 ± 4	4 ± 15
4	0	S	0	1	0	0	7679 ± 6	175 ± 3	202 ± 5
5	1	S	1	1	0	0	7557 ± 2	150 ± 1	279 ± 32
6	1	S	0	0	0	0	7536 ± 1	229 ± 1	166 ± 7
7	0	S/A	0	0	0	1	8629 ± 4	150 ± 2	190 ± 2
8	1	0	0	1	0	0	8020 ± 1	147 ± 1	141 ± 6
9	0	S/A	0	1	0	0	8230 ± 4	193 ± 3	196 ± 5
11	0	0	0	1	0	0	7217 ± 4	180 ± 3	81 ± 6
12	1	0	0	0	0	0	7652 ± 6	161 ± 7	277 ± 8
13	1	S	0	0	1	1	8639 ± 3	187 ± 3	177 ± 4
14	1	A	0	1	1	0	7116 ± 9	211 ± 3	258 ± 6
15	1	A	1	1	1	1	6405 ± 5	162 ± 4	141 ± 7
16	0	0	0	0	0	0	8157 ± 3	202 ± 2	282 ± 12
17	1	S	1	0	0	0	8268 ± 4	139 ± 3	112 ± 8
18	0	S	1	0	0	0	6950 ± 4	164 ± 6	260 ± 8
19	1	S	0	0	0	0	7676 ± 6	180 ± 5	235 ± 10
20	0	A	0	0	0	0	7853 ± 2	147 ± 1	261 ± 5
21	1	0	0	0	0	0	8949 ± 1	71 ± 1	138 ± 3
22	0	A	0	0	0	0	8519 ± 5	219 ± 5	177 ± 6
23	0	S/A	0	1	1	0	8858 ± 4	216 ± 3	325 ± 5
24	0	S	0	0	0	0	8884 ± 3	167 ± 3	178 ± 6
25	0	S	0	0	0	0	8252 ± 5	178 ± 5	282 ± 13
26	0	0	0	1	0	0	6907 ± 4	152 ± 6	54 ± 7
28	-	0	0	0	0	0	5507 ± 3	166 ± 2	315 ± 15
30	0	U	0	1	0	0	8412 ± 2	133 ± 2	347 ± 2
32	0	A	0	1	0	0	8057 ± 5	164 ± 6	246 ± 10
33	-	0	0	1	0	0	8101 ± 4	220 ± 4	24 ± 7
35	1	S	0	1	0	0	7254 ± 4	151 ± 4	207 ± 4
36	1	0	0	0	0	0	7480 ± 4	155 ± 3	113 ± 7
37	1	S	0	1	0	0	7795 ± 4	251 ± 4	5 ± 27
39	0	0	0	1	1	0	7200 ± 9	266 ± 5	271 ± 17
40	1	S	0	0	0	0	8165 ± 3	165 ± 3	7 ± 11
43	1	0	0	1	0	0	8070 ± 4	160 ± 3	63 ± 7
45	0	0	0	0	0	0	7764 ± 7	216 ± 5	292 ± 6
46	1	A	0	0	0	1	9147 ± 10	152 ± 5	329 ± 6
47	1	U	0	1	1	0	7208 ± 3	181 ± 2	102 ± 6
49	0	S	0	0	0	0	8887 ± 3	153 ± 3	162 ± 5
50	0	0	0	0	0	0	8406 ± 11	237 ± 11	287 ± 11
38	-	0	0	0	0	0	7331 ± 10	202 ± 24	209 ± 5
42	-	0	0	1	1	0	8454 ± 5	215 ± 27	38 ± 1
44	0	0	0	0	0	0	8381 ± 6	205 ± 16	128 ± 1
48	-	0	1	0	0	1	8607 ± 1	193 ± 8	183 ± 1
10	1	S/A	0	1	0	0	-	-	-
27	-	S/A	0	1	1	0	-	-	-
29	1	U	0	1	1	1	-	-	-
31	1	A	1	0	0	1	-	-	-

Table 3.1: Qualitatively derived features from inspecting the data cubes, the velocity fields and the xv diagrams, as well as results from the quantitative analysis of the velocity fields. The top part of the table are the galaxies with a successful fit to the velocity field, the middle part are the galaxies where a fit to the data cube was made and the bottom part lists the galaxies with kinematics that could not be described using simple tilted-ring models. A "0" indicates the absence, a "1" the presence of a feature. Some velocity fields are not resolved enough to perform an inspection of the kinematics, in these cases, the entry of column 1 is denoted as "-". In the case of galaxy 34 and 41 there is no data available. These rows are marked with "n/a". The columns describe respectively, galaxy ID (1), curved iso-velocity contours (2), presence of a warp: U- or S- shaped and/or A for asymmetric (3), close H I tail or complex (4), kinematical lopsidedness (5), morphological lopsidedness (6), obvious ongoing interaction (7). as well as quantities from the quantitative analysis: systemic velocity (8), rotation velocity (9) and position angle (10).

from spiral galaxies in general. One prerequisite for this is the derivation of rotation velocities and kinematical orientational parameters using tilted-ring models, as described in Sec. 3.4.1. Secondly, four nonparametric analyses of the asymmetries of the velocity fields are introduced and the results are presented.

3.4.1 Tilted-ring analysis

The software `KINEMETRY` (Krajnović et al., 2006) is used to fit tilted-rings to the velocity fields. This software performs harmonic decompositions along elliptical annuli and is thus analogous to the `reswri` software used in Chap. 2. It uses the following expression:

$$K(r_i, \psi) = c_0(r_i) + \sum_{n=1}^{N} s_n(r_i) \sin n\psi + c_n(r_i) \cos n\psi. \tag{3.1}$$

This expression describes a set of tilted-rings with radius r_i, azimuthal angle ψ and systemic velocity c_0. In a flat disk, with purely circular and concentric orbits, c_1 can be identified with the projected rotation velocity $V_{\rm rot} \cdot \sin i$, where $V_{\rm rot}$ is the rotation velocity and i is the inclination of the i-th ring at radius r_i. Nonzero s_1 and s_3 coefficients are occasionally used to estimate the elongation of the underlying potential (Schoenmakers et al., 1997). Similarly, non-zero c_2, s_2, c_3 coefficients indicate errors in the measured quantities such as position angle (Γ), inclination (i) and ring centre. `KINEMETRY` minimises the quantity $\chi^2 = s_1^2+s_2^2+c_2^2+s_3^2+c_3^2$ with respect to the inclination and position angle and finds a best-fit tilted ring model assuming circular orbits. Thus, where often the harmonic expansion is performed to learn about the non-circular motions present in the H I kinematics of a galaxy (e.g. Wong et al. 2004; Trachternach et al. 2008), it is in this case utilised in the minimisation of the figure of merit. As shown in Chap. 4, accurate determination of the profiles of non-circular motions are not possible at these distances. Considering the sum of the squared terms that give rise to deviations from circular orbits as residuals, which are to be minimised, is therefore a good alternative application of the harmonic expansion.

Moreover, in the case of strongly beam-smeared data, the radii at which the tilted-ring model is fitted have to be carefully selected. Tilted-rings are fitted to the velocity fields with the first radius $R = B_{\rm maj}$, where $B_{\rm maj}$ is the beam major axis length (which is equal to the beam minor axis length, see Sec. 3.2), until about 1.25 times R_{90} (R_{90} is the radius which contains 90% of the H I flux, see Wang et al. 2013 for its values) in steps of $\frac{1}{2}B_{\rm maj}$, such that the whole velocity field is considered. If this results in only one ring, its radius is set to $R = B_{\rm maj} + \frac{1}{2}(R_{90} - B_{\rm maj})$. This sampling scheme has the disadvantage that the rings are not independent. To reduce the number of free parameters, the photometric centres are used as (fixed) kinematical centres.

The uncertainty in the tilted-ring parameters is quantified on the basis of the 200 'perturbed' Monte-Carlo cubes from Wang et al. (2013) kindly provided by J. Wang (J. Wang, priv. comm., 2013). These are data cubes containing Gaussian noise convolved with the observational function (the Gaussian point spread function multiplied with a Gaussian with a full width at half maximum (FWHM) of two pixels in velocity direction to match the observed data cube). They are added to the observed data cube and the standard deviation of the Gaussian is repeatedly fine-tuned until it matches the standard deviation of the observed data cube. This is necessary since due to the smoothing, the distribution of the noise changes and its RMS is no longer equal to the RMS in the observed data cube. For each perturbed data cube, a Gauss-Hermite velocity field is calculated and a tilted-ring model is fitted to the data. For each ring and for each parameter, the average and the standard deviation are calculated, the rings are superimposed onto the velocity field and the projected velocities are plotted onto a xv diagram as a consistency-check (see appendix B for the velocity fields and xv diagrams). On the basis of these diagrams, a visual selection of the rings is performed, discarding the data points where the ring geometry does not match the velocity field or the measured velocity amplitude is not in agreement with the xv diagram.

In some cases, however, the fit to the velocity field does not converge due to a lack of independent data points. Analogous to Ch. 2.4.2, in these cases, a tilted-ring model is fitted to the data cube using the Tilted Ring Fitting Code (TiRiFiC, Józsa et al. 2007). To modify the number of free parameters to the limited number of independent data points, the TiRiFiC models are kept as simple as possible: position angle and inclination are not allowed to vary between rings (in other words, a flat disk is modelled and a warped disk geometry is not allowed). Since the TiRiFiC optimiser localises χ^2 local minima, accurate initial guess values are required for the parameters and therefore manual input is required. For this reason, TiRiFiC is only used for a small subset of galaxies from the "Bluedisk" sample. Since the results produced by TiRiFiC are relatively sensitive to the initial-guess values, estimating the uncertainties using the same method as for the velocity fields would not yield representative values. Therefore, an estimate for the uncertainties is obtained by repeating the fit for randomly generated starting values for $V_{\rm rot}$, i, $V_{\rm sys}$ and Γ in an environment around the best-fitting values and repeat the fit for n=100 times. For each of these parameters, the standard deviation of the output values is taken as the uncertainty in that parameter.

Galaxies with unsuccessful fits to the velocity fields are numbers 10, 27, 29, 31, 38, 42, 44 and 48. Galaxy number 10 has a complicated H I kinematical structure: its centre has low rotation amplitudes (c_1 terms) which rise according a rigid-body, whereas the outer radii show higher amplitudes. This could indicate either a fast-rotating outer H I ring or a very strong warp. Either of these cases is not possible to describe accurately using a model with a fixed inclination and position angle for all radii, and therefore this galaxy is excluded from the tilted-ring analysis. Galaxy 27 is very faint: it has the lowest flux of the sample and thus has very few independent data points. Besides, it shows signs of being warped and its disk is not extended. Modelling this galaxy therefore requires more complicated models, so it is excluded. Finally, galaxies 29 and 31 are excluded due to strong signs of interaction, making it very difficult to disentangle the kinematics of both galaxies. On the other hand, galaxies 38, 42, 44 and 48 could be successfully modelled using TiRiFiC. In summary, only 4 of the 48 sample galaxies could not be modelled. The kinematical parameters are shown in Table 3.1. The rotation velocities and position angles correspond to the outermost radii, whereas the systemic velocities are the average values over all rings.

3.4.2 Beam-smearing

A large source of uncertainty in the measurement of H I rotation curves is introduced by the finite size of the beam and is referred to as beam smearing (also called beam smoothing, see Teuben 2002 and Begeman 1987). In the case of large intensity and velocity gradients, the resulting rotation velocities will be biased to be skewed towards the region of higher surface brightness. E.g., in case of an outwards increasing rotation curve, the rotation velocities at the centre will be overestimated in case of an inwards decreasing H I surface density. Even in perfect observations without noise, the effect is still present (for a quantitative analysis see Józsa et al. 2007.) The beam smearing effect is especially pronounced in the case of intensity-weighted (first-moment) velocity maps and can be reduced by using Gauss-Hermite velocity fields (see e.g. Sec. 3.2 and de Blok et al. 2008).

Since the galaxies from the "Bluedisk" sample are located at larger distances than usually chosen for kinematic H I studies, beam smearing is the major limitation of a kinematical study, in particular if based on a velocity field analysis. The large distances result in small angular sizes of the galaxies: the median redshift distance of the sample is 117 Mpc, the median R_{90} is 46.5 arcsec whereas the beam size is approximately $(15-20)\times(15-20)/\sin\delta$ arcsec^2, corresponding to scales of roughly 9 kpc. The limited resolution causes significant beam smearing, most notably in (near) edge-on galaxies. Moreover, since the apparent size of the galaxies from the control sample is small (the median R_{90} is 39 arcsec) compared to the H I-rich sample (median R_{90} is 56 arcsec), this problem will play a larger role in the study of the control sample. The consequence of the beam smearing effect in this case is an enhanced stretching of the minor axis of the velocity field compared to the major axis, causing an underestimation of the inclination. Therefore, the inclinations resulting from the tilted-ring fits to the velocity fields cannot be used to convert projected velocity components into circular velocities and therefore, the r-band axis ratios from Wang et al. (2013) are used to convert the c_1 terms to rotation velocities. These axis ratios are converted into inclinations by

$$\sin i = \sqrt{\frac{1-(b/a)^2}{1-0.19^2}}, \tag{3.2}$$

following Pizagno et al. (2007). The factor 0.19 is the intrinsic axis ratio (see also Hubble 1926), hence the axis ratio if the galaxy is viewed edge-on ($i = 90°$). It thus takes into account the non-zero thickness of the disks, see also Sec. 4.4.2.

The role of the beam smearing effect in the analysis of kinematical properties of velocity fields, especially the distance dependence of the extracted parameters is studied in more detail in Sec. 4.4.1.

3.4.3 Comparison of position angles and systemic velocities

$\Delta\Gamma_{HI}$ is defined as the difference between the kinematical H I position angle (Γ) as determined from the velocity fields, and the morphological H I position angle from Wang et al. (2013). $\Delta\Gamma_{opt}$ is the difference between the kinematical H I position angle and the optical morphological Γ. In the galaxies where there are clear indications for a warp, however, Γ is ambiguous, since in these cases Γ is usually a function of galactic radius. Therefore, the Γ corresponding to the outermost radius is taken. As an optical position angle, the Γ derived from the r-band averaged light distribution is taken from Wang et al. (2013). This Γ offset measures the misalignment between the optical and the outer H I component of the galaxy, and deviations are indicative of warping of the H I disk (see Sec. 3.3). In the comparison of the H I morphological and optical Γ with the H I kinematical Γ, the galaxies are excluded which were also excluded in Wang et al. (2013). These are: galaxies 7, 13, 29, 31 and 46, which were classified in Wang et al. (2013) as interacting, and 1, 5, 10, 21, 28 and 37 as being oriented too face-on (H I axis ratio greater than 0.85). In all cases, the Kolmogorov-Smirnov (KS) test probability is computed, which is shown in the top-right of the figures (see Fig. 3.2). This test statistic is used to compare two distributions by comparing their cumulative probability distributions, and is independent of their underlying probability distribution. The KS-probabilities shown in this work can be interpreted as follows: a low value indicates a significant difference between the samples, whereas a high value suggests that both samples stem from the same population. Nevertheless, since the sample size is of the order $n = 20$ for each of the subsamples, the KS-probability merely gives an indication if there is a statistical difference between the populations, but will

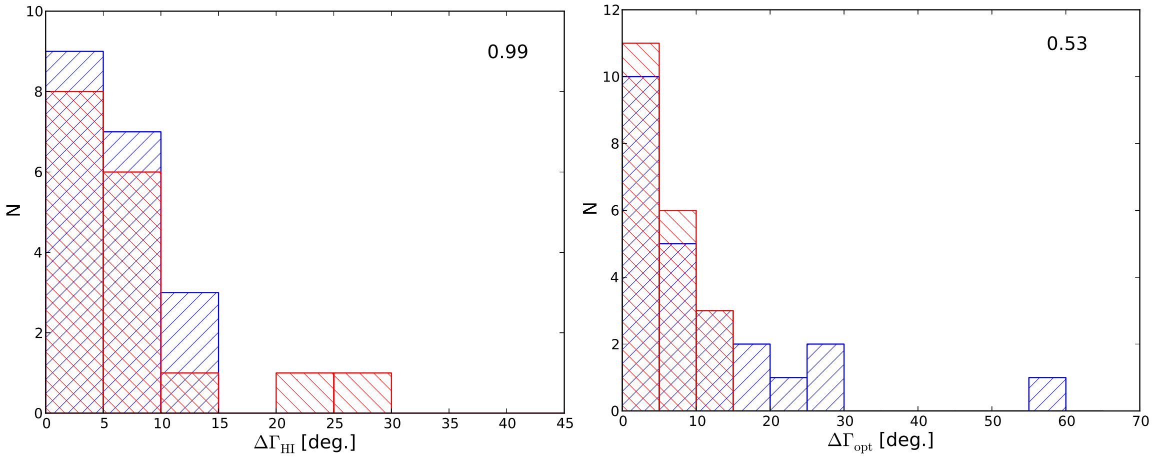

Figure 3.2: *Left*: difference between the kinematical and the morphological H I position angle. *Right*: difference between the kinematical H I position angle and the optical position angle. The H I-rich sample is shown in blue, the control sample in red. The number printed on the top-right is the KS-probability.

never present conclusive evidence.

Based on the KS-probability for the position angle differences, no statistical evidence is found for a difference between morphological and kinematical $\Delta\Gamma$ for the H I-rich and the control sample galaxies. Also in the comparison with the optical $\Delta\Gamma$ there does not seem to be a significant difference between the control- and the H I-rich sample. There are, however, some H I-rich galaxies that have a larger $\Delta\Gamma$ than the control sample galaxies. This fits to the result from the visual inspection: there are a few more H I-rich galaxies that show warping (19), but given the low number statistics, not significantly more than in the control sample (11). It is again pointed out that both visual inspection and the measurement and comparison of position angles to estimate if there are differences in the intrinsic orientation misalignment in the sample galaxies are biased or even restricted towards the detection of warping perpendicular to the line of sight. The visual inspection is biased in the sense that a position angle warp is identified more easily by eye than a change in inclination, while the study of the position angle differences at different radii is by definition restricted to the detection of position angle warps. Including the inclination could in principle deliver better statistics. It is here that one is hampered by the limitations of the finite resolution in combination with the usage of velocity fields, which makes a derivation of the inclination angle from the H I kinematics impossible. This systematical effect is also shown in more detail in Ch. 4.4.1. In any case, a possible explanation for a real discrepancy could be connected to the fact that, as shown in Wang et al. (2013), the sample galaxies follow the H I mass-size relation and hence the H I-rich have larger disks compared to the control sample galaxies. Since the H I disk is in general coplanar to the optical disk within R_{25}, and evolves at larger radii (Briggs, 1990), it is by selection more likely to encounter a warp in a H I-rich galaxy than in a control sample galaxy (García-Ruiz et al., 2002).

In Wang et al. (2013), the authors establish that the H I and optical centres-of-mass are not offset in right ascension and declination. To verify whether this is also the case in central velocity, a quantity $\Delta V_{\rm sys}$ is defined as the difference between recession velocity from the optical redshift and the fitted H I systemic velocity, which results from taking the mean over all the

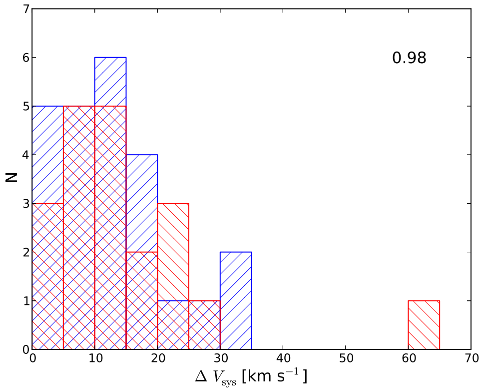

Figure 3.3: Difference between $V_{\rm sys}$ from the H I kinematics and from redshift. The values printed on the top-right are the KS-probabilities. The H I-rich sample is shown in blue, the control sample in red.

fitted rings (see Fig. 3.3). Based on the value of the KS statistic, there is no significant difference between the studied populations. Moreover, the overall differences are not very large, most are below 30 kms^{-1}, which corresponds to a redshift of 10^{-4} or 0.4% of the average redshift of the sample. Since the redshift accuracy of SDSS DR7 is of the order of 30 km s^{-1} rms[3], it can be concluded that there is no significant offset between the redshift and the systemic velocity resulting from the H I kinematics.

3.4.4 Deviations from a flat-disk

Here, a generic method is defined to identify the presence of any asymmetry in the H I disks of the "Bluedisk" sample. The parameters resulting from the tilted-ring fits are used to construct model velocity fields corresponding to a flat disk, hence, with fixed inclination and position angle. Then, a simple parameterisation of the rotation curve is applied, assuming that the terminal rotation velocities corresponding to the largest radius from Sec. 3.4.1 trace the maximum rotation velocity of the disks. The polyex model is used as a rotation curve parameterisation (Giovanelli & Haynes, 2002):

$$V_{\rm PE} = V_0 \left(1 - e^{-r/r_{\rm PE}}\right)\left(1 + \frac{\alpha r}{r_{\rm PE}}\right). \tag{3.3}$$

Here, V_0 is the maximum rotation velocity, $r_{\rm PE}$ is a scale length for the inner part of the rotation curve and α is a parameter describing the rotation curve decline. To interpolate the rotation curve, $\alpha = 0$ has been set (no rotation velocity decline). The slope is chosen such that at R_{90} the rotation velocity has reached $0.999V_0$, hence $r_{\rm PE} = \frac{-R_{90}}{\ln 0.001}$. For this, the parameters from Table 3.1 are used: the mean value of the position angle and systemic velocity over the rings and the outermost rotation velocity. To verify whether the assumed rotation curve describes the data sufficiently well, the rotation curves are superimposed onto the xv diagrams in Figs. B.3 and B.4 of the appendix.

These velocity fields are then subtracted from the observed velocity fields and the H I column-density weighted sum is computed. This number describes the global deviation from the simple

---

[3] http://www.sdss.org/dr7/

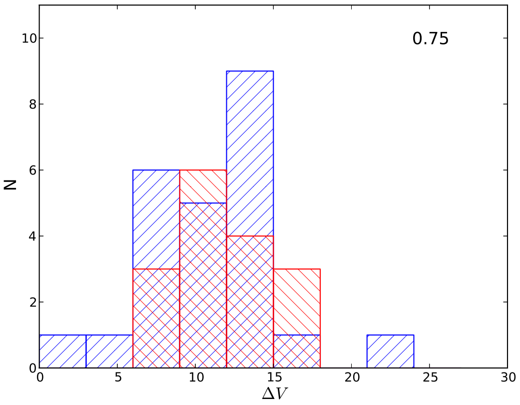

Figure 3.4: Deviation from flat rotating disk. The values printed on the top-right are the KS-probabilities. The H I-rich sample is shown in blue, the control sample in red.

flat disk model and Fig. 3.4 shows a histogram of the deviations. For this analysis, the galaxies 27, 29, 31, 38, 42, 44 and 48 are excluded since they are either interacting or are not well-resolved enough to perform this analysis. As an uncertainty measure, this analysis is repeated for all the velocity fields derived from the perturbed data cubes and a typical uncertainty of 5% is found. The KS probability does not present any statistical evidence for a difference between the samples. Assuming that the measured rotation velocities roughly trace the maximum rotation velocity, V_0, and that the used model rotation curve estimate the rotation curve sufficiently well, this residual directly traces the deviations from a symmetrical, flat disk. This quantity therefore suggests that the H I-rich sample has similarly regular H I kinematics as the control sample: the deviations from a flat disk model in both samples cannot be distinguished in the limits of this method. This number is, however, strongly influenced by the value of the inclination, which is taken from the optical axis ratio since it cannot be measured from the H I kinematics by using velocity fields.

3.4.5 Asymmetry analyses

This section presents a simple analysis of three measures of a galaxy's kinematic asymmetry that do not involve fitting a model to the data nor any assumptions about the galaxy inclination or the rotation curve using rotations and reflections. Each method is sensitive to a different asymmetry and therefore traces different warping modes. All measures quantify kinematical lopsidedness. In the following, the data is rotated and reflected about the centre.

The first asymmetry measure is a measure of point asymmetry (or central asymmetry) of the velocity field. It consists of subtracting the systemic velocity from the observed Gauss-Hermite velocity field, denoted as $V_0(i,j)$, and rotating $V_0(i,j)$ by 180 degrees about the centre to get $V_0^{180^\circ}(i,j)$. The original column-density weighted mean of the absolute values of this residual is taken as a measure of the asymmetry. This asymmetry measure is called Asymmetry 1 (A1):

$$\mathrm{A1} = \frac{\sum_{i,j} |V_0(i,j) + V_0^{180^\circ}(i,j)| \cdot N_{H\,i}(i,j)}{\sum_{i,j} N_{H\,i}(i,j)}, \tag{3.4}$$

where $V_0(i,j) = V(i,j) - V_{\rm sys}$. As an input, this quantity requires only an accurate measurement of the systemic velocity. This asymmetry measure will increase in the presence of galaxy lopsidedness and/or U-shaped and asymmetric warps, but is insensitive to (antisymmetric) S-shaped warping.

The second asymmetry measure analyses the mirror asymmetry about the minor axis of the velocity fields. To compute this, the systemic velocity is subtracted from the velocity field and the velocity field is rotated by -Γ and reflected it about horizontal axis. The residual is then calculated by adding the resulting maps. Asymmetry 2 (A2) is defined as the column-density weighted mean of the residuals, hence:

$$\mathrm{A2} = \frac{\sum_{i,j} |V_0^{-\Gamma^\circ}(i,j) + V_0^{-\Gamma^\circ}(i,-j)| \cdot N_{H\,i}(i,j)}{\sum_{i,j} N_{H\,i}(i,j)}. \tag{3.5}$$

Apart from lopsidedness, this quantity is sensitive to S-shaped warps but not to the occurrence of U-shaped warps. It requires inputs on the position angle and the systemic velocity.

The final asymmetry measure analyses the mirror asymmetry about the kinematical major axis. In practice, the images is rotated about -Γ and reflected it about the vertical axis. This velocity field is ten subtracted from the rotated observed velocity field. In this case, no subtraction of $V_{\rm sys}$ is required due to the corresponding symmetry. Asymmetry 3 (A3) is then defined to be the weighted average of this residual:

$$\mathrm{A3} = \frac{\sum_{i,j} |V^{-\Gamma^\circ}(i,j) - V^{-\Gamma^\circ}(-i,j)| \cdot N_{H\,i}(i,j)}{\sum_{i,j} N_{H\,i}(i,j)}. \tag{3.6}$$

This asymmetry measure is sensitive to kinematical lopsidedness as well as S- or U-shaped warps.

The statistical uncertainties are derived in the same way as in the previous sections and a typical uncertainty of 5-10% is established. The galaxies 10, 27, 29, 31, 38, 42, 44, 46 and 48 are excluded from all these asymmetry figures for having either an insufficiently resolved velocity field or the interaction companion influencing the measurement of the asymmetry figures. In all other cases of the interacting galaxies as listed in Sec. 3.3, the interaction companion cancels out due to addition or subtraction of a rotated or reflected map.

The distributions of the asymmetry parameters are shown in Fig. 3.5. In the case of Asymmetry1, the KS-probability indicates a (weakly statically significant) probability that there is a difference between the H I-rich and the control sample. This means that control sample galaxies have a higher value of Asymmetry1 and thus means that the control sample galaxies tend to show more U-shaped and asymmetric warping, a trend also observed in Sec. 3.3. However, if one removes galaxies 26 and 50 (the galaxies with the highest Asymmetry1 value) from the analysis, this probability drastically increases to 0.15, which would not be statistically significant.

Concerning asymmetry measures 2 and 3 it can be observed that the distributions of both samples largely overlap. Moreover, the KS probabilities are quite high and thus do not give any reason to suspect that the H I-rich- and control sample galaxies differ in the asymmetry of their H I kinematics.

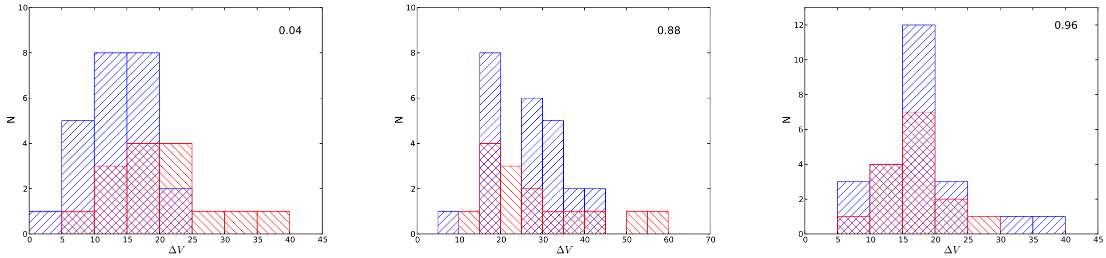

Figure 3.5: *Left*: Asymmetry1, *middle*: Asymmetry2, *right*: Asymmetry3. The values printed on the top-right are the KS-probabilities. The H I-rich sample is shown in blue, the control sample in red.

Weighting the residuals with the column densities possibly does not take into account the asymmetries in the fainter, low column density outer parts of the galaxies. Performing an identical analysis of these three asymmetry measures without the column density weighting gives similar histograms.

To sum up, considering these three asymmetry indicators, no significant difference between the H I-rich and the control sample galaxies is found, in line with the conclusions from the qualitative analysis. Only Asymmetry1 seems to confirm the trend that the control sample galaxies have slightly higher rate of U-shaped or asymmetric warping.

3.5 The H I Tully-Fisher relation for high mass gas-rich galaxies

As discussed for ETGs in Chap. 2, this section studies the K-band TFR and the baryonic TFR for the "Bluedisk" ensemble. The TFR is a tight correlation between the inclination corrected width of the H I line and the absolute magnitude, and therefore relates circular velocity to luminosity. The baryonic TFR is seen as a more fundamental relation between circular velocity and baryonic mass (Walker, 1999; McGaugh et al., 2000). More recent studies of the baryonic Tully-Fisher Relation (TFR, Tully & Fisher 1977) show that it is preferable to use asymptotic circular velocities resulting from resolved H I , CO and Hα rotation curves (see e.g. Verheijen 2001; Davis et al. 2011; McGaugh et al. 2001). Since for the "Bluedisk" galaxies, due to the limited resolution it is not feasible to fit fully-resolved rotation curves to the data, the velocities corresponding to the outermost ring can be considered as an intermediate measure of circular velocity between the line-widths and resolved rotation curves. For further details on the TFR, it is referred to Ch. 2.

For this sample it is particularly interesting to compare the K-band TFR with the baryonic TFR: if the baryonic TFR were the "true" underlying relation, one would expect the K-band TFR to be not very well defined and to have a larger scatter because a significant fraction of the baryons is in the form of neutral gas. This component, however, cannot be traced by the K-band emission. To derive the baryonic TFR, the stellar masses based on stellar population synthesis from Wang et al. (2013) are used. These masses were derived using the methods described in Bell et al. (2003), using a stellar mass-to-light ratio derived from the g-i colour. These coefficients from their Table 7 of the Appendix were corrected to be compatible with the MPA/JHU catalogue (J. Wang, priv. comm., 2013). Consequently, the baryonic mass is computed according to $\mathcal{M}_{\rm bar} = \mathcal{M}_\star + 1.33\mathcal{M}_{HI}$, where the same value of 1.33 as in McGaugh

(2012) is used to account for the presence of helium.

In this analysis, the galaxies 1, 5 and 37 are not considered since they have inclinations of 34, 21 and 31 degrees, respectively. These values are in the range where a small error in the inclination has a large impact on the rotation velocity (see Sec. 2.4). Also galaxy 21 is excluded since its r-band inclination of 51 degrees does not seem to agree with the H I inclination which seems to be lower (compare the H I intensity maps in the appendix of Wang et al. 2013). In the following, Sec. 3.5.1 compares the K-band TFR for the "Bluedisk" galaxies with the an existing K-band TFR for massive spirals galaxies, Sec. 3.5.2 presents the baryonic TFR for the "Bluedisk" ensemble, Sec. 3.5.3 compares the latter with a baryonic TFR for gas-rich galaxies at the low mass end. Finally, Sec. 3.5.4 considers the scatter of the TFR.

3.5.1 Comparison with the Noordermeer & Verheijen (2007) K-band TFR

Fig. 3.6 shows the K-band TFR in a comparison with the K-band TFR from Noordermeer & Verheijen 2007 (NV07, hereafter) in the left panel. The NV07 TFR is a TFR for nearby galaxies on the high-mass end based on circular velocities from resolved rotation curves (for more information, see Sec. 2.5.2.2). The K-band apparent magnitudes from the 2MASS catalogue (Skrutskie et al., 2006) were taken and converted into absolute magnitudes using the redshift distances with $H_0 = 70$ km s^{-1} Mpc, to be compatible with Wang et al. (2013). An uncertainty in H_0 of 5 km s^{-1} Mpc^{-1} has been assumed. Given the large scatter, it has not been attempted to quantify the scatter and offset of the "Bluedisk" TFR, since these quantities would not be statistically significant. Qualitatively, the TFR for the "Bluedisk" sample galaxies seems to be offset from the NV07 TFR. One reason for this could be the differing stellar populations in both samples. The NV07 sample includes many early-type spirals, while the "Bluedisk" sample is by selection gas-rich and actively star forming, such that their luminosity might be increased even in K-band. In that sense, a comparison of these two different samples is consistent with the assumption that the underlying physics of the TFR is rather connected to the baryonic stellar mass content or distribution and not the light distribution. This will be addressed in the next paragraph of this section. However, in the K-band TFR as presented here, one is indirectly neglecting a significant mass fraction provided by the gas. If it is assumed that the fundamental relation is the baryonic TFR, then the gas-rich and the normal spiral galaxies should be on the same baryonic TFR, as well as the NV07 galaxies. On the other hand, if for these galaxies, the K-band TFR is constructed, one would expect to observe an offset of the gas-rich galaxies towards lower K-band luminosities. The reason for this is that the K-band TFR only traces the stellar mass and not the total baryonic mass, because the gas component is not included. However, no evidence for such an offset is found. In other words, the fact that the galaxies from the sample seem to lie on the brighter side or alternatively the side with lower rotation speed of the NV07 relation, again indicates a significant difference in the stellar composition between the "Bluedisk" sample and the NV07 sample. Moreover, it is suspected that the K-band does not trace the disk mass of galaxies very well due to the contribution of TP-AGB stars (see e.g. Tonini et al. 2009, 2010 and also Sec. 2.6). A scatter of 0.48 mag is measured in the "Bluedisk" K-band TFR. This number exceeds their measured scatter of 0.34 mag corresponding to the NV07 asymptotic rotation velocity tracer.

3.5.2 The baryonic TFR for the "Bluedisk" galaxies

The right panel of Fig. 3.6 shows the baryonic TFR for the H I-rich galaxies compared to the galaxies from the control sample. Although statistically, TFRs of the control- and H I-rich galaxies are not offset, there does seem to be an offset of the blue points towards higher baryonic masses / lower rotation velocities. It thus seems that H I-rich galaxies are somewhat offset from the baryonic TFR as defined by the galaxies with a normal gas content. To study this in more detail, the residuals with respect to the McGaugh (2012) relation are shown (see the left panel of Fig. 3.7) in dependence of the H I to baryonic mass. The McGaugh (2012) baryonic TFR has been chosen as a reference, since it is a well-calibrated relation (see Sec. 3.5.3). In this graph, it seems that the larger the fraction of H I mass is, the higher the residual mass with respect to the reference baryonic TFR. This indicates that for increasing H I masses, the galaxies are located more above the reference baryonic TFR (at higher $\mathcal{M}_{\rm bar}$ and/or lower $v_{\rm rot}$). The purple diamonds, which represent the (low mass) galaxies from McGaugh (2012) do not participate in this trend. Therefore, this trend would only apply to the high-mass end. Despite the fact that this relation is not confirmed statistically, if this trend would prove to be real, it could imply two things: i) in the high mass regime, the baryonic TFR for gas-rich spirals is different baryonic TFR for normal (star dominated) spirals and/or ii) the stellar masses, in particularly the ones for the control sample, are not calculated correctly. In the control sample galaxies, $\mathcal{M}_{\rm bar}$ is dominated by stars, whereas in the H I-rich sample, a large part of the mass is in the form of gas. A systematic error in the determination of $\mathcal{M}_\star$ would therefore have a greater impact on the calculations of the stellar masses for the control sample galaxies than the H I-rich sample.

3.5.3 The baryonic TFR for gas dominated galaxies

A comparison of the baryonic TFR for the “Bluedisk” galaxies with the baryonic TFR from McGaugh (2012) and the baryonic TFR from NV07 is presented in Fig. 3.6. The sample of McGaugh (2012) consists by selection of nearby gas-rich galaxies. This has the advantage that the dependence slope and intercept of the baryonic TFR on the computation of the stellar masses is minimised, since the computation method of the gas masses is independent of the assumed initial mass function and colour based mass-to-light ratios. Therefore, this relation can be considered as a calibrated baryonic TFR since the large systematical uncertainties in stellar mass determination are minimised. Moreover, Catinella et al. (2012) confirmed the validity of this baryonic TFR for high-mass galaxies using a sample of about 500 galaxies with high stellar mass fractions.

The McGaugh (2012) masses based on Hubble-flow distances are corrected to correspond to the value based on the Hubble constant that is used in the mass estimates of this work. In NV07, the stellar masses were computed using a fixed K-band mass-to-light ratio of $(\mathcal{M}/L)_K = 0.8$, corresponding to a maximum disk scenario (see Sec. 2.5.2.2). Due to the mentioned contribution of the TP-AGB stars, as well as results from the DiskMass-survey (Bershady et al., 2010), which has shown that galactic disks are not consistent with the maximum-disk scenario (see e.g. Martinsson 2011; Bershady et al. 2011), this conversion factor is not used to compute the stellar masses. Instead, the stellar masses of the NV07 galaxies which are in the SDSS catalogue were recomputed using the same method used before to compute the masses of the “Bluedisk” ensemble (J. Wang priv. comm., 2013). The stellar masses from McGaugh (2012) are also based on stellar population synthesis models, so the methods by which the stellar masses have been acquired are similar in the compared works.

A global baryonic mass uncertainty 0.2 dex is taken (0.15 for $\mathcal{M}_\star$ and 0.05 for $\mathcal{M}_{\rm HI}$). The data seems to follow the McGaugh (2012) data very well, whilst appearing to have larger scatter than the K-band TFR. In units of $\log \mathcal{M}_\odot$, a scatter of 0.23 is measured, which is equivalent to 0.58 mag and therefore comparable to the “Bluedisk” K-band TFR scatter. An inverse fit is performed to the data points keeping the slope fixed to the McGaugh (2012) baryonic TFR and an intercept of 1.84 ± 0.04 is found, matching the intercept he found.

Also the circular velocity versus stellar mass (left panel) and the circular velocity versus H I mass (right panel) are shown in Fig. 3.8. The stellar mass TFR seems to agree well with the McGaugh (2012) and the NV07 data points. In the figure describing the rotation velocity versus H I mass relation, there seem to be a number of galaxies which fall below the trend, having less H I mass than would be suspected from the correlation. This is visible for the galaxies from all three samples. It is unclear what causes this deviation. One can exclude molecular gas as a cause since the COLD GASS survey (Saintonge et al., 2011), which is a large scale survey of molecular gas in nearby galaxies, has shown that the molecular gas does not constitute a large part of the gas mass and can be neglected in studying the baryonic TFR (Catinella et al., 2012).

3.5.4 Scatter in the (baryonic) TFR

Apart from unregarded measurement uncertainties, a few reasons for the observed, larger scatter in the "Bluedisk" baryonic TFR are discussed here.

- One possibility could be connected to the low resolution of the H I observations. Several galaxies are not well resolved by the WSRT. Therefore, it is uncertain whether or not one is measuring the circular velocity on the flat part of the rotation curve. This is illustrated by the position velocity diagrams in the Appendix: in several galaxies, e.g. galaxy 36, it could be possible that one is measuring the rotation velocity at a radius where the rotation curve has not flattened yet and therefore one possibly underestimates the rotation velocity. If this were true, however, one would expect to observe a systematic offset especially of the control sample with generically a smaller size of the disks in the baryonic TFR towards higher velocities, which is not observed.

- The other systematic effect is the usage of the r-band axis ratios to determine the disk inclination, see Sec. 3.4.2. The inclination of the stellar disk is not necessarily identical to that of the H I disk, see e.g. Briggs (1990), but it cannot be said that it is generally smaller or larger. Another possible source of scatter could be ongoing accretion suspected to take place in the H I-rich galaxies. If the galaxies are actively accreting gas via minor mergers, the gas has possibly not settled on circular orbits, and instead, this gas could be rotating on elliptical orbits, causing additional scatter in the measured rotation velocity and therefore additional scatter in the baryonic TFR.

- A third reason might be sought again in the stellar composition of the galaxies in the sample. McGaugh (2012), with which this work's results are compared, studies gas dominated galaxies which allow a mass determination that is less dependent on the initial-mass function (IMF). If, for some reason, the composition of the sample galaxies does not allow for a mass determination as accurately as used for the McGaugh sample, the result could be a larger spread.

In summary, except for the larger scatter, there is no strong evidence that the baryonic TFR of the "Bluedisk" sample differs from the baryonic TFR of gas-rich galaxies as shown by McGaugh (2012). There are some indications that the K-band TFR of the "Bluedisk" sample is distinct from the K-band TFR of early-type spirals as shown by NV07. As in former studies, these results indicate that the physics behind the TFR is related to the total mass content and the

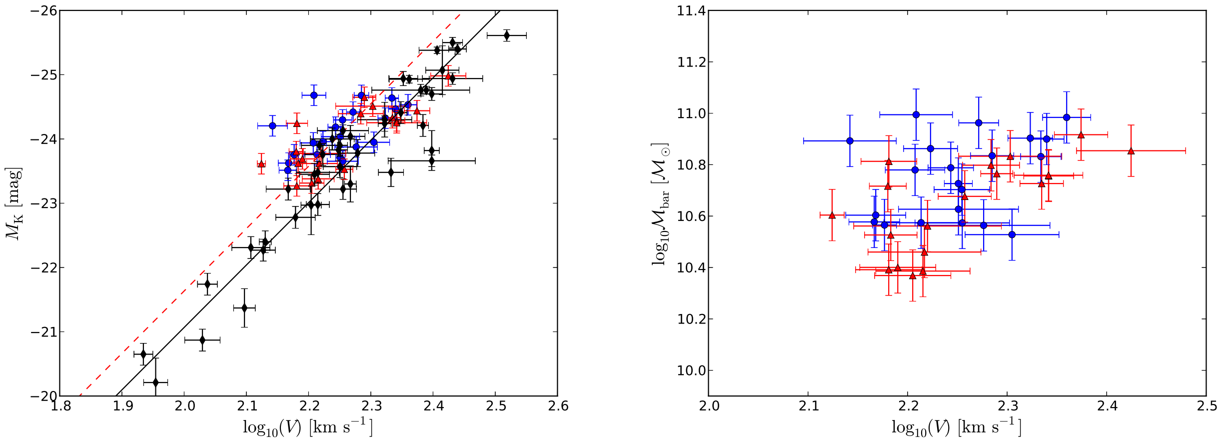

Figure 3.6: *Left*: K-band TFR compared with the NV07 sample. The black diamonds are the NV07 galaxies and the black solid line their best-fitting TFR based on their asymptotic rotation velocities. The blue circles are the H I-rich galaxies and the red triangles the control galaxies. The red dotted line is the line describing the fit to the data points with a slope fixed to the NV07 slope. *Right*: baryonic TFR for the H I-rich (blue circles) and control sample (red triangles) galaxies.

intrinsic mass distribution in spirals, no strong evidence is found that especially the intrinsic mass distribution may be different in both sub-samples of the target galaxies.

3.6 Discussion and outlook

The kinematics of the H I gas of a sample of 48 galaxies as part of the “Bluedisk”s project is studied. The sample is composed of 25 galaxies with an excess H I content as predicted by stellar mass surface density and optical-/UV colour, and 23 spiral galaxies of comparable redshift, stellar mass, stellar surface mass density and inclination without this excess H I. Velocity fields are derived from the data cubes by fitting Gauss-Hermite polynomials to the line profiles. These are used to search for kinematic disturbances and asymmetries.

Due to the large distance of the galaxies, the H I distributions of the galaxies are insufficiently resolved to explicitly model kinematical lopsidedness and other deviations from a flat rotating disk by using the velocity fields. Moreover, radial profiles of the inclination angle and position angle cannot be extracted and therefore, warping of the disks cannot be explicitly modelled. Therefore, firstly a visual analysis of the data is undertaken to investigate whether there are are any notable kinematical differences between the galaxies in the sample. Secondly, tilted-ring fits are performed to constrain the rotation velocities as well as position angles and systemic velocities. Thirdly, under the assumption that ongoing accretion results in first order kinematical asymmetries in the galaxies, three asymmetry measures are defined and the results are compared between the two subsamples.

Based on the current knowledge of galaxy formation and evolution, cold accretion is an important phase in the creation of disk galaxies (White & Rees, 1978; Sancisi et al., 2008). The

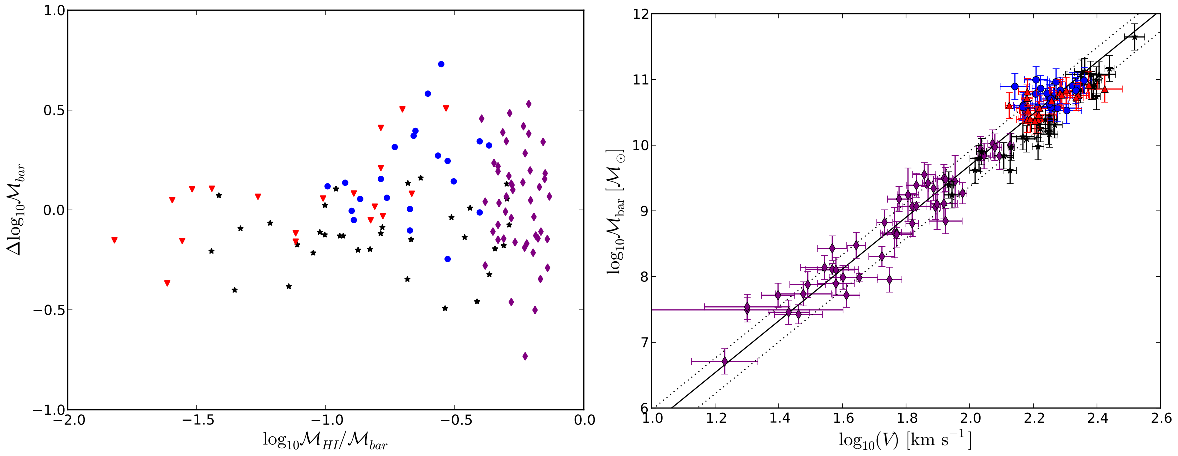

Figure 3.7: In these figures, the purple diamonds are gas-dominated galaxies from McGaugh (2012), the black stars are the NV07 galaxies with recomputed stellar masses. The blue circles are the H I-rich galaxies and the red triangles are the control sample galaxies. *Left*: logarithmic H I to baryonic mass fraction vs. offset from the McGaugh (2012) relation. *Right*: baryonic TFR comparing the different samples. The black solid line is their best-fitting line corresponding all the data points from McGaugh (2012).

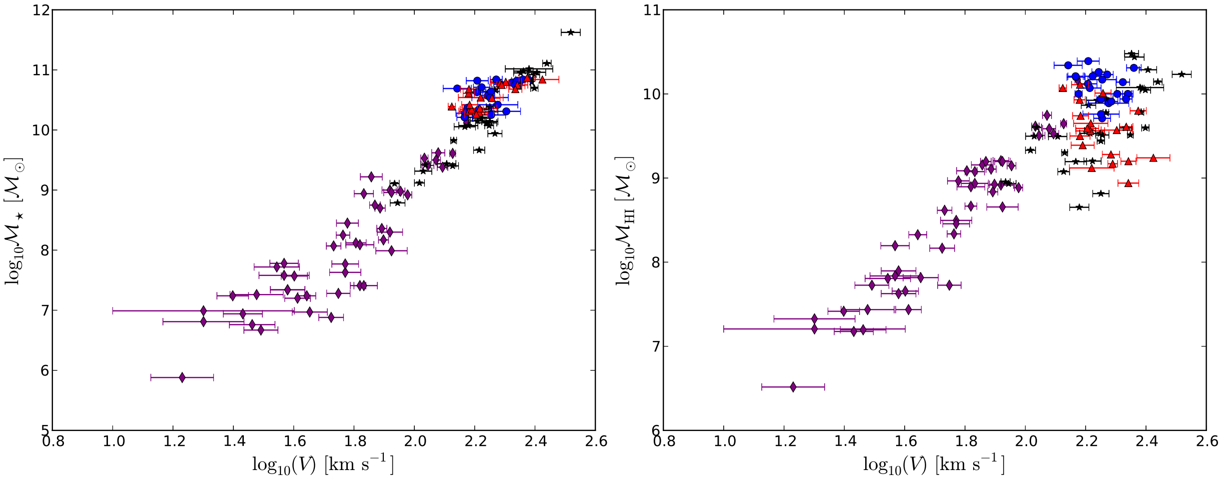

Figure 3.8: *Left*: Rotation velocity vs. stellar mass. *Right*: Rotation velocity vs. H I mass. The meaning of the symbols is the same as in Fig. 3.6.

corresponding signatures such as lopsidedness and warps are expected to be more strongly observable in the H I-rich sample compared to the control sample. To study whether there is evidence for clearer signs of accretion between these samples is the goal of this chapter.

Features such as warps and lopsidedness have been connected to accretion (e.g. Sancisi et al. 2008). However, it is unclear which of the proposed features can be connected to gas accretion, and which could result in the required (continuous) transport of gas to the star forming regions of a galaxy. If the H I-rich galaxies were accreting gas more actively than the control sample galaxies, one would expect to see a significantly larger fraction of these galaxies to show signs of lopsidedness and asymmetric warping compared to the control sample galaxies. One would also expect them to be in a richer environment. The latter will be the subject of a future study, presenting a systematic analysis of the environments of the galaxies in the H I-rich ensemble. Here a short list is presented, summarising the main points of this work:

1. From the qualitative analysis, the fraction H I-rich galaxies showing signatures of symmetric warping or having an H I cloud complex or H I tail is larger than in the case of the control sample galaxies. For the case of lopsidedness and asymmetric warping the opposite trend is found. These results may hint at a trend but have a low statistical significance.

2. Beam-smearing is a very important factor in studying the H I kinematics of galaxies located at these distances: one is not able to fit more than one or two independent tilted-rings to the velocity field, excluding the possibility of obtaining a resolved rotation curve. This is most relevant for the control sample galaxies, which in most cases contain less H I gas, and with that smaller H I disks.

3. The results from the tilted-ring fits are used for a simple interpolation of the rotation curve to construct model velocity fields corresponding to a flat rotating disk. These are used to quantify the strength of deviations from the kinematics of a flat disk for both samples and no difference is found between both subsamples.

4. The velocity fields are used to compute different asymmetry measures and no difference is found between the gas-rich and the control sample galaxies.

5. The K-band TFR of the complete sample, including H I-rich and control galaxies is slightly offset towards lower velocities or alternatively higher luminosity from the K-band TFR found by NV07. However, the baryonic TFR of the sample galaxies, the baryonic TFR of a subsample of NV07, for which photometric information could be acquired from SDSS, as well as the baryonic TFR of gas-rich galaxies presented by McGaugh (2012) are largely consistent with each other. The scatter of the baryonic TFR of the "Bluedisk" sample is slightly larger than expected, which may be explained by a larger spread in the stellar population properties and/or beam smearing effects due to the large distances of the galaxies. It can be concluded that while it is confirmed that the TFR is mass driven, there is an indication that the especially H I-rich galaxies lie above the baryonic TFR as defined by the control sample galaxies which have a normal H I content.

The goal of this chapter is to study the possible presence of signatures in the H I kinematics indicating accretion of cold gas. There are no signatures of an enhanced asymmetry in the H I-excess galaxies, pointing to very regular gas accretion. Moreover, the central velocities of the H I and optical part of the galaxies are very similar, also supporting the fact that the gas is not episodically accreted resulting in large angular momentum input. In summary, no conclusive evidence of an enhanced episodic gas accretion for extremely gas-rich spiral galaxies is found.

These results are in line with the findings of Wang et al. (2013) and Wang et al. (2014), the observational focus of which lay on the quantification of the morphology of the H I disks. Again, if accretion is taking place, a smooth mode of accretion is implied rather than the collimated inflow of gas into the central regions, where the disk resides. Wang et al. (2014) were able to show that this is in principle consistent with the standard picture of galaxy formation and an inside-out scenario of well-ordered accretion as from hot coronal gas, while cold, direct and filamentary accretion, as well as cold gas accretion from satellites, seem to play a less important role for the galaxies in the sample. This could be related to the redshift range which is considered in the "Bluedisk" survey. The galaxies in the sample are in a redshift range of $0.01 \leq z \leq 0.03$. The number of Lyman-α clouds (via the Lyman-α forest), which are neutral hydrogen clouds that absorb Ly-α radiation along the line-of-sight, gives an indication on the amount of cold gas depending on the redshift. The number density of these clouds varies according to $\frac{dN}{dz} = (\frac{dN}{dz})_0 \, (1+z)^\gamma$, where $1.9 \leq \gamma \leq 2.8$ (Rauch, 1998). This implies that observations at a higher redshift have to be performed to investigate cold accretion. The Square Kilometer Array (SKA), which will have a higher angular resolution compared to the current arrays such as the WSRT (about 1 arcsec. vs. 30 arscec., see Huynh & Lazio 2013) and a higher sensitivity, will be able to investigate cold accretion at higher redshifts.

Nevertheless, the fact that no difference in accretion signatures between the samples is found poses the question whether one is measuring the correct quantity. Another possibility is that all galaxies are actively accreting gas, but at different rates. Since there is no information available on accretion rates and relevant time scales, one cannot investigate this possibility. Alternatively, it is possible that there are other parameters that has not been studied, which cause the difference in H I content between the galaxies from the sample. Such a factor could be the environment: the H I-rich subsample could be in slightly denser environments. A slightly higher presence of gas around the galaxies could lead to H I-rich systems.

In the future, with the introduction of large-scale H I interferometric surveys, kinematical studies of very large samples of galaxies will become possible at distances of the order of 100 Mpc. The tilted-ring fitting method used in this work to fit the velocity fields using `KINEMETRY`, offers a fast, stable and uncomplicated method of studying the global kinematics of these galaxies. However, the major shortcoming is that by creating a velocity field, the beam smearing effect prohibits the derivation on the H I inclination from the kinematics. Instead, for future work, a modelling of the full data cube is suggested, utilising the full potential of the data and allowing a more complete description of the H I kinematics which includes warps and kinematical lopsidedness.

Chapter 4

Systematic effects in the analysis of H I kinematics

4.1 Introduction

In this chapter the focus is on the accretion of gas in spiral galaxies. However, the sample definition and therefore, the method of analysis is fundamentally different in comparison to Chap. 3. In Chap. 3 the focus was on a larger number of relatively distant galaxies (around 120 Mpc). Here, the focus is on a case study of one nearby galaxy: NGC 2403 with a distance of 3 Mpc. The fundamental difference is that due to the proximity of the object, the observations are much more detailed. This means that one can build models with a large number of parameters describing the geometry of the galaxy and its dynamical properties. In the case of the "Bluedisk" galaxies, the number of independent data points is very limited and therefore, only a few parameters can be taken into account. This results in an analysis of a more statistical character.

A wealth of additional information can be acquired by studying nearby galaxies. Using H I interferometric observations has the advantage that one can study their kinematics in great detail. Apart from requiring more complicated models, it also confronts the observer with a fundamental problem in radio interferometry: the missing-spacing information. This problem results from the fact that any interferometer has a gap at the centre of the (u, v)-plane[1]. The interferometer is therefore unable to detect emission at the small spatial frequencies, which trace the large-scale diffuse gas of the interstellar medium (ISM). This has to be corrected for by making additional observations with a single-dish telescope and combining them with the interferometric observations in a sensible manner. It is known that an interferometer alone underestimates fluxes for observations of diffuse gas spread out over large scales. It has, however, not been investigated what the effect on the kinematics of the gas is. This is important regarding the study of the mechanisms of accretion and connects to the previous chapter. If galaxies accrete the warm, diffuse gas from their cooling halos, this gas can possibly be observed by the single dish telescope. However, the interferometer, at the distance of NGC 2403, cannot detect such emission. Instead, the interferometer traces the cold, more clumpy and dense structures. The aim of studying the kinematics of a short-spacing correction (SSC) data set is thus to gain more insight into the dominating accretion channel. Therefore, the combined data allows to also study the accretion characteristics of the diffuse part of the emission of NGC 2403, which has not been studied so far.

A detailed study of a single object which will be investigated here, also provides the opportunity to consider other types of possible systematic effects: gaseous disks are usually not thin, flat objects, but are usually bent, lopsided and have a thick disk component. Finally, there

---

[1] This is the plane that describes which spatial frequencies can be observed by an interferometer array. This depends on the antenna configuration of the array, see Sec. 4.2.1.

exist different methods to analyse the H I kinematics of galaxies: one is based on the velocity field and one on the data cube. Most of the current research uses 2-dimensional velocity fields to model the gas kinematics. However, it is known that distance affects the measured kinematical properties from velocity fields through beam smearing. The distance dependence of the derived parameters is different for each parameter. In Chap. 3, it was found that only global parameters such as the position angle and asymptotic rotation velocity can be extracted. It is, however, not clear, which parameters can still be derived depending on the distance. Since in future interferometric surveys, data for a very large number of galaxies at different distances will become available, it is essential to know what the limits of the conventional analyses are.

This chapter is structured as follows: Chap. 4.2 presents the theoretical foundation necessary for this chapter. Chap. 4.3 presents a study of the effects of the SSC on the kinematics of NGC 2403. Chap. 4.4 discusses systematic effects of the analysis of velocity fields. Finally, Chap. 4.5 summarises the results and presents an outlook.

4.2 Theoretical background

This section provides a theoretical background for the study presented in this chapter. Firstly, in Sec. 4.2.1, the principle of the SSC is introduced. SSC complements the interferometer data with the diffuse gas component, which is possibly related to the accretion of cold gas (see e.g. Chap. 3.1, Sancisi et al. 2008). Sections 4.2.2 and 4.2.3 discuss how kinematical parameters, such as the rotation curve and the disk geometry, can be extracted from the data; both from the velocity field and the data cube. This will be needed for the estimation of the H I mass flow as well as for the study of the systematic effects of other kinematical parameters. As introduced in Chap. 2, the basic model used is the tilted-ring model. However, in Chap. 2, the focus is on the derivation of a characteristic rotation velocity, whereas in this chapter, the radial mass flow is also an object of study. Moreover, the high resolution of the data in this case allows one to construct a model with more model parameters.

4.2.1 Zero-spacing correction

In this section, the principle of SSC is introduced and its influence on the measured H I fluxes is discussed briefly. For a more extensive treatment of interferometry, see .e.g Taylor et al. (1999) and on the SSC, see Faridani (2014). The short spacing problem emerges from the different observational approach between interferometers and single-dish instruments. Single-dish telescopes collect radio waves emitted by a source and directly measure its intensity distribution: $I(x, y, \nu)$, hence, in position- and frequency space. Interferometers consist of $n \geq 2$ antennae, which signals are correlated to yield an interference pattern. This pattern depends on the geometrical phase difference between antenna pairs caused by the different arrival times of the waves. Interferometers therefore, do not directly yield an image, but instead measure correlations, which are termed visibilities and are described by the visibility function $V(u, v)$. This function describes the strength of the interference depending on spatial frequency coordinates (u, v), which describe the baseline vector (the geometrical vector spanned by an antenna pair), $\vec{b}/\lambda = (u, v)$. The visibility function is the Fourier transform of the brightness distribution, hence, the source image can be retrieved trough an inverse Fourier transform of the visibility function:

$$B(x, y) = \mathcal{F}^{-1}\, V(u, v). \tag{4.1}$$

The most significant advantage of interferometers is that the maximum resolution is determined not by the diameter of the dish, but by the largest geometrical separation of an antenna pair. Thus, the resolution is greatly enhanced compared to a single-dish telescope.

One of the main drawbacks of interferometers is that the spatial frequency plane cannot be completely sampled. In particular, the central part of the plane cannot be sampled at all due to the finite size of two adjacent antennae. The fact that $V(0,0)$ cannot be measured, implies that $S_{\text{tot}} = V(0,0) = 0$ (the sum of the total flux amounts to naught). Thus, if an object emits large scale, diffuse radiation, an interferometer cannot be used to measure the total flux of a source. The impact of this effect does depend on the distance or angular size of the object under study, for a concise treatment it is referred to Faridani (2014). Thus, to complement the missing-flux information of the interferometer, one has to complement these images with single-dish maps, since they contain information about the total flux. There are, however, a multitude of possibilities to achieve this. Algorithms differ for instance regarding the domain in which the data sets are combined. The data can either be combined in the image- or in the conjugate (Fourier) domain. The combined data used in this work stems from Faridani (2014). This author developed an algorithm that operates on calibrated and science-ready data sets and performs the SSC in the image domain. In short, this algorithm regrids the single-dish image onto the interferometer grid and convolves the interferometer data to the resolution of the single-dish data after which the latter is subtracted from the former. This residual is weighted with the ratio of the beam sizes of the interferometer and the single-dish (for data sets in units of Jy/beam):

$$\alpha = \frac{\Omega_{\text{int}}}{\Omega_{\text{sd}}}, \tag{4.2}$$

and is then defined to be the "missing flux" (excess flux measured by the single-dish telescope with respect to the interferometer), which is henceforth added to the interferometer data.

4.2.2 Derivation kinematical parameters using velocity fields

The modelling of velocity fields is based on the tilted-ring model as introduced in Sec. 2.4. In Chap. 2, however, the focus was on constraining v_{rot}, for which the inclination had to be constrained. This was done by performing an harmonic decomposition of the velocity field and minimising the c_3 term as a function of the inclination. In this chapter, however, an additional parameter that has to be constrained is the radial velocity, v_{rad}, with which the radial mass flow can be derived (see e.g. Wong et al. 2004). The extraction of the other geometrical and kinematical parameters from the data is similar to Chap. 2. The derivation of the radial mass flow is described in the following section.

4.2.2.1 Mass inflow

The method used here to study the radial mass flow using velocity fields is based on the work of Wang (2010), who derived the mass inflow for M83. The crux of this analysis is to perform a harmonic decomposition on the $v_{\text{los}}(x, y)$ as given by the velocity field and to use the resulting Fourier coefficients to separate the rotation- and radial velocity components. The radial velocity distribution is then used to model the H I mass inflow. The derivation by Wang (2010) starts with the basic tilted-ring model:

$$v_{\text{los}} = v_{\text{sys}} + v_{0,\text{rot}} \cos\theta \sin i + v_{0,\text{rad}} \sin\theta \sin i, \tag{4.3}$$

where

$$\cos\theta = \frac{-(x-x_0)\sin\Gamma + (y-y_0)\cos\Gamma}{R}, \tag{4.4}$$

and

$$\sin\theta = \frac{-(x-x_0)\cos\Gamma - (y-y_0)\sin\Gamma}{R\cos i}. \tag{4.5}$$

v_{los} is the line of sight velocity component as measured in a velocity field, v_{sys} is the systemic velocity, $v_{0,\mathrm{rot}}$, $v_{0,\mathrm{rad}}$ are the rotation- and radial velocity, respectively, θ the azimuthal angle, i the inclination, Γ the position angle, (x_0, y_0) the coordinates of the centre, and R the radius of the orbit. The strategy of Wang (2010) is analogous to the one in Chap. 2, except for the v_{rad} term which was set to 0. Firstly, this model is fitted to the data and then its ring geometry is used to fit a Fourier series to the data. He defines the following quantities:

$$v_{\mathrm{los}}(R,\theta) = c_0 + \sum_k (c_k \cos k\theta + s_k \sin\theta), \tag{4.6}$$

$$v_{\mathrm{rad}}(R,\theta) = B_0 + \sum_k (A_k \sin k\theta + B_k \cos\theta), \tag{4.7}$$

$$v_{\mathrm{rot}}(R,\theta) = D_0 + \sum_k (C_k \sin k\theta + D_k \cos\theta), \tag{4.8}$$

which are the Fourier decompositions of v_{rot}, v_{rad} and v_{los}. Substituting them into Eq. 4.3 yields:

$$\begin{aligned} v_{\mathrm{los}} &= c_0 + \sum_k (c_k \cos k\theta + s_k \sin\theta) \\ &= v_{\mathrm{sys}} + \frac{1}{2}((A_1 + D_1) + (2B_0 + C_2 - B_2)\sin\theta + (2D_0 + A_2 + D_2)\cos\theta \\ &+ (B_1 + C_1 + C_3 - B_4)\sin 2\theta + (D_1 - A_2 + D_3 + A_3)\cos 2\theta + (B_2 + C_2 + C_4 - B_4)\sin 3\theta \\ &+ (D_2 - A_2 + D_4 - A_4)\cos 3\theta + (B_3 + C_3 + C_5 - B_5)\sin 4\theta + (D_3 - A_3 + D_5 + A_5)\cos 4\theta \\ &+ ...)\sin i. \end{aligned} \tag{4.9}$$

The c_k and the s_k are the Fourier coefficients resulting from a fit to the velocity field and the A_k, B_k, and C_k and D_k are the Fourier coefficients of the radial and rotation velocities, respectively. These line of sight coefficients are known after a fit to the velocity field, whereas the coefficients corresponding to the radial and rotational components are unknown. Moreover, these coefficient are degenerate with respect to e.g. viewing angles i and Γ (Schoenmakers et al., 1997). Analogous to Wang (2010), the coefficients (A_k, B_k, C_k, D_k) are set to 0 for $k > 2$. Eq.

4.9 therefore, simplifies to:

$$\begin{aligned}
v_{\text{los}} &= c_0 + c_1 \cos\theta + s_1 \sin\theta + c_2 \cos 2\theta + s_2 \sin 2\theta + c_3 \cos\theta + s_3 \sin\theta \\
&= v_{\text{sys}} + \frac{1}{2}((A_1 + D_1) + (2B_0 + C_2 - B_2)\sin\theta + (2D_0 + A_2 + D_2)\cos\theta \\
&+ (B_1 + C_1)\sin 2\theta + (D_1 - A_1)\cos 2\theta + (B_2 + C_2)\sin 3\theta + (D_2 - A_2)\cos 3\theta)\sin i.
\end{aligned} \tag{4.10}$$

Inspecting Equations 4.3 and 4.10, it follows that $B_0 = v_{0,\text{rad}}$ and $D_0 = v_{0,\text{rot}}$. Moreover, it allows the computation of $A_1, D_1, B_2, C_2, A_2, D_2$, assuming that v_{sys}, $v_{0,\text{rad}}$, $v_{0,\text{rot}}$, and the inclination are known:

$$\begin{aligned}
A_1 &= c_0 - v_{\text{sys}} - c_2/\sin i \\
D_1 &= c_2/\sin i + c_0 - v_{\text{sys}} \\
C_2 &= s_3 - B_0 + s_1 \\
B_2 &= s_3 + B_0 - s_1 \\
D_2 &= c_3 + c_1 - D_0 \\
A_2 &= c_1 - c_3 - D_0.
\end{aligned} \tag{4.11}$$

The calculation of B_1 and C_1 is not directly possible, since these parameters are degenerate with s_2. Wang (2010) solves this degeneracy by setting:

$$\begin{aligned}
B_1 &= s_2/2 \\
C_1 &= s_2/2,
\end{aligned} \tag{4.12}$$

in which the s_2 term is assumed to contribute an equal amount to the rotation and the radial velocity. This approach is slightly different from the approach chosen by Wong et al. (2004), in which the s_1 term is completely attributed to the radial velocity, whereas here it affects both radial and rotational velocity (B_2 and C_2).

Using the terms from Equations 4.11, 4.12 and 4.7, the radial mass flow can be computed using the following expression:

$$\dot{\mathcal{M}}(R) = \frac{d\mathcal{M}(\mathcal{R})}{dt} = \int R\Sigma(R,\theta) v_{\text{rad}}(R,\theta) d\theta, \tag{4.13}$$

where Σ is the surface mass density, R the radius, θ the azimuthal angle and v_{rad} the radial velocity profile.

4.2.3 Derivation of kinematical parameters using data cubes

A fundamental difference between the analysis of the kinematics using the data cube and velocity fields is that data cubes contain many more independent data points. A velocity field contains a number of data points of the order of the number of Nyquist sampled data points corresponding to the number of statistically independent beams. In the case of observations with a limited resolution, the dependence between the pixels has to be taken into account. The reason for this is beam smearing. By using the data cube, this number is roughly multiplied by the number of statistically independent velocity channels. Another difference is that the velocity field is a projection of the data cube in two dimensions, implying not just a decrease in the number of data points, but also a loss of the line-of-sight velocity distributions (LOSVDs).

In the previous chapters, the Tilted Ring Fitting Code (TiRiFiC, Józsa et al. 2007) [2] is used to make simple models of the data cube to constrain the global parameters. It can, however, also be used to make more advanced models of the in- and outflow motions in galaxies. TiRiFiC is able to analyse the vertical density distribution and velocity structure. This cannot be done with velocity fields. TiRiFiC assumes that the 3-dimensional luminosity function $J_1(R, \phi, z)$, which is separable into a surface brightness distribution, $\Sigma(R, \phi)$, and a scale profile, $H(z)$:

$$J_1(R, \phi, z) = \Sigma(R, \phi) \cdot H(z). \tag{4.14}$$

$H(z)$ is parameterised by a function describing the scale height, e.g. a constant scale height or a hyperbolic secant (sech). The latter is assumed in for the models in this work, hence, the vertical density distribution is parameterised by:

$$H(z) = \frac{sech^2(zZ_0^{-1})}{2Z_0}, \tag{4.15}$$

where z is the coordinate above the plane and Z_0 is the scale height. Moreover, also the vertical velocity structure can be modelled using vertical gradients of the velocity vector, described by parameters:

- the vertical gradient in radial velocity (*DVRA*) and the vertical gradient in rotation velocity (*DVRO*), which have units of km s^{-1} arcsec^{-1}, and
- the onset height of these parameters above the plane of the disk, through the onset height above plane for a change in radial velocity (*ZDRA*) and onset height above plane for a change in rotation velocity (*ZDRO*).

In particular, with regard to accretion, a vertical gradient in the radial velocity can be interpreted as gas accretion. Recent work by Schmidt et al. (2014) is a prime example for this: in this work the authors quantify the H I kinematics in the case of dwarf galaxy UGCA 105. They use TiRiFiC to model a scenario with vertical gradients in rotation and rotation velocity. They interpret this motion to be the result of either an extreme fountain flow or newly accreted gas. The inflow is quantified using the inflow rate trough a cylinder at radius r:

$$\dot{\mathcal{M}}_{\mathrm{rad}} = 2 \int_{Z_i}^{\infty} 2\pi r v_{\mathrm{rad}} \sigma(r) H(z) dz, \tag{4.16}$$

where z is the height above the plane, $\sigma(r)$ the surface density, $H(z)$ the vertical density distribution, Z_i the onset height above the plane and v_{rad} is parameterised by:

$$v_{\mathrm{rad}} = \begin{cases} \Delta v_{\mathrm{rad}}(z - Z_i) & : z \leq Z_i \\ 0 & : z < Z_i \end{cases} \tag{4.17}$$

4.3 Study of the effect of SSC and the kinematics of NGC 2403

This section presents a case study of the influence of the SSC on the gas kinematics. In Chap. 4.2.1 it has been highlighted that the missing-spacing problem is particularly present in the measurement of H I fluxes of nearby extended objects. In this section, the effect on the kinematics is considered by performing a case study of NGC 2403. In Chap. 4.3.1, the

---

[2] http://www.astron.nl/ jozsa/tirific/

Characteristic	Value	Reference
Hubble type	SABcd	1
Cepheid Distance	3.18 Mpc	2
M_B	-19.43 mag	3
SFR	$0.331 \pm 0.017\ \mathcal{M}_\odot/\mathrm{yr}^{-1}$	4
Mean H I inclination	62.9°	5
Mean H I position angle	303.7°	5
v_sys	132.8 km s^{-1}	5
r_{25}	7.4 kpc	6
H I disk radius	22.5 kpc	7
H I total mass	$3.2 \times 10^9\ \mathcal{M}_\odot$	7
Total baryonic mass	$9.5 \times 10^{10}\ \mathcal{M}_\odot$	7

Table 4.1: NGC 2403 characteristics. References: (1) de Vaucouleurs et al. (1991), (2) Madore & Freedman (1991), (3) Walter et al. (2008), (4) Heesen et al. (2014) (radio continuum). It is noted that this value is very different from the SFR these authors measure from the FUV combined with the 24μm tracer, so the systematic uncertainty is probably larger than denoted here, (5) de Blok et al. (2008), (6) Trachternach et al. (2009), (7) Fraternali et al. (2002).

H I interferometric, single-dish, and combined data of the nearby spiral galaxy NGC 2403 is introduced. In Chap. 4.3.2, the H I kinematical parameters are derived using an analysis based on velocity fields. In Chap. 4.3.3, these parameters are extracted using an approach based on a direct model fit to the data cube. In Chap. 4.3.4, these results are compared and the implications are discussed.

4.3.1 NGC 2403

NGC 2403 is a nearby ($D \approx 3$ Mpc), SABcd (T-type 6.0) spiral galaxy (de Vaucouleurs et al., 1991). Table 4.3.1 shows the most important characteristics of NGC 2403. NGC 2403 has been the subject of several studies. The optical appearance is characterised by several large H II regions and Wolf-Rayet stars (Drissen et al., 1999). The star formation rate (SFR) based on the radio continuum emission is roughly 0.3 $\mathcal{M}_\odot\ \mathrm{yr}^{-1}$ (Heesen et al., 2014), whereas they find a level of 0.9 $\mathcal{M}_\odot\ \mathrm{yr}^{-1}$ from the MIR and UV. This galaxy was firstly observed by a radio interferometer with the Westerbork Synthesis Radio Telescope (WSRT) by Wevers et al. (1986). Begeman (1987) presented a more detailed analysis of its rotation curve and orientation parameters. Fraternali et al. (2002) performed an even more extensive analysis of the dynamics of NGC 2403, using a sensitive H I-survey (48 hours observation time) with the Very Large Array (VLA) instrument. They established the presence of an "anomalous" gas component, consisting of "lagging" wings of extended emission, hence rotating 25 to 50 km s^{-1} slower than the cold thin disk. They interpreted this component as a thick H I-layer surrounding the cold disk with a gas inflow directed to the centre. They performed a two-component fit to the LOSVDs to separate the "anomalous gas" from the cold disk component. From this, they estimated the mass of the "anomalous" component to be 1/10th of the mass of the cold disk.

In Sec. 4.2.1, it has been mentioned that the algorithm that performs the SSC requires a single-dish and an interferometer data set as inputs. In the case of NGC 2403, the single-dish data stems from the Effelsberg Bonn H I Survey (EBHIS, Kerp et al. 2011). This is an all-sky survey north of a declination of $-5°$ with $z \leq 0.07$ and an H I-mass sensitivity of $3 \times 10^7\ \mathcal{M}_\odot$.

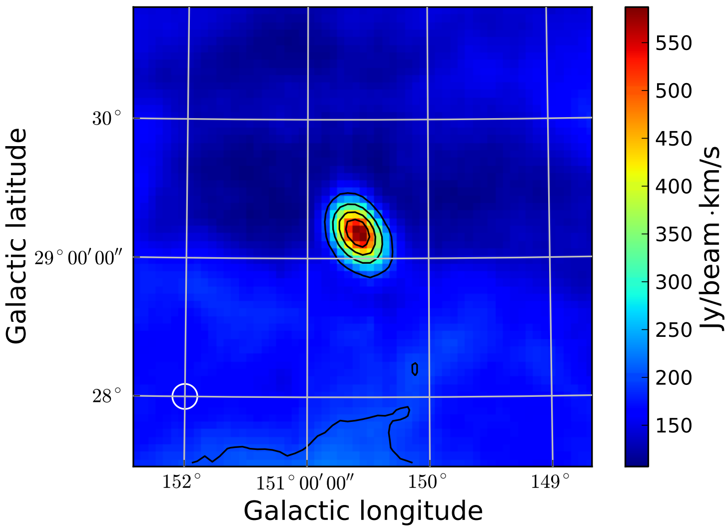

Figure 4.1: EBHIS total intensity map.

The total intensity image is shown in Fig 4.1. In this image, NGC 2403 appears as a point source, since the half power beam width (HPBW) of the EBHIS survey is around 11 minutes of arc, which is roughly 10 kpc. This is a substantial part of the H I disk (see Table 4.3.1). In Fig. 4.2, the corresponding velocity field is shown. In the spectrum (see Fig. 4.9), the galaxy is visible from roughly -20 km s^{-1} to 270 km s^{-1}. Since the emission from the Milky Way (MW) is very strong even at this galactic latitude, this image is for a large part contaminated by MW emission. Therefore, even at higher radial velocities (until roughly 50 km s^{-1}), the intensity of the MW emission is still quite high compared to the emission from the galaxy, causing the velocity as traced by the first-moment map to be significantly biased towards 0 km s^{-1}. In the right figure, the channels with velocities up to 40 km s^{-1} were removed from the data cube and the first-moment map was created. This removes most of the contamination from the image. However, this also removes a significant portion of the approaching side of the galaxy.

The interferometer data used here consists of the visibilities from the The H I Nearby Galaxy Survey (THINGS, Walter et al. 2008). The data reduction takes the following strategies into account (S. Faridani, priv. comm., 2014):

- *Weighting of the visibilities*: As mentioned in Sec. 4.2.1, interferometers measure visibilities on a (u, v)-plane. Each of these visibilities is characterised by a baseline vector, which length is inversely proportional to the measured angular scale: short baselines measure large angular scales and long baselines measure the small angular scales. One step of the data reduction is to weight the visibilities to select the scales that will be emphasised in the resulting image. Since the subject of study is the SSC, and therefore the focus is on the diffuse emission, natural weighting (see e.g. Briggs 1995) has been used. More precisely, a robust factor of -2 has been chosen. This is the robust factor as defined in the Astronomical Image Processing System (AIPS, Greisen 2003) software package.

- *Primary beam correction*: The final interferometric image is a multiplication of the sky

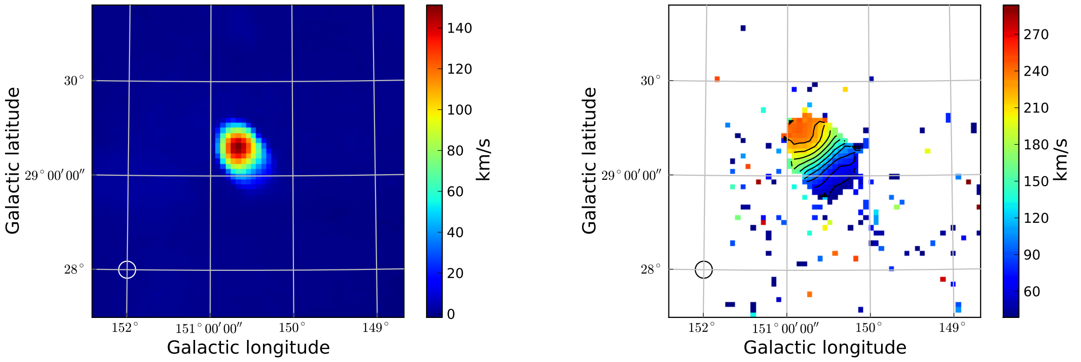

Figure 4.2: EBHIS first-moment maps. *Left*: A velocity field from the data cube, where all intensities under $3\sigma_{\rm rms}$ have been clipped. *Right*: A velocity field with the same clipping but only based on radial velocities above approximately 40 km s^{-1} to minimise contamination from the MW.

image with the primary beam pattern of the telescope. The primary beam is different for each telescope. This correction is required for an accurate representation of the fluxes since it accounts for the decreasing sensitivity of the primary beam towards the edges of the field of view.

- *Residual rescaling*: Interferometric maps are the result of a convolution of the source brightness distribution with an instrumental function. In order to retain the original brightness distribution, the image therefore has to be deconvolved. This can be done by running the `CLEAN` algorithm (Högbom, 1974). This algorithm decomposes the image as a distribution of point sources which are used to construct a model of the data (clean components). Fluxes (in units of Jy/beam) are in general measured using the cleaned map. This map is a sum of the clean components and the residuals, each are characterised by different beams; the clean beam and the dirty beam, respectively. However, a correct estimation of the flux should be based on the cleaned part of the data. The data has to be corrected for this to achieve a correct estimation of the flux values. The data is flux residual rescaled by (Walter et al., 2008). For more information, see Jorsater & van Moorsel (1995); Faridani (2014).

4.3.2 Analysis of the H I kinematics using velocity fields

In this section, an analysis of the kinematics of NGC 2403 based on velocity fields is presented. Firstly, the velocity fields that will be used in this procedure are described. Secondly, the recipe, by which the inflow of cold gas is calculated, is presented, as well as the fitting method. Finally, the results are presented and discussed.

4.3.2.1 Velocity fields

The most common way to study the H I kinematics of disk galaxies is by using velocity fields. As discussed in e.g. Teuben (2002), there are multiple ways to construct a velocity field and each method has different advantages and biases. In Chap. 3, the galaxies are located at large distances, therefore the beam is relatively large compared to the angular extents of the galaxies. Moreover, the signal-to-noise ratio in these observations is relatively low and therefore, the approach of fitting Gauss-Hermite polynomials to the LOSVD was chosen. In the case of NGC 2403, beam smearing plays only a small role and the signal-to-noise ratio is very high, and therefore, this type of velocity field is not considered here. Instead, the commonly used moment maps are considered in this chapter.

4.3.2.2 Fitting method

Analogous to Chap. 2, the `rotcur` and `reswri` routines are used to fit a kinematical model to the velocity field. The fitting strategy is a multiple-step approach, which is in principle similar to the approach by Wang (2010):

1. Using the parameters for the i, Γ, $v_{\rm rot}$, $v_{\rm sys}$ from Fraternali et al. (2002) as initial guess values, `rotcur` is used to fit these parameters, as well as the centre position to the velocity field. $v_{\rm rad}$ is kept fixed to 0 in this step. As a ring separation and ring width, 30 arcsec $\approx 1 \cdot HPBW$ are taken.
2. In the next iteration, $v_{\rm sys}$ is fixed to one value for all the rings just as the centre position.
3. As a next step, $v_{\rm rad}$ is included in the fitting.
4. Using these parameter values, i, Γ, $v_{\rm rot}$ and $v_{\rm rad}$ are fitted simultaneously keeping all the other parameters fixed using `reswri`.
5. Having constrained these parameters, `reswri` performs an harmonic decomposition up to the 3$^{\rm rd}$ order.

The parameter uncertainties of the harmonic coefficients are determined by multiplying the formal `reswri` uncertainties by a factor of $\beta = \frac{4\pi\sigma_x\sigma_y}{\delta_x\delta_y}$, to account for the correlation between points due to the beam smearing effect (see Schoenmakers et al. 1997 and Sicking 1997). In this Equation, σ_x, σ_y are the beam dispersions in arcsec in the directions of x and y, and δ_x, δ_y are the pixel sizes in arcsec. Since the pixel size is chosen to be 4 arcsec, and the data cubes are smoothed to a full width at half maximum (FWHM) of 30 arcsec. This is equivalent to a dispersion of $\sigma = \texttt{FWHM}/(2\sqrt{2\ln 2}) = 30/2.3548 = 12.74$. This yields a β of 11.3. Moreover, the uncertainties are quantitatively assessed by inspection of the residual velocity fields.

4.3.2.3 Results from the VLA maps

The velocity field is shown in Fig. 4.3. The tilted-ring fit for this velocity field is straightforward. Firstly, based on the initial guess values from Fraternali et al. (2002), all parameters including the centre position and systemic velocity are fitted simultaneously for all rings. The result is shown in Fig. 4.4. From this figure, the alleged warp (Fraternali et al., 2002) is visible in i, whereas Γ is nearly constant for all radii. The X_0 position of the kinematical centre varies rather strongly, which is in agreement with the results form Trachternach et al. (2008). It is noted that the parameters can be measured reliably out to about 850 arcsec ($\approx$ 13 kpc). The data from Fraternali et al. (2002) results from a survey with a significantly larger observation time. Therefore, the kinematics can be modelled until larger radii, since the faint gas is detected with a larger signal-to-noise ratio. de Blok et al. (2008) also model THINGS observations of this galaxy and can also to determine reliable parameters until about 850 arcsec.

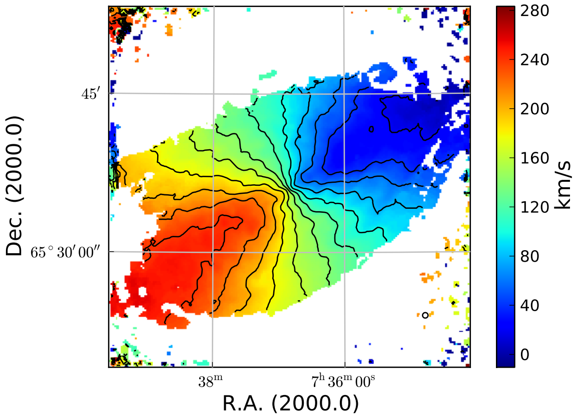

Figure 4.3: Moment-1 velocity field for the VLA interferometer maps.

Despite the radial fluctuations in the dynamical centre, as well as in the systemic velocity, the velocity field can be reliably fitted by taking a fixed v_{sys} as an average over all radii and the fixed kinematical centre from `tirific` (see Sec. 4.3.3). The parameters taken as input for `reswri` are shown in Fig. 4.5. The systemic velocity is taken as $v_{\mathrm{sys}} = 133$ km s^{-1} and the kinematical centre (RA, DEC) = $(114.2080°, 65.600°)$.

The `reswri` output is shown in Fig. 4.6. From this plot, it can be seen that the parameter $c_3(R) = 0$ within its uncertainties. This indicates that the inclination (i) has been correctly determined using `rotcur`. Moreover, there are clear indications for radial motions due to s_1 amplitudes up to 15 km s^{-1}. These motions are directed inward, given that Groningen Image Processing System (GIPSY, van der Hulst et al. 1992) uses a right handed coordinate system rotating counterclockwise and the NGC 2403 rotates counterclockwise (inverting the sign). Furthermore, the s_2 and c_2 parameters are non-zero. This is a direct reflection of the varying position in the dynamical centre found in the `rotcur` analysis. This can have two possible reasons: (i) an incorrect estimation of the dynamical centre pointing to a varying dynamical centre from ring-to-ring and/or, (ii) physically relevant s_2 and c_2, e.g. due to spiral arms. Since from a dynamical point of view, a varying centre is not very likely, these terms most likely contain physical information about the galaxy, e.g. about spiral arms or kinematical lopsidedness (see Schoenmakers et al. 1997). The residual velocity field, which describes the difference between a model velocity field, based on the harmonic coefficients and the observed velocity field is shown in Fig. 4.6. The ring-like structures inside the galaxies are missing due to the fact that the rings differ in i and Γ and the separation between the rings equals the ring-width, giving rise to disjoint rings. As a next step, the radial velocity distribution is estimated according to Chap. 4.2.2.1.

The left panel of Fig. 4.7 shows the distribution of the mass flow $\dot{\mathcal{M}}(R, \theta)$. The largest radial gas motions are at a distance of 500 arcsec ($\approx$ 7.7 kpc), since the dominant term describing the radial motion, s_1, is highest at these radii. To derive a radial profile of the mass flow, the GIPSY task `ellint` is used. The ellipses along which the radial profile is derived are given by the ring geometry described by the position angle and inclination as derived from `rotcur`. It is assumed that the mass flux along each ring can be well characterised by the mean, and this value is multiplied by 2π to compute $\dot{\mathcal{M}}(R)$. This result is shown in the right panel of Fig. 4.7. Also in this figure, the highest inflow is observed around 8 kpc with an amplitude of around 1 $\mathcal{M}_{\odot}$ yr^{-1}. The error bars are the rms of the `ellint` values of the mass inflow along the rings and only represent a rough statistical estimate of the true uncertainty based on the

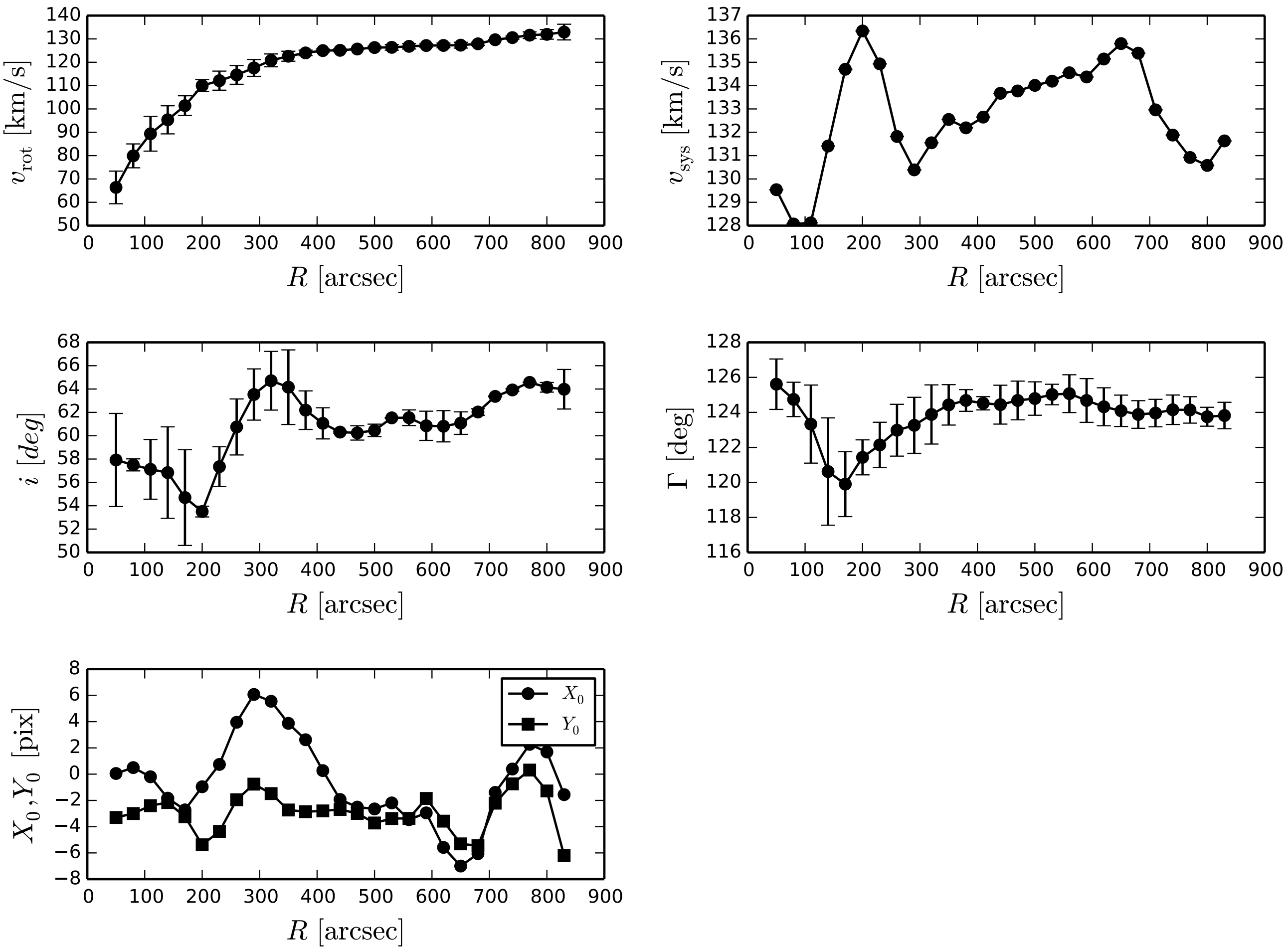

Figure 4.4: NGC 2403 first-moment `rotcur` parameters in the case where all parameters are unconstrained. From left to right, top to bottom these profiles show the rotation velocity, systemic velocity, inclination, position angle and kinematical centre.

H I morphological heterogeneities. The model assumes a smooth H I disk, where a continuous mass flow can be assigned to the corresponding ellipses. This assumption is apparently not valid due to the clumpiness of the H I disk, and therefore this is used for a rough estimation of the uncertainties. It is noted that the uncertainties of the harmonic decomposition are not taken into account at this point. These are, however, at least in the case of the VLA data, not the main source of uncertainty in the determination of a radial profile describing the mass inflow. The main source of error lies ostensibly in the model premises. This is discussed in Chap. 4.3.4.

4.3.2.4 Results from the SSC data

The velocity fields resulting from the SSC data are shown in Fig. 4.8. The first-moment velocity field as well as the peak velocity field are shown here. The peak velocity field has been constructed by assigning a velocity to each position, where the velocity is that of the peak of the LOSVD. The contour levels are the same as the levels in Fig. 4.3, hence from -20 to 300

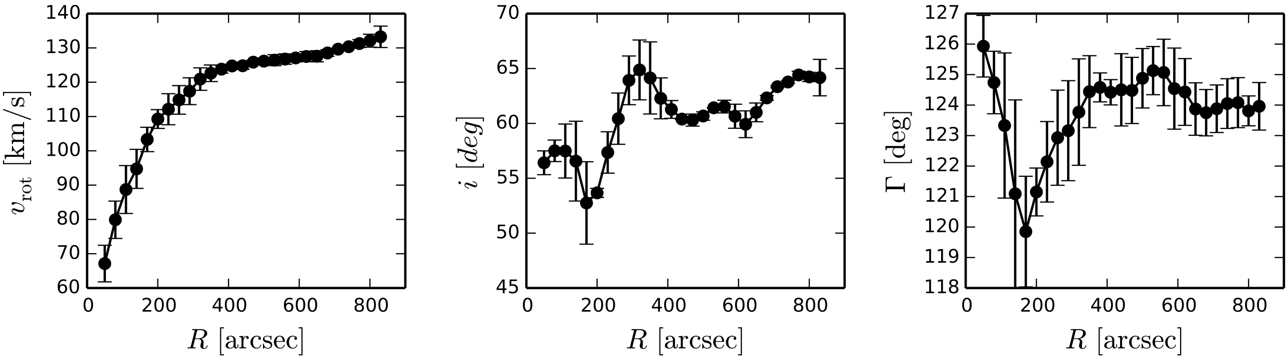

Figure 4.5: NGC 2403 VLA first-moment `rotcur` parameters (rotation curve, inclination and position angle radial profiles) with fixed $v_{\rm sys}$ and centre.

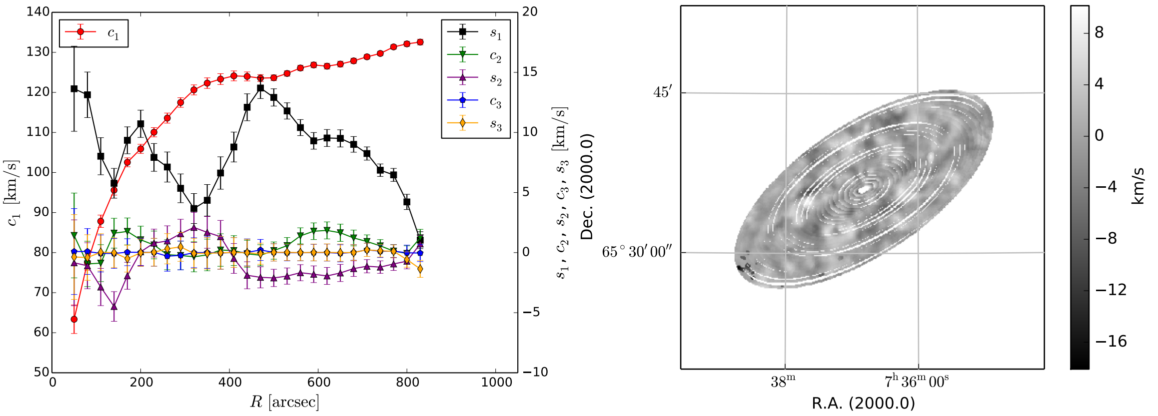

Figure 4.6: Output of the harmonic analysis based on the NGC 2403 VLA first-moment map. *Left*: harmonic coefficients. *Right*: residual velocity field (see text).

km s^{-1} in steps of 20 km s^{-1}, and also the colour scale is identical. Comparing these maps, one immediately notices that in the case of the first-moment map, the radial velocities are systematically lower compared to the interferometer map only. In the peak velocity field, it seems that many data points are missing. This can be explained as follows:

- The combined first-moment map shows large deviations with respect to the interferometer-only map which increase toward the receding side of the galaxy (left-bottom). This can be explained by the influence of the MW emission. As shown in Sec. 4.3.1, due to the low galactic latitude of NGC 2403, the antenna pattern of the Effelsberg telescope is strongly sensitive to MW emission, in particular at radial velocities close to 0 km s^{-1} due to the overlap with the galaxy's rotation curve. After the combination, this emission is also contained in the SSC data cube. The first-moment is the intensity-weighted mean velocity, hence, due to the high intensity of the emission at 0 km s^{-1}, the radial velocities of the galaxy in the first-moment map will be severely biased toward 0 km s^{-1}. This is best illustrated by a comparison of the sum spectrum of the interferometer-only and the combined data cube. In Fig. 4.9, the logarithmic flux densities are plotted for both maps. In the spectrum based on the interferometer-only data cube, the spectrum can be described well by a double-horn profile, where the intensities of the approaching and

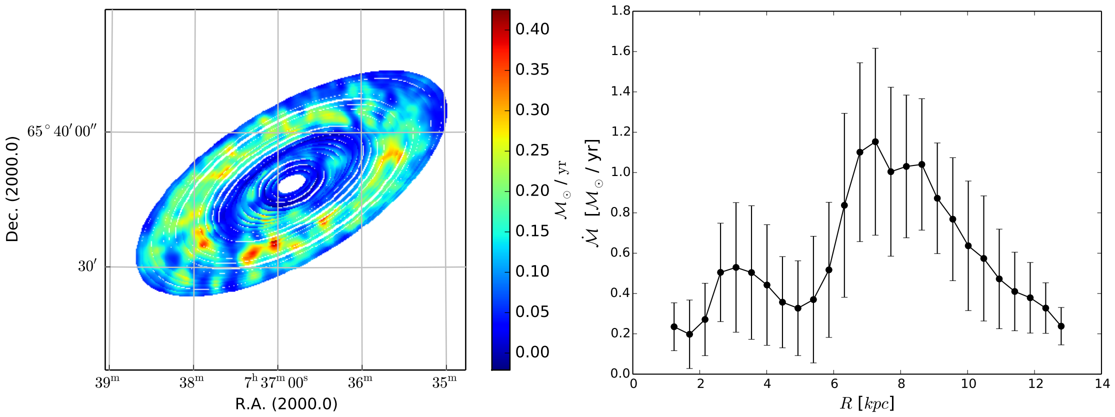

Figure 4.7: *Left*: Map describing the mass flow derived from the VLA map. This map is a pixel wise multiplication of the column density map $\Sigma(R,\theta)$ converted to units of $\mathcal{M}_\odot/\mathrm{pc}^2$ and the $R \cdot v_{\mathrm{rad}}(R,\theta)$ map in units of pc^2/yr. *Right*: Radial profile of the mass flux derived along the ellipses from `rotcur`.

the receding sides of the galaxies are comparable. In the case of the spectrum of the SSC cube, the intensity at radial velocities close to 0 km s^{-1} is more than one order of magnitude larger compared to the interferometer spectrum. Therefore, in the sum $\sum_i I_i \cdot v_i$, where index i denotes the channel number, the large intensities at 0 km s^{-1} not originating from the galaxy itself, cause a negative bias.

- The first-moment velocity field of the SSC data cube is not an accurate representation of the H I kinematics of NGC 2403. However, also the peak velocity field suffers from systematic effects. At all locations in the galaxy, the MW emission is present at 0 km s^{-1} with a certain intensity. This causes problems in areas of the galaxy where the signal of the galaxy itself is not very strong compared to the amplitude of the MW signal. This is most significant in the outer ranges of the galaxy, which is characterised by low intensities compared to that of the MW contribution. In these areas, the peak flux is therefore, located at 0 km s^{-1}. Subsequently, the value of the peak velocity field at these coordinates is set to a value around 0 km s^{-1}. This is visible in Fig. 4.8, where the outer ranges of the galaxy are not included in the velocity field.

From these considerations, it becomes clear that neither a first-moment, nor a peak velocity field can, without further processing, be used to fit quantitative models to the data. The first-moment data is severely biased and therefore, unusable. In the peak velocity field, all velocities in an interval of approximately ±30 km s^{-1} around 0 km s^{-1} have to be blanked. The interferometer spectrum shows that the approaching flank of the galaxy ranges down to velocities below these values, and thus, the galaxy's rotation curve intersects with 0 km s^{-1}. Masking these values would thus mean a significant loss of data points. In this case, it would not be possible to model the outer ranges of the galaxy where possibly the warmer, low column density gas is located. Moreover, it is not clear how the MW emission, inherent to the single-dish data is processed in the combination. The difference in the spectra between the interferometer and the combined data becomes increasingly small for higher radial velocities as seen in Fig. 4.9. It is, however, not possible to establish what part of the difference between the combined data and the interferometer is due to diffuse emission from NGC 2403 and which part is due to MW confusion.

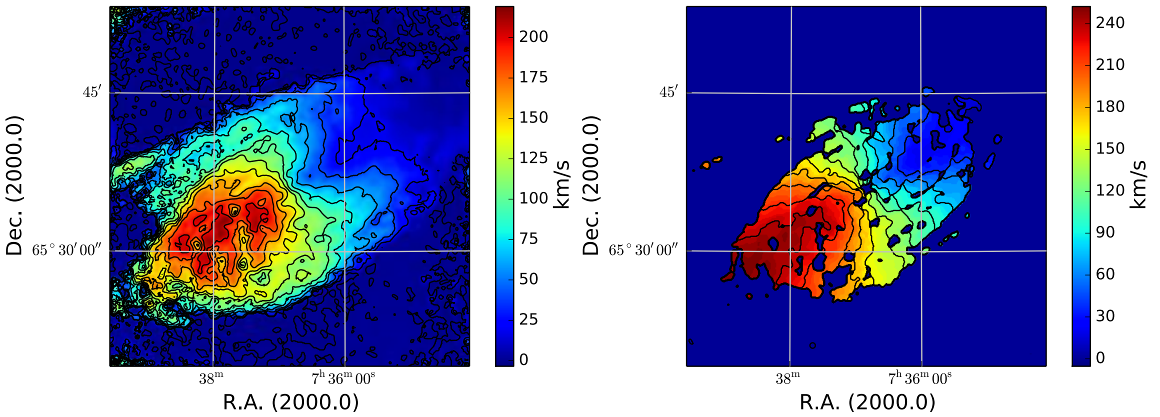

Figure 4.8: Velocity fields for the combined (VLA interferometer and Effelsberg single-dish) map. *Left*: first-moment velocity field, *right*: peak velocity field.

Taking these considerations into account, it has to be concluded that the basic analysis of velocity fields by means of Fourier analysis cannot be performed on the SSC velocity fields without systematic effects dominating the results. Before studying the effect of SSC by constructing model data cubes, however, an alternative approach based on the work of Fraternali et al. (2002) is attempted here. Fraternali et al. (2002) performed a Gaussian decomposition of the data cube. They firstly fit a Gaussian to each pixel of the data cube and then subtract these Gaussians from the data. A data cube spanned by these (narrow) Gaussian components is therefore considered to constitute the cold gas disk with regular rotation. The residual is interpreted to be the anomalous gas component with spectral lines broader than the cold disk and lower amplitudes. To perform an analogous analysis using the SSC data would be highly interesting. Assuming that indeed the SSC adds signal to the data in the form of diffuse emission, subtraction of the cold gas disk would result in a stronger anomalous gas component than obtained from the interferometer-only data. However, also this analysis is complicated by MW emission: fitting to the SSC data is therefore not feasible, since often the fitting-algorithm will fit a Gaussian to the MW component. Assuming that the cold-disk component of the SSC data is identical to the one in the interferometer-only data, the analysis from Fraternali et al. (2002) has first been performed on the interferometer data and the data cube containing these Gaussians - assumed to contain only the cold disk - is subtracted from the SSC data. This residual therefore contains the anomalous gas component as well as the MW contribution.

The Ansatz that has been attempted here is to fit Gaussians centred on 0 km s^{-1} to each pixel in the “anomalous + MW” data and subtracting the best-fitting Gaussians pixel-wise. Unfortunately, this approach has been unsuccessful: the channels around 0 km s^{-1} still contain significant MW emission, which is still about one order of magnitude larger than the signal of the galaxy itself. This leads to the conclusion that the impact of the MW on the data cannot be parameterised by a simple Gaussian: the MW contribution also contains peaks away from 0 km s^{-1}, which contain substructure. This is illustrated in the right hand side of Fig. 4.9. In this figure, the sum spectrum of the interferometer data is compared with the combined data after subtraction of the cold disk and the MW contribution. On the right hand side of the graph, it is visible that the subtraction of the MW contribution has not been successful: the residuals of the MW remain still roughly a few times larger than the highest amplitude at velocities where the MW emission does not play a large role (the low velocity channels, or high radial velocities). Moreover, in several channels, too much emission has been subtracted from

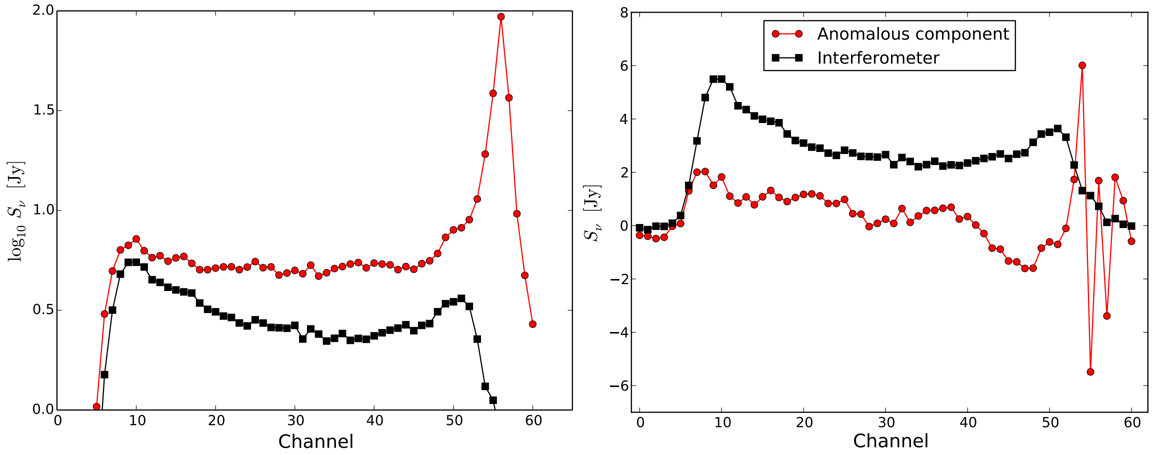

Figure 4.9: *Left*: Sum spectra in logarithmic flux scale. Increasing channel number denotes decreasing radial velocities. The channel width is 5.1 km s^{-1} The zeroth channel is at a radial velocity of 288.39 km s^{-1}, channel number 56 is at 0 km s^{-1}. The black squares denote the spectrum of the VLA interferometer data cube. In this case, the total flux in the first few channels is negative and therefore these values are not plotted in the logarithmic sum spectrum. The red circles correspond to the spectrum of the combined data. *Right*: Sum spectra of the interferometer data (black squares) and the SSC data after subtraction of the cold disk and the MW contribution (red circles). In case of a successful MW emission subtraction, this would show the contribution of the anomalous component.

the data, giving rise to negative values. An explanation could lie in the presence of turbulences in the MW gas. In fact, the MW does contain significant turbulences in the H I component (see e.g. Kalberla & Kerp 2009). However, even if an accurate model of these turbulences would be available, the single-dish response at the corresponding galactic latitude would have to be modelled as well as the influence of the SSC would have to be studied, making such an analysis extremely expensive and uncertain.

To conclude, the "standard" methods involving the analysis of moment maps, cannot be used to model the SSC data of NGC 2403. The cause for this is the MW emission. Simple ways to subtract the MW emission do not lead to any usable result. An alternative Ansatz to solve this problem would be simply to discard the channels of the data cube which contain mostly MW emission. There are, however, at least three problems with this: (i) this would involve fitting only to a subset of the channels which reduces the number of data points. When searching for radial motions by fitting 3rd order Fourier terms to the data, these missing data points are likely to play a large role, (ii) due to the discussed turbulences, it is unclear until which velocity channel the MW emission contributes to the total signal, (iii) Eq. 4.2.2.1 calculates the inflow rate through a multiplication of v_{rad} with $\Sigma(R,\theta)$, omitting a range of channels causes Σ to be incomplete and therefore the mass flow is underestimated. Also in this case, assumptions about symmetries in the galaxy would be required.

4.3.3 Analysis of the H I kinematics using a 3-dimensional model

In this section, the software package TiRiFiC is used to model the kinematics of NGC 2403. As opposed to Chaps. 2 and 3, in which the data cube of some galaxies were crudely modelled without taking warps and other such features into account, NGC 2403 is a very nearby galaxy for which the kinematics can be modelled with a higher level of precision. Firstly, some necessary background information is provided on the TiRiFiC model geometry and how it differs from the modelling of velocity fields. Secondly, the modelling strategy is discussed. Finally, the model results are presented and the discussed.

4.3.3.1 Modelling strategy

As discussed in Chap. 4.2.3, the TiRiFiC model has many degrees of freedom. Moreover, the fitting algorithm uses a local optimiser. This means that it does not probe the full parameter space, but only searches for a χ^2 minimum near the starting values. These circumstances require careful considerations on the starting values and the choice of parameters taken into account by the model. As in the velocity field analysis, the starting values for the fit are taken from Fraternali et al. (2002). This model assumes that the disk of NGC 2403 shows a warp in position angle and inclination. From the velocity field analysis, it followed that the warp is not larger than 10 deg in i and Γ and is confined to the centre (roughly the first 6 kpc). There are, however, reasons to assume that this might not be a real warp, but instead just appears as one, due to projection effects. According to Briggs (1990): "The H I layer typically is planar within R_{25}, but warping becomes detectable at $R_{\mathrm{Ho}} = R_{26.5}$". R_{25} is in the case of NGC 2403 larger than 8 kpc, beyond the radius where the warp is observed. Therefore, also the possibility of a bar-streaming motion in the centre of the H I distribution of the galaxy is investigated instead of warping of the disk to verify if bar streaming can also reproduce the observed kinematics.

The accuracy of the models is assessed through visual inspection of the data cubes as well as the position-velocity (xv) diagrams. The contours of the model data cubes are overlaid on the contours of the observed data cube. If these contours do not match, the relevant parameters are refitted. This procedure is iterated until model and data show a satisfactory agreement. In the modelling of the data cube, the data is smoothed to an FWHM of 30 arcsec. To construct this model, the pixel size is also increased from 2 arcsec to 10 arcsec to improve the signal-to-noise ratio. The usage of the fully resolved data cube with an FWHM of 9 arcsec results in excessive computation times. Moreover, inhomogeneities in the surface brightness distribution, which complicate the fitting are present in the fully resolved data. By smoothing the data to 30 arcsec, computation times are drastically reduced and the surface brightness distribution of the galaxy is smoother.

All models are symmetric with respect to the galaxy minor axis. The parameter uncertainties are estimated using a separate fit to the receding and the approaching side and is computed as the difference of the parameter values for each separate side.

The effect of the SSC on the TiRiFiC models is then investigated by a two-step approach:

- The best-fitting model parameters corresponding to the interferometric data is obtained.
- This set of parameters is used a first-guess parameter set, and a subsequent fit to the SSC data is performed.

The justification for the latter step is that the interferometer-only and the SSC data do not show large differences in the data cube sufficiently far away from 0 km s^{-1}. This is illustrated in the appendix, see Fig. C.1. In most of the velocity channels, only the contours corresponding to $1 - \sigma_{\mathrm{rms}}$ show a difference between the data sets.

4.3.3.2 Warped model

The best-fitting parameter values of the TiRiFiC model based on the interferometer-only data are shown in Fig. C.2. Due to the large number of parameters modelled, one has to carefully make a selection of which parameters are included in the model, and at which radii these are fitted. The highlighted red points in this figure show the data points which are fitted; the points in grey either result from an interpolation between these points or are fitted together as a group. The corresponding xv diagrams are shown in Fig. 4.10 and the model is compared to the data cube by overlaying its contours on several velocity channels of the data cube in Fig. C.4 of the appendix. It is noted that due to the limited field of view, the outer ranges of the galaxy are not completely contained in the data cube. Hence, the outer radii cannot be fully modelled. The outer radius modelled is at 1040 arcsec (corresponding to $\approx 16\,\mathrm{kpc}$). The xv diagram along the major axis shows that the fit of the beard emission has been successful. Most of the deviations are due to kinematical and morphological lopsidedness in the galaxy: a symmetrical model has been fitted to the data cube, meaning that such asymmetries are not considered in the model. In principle, TiRiFiC has the possibility to fit the approaching- and receding half of the galaxy separately. This is used to determine the uncertainties of the parameters (as in the velocity field analysis). However, to reduce the number of parameters it has been chosen to fit a symmetric model. Moreover, fitting the receding and approaching side separately is, except in the case of strong lopsidedness, not physical, since it splits the disk in two sub disks that are independent of each other.

The onsets of the gradients in radial and rotation velocity above the plane ($ZDRA$, and $ZDRO$, see section 4.3.3.1) are kept constant for all radii. Their best-fitting values are found to be 8 ± 2.4 and 22 ± 0.2 arcsec. The scale height, $Z0$, is found to be 40.8 ± 3.8 arcsec, which is roughly 630 pc. Fraternali et al. (2002) find a thickness of the cold disk of 400 pc. This is after the removal of the anomalous gas component. For the latter, they find a thickness of < 3 kpc. However, in this chapter, NGC 2403 is modelled as a single disk object. This is in contrast to the approach of Fraternali et al. (2002), where the neutral atomic hydrogen (H I) gas is modelled as a two component model. Thus, the thickness measured in this work is a superposition of the cold disk and the anomalous gas and is therefore larger than the thickness of the cold disk as determined by Fraternali et al. (2002).

It should be noted that the gradient in radial velocity above the plane of the disk is relatively uncertain in the centre of the galaxy. The fit is in this case not very stable since it yields strong radial variations of the $DVRA$ parameter. The radial range from 300 to roughly 600 arcsec, however, gives a very stable result with a velocity gradient of about $0.5\,\mathrm{km\,s^{-1}\,arcsec^{-1}}$. Nonetheless, the minor axis xv diagram shows a relatively good fit above the 2-σ_{rms} level. However, especially at the 1-σ_{rms} level, corresponding to the outermost contour, the model seems to deviate from the data. In the minor axis xv diagram, the parameter value at a certain radius has an effect on the neighbouring data points. Hence, the $DVRA$ value at a certain radius cannot be directly associated to a radial offset coordinate (to a angular offset coordinate on the abscissa). Moreover, also the presence of a warp in the centre makes it more difficult to integrate a $DVRA$ component into the model since its effect on the model data depends on the geometry of the warp. Hence, fitting this parameter is not trivial and its values for the inner radii are not very well determined.

Figure C.2 in the appendix shows the best-fitting parameters of the warped model and Fig. C.4 shows the comparison of several channels of the data cube to this model. In the latter figure, it confirms that the vertical gradient in radial velocity is not very accurately mapped in the centre. This can be observed in channels 17 to 23 and 41 to 44 as model data cube

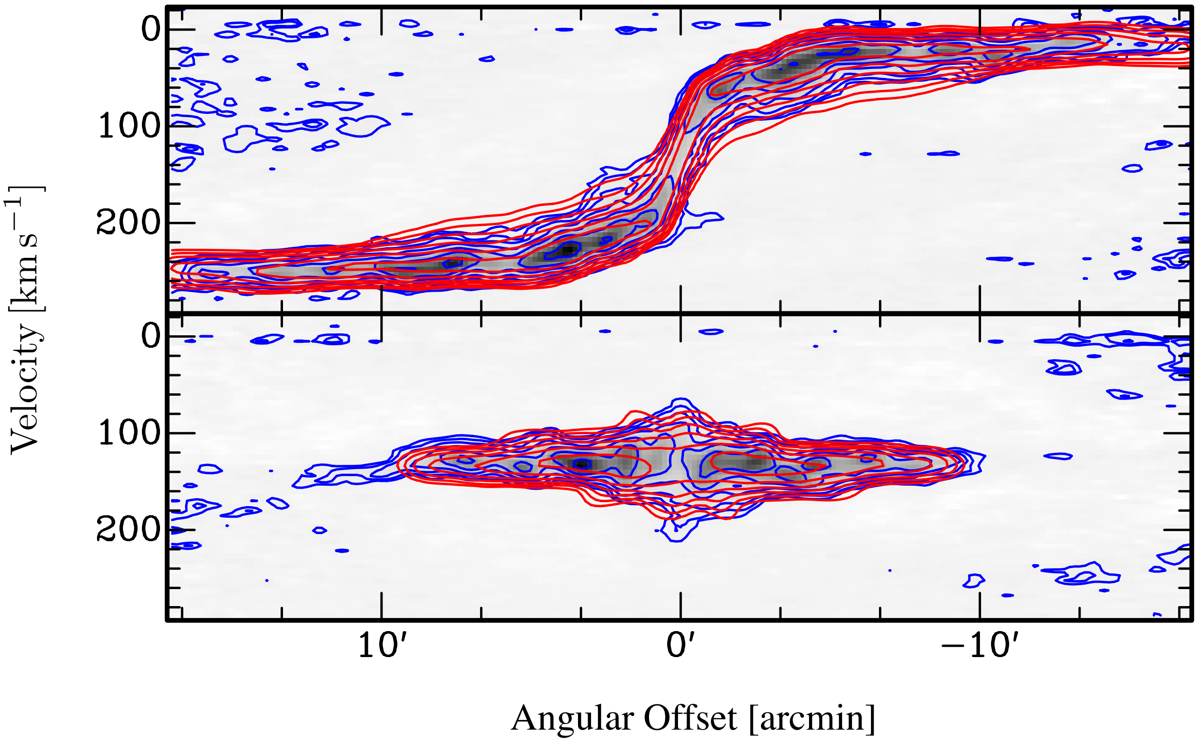

Figure 4.10: NGC 2403 position velocity diagrams of the warped model. The major axis slice (top) is taken along a position angle of 304.5 degrees, which is the average Γ of Fraternali et al. 2002. The minor axis xv diagram is measured 90 deg. perpendicular to that. The contours correspond to levels of 1, 2, 4, 8, 16.. units of $\sigma_{\rm rms}$ of the primary beam corrected data cube, where the red contours correspond to the model and the blue contours represent the data.

contours lagging slightly too much behind the rotation of the cold disk component. Comparing the inclination and position angle values to the ones found in the velocity field analysis and by Fraternali et al. (2002), it can be seen that their parameters behave analogously. The amplitude of the inclination angle, however, seems to be higher in the velocity field analysis compared to the one resulting from the TiRiFiC model.

Figure 4.11 (left panel) shows the estimated radial inflow as computed according to Sec. 4.3.3.1 corresponding to the warped model. Due to the negative *DVRA* parameter, as shown in Fig. C.2, the central region shows an inflow. However, as mentioned before, the fitting in this region is problematic. The xv diagram along the minor axis, however, seems to suggest that the negative *DVRA* component is needed such to achieve the skewness of the contours. In the next section it is therefore investigated if bar-streaming can reproduce this behaviour without including a *DVRA* and *DVRO* component in the centre.

The SSC data has been analysed by taking the resulting model with the parameters from Fig. C.2 and performing one fitting iteration to the SSC data cube. Figure 4.12 shows the xv diagrams of the SSC data. Clearly visible at a velocity of naught is the MW emission. Another feature that is visible is the velocity structure inherent to the MW contamination, this is visible as regions of non-uniform emission associated to the MW contribution. In particular the major-axis xv diagram shows that the approaching side of the galaxy is significantly affected by the influence of the MW. The right panel of Fig. 4.11 shows the inflow as calculated from the SSC

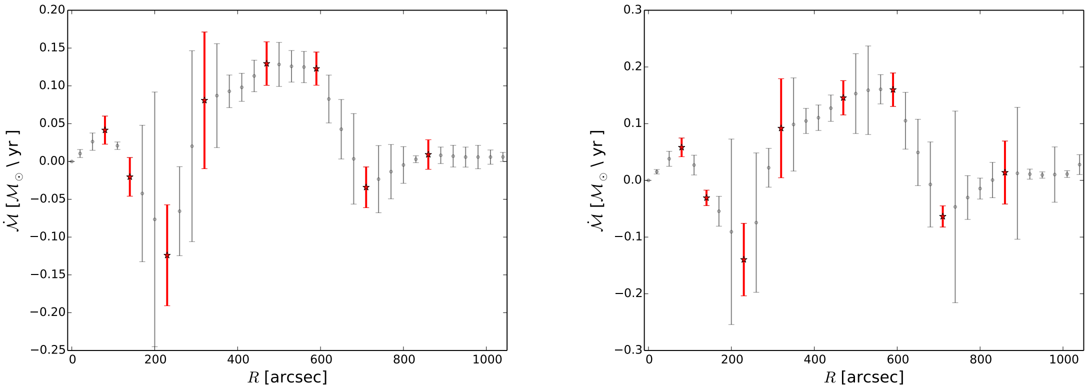

Figure 4.11: NGC 2403 radial inflow of the warped model. *Left*: the interferometer-only data. *Right*: the combined data. A positive $\dot{\mathcal{M}}$ stands for an inflow motion. Note that the points in red are the points fitted in the model. The grey points either result from interpolation between the red points or are fitted together as a group.

data. This profile looks very similar to the one based on the interferometer model only. The only difference is that the inflow in the range around 500 arcsec is somewhat higher than in the interferometer data: the maximum inflow based on the interferometer data is $0.13 \pm 0.06\,\mathcal{M}_\odot$ yr^{-1}, whereas the combined data yields an inflow of $0.16 \pm 0.05\,\mathcal{M}_\odot$ yr^{-1}. Inspection of the xv diagram suggests that this enhanced inflow in the SSC data could be significant and is indeed a real effect. As also visible in the comparison of the data cubes for the SSC and the interferometer-only data in Fig. C.1, the difference between the data is mostly on the 1-$\sigma_{\rm rms}$ level. Thus, on the basis of the magnitude of this difference, one expects the differences to be subtile, which they are found to be.

4.3.3.3 Unwarped model, bar-streaming

In the model containing a warp, it proved to be difficult to accurately model the inner part of the galaxy. This is due to the suggested presence of a warp in the centre by the velocity field analysis (see 4.3.2.3 and Fraternali et al. 2002) and its degeneracy with the parameters $DVRA$, $Z0$, $ZDRA$. For this reason, as well as the unlikeliness of the presence of a warp at such radii (see Chap. 4.3.3.1), in this section, it is attempted to model the NGC 2403 kinematics without resorting to modelling a bent disk. Instead, it is assumed that the inner part of the disk can be modelled using bar streaming motions and that the disk is flat ($i = const.$, $\Gamma = const.$). The TiRiFiC parameters used for this are $RO2A$, $RO2P$, $RA2A$ and $RA2P$, hence, the amplitude and phase of the harmonic tangential rotation and radial velocity of 2nd order, respectively. As starting values for i and Γ, the means of these parameters in the warped model are taken at large radii. These parameters are kept constant and are varied as a group. The bar is parameterised by fitting a varying amplitude and a constant phase for the first ten data points (until 260 arcsec). Beyond 290 arcsec, the parameters describing the bar are set to naught since at these radii the disk is mostly flat (see e.g. Fig. 4.4, Chap. 4.3.3.2 and Fraternali et al. 2002). Moreover, also the parameters $DVRA$ and $DVRO$ are set to naught for the inner part of this galaxy. The motivation for this is that bar motion can produce similar results as vertical motions above the plane of the galaxy. Furthermore, an outflow in the centre of the galaxy is not suggested by the velocity field analysis and does not seem physical.

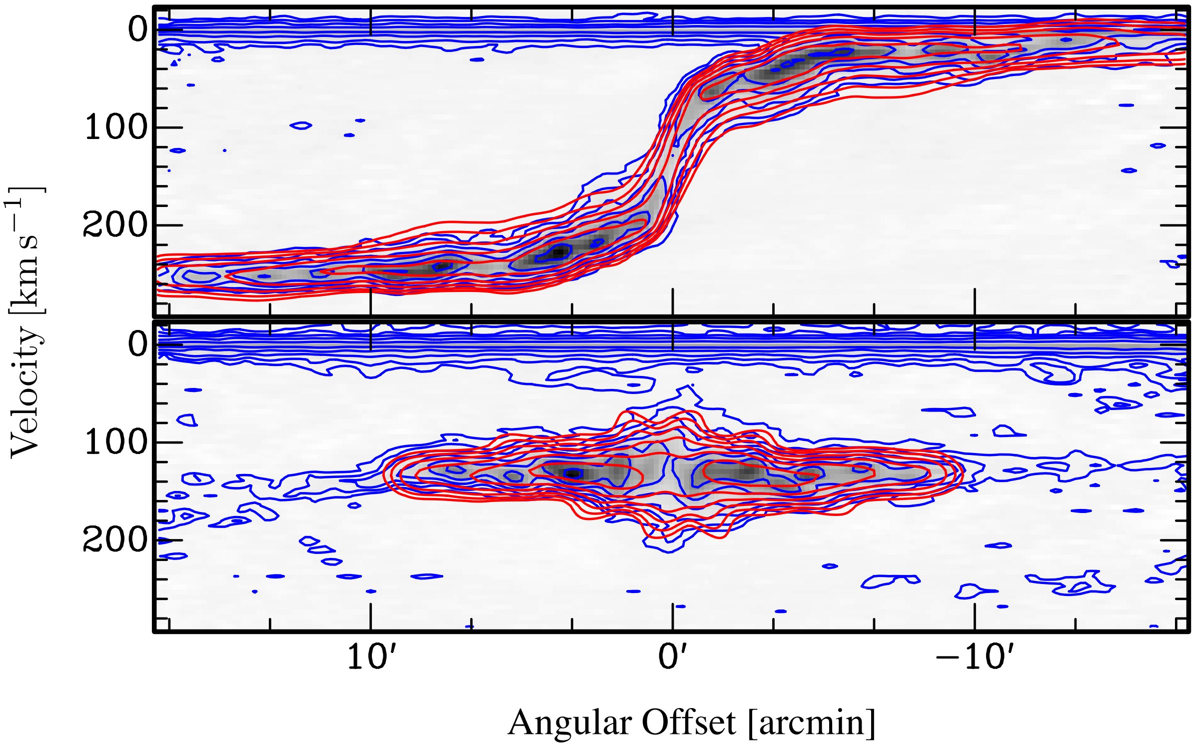

Figure 4.12: NGC 2403 position velocity diagrams corresponding to the SSC data for the case of the model which includes a warp. *Top*: slice along the major axis. *Bottom*: slice along the minor axis. The contour levels are the same as in Fig. 4.10

The xv diagram is shown in Fig. 4.13. Especially the minor axis xv diagram motivates that the bar describes the inner part of the galaxy significantly more accurately than the warped model. In the major axis plot, the bar model also performs at least as well as the warped model. The improvement over the warped model is also very prominently visible in the data cube, see Fig. C.5: where in the warped model, there are some discrepancies in several channels in the data cube, very few of such deviations can be observed in the bar model. Most of the remaining deviations can be attributed to lopsidedness of the galaxy. The best-fitting model parameters are shown in Fig. C.3. Except for the vertical gradients in rotation and radial velocity ($DVRO$ and $DVRA$), which describe the "beard" in the xv diagrams and the flat disk geometry (i =const, Γ =const.), most parameters are similar to the warped model. The H I mass inflow profile is shown in Fig. 4.14. In the bar model, the $DVRA$ parameter in the central region is set to naught and is replaced by a bar streaming motion. Bar streaming motion is a form of non-circular motion, but produces no net inflow since the orbits are elliptical. In velocity fields, a bar-like potential produces the same signatures in a velocity field as axisymmetric inflows or outflows (Wong et al., 2004). In the analysis of data cubes, it is also very difficult to distinguish between an inflow motion and motions as caused by a bar-like potential, since both show similar patterns in the data cube. Comparing the xv diagrams and the channels of the data cube, however, strongly suggests that the inner part of the kinematics of this galaxy can be most accurately described by bar streaming. The mass inflow also peaks at about 500 arcsec, in agreement with the velocity field analysis. Its amplitude as derived form the left panel of Fig. 4.14 is of the order $0.12 \pm 0.05\,\mathcal{M}_\odot\ \mathrm{yr}^{-1}$ from 300 to 600 arcsec.

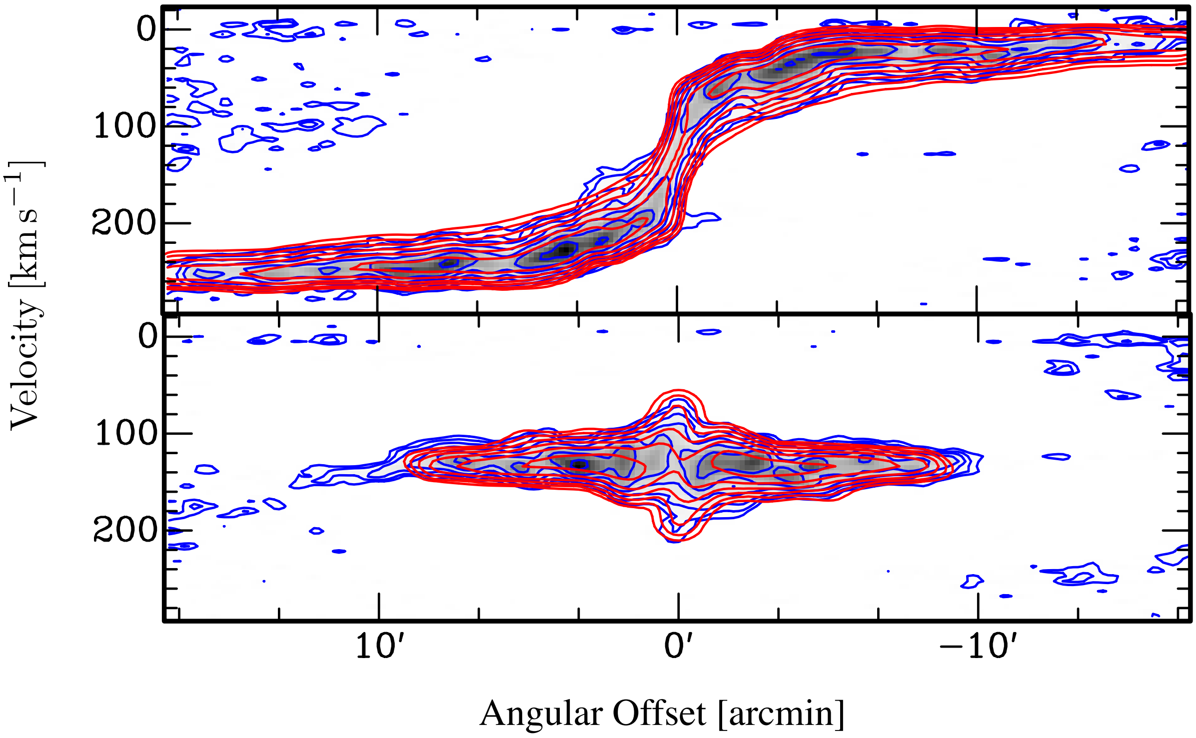

Figure 4.13: NGC 2403 xv diagrams corresponding to the interferometer data for the model in which the inner part is modelled by a bar instead of a warp. *Top*: slice along the major axis. *Bottom*: slice along the minor axis. The contour levels are the same as in Fig. 4.10.

The corresponding value for the SSC data from the right panel is $0.14 \pm 0.05\,\mathcal{M}_\odot\ \mathrm{yr}^{-1}$. This is somewhat less than in the case of the model which included a warp, but consistent within the uncertainties. Also these values suggest that the SSC data show an enhanced mass inflow, but due to the large uncertainties, this is not conclusive evidence.

4.3.4 Conclusions and discussion

In this section, the effect of SSC in the case of MW confusion on the H I kinematics has been studied using NGC 2403 as a test case. Moreover, the signatures of accretion in this galaxy have been modelled using model data cubes. It has been shown that the inner part of NGC 2403, which is commonly described by a warp in the analysis using velocity field, is better modelled using a model with a flat disk geometry (constant inclination and position angle) and bar streaming motion in the centre. One fundamental difference between these models is that in a scenario without a bar, an outflow in vertical direction is implied by the model. To verify whether such a scenario is likely, the star formation activity is considered. In Heesen et al. (2014), the star formation rate of NGC 2403 is investigated in great detail. They construct a hybrid star formation tracer from a linear combination of FUV and MIR data and measure the star formation rate trough the radio continuum emission. The star formation rate surface density profile shown in Fig. 18 of their work, $\Sigma_{\mathrm{SFR}}(R)$, suggests that star formation activity is highest in the central 3 kpc of the galaxy, then drops, and stabilises at a somewhat lower level. This does not allow one to exclude the scenario of a possible outflow;

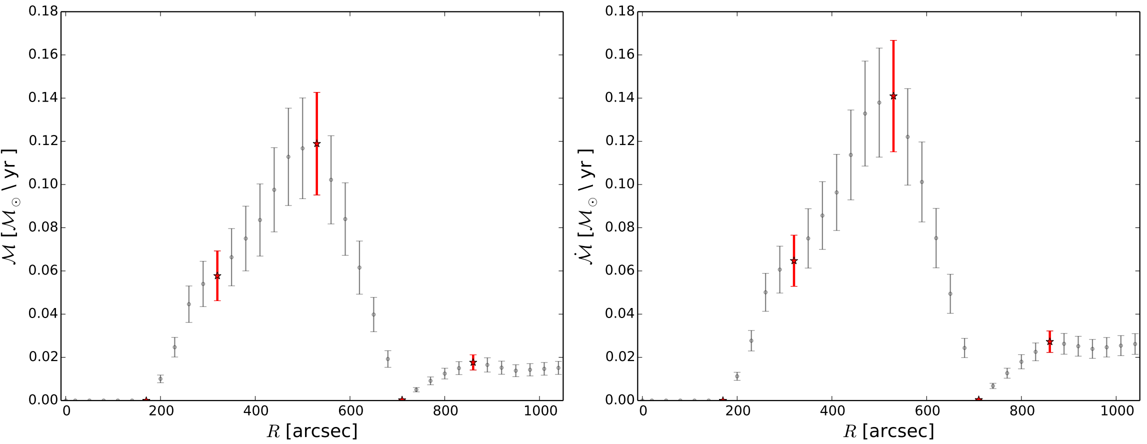

Figure 4.14: NGC 2403 radial inflow of the bar model. *Left*: the interferometer-only data. *Right*: the combined data. A positive $\dot{\mathcal{M}}$ stands for an inflow motion. Note that the points in red are the points fitted in the model. The grey points either result from interpolation between the red points or are fitted together as a group.

supernovae associated to massive stars could expel neutral gas from the disk, giving rise to the observed outflow component. Moreover, the radial interval where gas inflow is found in this work (around roughly 8 kpc), does not show enhanced star formation activity. However, it has to be noted that these measurements only run until 8 kpc and the uncertainties become increasingly large with increasing distance from the galactic centre. A possible scenario is that the gas falls onto the disk, but has an energy that is too high for star formation. This gas would then move into the disk to the edge of the H I bar, which is located around 4 kpc from the centre. At this point, the bar could remove angular momentum and energy from the gas moving inward. Via the associated molecular lines, the gas can cool even further and collapse, to initiate star formation. The end points of the bar are intersections of gas streams, these intersections cause shocks, which dissipate the energy (see e.g. Athanassoula 1992). This causes a phase difference between the phase of the bar potential and the gas orbits, which results in an exerted torque. This torque removes angular momentum from the gas and transports it outwards. The resulting low energy gas can form molecules which are arranged on inner rings with radii where the Lindblad resonances corresponding to the bar potential are located. The gas can then cool via the molecular lines and star formation can take place. Such rings have been detected (e.g. Regan et al. 2002). In the case of NGC 2403, molecular gas in the form of carbon monoxide (CO) has been detected in its central regions (Schruba et al., 2012), but the presented information does not allow to conclude whether this gas is present in the form of a ring.

The accretion rate found by analysing the data cube in the warped and barred model is about 0.13 ± 0.06 and 0.16 ± 0.05 $\mathcal{M}_\odot\,\mathrm{yr}^{-1}$ in the case of the interferometer and 0.12 ± 0.05 and 0.14 ± 0.05 $\mathcal{M}_\odot\,\mathrm{yr}^{-1}$ in the case of the combined data, respectively. The difference between the interferometer-only and the SSC inflow rate is brought about by the slightly higher surface brightness and disk thickness resulting from the fit. It can, however, not be concluded if this difference is only due to the additional single-dish emission or if it is caused by the MW contamination. The mass inflow derived from the SSC data is slightly larger than that derived from the interferometer data. Moreover, also the flux of the combined data is higher than the flux of the interferometer map (J. Kerp, in prep.). This makes it likely that the additional mass flow in the combined data is taking place via smooth accretion of diffuse gas. The interferometer data used in this chapter is from the THINGS survey. In Walter et al. (2008) the authors report a sensitivity of 4×10^{19} cm^{-2}, which in the case of NGC 2403 results in a sensitivity of the order of $10^4 \mathcal{M}_\odot$. This would allow the detection of a typical high-velocity cloud (HVC) of $10^5 \mathcal{M}_\odot$ (Putman et al., 2012) by the interferometer. Therefore, at least part of the accreted gas is possibly constituted by cold gas.

The gas inflow rate found by analysing the data cubes is several times lower than the SFR as found in Heesen et al. (2014), who find a SFR of 0.331 and 0.868 $\mathcal{M}_\odot\,\mathrm{yr}^{-1}$ from the radio continuum and FUV and MIR emission, respectively. The value found by the analysis of the velocity fields is greater than 1 $\mathcal{M}_\odot\,\mathrm{yr}^{-1}$ and thus exceeds the star formation rate. Due to the large systematics that are inherent to the analysis and interpretation of radial motions using velocity fields (see also Chap. 4.4), the result from a fit to the data cube is considered to be significantly more accurate than the resulting accretion rate from the velocity field.

It has been shown that the contribution from the MW prohibited an analysis of the SSC using velocity fields. Moreover, it has been shown that modelling the kinematics using the data cube does not suffer from this limitation to the same extent: accurately modelling the SSC data is still possible, albeit with larger uncertainties.

In this section it has been attempted to separate the anomalous gas component from the cold disk component as performed by Fraternali et al. (2002) on interferometer data only. This cold disk component is then subtracted from the SSC data cube, only leaving the warm gas and the MW emission. Then it was attempted to extract the warm gas component by subtracting the MW. This attempt, however, fails in the case of the combined data due to the velocity structure of the MW contamination. Eliminating the MW contribution from the combined data is a complicated problem, since the MW contribution is not uniform, but has a certain velocity structure, and strongly varies with radial velocity. This has consequences for the study of nearby (dwarf) galaxies which are located at a line of sight close to the plane of the MW: if the MW contribution is not accurately modelled and subtracted from the data, the effect of SSC cannot be distinguished from the influence of the MW. Therefore, if one aims to study accretion by (dwarf) galaxies, one is limited to either study interferometer data, accurately modelling the MW contamination of the SSC data, or to study SSC data sets which are not hampered by MW emission.

Finally, it has to be emphasised that the study of accretion is highly complicated: NGC 2403 is one of the galaxies which is known to have anomalous gas surrounding the cold disk and possesses the optimal geometrical orientation for studying this effect. To detect this anomalous gas, deep observations are needed as well as careful modelling. This work uses an observation with an integration time < 10h, whereas Fraternali et al. (2002) base their results on a observation of 40h, resulting in a higher sensitivity. Due to the proximity of NGC 2403, degrading the resolution to achieve a better sensitivity does not prohibit a detailed kinematical analysis. However, for more distant galaxies, a lower resolution has more severe consequences on the measured parameters. This is discussed in the next section.

To summarise, studying accretion in nearby galaxies is on the one hand side complicated by MW emission and on the other hand, sensitive observations are needed as well as careful modelling to estimate accretion rates.

4.4 Systematical effects of the analysis of velocity fields

It is well known that the problem of beam smearing generally affects the rotation curve derived from a tilted-ring fit to a velocity field (see e.g. Begeman 1987). Unknown is, how beam smearing affects the measurement of other parameters such as the radial velocity. It is not known how resolution effects caused by observing galaxies at larger distances relate to the measurement of such parameters. Moreover, the analysis of velocity fields is subject to systematics, one of which is the fact that if there are strong warps, i.e., if the line of sight vector intersects the disk more than once, the galaxies' kinematics cannot be described by the velocity field (see e.g. Józsa et al. 2007). Furthermore, there are other effects, such as the finite thickness of the disk and a rotation/radial velocity gradient above the disk (as shown to likely be present in NGC 2403), which might cause effects on the measured kinematical parameters.

Chap. 4.4.1 investigates the effect of distance on the velocity fields, Chap. 4.4.2 studies the effect of a non-zero scale height and Chap. 4.4.3 studies the effect of the vertical velocity structure on the velocity field.

4.4.1 Distance

In this section, the question is pursued until which distance (D), which kinematical components can still be described correctly using the velocity field. NGC 2403 has a distance of about 3 Mpc, and therefore, is located at a much lower distance than the galaxies in Chaps. 2 and 3. The resolution is limited by the Rayleigh Criterion ($\alpha \propto \frac{\lambda}{D}$), where α is the smallest angle that can be resolved and λ the wavelength at which is observed. Hence, for larger distances, the angular resolution becomes more coarse. This has at least three effects on the data:

- *Beam-smearing.* Since data points inside one beam are correlated, the information is "smeared out" across the beam.
- *Noise.* Noise is a characteristic of the observation and is described by the radiometer equation:

  $$\delta T \approx \frac{T_{\mathrm{sys}}}{\sqrt{\Delta\nu\,\tau}}, \tag{4.18}$$

  where T_{sys} is the system noise temperature, which is a sum of the elements of the observation giving rise to noise such as the CMB, the source, the atmosphere and most of all, the receiver. δT is the rms noise of the observation, $\Delta\nu$ is the bandwidth of the observation and τ the integration time. Thus, for any observation (no matter how distant the object), the rms noise is set by the properties of the observation (T_{sys}, $\Delta\nu$ and τ). On the other hand, the strength of the signal does vary with distance. The flux density is given by $S_\nu = \int I_\nu d\Omega$, where I_ν and Ω are the intensity and solid angle, respectively. The intensity is an intrinsic property of the source, whereas the solid angle varies as $1/D^2$. Thus, the noise is constant, but the signal decreases with the distance squared. Therefore, the decreasing signal-to-noise ratio of the observation will also be an issue in studying galaxies at larger distances.
- *Characteristic scales of the ISM.* Observing galaxies at different distances with an interferometer causes the angular scale to measure different length scales in the galaxy. The baselines will therefore trace different parts of the ISM.

At the wavelengths in the range of the H I transition, resolution is an issue. The decreasing signal-to-noise ratio will also have an effect on the data. ISM components can be separated also in frequency space, which is not affected by increasing distances. The first two effects therefore, are expected to have the largest effects on a study of the kinematics and therefore, these will be considered in this section.

4.4.1.1 Simulations of galaxies at different redshifts

To study the effect of beam smearing on the derived parameters more quantitatively, the data is projected at different distances using a convolution. NGC 2403 is therefore projected into distances of 20 Mpc, 60 Mpc and 120 Mpc. The first is a characteristic distance for the galaxies from Chap. 2, the latter for the galaxies from Chap. 3 and the other distance represents an intermediate distance. The original beam of the available observation is characterised by a beam major axis of 9 arcsec. Given that NGC 2403 is located at a distance of roughly 3.2 Mpc, the data would need to be convolved with a Guassian kernel of a FWHM of 56, 159 and 338 arcsec to have a similar resolution if the galaxy would be observed at 20, 60 and 120 Mpc, respectively. For simplicity, the convolution kernels used are 60, 180 and 360 arcsec, corresponding to distances of 21.3, 64 and 128 Mpc. The exact procedure that is used here is:

1. The beam size is reduced by a factor of $D/3.2$ (both the *BMAJ* and *BMIN* keywords in the header).
2. The pixel size is reduced by a factor of $D/3.2$ (the keywords *CDELT1* and *CDELT2* in the header).
3. The intensities are scaled by a factor of $(D/3.2)^2$. This is necessary, since the pixel size is reduced and also the beam size is shrunk.
4. This data cube is convolved with a symmetric 2-dimensional Gaussian such that the output set of images has a beam equal to that of the original image[3]. This assures that the data cube has the resolution corresponding to the distance D.
5. This image is masked using a 1-$\sigma_{\rm rms}$ clipping level.
6. This data cube is regridded to have to the pixel size corresponding to that of the the input image.
7. A noise data cube is created by repeating the line free channels of the input data cube. However, since the original data cube only contains six line free channels, repeating these channels will cause local noise peaks in the output data. To reduce this effect, each channel of the cube containing the noise data is calculated as a linear combination of the randomly rotated (either about 90, 180, 270 or 360 deg.) channel maps. These weights are pseudo random numbers between 0 and 1 and for the final noise data cube to have the same $\sigma_{\rm rms}$ noise, each map has to be weighted by the sum of the squared weights.
8. The noise cube is added to the scaled, convolved and regridded image. This results in a data cube having the correctly scaled flux densities, resolution, and the exact noise level from the observation.

---

[3] This is done with the Multichannel Image Reconstruction, Image Analysis and Display (MIRIAD, Sault et al. 1995) task `convol` setting `options=final`.

There are several matters not taken into account in this analysis. However, the emphasis in this section is on finding systematic trends. Therefore, the not considered following points does not have a large impact on the observed trends:

- One detail that is neglected in this scheme is the change of the systemic velocity of the galaxy; if a galaxy is redshifted, the line-of-sight velocities would have to be corrected for this. Using the radio definition of recession velocity, this would just cause a linear shift in velocity which does not cause any systematics.

- Another effect not considered in this scheme, which relates to the surface brightness, is redshift dimming. The latter is proportional to $(1 + z)^4$. This is not accounted for but would cause the signal-to-noise ratio to decrease. In particular for the 128 Mpc case, corresponding to $z \approx 0.032$ (assuming $H_0 = 75$ km s^{-1} Mpc^{-1}, the surface brightness decreases by an additional factor of about 13 per cent.

- Finally, cosmological line broadening is not accounted for, since this effect is not very large for these distances (a factor of 1+z) and this systematic effect can be completely accounted for.

- Influence of MW emission. Since interferometer data is used in this section, the MW contamination does not play a significant role.

The next step in this analysis is to study the effect of degrading the resolution on the kinematics. To study this, a model is fitted to the velocity field. The tilted-ring model corresponding to the interferometer-only data is taken as a starting point, and is fitted to the first-moment maps after resolution degradation. The separation between the rings is kept at around one FWHM of the beam, thus, in the discussed cases, the number of rings is reduced by a factor of 2, 6 and 12 respectively. Hence, to make the models comparable, the parameters have to be determined at the same radii.

4.4.1.2 Analysis of the distance dependence of the kinematical parameters

As mentioned before, the most commonly used velocity field is the first-moment map and thus, the following analysis is performed on these velocity fields. The velocity fields are analysed using the same method as discussed in Sec. 4.3.2.2. The results of this analysis for the $D = 21.3$ Mpc case is shown in the top panels of Figs. 4.15 and 4.16, where the red triangles describe the fit result of the 21 Mpc data and the grey points the input data. The parameters v_{rot} , i, and Γ are within their uncertainties equal to the parameters determined in the analysis of the original data. The results of the harmonic decomposition show that the uncertainties are larger compared to the analysis of the galaxy at its proper distance. Markedly the inflow signature between roughly 6 and 9 kpc as indicated by the s_1 term as shown in e.g. Fig. 4.6 is still visible in the top panel of Fig. 4.16, albeit the uncertainties are significantly larger. Qualitatively, the curved iso-velocity contours[4] still show a similar behaviour as in the non-smoothed data (see e.g. Fig. 4.3) and thus, the non-circular motions are still preserved in the case where the resolution is downgraded to the corresponding resolution were the galaxy is at a distance of 21 Mpc.

The xv diagrams are shown in Fig. 4.17. In the xv diagrams, the features that indicate gas accretion and bar motion, hence, the beard component, can still be distinguished. Thus,

---

[4] Iso-velocity contours are lines of constant line-of-sight velocity

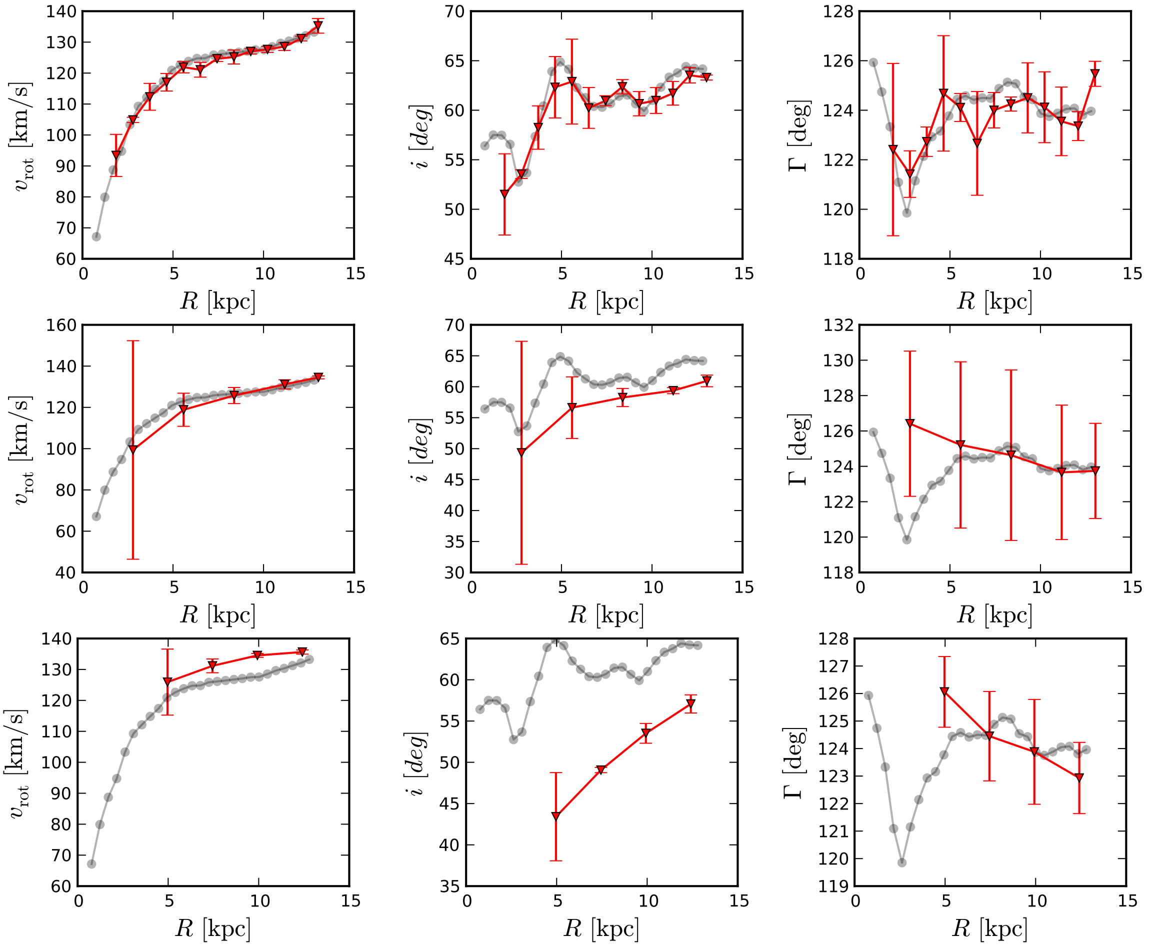

Figure 4.15: Results from the tilted-ring fit to the first-moment velocity field for NGC 2403 at three different distances. The top panels shows NGC 2403 at 21 Mpc, the middle panels at 64 Mpc and the bottom panels at 128 Mpc. From left to right, the graphs describe profiles of the rotation velocity ($v_{\rm rot}$), the inclination (i), and the position angle (Γ). The grey points denote the results from the fit to the resolved data cube and the red points represent the fit to the redshifted velocity field.

the signatures of gas accretion and bar motion are still contained in the data. The repeating artefacts are caused by the addition of the noise.

The velocity field and the parameters derived from it in the 64 Mpc case are shown in the middle panels of Figs. 4.15 and 4.16. The parameters derived at the inner radii show large uncertainties and in particular the position angle (Γ) cannot be accurately derived. The asymptotic rotation velocities can, however, still be estimated correctly. The inclination is, on the other hand, slightly underestimated for all radii. This is a systematic effect that occurs since beam smearing causes the minor axis to be more smeared out compared to the major axis of the velocity field. This causes the velocity field to appear more circular, and thus causes an underestimation of the ellipticity (a lower inclination angle), see also Chap. 3. In this case, the effect of this on the rotation velocity is nevertheless, not very large, due to the inclination angle of the galaxy (see e.g. Fig. 2.1 in Chap. 2.4).

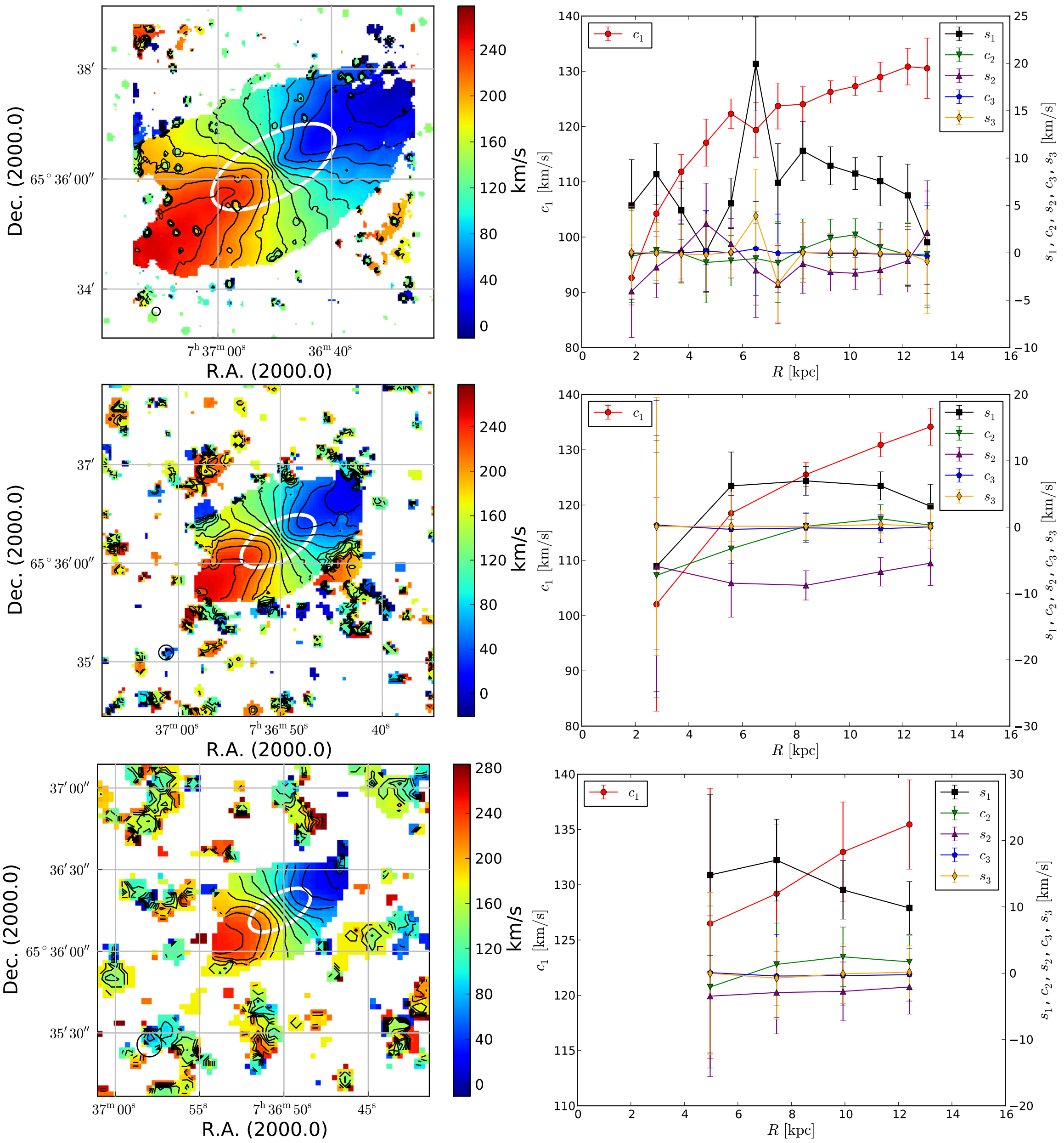

Figure 4.16: NGC 2403 velocity fields and harmonic coefficients depending on the distance. The left panels are the first-moment velocity fields, the right panels the result of the harmonic decomposition of this velocity field. The two graphs on top represent the 21 Mpc scenario, the middle ones the 64 Mpc scenario and the bottom graphs the 128 Mpc case. The white ellipse indicates the location of the ring at 7.7 kpc (see text). The left scale is for the c_1 parameter and the right scale for the remaining parameters. The beam is represented by the black circle on the bottom left of the velocity fields.

The curvature of the iso-velocity contours has for the most part disappeared. This is also visible in the results from the harmonic decomposition: the s_1 term does show a non-zero value in the ranges where inflow is suspected, however, it is significantly reduced in amplitude. Moreover, the xv diagrams, shown in the left panel of Fig. 4.18 show that the signatures of the

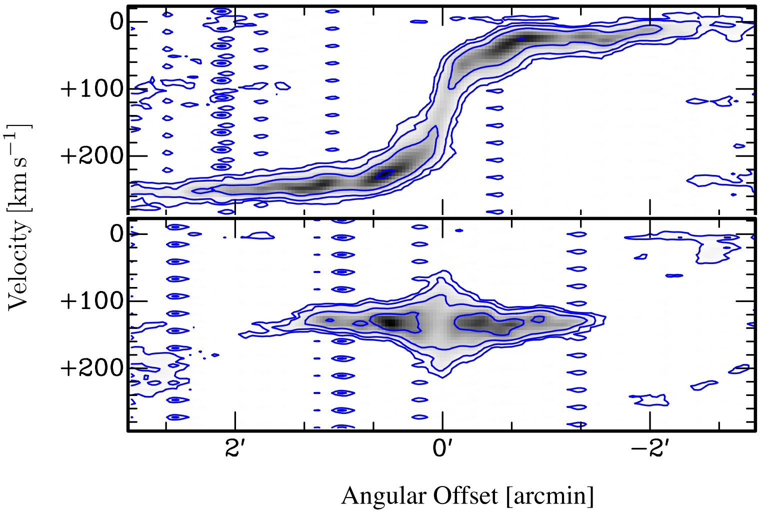

Figure 4.17: xv diagram of NGC 2403 at 21 Mpc. In this case, the contours are drawn at 2, 8, $32\sigma_{\rm rms}$, ...

anomalous halo gas have largely disappeared. Apart from resolution effects, one reason for this is the decreased signal-to-noise of the data: the accretion signatures in the fully-resolved data were strongest at a 1-$\sigma_{\rm rms}$ level. In the 64 Mpc case, the galaxy has become a factor of 400 fainter, therefore the signal-to-noise is strongly reduced, and the traces of gas inflow motions have been eliminated. Thus, it can be concluded that if the galaxy is redshifted out to 64 Mpc, the global kinematical parameters can still be extracted at large radii (above 5 kpc), but most of the detailed information on non-circular motions, and thus, accretion signatures, cannot be extracted any more from the velocity field.

The graphs resulting from the analysis of the 128 Mpc case are shown in the bottom panels of Figs. 4.15 and 4.16. The velocity field illustrates that the beam size is in this case a substantial fraction of the minor axis length of the galaxy, such that beam smearing is expected to play a large role in the derivation of the parameters. Moreover, the curvature of the iso-velocity contours cannot be distinguished any longer. Note that the titled-ring fitting has been performed using a smaller separation of 4 arcsec between the rings, making the different rings dependent of one another. The tilted-ring fitting still allows a rough derivation of the bulk rotation velocity. This is due to the aforementioned interval in which the inclination angle does not dominate the determination of the rotation velocity. The inclination is substantially underestimated at all radii, specifically in the centre of the galaxy. This effect is significantly stronger compared to the 64 Mpc case. As the iso-velocity contours suggest, the harmonic decomposition seems to yield no solid results. The s_1 term is smeared out over the whole spatial extent of the galaxy, and since it is degenerate with the position angle (see Chap. 4.4.2), it is not necessarily significant.

The xv diagrams for this case are shown in the right panel of Fig. 4.18. These diagrams are largely featureless. In the major axis xv diagram, it is clearly visible that no sensible rotation curve can be derived for this data set. As is the case in the 64 Mpc scenario, this figure shows that the beard emission has been smeared out over the whole radial range. This illustrates that one is no longer able to accurately map the gas inflow signatures.

To conclude the analysis of the resolution degraded velocity fields, the azimuthal profile

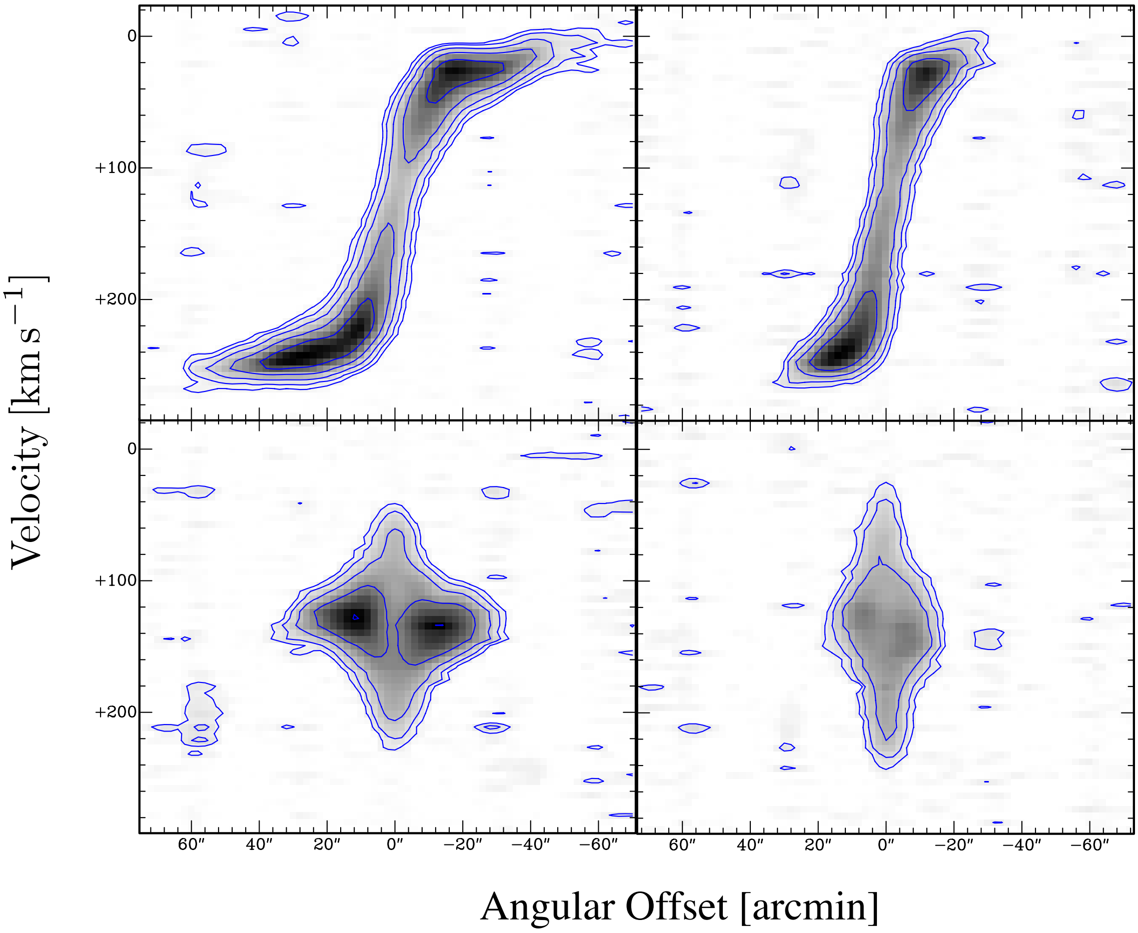

Figure 4.18: xv diagram of NGC 2403 at 64 Mpc (*left*) and at 128 Mpc (*right*). The contours show the 2, 8, 32$\sigma_{\rm rms}$, ... levels.

corresponding to a radius of 500 arcsec (7.7 kpc) in the original velocity field is considered in more detail. These ellipses are also shown in the velocity fields presented in this section (left panels of Fig. 4.16). The reason for studying the profile at this radius is that the strongest signature of inflow motion is located at this radius (see Figs. 4.7 and 4.11). In Fig. 4.19, the azimuthal velocity profiles $v_{\rm rad}(R, \theta)$ are shown. The geometry of the ellipses corresponds to the best-fitting i and Γ from Fig. 4.5, hence, $i = 62$ deg. and $\Gamma = 119.81$ deg. In these figures, one can see that the number of data points is decreasing with every step in distance. Moreover, the amplitude of the line-of-sight velocity does not change significantly with distance. This is even more clear if one inspects such profiles for larger radii. The lines plotted on the profiles correspond to the model from Eq. 4.3: the blue line corresponds to the case where $v_{0,\rm rad} = 0$, and thus only describes the rotational motion:

$$v_{\rm los} = v_{\rm sys} + v_{0,\rm rot} \cos\theta \sin i, \tag{4.19}$$

whereas the magenta line includes the radial component of motion. In this case, it is set to 13 km s^{-1}, corresponding to the result of the analysis of the first-moment map as presented in Sec. 4.3.2.3. This figure shows that especially for the original data at 3.18 kpc, as well as the 21 Mpc case, the model with an inflow clearly fits the data better. In the 64 and 128

Mpc cases, the latter in particular, the accuracy of the models cannot be distinguished clearly, and thus, radial motions can no longer be derive from the data. It is noted, however, that a slightly lower value for the radial component might yield a better correspondence to the data as suggested by the middle and bottom panels of Fig. 4.16. Another issue is the number of independent data points available for a fit. The original velocity field contains about 3,500 data points at a radius of 500 arcsec with a ring width equal to one beam FWHM. In the case of 21.3, 64 and 128 Mpc, these are 500, 170 and 80 data points, respectively. These are, however, not independent data points, but are correlated through the beam. Thus, the number of independent data points is reduced by a factor of $\beta \approx 6.8$ (see Sec. 4.3.2.2). The tilted-ring model has 2 geometrical parameters (aside from the position of the centre), i and Γ plus $v_{\rm rot}$ and $v_{\rm sys}$. Hence, in the case of 128 Mpc, there are about 12 independent data points. Obviously, if one performs a 3rd order Fourier analysis on this data, thus fitting 5 additional parameters to the data, the ratio of the number of parameters and independent data points approaches one and overfitting the data is imminent.

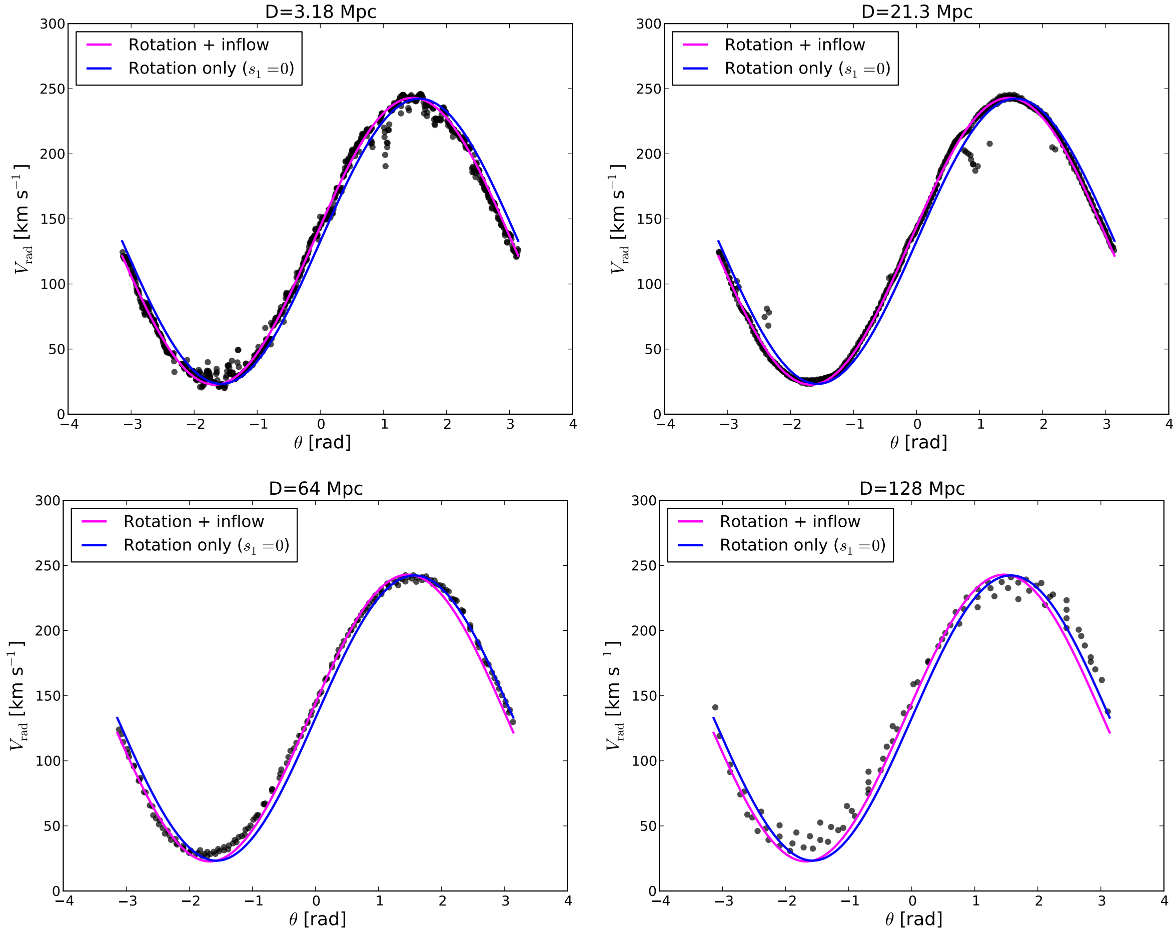

Figure 4.19: Azimuthal radial (along the line-of-sight) velocity profiles of the velocity fields at a radius of 7.7 kpc for the NGC 2403 velocity field projected out to different distances. The blue line describes the a model only using rotational motion and no radial motion, whereas the magenta line includes an inflow component. In the case of the original resolution (at 3.18 Mpc), a large portion of the data points have not been shown for clarity.

4.4.2 3-dimensional disk structure: scale height, thick disk

An important premise of velocity field based analyses is that it is assumed that galaxies are flat, symmetric disks. In practice, galaxy disks are not flat. Instead, they have a finite thickness and in several cases even a halo component has been observed. This is the case in the MW (see e.g. Steinmetz 2012), and is also clearly visible in nearby galaxies observed in an edge-on orientation, such as NGC 891, which shows a cold gaseous halo (Oosterloo et al., 2007) and obviously also in NGC 2403. The goal of this section is to present a few exemplary considerations of how the analysis of velocity fields is influenced by finite scale height. TiRiFiC is used to simulate several scenarios in order to establish trends. It is obvious that the inclination of a galaxy plays a role: in galaxies observed face-on, the effect of a non-zero thickness of the disk will play a different role compared to galaxies observed edge-on. Also the observed geometry of the H I disk is suspected to be influenced by the scale height: in the case of a varying position angle and inclination with radius, i.e., warping of the disk, a finite disk thickness is expected to influence the measurement of these parameters. In the following, several scenarios in connection to the thickness of the disk are considered. In all cases, the surface brightness profile and the rotation curve have been taken from Chap. 4.3.3.3. Moreover, a ring at 400 until 600 arcsec with an inward radial velocity (as is found in the previous analyses) with an amplitude of 20 km s^{-1} (inward motion) is included in the model. This is higher than the value found in Chap. 4.3.2, but better brings out the systematic effects. The scale height is chosen to be 1 kpc. This is a rather large value but serves well to illustrate the relevant systematics[5]. The plotted velocity fields in the following represent the ones corresponding to the thick disk; since the thick disk scenario causes the galaxy to appear more face-on, meaning the velocity field has a larger minor axis and is thus rounder.

4.4.2.1 Flat thick disk, intermediate inclination

In this case, the term “flat disk” also refers to an unwarped disk (position angle and inclination are constant with radius). The terms “thin/thick disk” refer to a the scale height ($Z0 = 0$ / $Z0 \neq 0$). A simple model has been simulated with comparable properties to NGC 2403: the inclination is chosen to be 62 deg. and also Γ is chosen to be constant over the whole disk. The velocity field is shown in the left panel of Fig. 4.20, where the blue contours describe the iso-velocity lines for the thin disk, and the red contours the thick disk. The corresponding parameters are shown in Fig. 4.21. The blue points describe the parameters resulting from the `rotcur` tilted-ring fit to the velocity field of the thin disk. The red points show these values in the case of a thick disk. The grey points are the parameters set in the TiRiFiC input model. From this, several trends can be derived:

i) Except for the very centre of the velocity field, the tilted-ring fits to the velocity field of the thin disk trace the input parameters of the data cube simulation almost perfectly.

ii) Immediately visible is the larger angular size spanned by the velocity field of the thick disk. Moreover, the contours at the outer radii appear to trace perpendicular to the minor axis of the velocity field, and thus demonstrate rigid body rotation (showing a rising rotation curve). This can be explained by geometry: since in the region of rigid-body rotation one observes the disk from an increasingly face-on angle, the inclination converges to naught and therefore the rotation velocity diverges. This is confirmed by the `rotcur` fitting results

---

[5] It should be noted, however, that Fraternali et al. (2002) did find that the thickness of the anomalous disk can be up to 3 kpc, therefore, the value of 1 kpc is perhaps not very unrealistic.

shown in Fig. 4.21: the fitting results for the thick disk simulation (red stars) show that the inclination angle converges to naught for large radii whereas the rotation velocity diverges. This is not observed in the thin disk scenario (blue squares): in this case, these parameters stay approximately constant with radius.

iii) Another difference between the velocity field of the thick disk and the thin disk is found in the centre: the contours corresponding to the thick disk run more parallel to the minor axis than the contours of the thin disk, which seem to emerge from one point following a x-like pattern. This could point to rigid body rotation in the centre, which could point to enhanced beam smearing. This is confirmed by the radial profile of the inclination in Fig. 4.21, in which the inclination converges to a value of naught for decreasing radius in the case of the thick disk.

iv) The inclination of the thick disk is underestimated at all radii, the complete velocity field hence appears more face-on due to the finite thickness. This is not the case for the thin disk.

v) The radial dependence of position angle (Γ) in the case of the thick disk shows a peculiar behaviour: at small radii (before the $v_{\rm rad}$ gradient), it is overestimated, whereas in the radial interval where the $v_{\rm rad}$ gradient is present, it is underestimated. This is closely linked to the presence of the gradient in $v_{\rm rad}$, since the amplitude of this parameter is significantly underestimated if estimated from the velocity field.

vi) Not just the amplitude of $v_{\rm rad}$, but also its radial profile is not correctly recovered in the fit to the thick disk velocity field. From its radial profile, it becomes apparent that its profile has been smeared out over a larger radial interval from roughly 200 to 800 arcsec (as compared to the actual input profile, which has a non-zero $v_{\rm rad}$ only from 400 to 600 arcsec).

Point v can be understood in the framework of Schoenmakers et al. (1997): the $v_{\rm rad}$ component is traced by the s_1 Fourier component in the harmonic expansion of the velocity field. s_1, however, is correlated with Γ. Thus, if the position angle is incorrectly estimated, i.e., in the case of the tilted-ring fit to the thick disk, s_1 and therefore, $v_{\rm rad}$ will be estimated incorrectly. Schoenmakers et al. (1997) derive the following relation for this from an epicycle expansion:

$$\cos\theta = \cos\hat{\theta} - \frac{\delta\Gamma}{4}\left[\left(3q + \frac{1}{q}\right)\sin\hat{\theta} + \left(\frac{1}{q} - q\right)\sin 3\hat{\theta}\right], \tag{4.20}$$

where $\delta\Gamma$ is the uncertainty in position angle, θ and $\hat{\theta}$ are the correct and incorrect azimuthal angles and $q = \cos i$. It thus follows that if Γ is wrongly estimated ($\delta\Gamma \neq 0$), an additional $\sin\hat{\theta}$ pattern is measured in the velocity field. This pattern is interpreted as a radial velocity by the tilted-ring fitting software.

4.4.2.2 Warped thick disk, intermediate inclination

In the next simulated velocity field, a warp is added to the model. This warp is chosen to be a one step warp in i and Γ, where the steps are 5° in i and 10° in Γ, respectively, at a radius that coincides with the interval where $v_{\rm rad}$ is non-zero (see also Fig. 4.22). The corresponding velocity field, as shown in the right panel of Fig. 4.20, shows a complicated velocity structure in this radial interval. In the centre and at large radii, however, it is similar to the flat disk

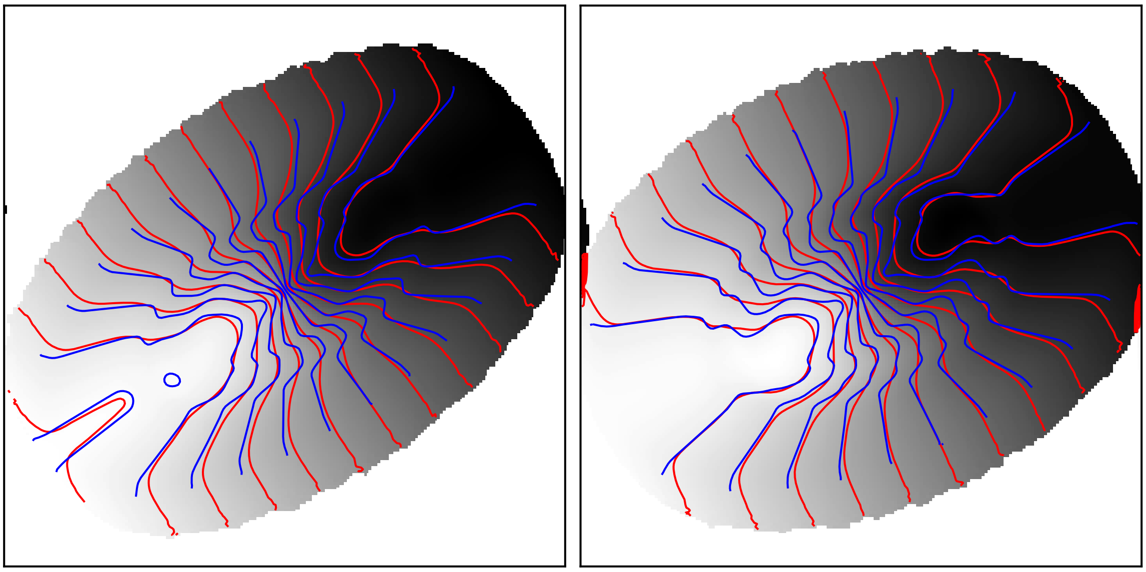

Figure 4.20: Velocity fields describing the effect of an intermediately inclined disk with non-zero thickness. In both cases, the blue contours describe the infinitesimally thin disk, the red contours the thick disk. The grayscale diagram describes the thick disk, since its angular size is larger than that of the thin disk. *Left*: Velocity field corresponding to the flat disk with 62° inclination. *Right*: Velocity field corresponding to the warped disk.

case (blue contours). The parameters from the tilted-ring fitting are shown in Fig. 4.22. The colours are the same as in the previous section; the blue contours/squares represent the flat disk scenario and the red contours/squares the thick disk scenario.

It can be observed that also in the warped velocity field, the tilted-ring fit to the velocity field of the thin disk is very successful (except in the very centre). For the thick disk, the rotation velocity is somewhat overestimated in the central regions due to the underestimated inclination. This is analogous to the results of the unwarped disk (note the different scale of the axes). Also in this case, the inclination angle is underestimated at all radii in the case of the thick disk. Moreover, the warp in inclination cannot be well retrieved: the fitting results show that the radius at which the warp occurs is too high, whereas the amplitude is underestimated. The radial profile of Γ also shows deviations from the input parameters in the case of the thick disk. The radial inflow is also not accurately traced for the thick disk, albeit the maximum amplitude is more close to the input value of 20 km s^{-1} than is the case in the thin flat disk. Analogous to the flat disk scenario, also in this case the radial velocity profile is smeared out over a larger range in radius.

4.4.2.3 Warped thick disk, edge-on orientation

Finally, both scenarios corresponding to a thick and a thin disk are simulated for a highly inclined galaxy ($i = 75°$) which has a warp in inclination and position angle (see the grey circles in Fig. 4.24). Note that in this case, the warp is modelled from lower to higher inclinations: from 68 to 75°. The velocity field, shown in Fig. 4.23, shows large differences between the thin and the thick disk. In the thin disk case, the contours (shown in blue) show the small scale structure of non-circular motions comparable to the flat disks in the intermediate inclination case, the only difference being that they appear more jagged due to the edge-on viewing angle.

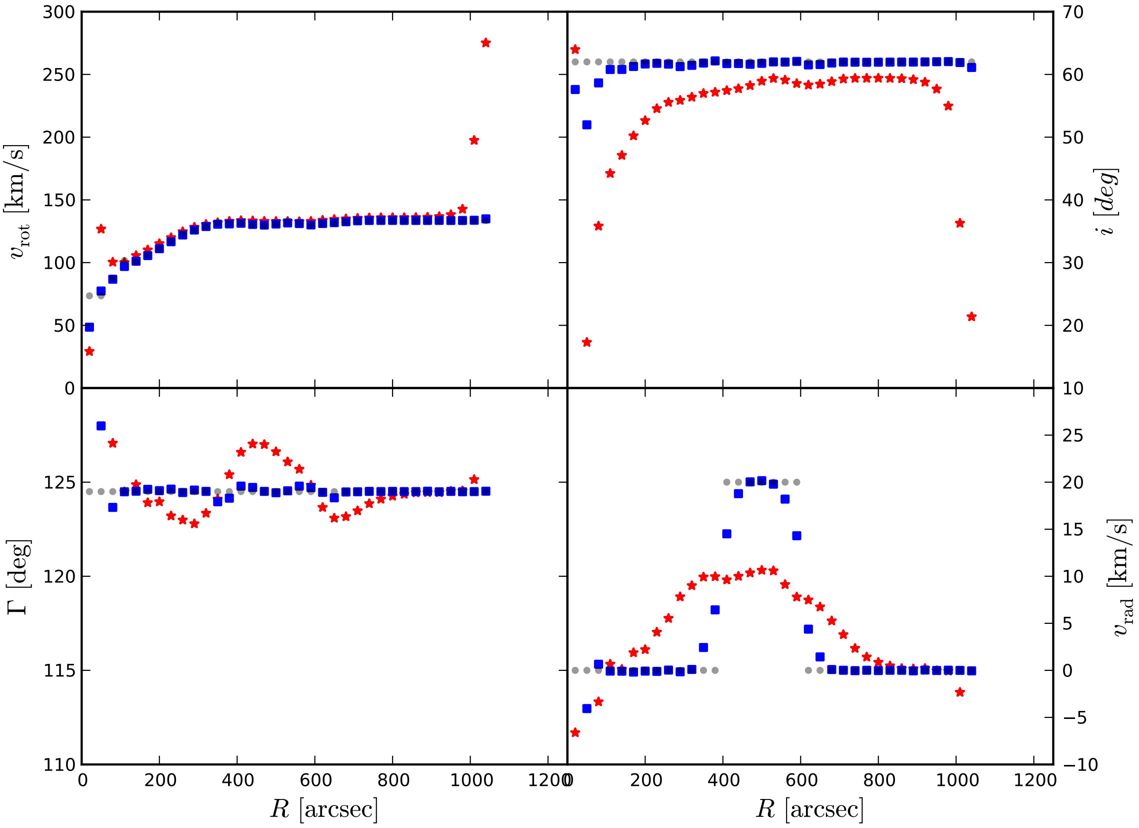

Figure 4.21: Parameters corresponding to the left panel of Fig. 4.20, hence a flat disk with $i = 62°$. $v_{\rm rot}$ is the rotation velocity, i the inclination, Γ the position angle, and $v_{\rm rad}$ the radial velocity. The grey circles describe the TiRiFiC model data cube input parameters. The red and blue points correspond to the red and blue contours from Fig. 4.20: the blue squares describe the thin disk ($Z_0 = 0$) and the red stars thick disk.

In the thick disk scenario (shown in red), the disk appears much rounder compared to the thin disk.

The results of the tilted-ring fitting are shown in Fig. 4.24. In the scenario of a more edge-on and warped galaxy, the tilted-ring fit to the velocity field of the thin disk also shows deviations from the TiRiFiC input model. The rotation curve shows a slight drop at roughly 500 arcsec, this drop coincides with an underestimation of the radial velocity and position angle. The latter is underestimated for large areas of the velocity field. The warp in inclination is also not retrieved very well: in this case it is even overestimated at radii before the occurrence of the warp, after which it drops whereas the actual inclination rises again. The $v_{\rm rad}$ profile seems to have been shifted as a whole to higher radii; it is underestimated at low radii and overestimated at higher radii.

In the thick disk case, the behaviour of the profiles is very similar to the thick disk scenario of the warped, intermediately inclined disk, albeit the differences are larger. Thus, in the case of a disk observed rather edge-on, with a finite thickness and a warp, it is thus not just difficult to extract the radial velocity component, but also the geometry of the disk cannot be determined exactly. However, also if the disk were infinitely thin, it has been shown that a fit to the velocity field can still yield false information.

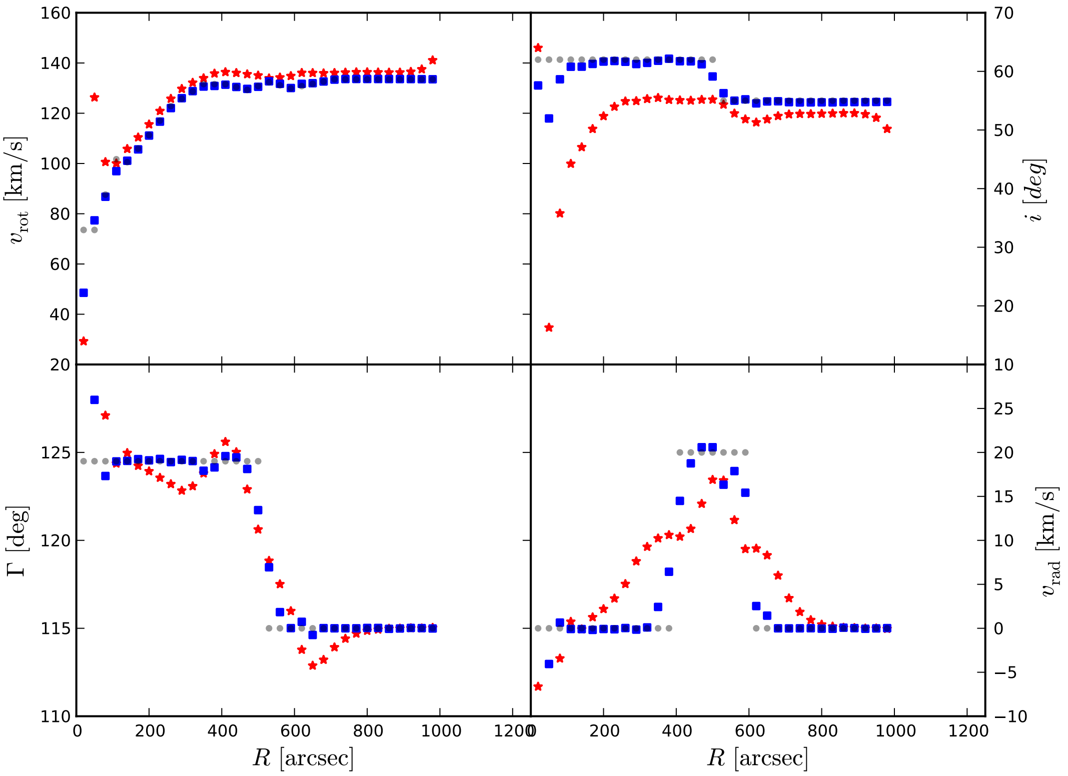

Figure 4.22: Parameters corresponding to the velocity fields of a warped disk at an intermediate inclination, shown in the right panel of Fig. 4.20. The meaning of the colours and variables is the same as in Figs. 4.20 and 4.21: blue represents the flat disk, red the thick disk.

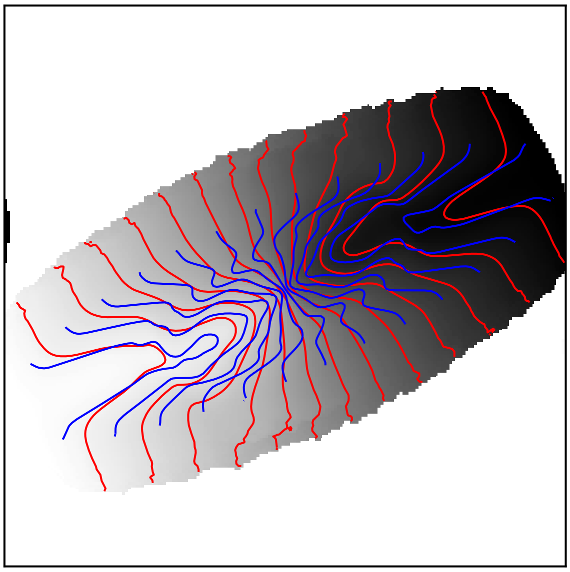

Figure 4.23: Velocity field corresponding to the warped disk with an edge-on orientation. The blue contours describe the infinitesimally thin disk, the red contours the thick disk.

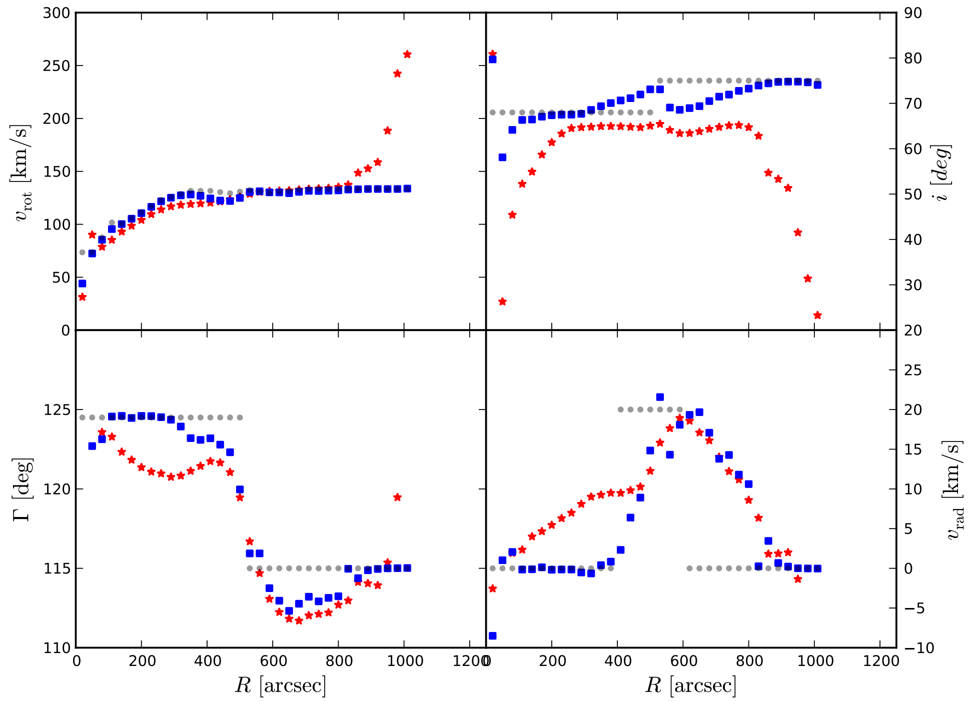

Figure 4.24: Tilted ring parameters corresponding to a warped, edge-on disk. The corresponding velocity field is shown in Fig. 4.23. The grey circles describe the TiRiFiC model parameters, the blue squares the thin disk ($Z_0 = 0$), and the red stars thick disk. $v_{\rm rot}$ is the rotation velocity, i the inclination, Γ the position angle, and $v_{\rm rad}$ the radial velocity.

4.4.3 3-dimensional velocity structure: vertical gradients in radial and rotation velocity

Using synthetic data cubes, the question is pursued whether and how these features influence the study of a the H I kinematics using a 2-dimensional velocity field. In Chap. 4.2.3, it has been mentioned that TiRiFiC is able to analyse the vertical velocity structure. This means that it can extract the kinematics above the plane of the galaxy. Considering accretion from a velocity field modelling point of view, the gas flows radially inwards in the plane of the disk, whereas from the data cube modelling picture, there is a certain amount of gas located above the disk. This gas lags in rotation with respect to the cold disk, and it slowly spirals onto the disk. In TiRiFiC, this is implemented through the parameters $DVRA$ and $DVRO$; the vertical gradients in radial- and rotation velocity as discussed in Chap. 4.2.3. Only $DVRA$ contributes to the in- or outflow of gas. It is not immediately obvious, however, how these parameters affect the velocity field and the extracted tilted-ring parameters. Therefore, two cases are considered here: firstly, a data cube with only a vertical gradient in radial velocity, $DVRA$, is constructed and the velocity field is analysed. Secondly, a scenario is considered in which a vertical gradient in rotation velocity, $DVRO$, is present.

A data cube is constructed with the same global properties as in Chap. 4.4.2, but with a smaller scale height. The parameter $DVRA$ is then introduced instead of a radial velocity, $v_{\rm rad}$, in the plane of the galaxy (a constant value at the same radial interval). A velocity field is then computed (see blue contours on the left panel of Fig. 4.25). It follows that the introduction of the *DVRA* parameter produces the same signature in the velocity field as an inward radial velocity in the plane from the previous section. The strength of the signature depends, however, not only on the amplitude of *DVRA*, but also on the onset height of the gradient above the plane of the disk, *ZDRA*: the lower the latter value is, the stronger the signature of non-circular motions in the velocity field. The *DVRA* value is roughly 1 km s^{-1} arcsec^{-1} with a corresponding *ZDRA* of 8 arcsec. The velocity field contours (in blue) are compared to that of the non-warped thick disk (red) from Fig. 4.20 in Fig. 4.25 and are tuned to make the contours similar. The signatures of the parameters *DVRA* in the case of the data cube model and v_{rad} in the case of the model velocity fields on the velocity field are thus very similar. This is also illustrated by the red points in Fig. 4.26. These points describe the measured tilted-ring parameters from the velocity field with a *DVRA* component. These are, except in the central region, very similar to the parameters resulting from the thick disk scenario without a warp, which parameters values are shown in grey The main difference is that the position angle of the peak of the radial velocity profile is shifted to higher radii as compared to the thick disk model. Thus, from the velocity field alone, one cannot distinguish between the scenarios the inflow of gas onto the disk through a vertical velocity gradient or by means of an inward radial velocity in the plane of the galaxy. Moreover, as discussed in the previous section, the approximation of the v_{rad} parameter is strongly influenced by the disk geometry: if the disk is warped or barred, v_{rad} becomes strongly degenerate with the parameters describing these features.

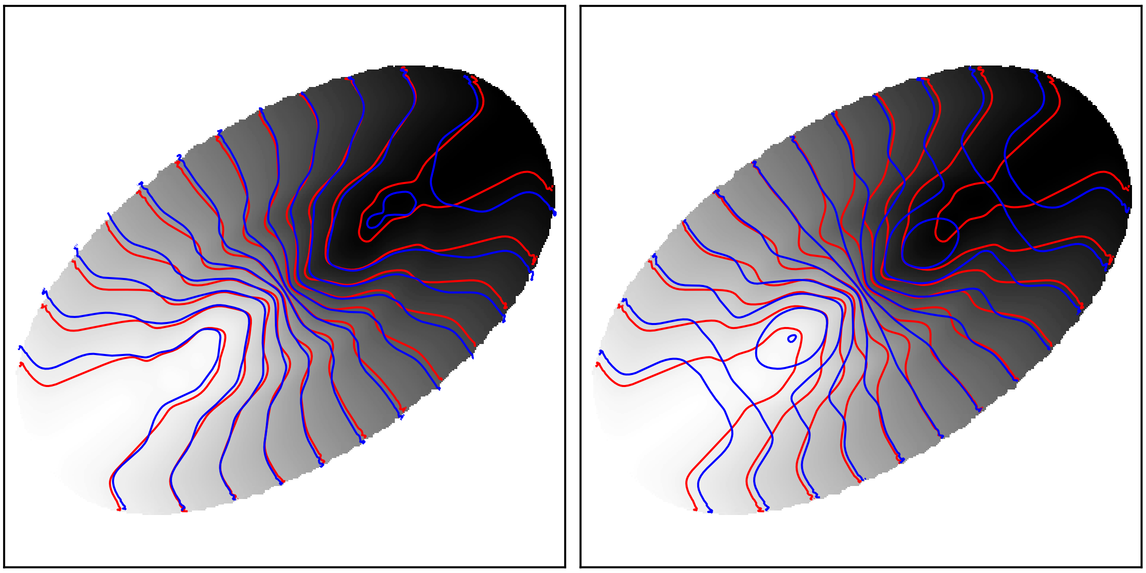

Figure 4.25: Velocity fields showing vertical motions above the disk. *Left*: velocity field illustrating the effect of a vertical gradient in radial velocity. The red contours represent the case as presented in Sec. 4.4.2.1, i.e., an intermediately inclined flat (unwarped) disk with an inward radial velocity in the plane. The blue contours describe the scenario of the vertical radial velocity gradient. *Right*: The red contours are the same as in the left panel, the blue contours present the case of a vertical gradient in rotation velocity.

As a next step, the introduction of a gradient in rotation velocity is considered. In the simulated data cube, the *DVRO* parameter is set to -5 km s^{-1} arcsec^{-1} for the same radial

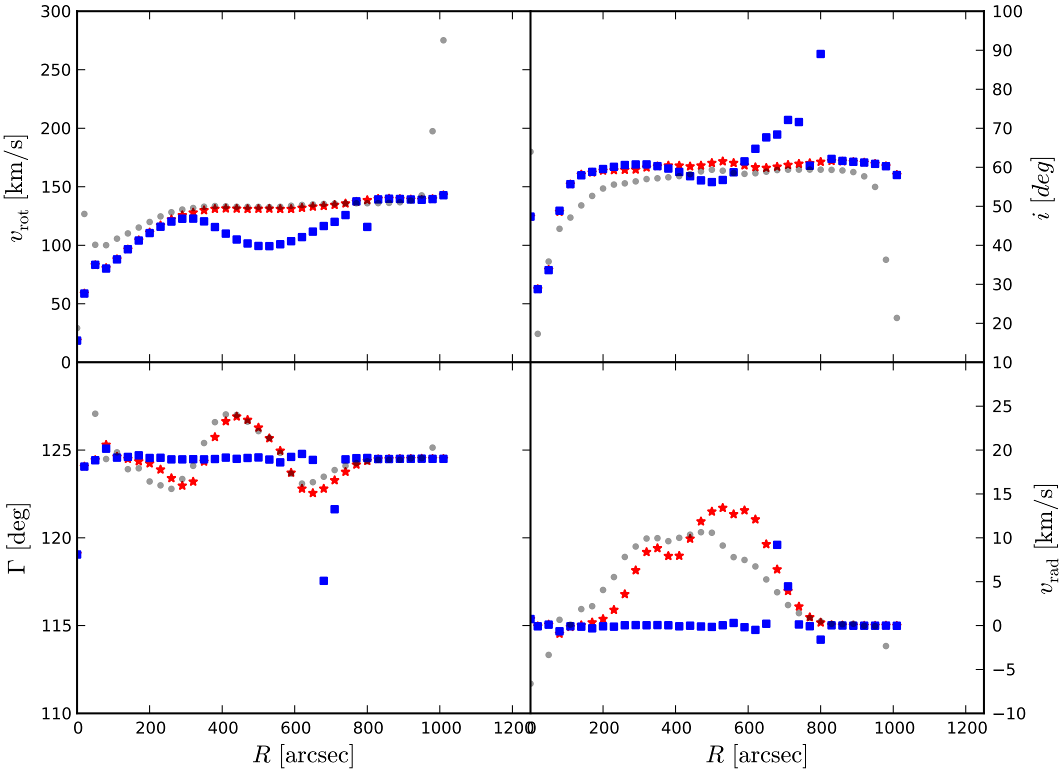

Figure 4.26: Parameters resulting from the simulated velocity fields after including vertical velocity gradients. The grey points are the parameters resulting from the thick disk scenario with $i = 62°$, the red points are the parameters measured in the velocity field after a *DVRA* term is introduced in the data cube and the blue points show the measured parameters in the case of a presence of a *DVRO* term. $v_{\rm rot}$ is the rotation velocity, i the inclination, Γ the position angle, and $v_{\rm rad}$ the radial velocity.

interval as the *DVRA* component. The corresponding iso velocity contours are shown in the right panel of Fig. 4.25. The red contours are identical to the ones from the left panel. At a first glance, the effect of this parameter on the velocity field looks comparable to the *DVRA* parameter. However, the symmetry is a different one: the vertical gradient in radial velocity produces asymmetric iso velocity contours, whereas the one in rotation velocity produces symmetric contours with respect to the minor- and major axes. The measured parameters from this velocity field are shown in Fig. 4.26 as blue squares. Two things can be noted from this plot:

- First, the rotation velocity is underestimated in the region where $DVRO \neq 0$ and therefore, it can be concluded that a negative vertical rotation velocity gradient projects as a decreasing $v_{\rm rot}$ in the galactic plane. Therefore, if a gradient in the rotation velocity above the plane of the galaxy is present, this has consequences for the measured rotation curve.

- Second, at the radius where this *DVRO* returns to naught (at around 800 arcsec), the orientation of the disk (i, Γ) as extracted from the velocity field, is not measured correctly. This seems to cause a non-zero $v_{\rm rad}$, which again is perhaps due to a deviating position angle. The latter, however, cannot be generalised to all orientations.

4.4.4 Summary

If velocity fields are considered to extract kinematical information about a galaxy, systematic errors can be made. From the considerations is this section, it becomes apparent that kinematical signatures present in velocity fields gradually disappear if larger distances are considered. At a distance of the order 20 Mpc, most of the kinematical properties, including radial motion, are still present in the velocity field. At about three times this distance, however, the radial profiles of the inclination, position angle and rotation velocity cannot be measured accurately any more. Especially the inclination is systematically underestimated. The inner radii cannot be used anymore to measure parameters, however, the global position angle and rotation velocity can still be extracted at this distance, if the galaxy is not too face-on or edge-on. At the largest distance considered here, 128 Mpc, only the outer radii can be sensibly used to estimate kinematical properties. Moreover, a harmonic decomposition is not feasible any more, since the parameters are smeared out over the whole radial range. Therefore, it has to be concluded that, as done in Chap. 3, velocity fields for galaxies located at distances of the order 120 Mpc can only be used to extract global information about the position angle and the rotation amplitude; the resulting inclination is significantly biased and radial profiles of the parameters can no longer be retrieved.

Another cause for systematic errors could be the assumption that gaseous disks are infinitely thin. By means of several simulated scenarios, it has been shown that depending of the orientation of the galaxy, significant systematic errors can be made if the thin disk assumption were to be invalid.

Finally, the vertical velocity structure of the disk is important to take into account when studying gas accretion. The vertical gradient in rotation velocity is projected onto the velocity field as a radial velocity component, whereas the vertical gradient in rotation velocity is produced as a gradient in the rotation curve. Hence, no information about the vertical motion in the disk can be retrieved from the velocity field.

It has to be noted, however, that these results cannot be generalised to all galaxies. In particular, in the study of the velocity fields from the ATLAS^{3D} sample, the H I masses are in general much lower than the mass of NGC 2403 and due to the presence of H I ring structures and non-settled morphologies, the kinematical structure is much more complex, strongly enhancing the systematic effects derived from the analysis presented here.

4.5 Conclusions and outlook

Several sources of systematic errors in analysing velocity fields were considered in this chapter:

- Firstly, interferometric observations of nearby galaxies suffer from missing short spacings. This can be corrected by performing an SSC. However, depending on the galactic latitude, and if the rotation curve of a galaxy is such, that the galaxy is observed in channels around 0 km s^{-1}, MW emission will enter the SSC data cube through the velocity channels around 0 km s^{-1} of the single-dish telescope. If consequently a velocity field is constructed directly from a short-spacing corrected data cube, the velocities are largely significantly underestimated. Performing a tilted-ring analysis on the velocity field will therefore yield incorrect results. This has consequences for the analysis of the H I velocity fields for (dwarf) galaxies located on a line of sight in the plane of the MW: an analysis with interferometer data will be possible, but the analysis of the kinematics of the diffuse gas component will only be possible if an accurate model of the MW emission is constructed.

Alternatively, this analysis has been performed by fitting a model directly to the data cube using TiRiFiC. This method allows for successful modelling of the SSC kinematical data. The result hints at a slightly higher H I mass inflow rate if the short spacings are included. It can, however, cannot be quantified how much of this is due to MW emission.

- The kinematics of NGC 2403 have been revised using TiRiFiC. The best-fitting model includes bar-streaming motion in the central regions as well as a moderate inflow centred around roughly 8 kpc. This value is of the order 0.1 $\mathcal{M}_\odot$ yr^{-1}, which is significantly lower than the rate derived from the velocity field. This is most likely caused by the model premises for the derivation of the mass inflow from the velocity field: on the one hand, gas is unlikely to flow radially towards the centre in the plane of the disk and on the other hand, the derivation of the infall velocity with which this gas moves is subject to systematic errors.

- Distance is a very important factor that strongly influences the derivation of kinematical properties using velocity fields. For nearby galaxies with distances of the order 20 Mpc, radial profiles of the inclination, position angle, rotation- and radial velocity can be retrieved relatively accurately. For larger distances, the inclination is severely underestimated and also the radial velocity can no longer be measured correctly.

- Finally, the vertical density and velocity structure of the disk play a role in the description of the kinematics from the velocity field. A disk that is not perfectly flat can lead to a erroneous derivation of the inclination and also seems to enhance the degeneracy between the position angle and the radial velocity.

These results illustrate that using velocity fields in order to derive rotation, orientation, and inflow parameters is subject to major systematic effects. Thus, in most cases, the data cube has to be analysed directly without taking the intermediate step of computing a velocity field. This is a problem for the upcoming H I interferometric surveys, which will be performed with the Australian Square Kilometre Array Pathfinder (ASKAP, Johnston et al. 2007) and Apertif (Verheijen et al., 2009). As demonstrated in this chapter, modelling the galaxies with TiRiFiC is time-consuming; the user has to differentiate between various scenarios such as bar motion, warping or gas inflow/outflow. This makes it unfeasible to analyse thousands of galaxies this way and therefore, considerations have to be made how to study accretion of gas in nearby galaxies for a large sample. One Ansatz could be a parameterisation of TiRiFiC which would allow the construction of simple models with and without accretion signatures and the analysis of a large sample of galaxies would provide information about their accretion properties. Another Ansatz is the study of the environments of galaxies to look for accretion signatures. In the case of the “Bluedisk” survey, this work is in progress.

Chapter 5

Conclusions

5.1 Summary

After the first detection of the neutral atomic hydrogen (H I) line with radio telescopes by Ewen & Purcell (1951), there have been many applications of this spectral line in this field. One of its most important applications is the modelling of rotation curves of external galaxies (Begeman, 1987) and also of that of the Milky Way (MW) (Fich et al., 1989). The H I line traces the gas component of a galaxy out to large radii, in the regime where the alleged dark matter halo dominates gravitation. Therefore, mass decompositions can be made (Martinsson et al., 2013) and also the Tully-Fisher Relation (TFR, Tully & Fisher 1977) can be constructed. Moreover, hydrogen as the most abundant element in the universe plays a fundamental role in the cycle of star formation and galaxy evolution. This work focussed on the kinematical aspect of the H I line to learn about aspects of galaxy evolution: it studied the TFR for early-type galaxies (ETGs) to investigate the evolution of this category of galaxies (Chap. 2). Moreover, it studied the mechanism by which spiral galaxies obtain their gas supply to sustain their star formation (Chap. 3). Finally, there are several measurement uncertainties of systematical nature inherent to the analysis of H I kinematical data. A selection of such effects was investigated (Chap. 4).

The first part of this thesis focussed on the TFR for ETGs. However, instead of investigating its classical application, i.e., the determination of distances in the Local universe (Pierce & Tully, 1988), it investigated evolutionary aspects of galaxies. As a matter of fact, instead of studying this scaling relation for spiral galaxies, as is common, the TFR was used to study ETGs. In particular, the H I survey (Serra et al., 2012) of the ATLAS^{3D}project (Cappellari et al., 2011a) with the Westerbork Synthesis Radio Telescope (WSRT), revealed that many ETGs contain significant amounts of cold gas. Therefore, the H I line has been used to study the TFR for this class of galaxies. By modelling the outer radii of H I velocity fields, it has been shown that:

- By using 2MASS K-band luminosities to construct a “classical” TFR, it has been shown that an ETG TFR exists, albeit with large scatter.
- If the baryonic TFR is constructed, considering the total baryonic mass instead of the NIR luminosity, the result is a scaling relation that is much better defined (has a lower scatter) than the classical formulation of the TFR.
- The H I TFR is in principle consistent with the TFR from carbon monoxide (CO), constructed for the ATLAS^{3D} sample by Davis et al. (2011). This result could have important consequences for future observations with the Atacama Large Milimeter Array (ALMA). CO is mostly found in the inner regions of galaxies, where the stellar population has a

significant contribution to the gravitational potential. H I on the other hand, is found out to very large galactic radii. The result that the CO and H I TFRs are consistent, implies that the drop in rotation velocity is minimal, and ALMA could be used to measure the TFR at larger redshifts to investigate the redshift evolution of the TFR.

- The maximum-disk hypothesis states that stars dominate gravity in the range of the stellar disk as opposed to dark matter. The study of the H I baryonic TFR for ETGs showed that if the TFR for spirals is compared to the TFR for ETGs, the ETG TFR lies below the relation for spirals. It is therefore likely that the mass-to-light ratio for spiral galaxies does not correspond to that of a maximum-disk scenario, but instead, dark matter also plays a role in the more central regions of spiral galaxies.

The second part of this thesis dealt with spiral galaxies. One of the most important unsolved problems of galaxy evolution is how galaxies obtain their gas supplies to form stars (e.g. Sancisi et al. 2008). There are two main hypotheses proposed for this mechanism; either the continuous cooling of hot coronal gas (White & Rees, 1978) and the episodic accretion of cold gas from the environment (Sancisi et al., 2008). The latter was the subject of study in this work. A sample of WSRT observations of 48 galaxies from the “Bluedisk” ensemble (Wang et al., 2013) has been studied to search for accretion signatures. Half of these galaxies have been selected with optical predictors to contain a normal H I content, and the other half have been selected to contain an excess amount of H I. H I velocity fields have been produced and an elaborate qualitative inspection of the data, as well as a quantitative analysis has been performed. In the former, particular attention has been paid to the diagnosis of phenomena that are typically connected to cold gas accretion, such as lopsided features, warps, and non-circular motions.

- This analysis, however, showed by inspection that the H I-rich half of the sample does not have a higher frequency of occurrence of phenomena related to cold accretion from the environment than the control sample.

- In the quantitative study of the velocity fields, tilted-ring models were fitted to the data to extract their global kinematics. Moreover, asymmetry diagnostics were calculated to quantify the symmetry of these velocity fields. None of the introduced quantities that measure asymmetry in the velocity fields showed any evidence of the H I-rich galaxies having a more asymmetric velocity structure than the normal spirals.

- Thus, from these analyses no indications were found that the sample with an excess H I content is more asymmetric than the control sample.

- These results imply that at the redshift interval of the sample, the signatures of cold accretion are not strong enough to be detected. Therefore, it is likely that at these redshifts, a smooth mode of accretion dominates. Hence, to be able to detect the signatures of cold accretion, one has to study galaxies at higher redshift with a higher resolution (e.g. with the SKA), or focus on nearby galaxies using the short-spacing correction (SSC).

- Beam-smearing, which is introduced by observing structures characterised by spatial scales below the angular resolution of the observations, has a large impact on the data. In particular, no radial profiles of the tilted-ring parameters such as the inclination and rotation velocity can be derived at the distances of the sample. This strongly inhibits the derivation of kinematical properties from the data such as warps and radial motions in the plane of the galaxy.

The final chapter presented a treatise of systematical effects inherent to H I observations. It analysed a selection of effects that will be of significant importance for the design of future H I surveys with regard to the methods used to analyse the data. Since velocity fields are generally studied to quantify the H I kinematics of galaxies, especially systematics regarding these data products are considered in detail. The advantage of velocity fields is that they are easy to calculate and to interpret. Their disadvantage is that they are simplifications of the observations, and therefore do not allow for an accurate description of more complex phenomena.

- Galaxy kinematics are often investigated using interferometry data. However, especially for nearby galaxies, which contain large amounts of warm, diffuse gas, this component is not fully measured by interferometers. SSC complements the interferometric data with the diffuse gas component as measured by a single-dish telescope. In particular, it has been attempted to analyse the systematical effect if the single-dish observations, required for the combination, are contaminated by MW emission. Using NGC 2403 as a case study, it has been shown that if velocity fields are used to quantify the kinematics of the SSC data set, large errors are made. These errors are caused by the fact that MW emission enters the single-dish data and propagates into the SSC data set. By also modelling the full data cube of the SSC data set with the aim of studying the accretion properties of NGC 2403, it has been shown that there is a difference in the H I mass flow if calculated from the interferometer- or the SSC data. This illustrates the importance of the SSC: accretion of warm gas is an important component of the global accretion of galaxies. Interferometers, however, are unable to detect this diffuse gas in the case of nearby galaxies. A likely scenario for gas accretion is therefore “galactic rain” of large-scale condensations (Kerp, 2013). In the MW, clouds with a mass of $10^6\,\mathcal{M}_\odot$ are observed with an extent of 5 pc at a distance of 500 kpc. It is, however, not possible to resolve such clouds in external galaxies, even with the SKA. The single-dish telescope, however, can detect the gas in the warm phase and complement the interferometer data as is done in the SSC.
- It has been shown which parameters can still be reliably derived from velocity fields depending on the distance of the galaxy under consideration. It has been confirmed that in the case of distances corresponding to those of the “Bluedisk” galaxies, the inclination can no longer be reliably extracted from the velocity fields. It has also been shown that at these distances, velocity fields can no longer be used to quantify non-circular motions in galaxies which are possibly related to the accretion of gas.
- Finally, other sources of systematical error are the assumptions about the composition of (disk) galaxies and interpretations of phenomena observed in velocity fields. It has been shown that the vertical morphological and kinematical structure of the disk cannot be taken into account by analysing a velocity field. Moreover, under certain circumstances, the projection of these parameters onto the velocity field can give rise to incorrect tilted-ring parameters. In these cases, a careful analysis of the full data cube is required.

5.2 Outlook

The study of accretion mechanisms in galaxies is not yet resolved and will remain an interesting topic in the near future, especially with the introduction of new telescopes with high resolution and sensitivity. These telescopes will produce data sets for many galaxies. However, these galaxies have to be observed at larger distances. As mentioned in the summary, limited spatial resolution plays a large role in H I observations of galaxies at large distances. Especially in galaxies at a distance of the order 100 Mpc, only global kinematical properties can be extracted from the H I interferometer data if analysed with the traditional method of tilted-ring fitting to velocity fields. This has important consequences for future analyses of kinematical data from H I surveys aimed at quantifying gas accretion, possibly to be performed by e.g. Australia's Square Kilometer Array Pathfinder (ASKAP, Duffy et al. 2012). On a modelling level, one can not resort to velocity fields to derive deviations from circular motion. Instead, one solution could be to construct models of the full data cube with software such as Tilted Ring Fitting Code (TiRiFiC, Józsa et al. 2007). However, modelling with this software is very time consuming, and therefore not easily realised for larger samples. Two solutions are suggested: firstly, a parameterisation of this software along with a fitting algorithm that uses a global optimiser. Important would be to incorporate a parameterisation that can identify the discussed accretion signatures in this work. By realising a survey such as the "Bluedisk" survey, with a dichotomy in the sample selection (H I-rich versus normal spiral galaxies), one could then investigate if the H I-rich sample has on average a higher amplitude of an accretion parameter. The other solution would be, instead of focusing on modelling the kinematics of each galaxy individually, to study the galaxies as an ensemble. One possibility would be to focus on the environment, such a study is being performed for the "Bluedisk" sample. Moreover, mass-inflow signatures are measured trough the non-circular component of motion. This component has in most cases only a fraction of the amplitude of the circular component. One way to circumvent this is to perform a stacking analysis (superposition of spectra) of the H I-rich subsample on the one hand and the sample with a regular H I content on the other hand, and to perform an analysis of the non-circular component of the stacked samples. This is, however, complicated by several factors such as warping of disks, lopsidedness and possible degeneracies between warping and inward gas motions in the galactic plane. Therefore, on the short term, the most promising method to study accretion is to study the SSC of nearby galaxies. The SKA will have a resolution of about 30 times the WSRT resolution. Therefore, analyses such as presented for NGC 2403, can be extended to galaxies with distances of the order 100-150 Mpc.

Acknowledgements

Firstly, and most of all, I would like to thank my supervisor, P.D. Dr. Jürgen Kerp, not just for enabling and motivating me to pursue this thesis, but even more for his valuable advice on the thesis work and on my future career.

Prof. Dr. Michael Kramer, the Max-Planck Institut für Radioastronomie and the International Max-Planck Research School (IMPRS) financially supported me during this thesis. I would like to express my sincere thanks for this generosity.

I would like to thank Prof. Dr. Pavel Kroupa for being a member of my IMPRS thesis committee and Ph. D. committee and for spending the time evaluating this work.

Moreover, I would like to thank Prof. Dr. Jochen Dingfelder and P.D. Dr. Petra Friederichs for their interest in my work and for taking the time to be members of the Ph.D. committee.

I would also very much like to thank Dr. Gyula Józsa for all the hours he invested in explaining me details about TiRiFiC and other subjects. I wish him all the best in South Africa.

Shahram Faridani I am also indebted to. Despite him being in the final phase of his Ph. D. work, we still managed to have many valuable discussions and his comments significantly improved the quality of this thesis. I also thank Tobias Röhser and Daniel Kröll for reading through my work and offering their comments. Moreover, I would like to thank the rest of my research group for always having an ear for discussions, stories and complaints and for creating a pleasant atmosphere. Christina Stein-Schmitz and Andreas Bödewig I owe my gratitude for being the foundation of the institute.

I also would like to thank Dr. Paolo Serra and Prof. Dr. Tom Oosterloo. They have helped me with the necessary data for this thesis, useful discussions, useful programming code, and with many comments on the text. In particular I thank Prof. Dr. Tom Oosterloo for providing a script to calculate Gauss-Hermite velocity fields.

I also thank the members of the ATLAS^{3D} team; Michele Cappellari, Davor Krajnovic, Timothy Davis, Tim de Zeeuw, Anne-Marie Weijmans, Raffaellla Morganti, Thorsten Naab and Pierre-Alain Duc, who provided me with the necessary data and with significant feedback on the text by many comments and suggestions. I also thank the members of the Bluedisk team; Jing Wang, Thijs van der Hulst, Guinevere Kauffmann, Jarle Brinchmann, David Carton, Mei-Ling Huang, Frank Bigiel and Diane Cormier. They have played an important role in the development of this part of my thesis and have contributed greatly to the quality of the text by providing many comments and suggestions.

Finally, I would like to thank my girlfriend, Agustina, for her patience and support. Also my parents, Frits and Carry, I am indebted to for always listening and for their advice.

Appendix A

Atlas of H I TFR for ETGs velocity fields

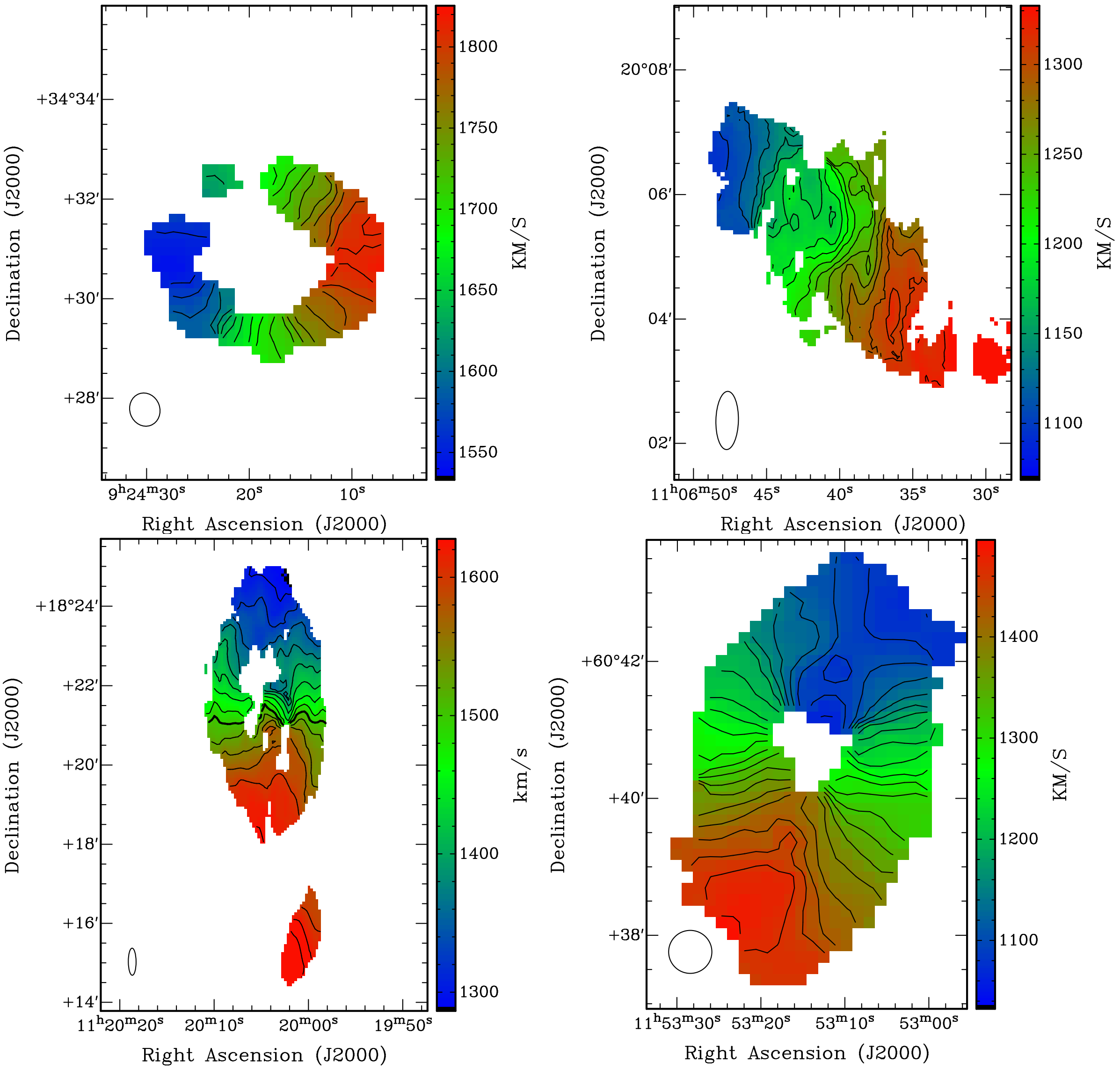

Figure A.1: H I velocity fields. From left to right NGC 2859, NGC 3522, NGC 3626, and NGC 3945. In each plot, the beam is shown on the bottom-left.

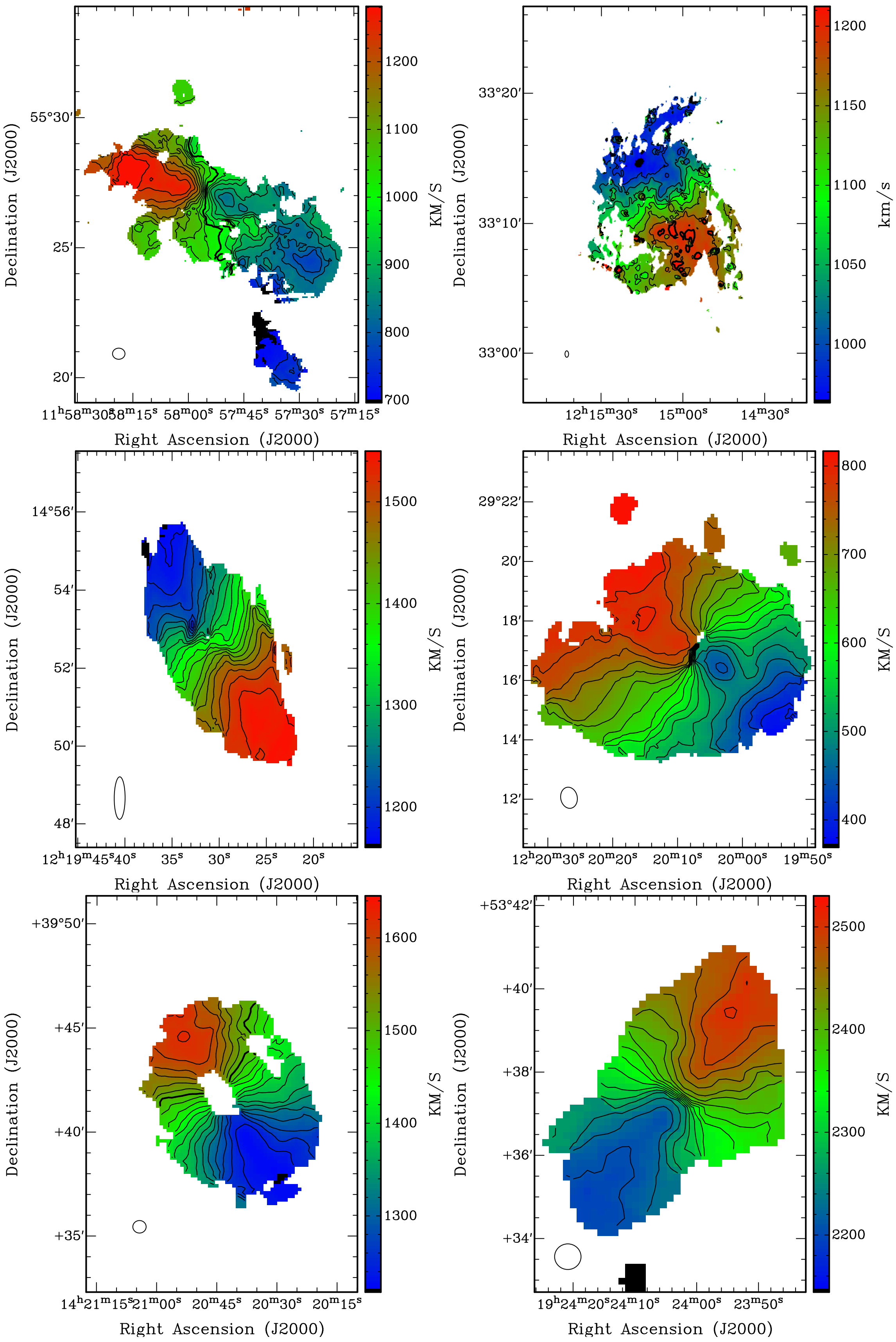

Figure A.2: NGC 3998, NGC 4203, NGC 4262, NGC 4278, NGC 5582, and NGC 6798.

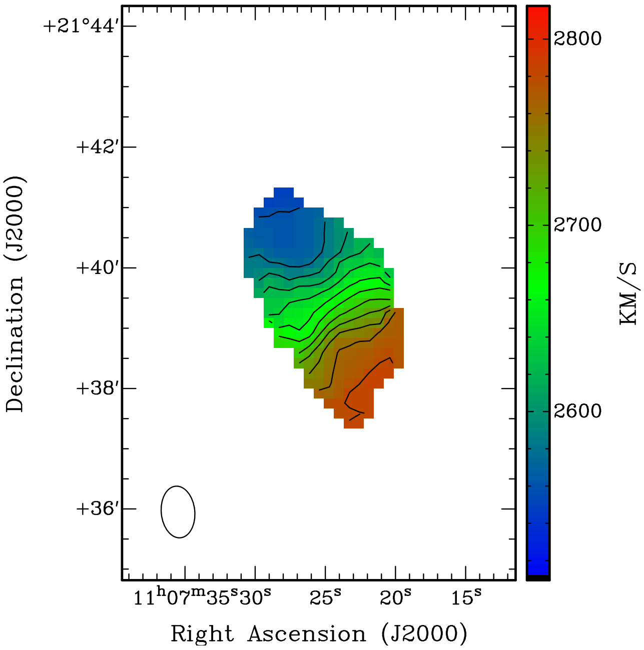

Figure A.3: UGC 06176.

Appendix B

Atlas of Bluedisk galaxies

Here the derived Gauss-Hermite velocity fields as well as the position-velocity diagrams along the kinematical major axes of the galaxies are presented. Fig. B.1 shows the velocity fields for the cases in which a successful tilted-ring model could be fitted. The superimposed rings show the ring geometries along which the tilted-ring fit has been performed. Figure B.2 shows the velocity fields for the galaxies for which a tilted-ring fit could not be performed (see Section 3.4.1), therefore they have no rings superimposed. The white contours represent the contours of the receding side, from the systemic velocity upwards in steps of 20 km s^{-1}, the black contours show the approaching side, downwards from $V_{\mathrm{sys}} - 20$ km s^{-1} in steps of 20 km s^{-1}. The circles on the bottom-right of the figures are the beam sizes. The velocity fields are all presented using the radio definition. The numbers on the left-bottom of the diagrams are the galaxy IDs from Table 3.1. The symbols shown at the top of each figure summarise the features seen in the inspection of the data (see Section 3.3). The meaning of the symbols is as follows: "C" stands for curved velocity field contours, "S" for a S-shaped warp, "U" for a U-shaped warp, "A" for an asymmetric warp, "L" for kinematical or morphological lopsidedness, "I" for an ongoing interaction and "Cl/T" for the presence of H I clouds or an H I tail. Note that the inspection as performed in this work is based on the data cubes, velocity fields and position-velocity (xv) diagrams and therefore not all features are visible in the velocity field.

Fig. B.3 shows the xv diagrams for the cases in which a tilted-ring fit was successful. The white points show the projected rotation curve. The dashed line is the interpolated rotation curve from Section 3.4.4 used to create the model velocity fields of the flat disks. All xv diagrams are in the optical definition of velocity. The drawn contours represent intensities at [$-2\sigma_{\mathrm{rms}}$, $+2\sigma_{\mathrm{rms}}$, $+4\sigma_{\mathrm{rms}}$, $+8\sigma_{\mathrm{rms}}$, ...], where σ_{rms} is the standard deviation of the data cube computed using the mean absolute deviation (MAD). The numbers printed at the bottom-right of the figures are the galaxy IDs from Table 3.1.

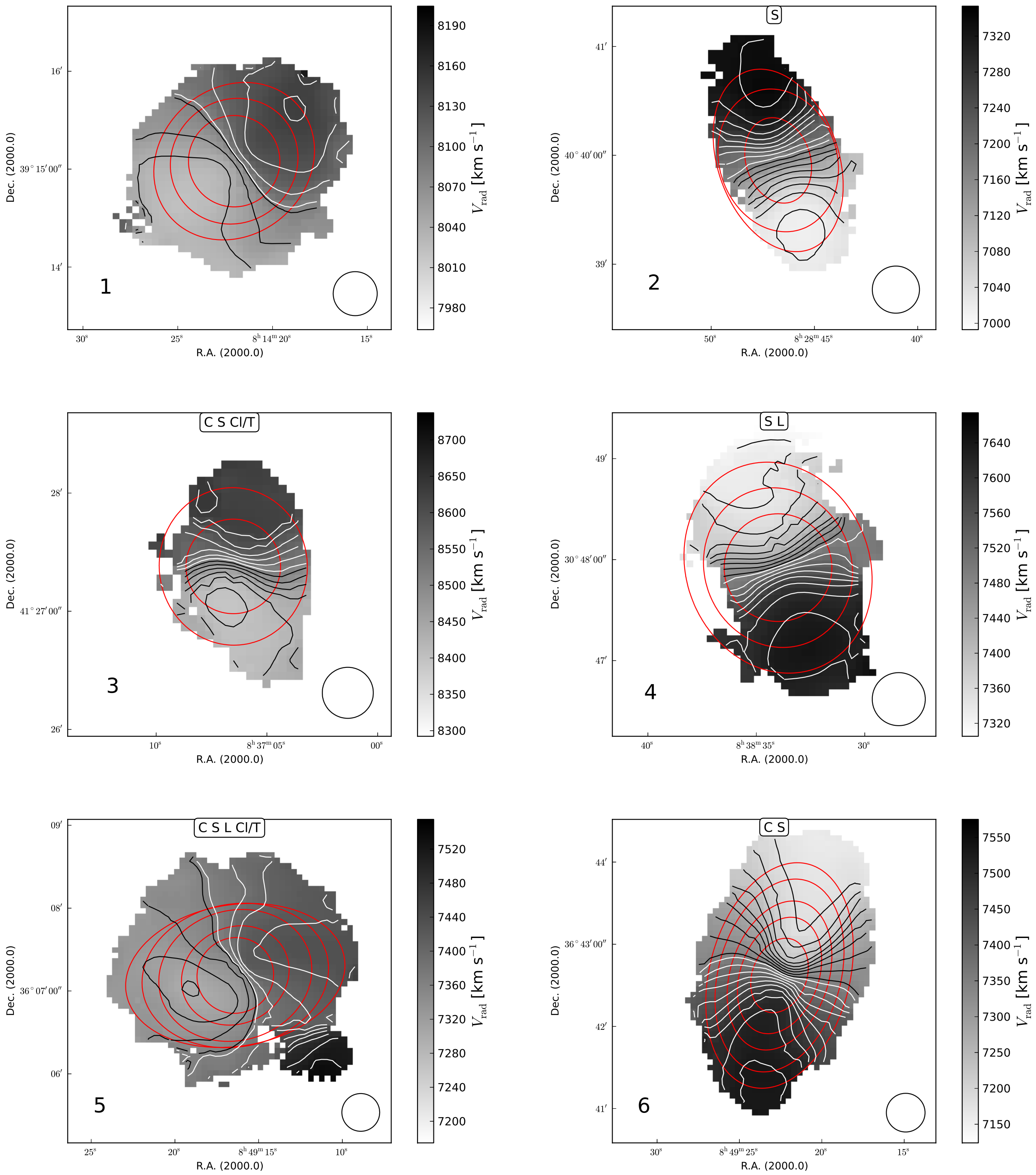

Figure B.1: Gauss-Hermite velocity fields with superimposed rings that describe the geometry of the fitting ellipses. See the text for a description.

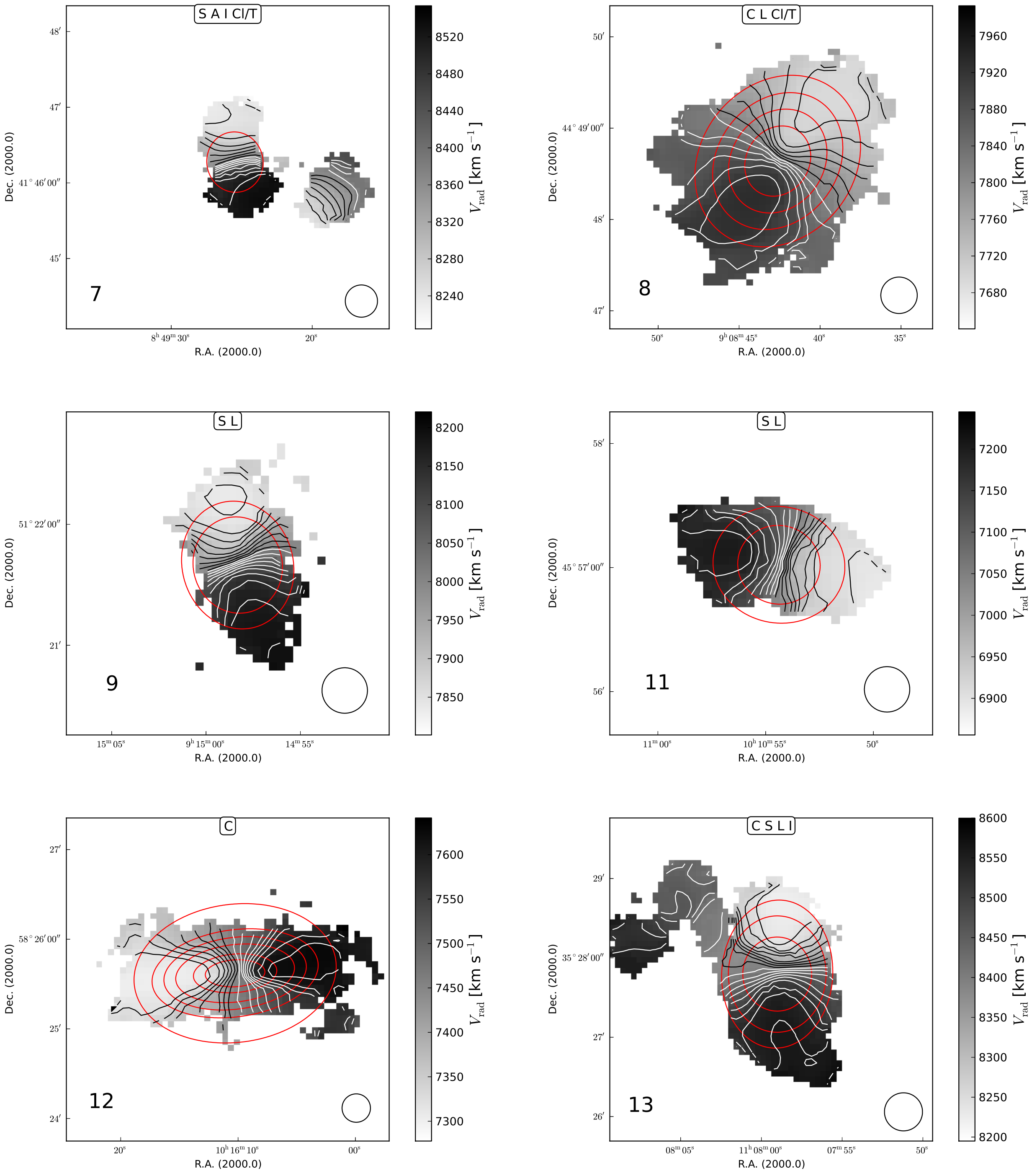

Figure B.1: cont.

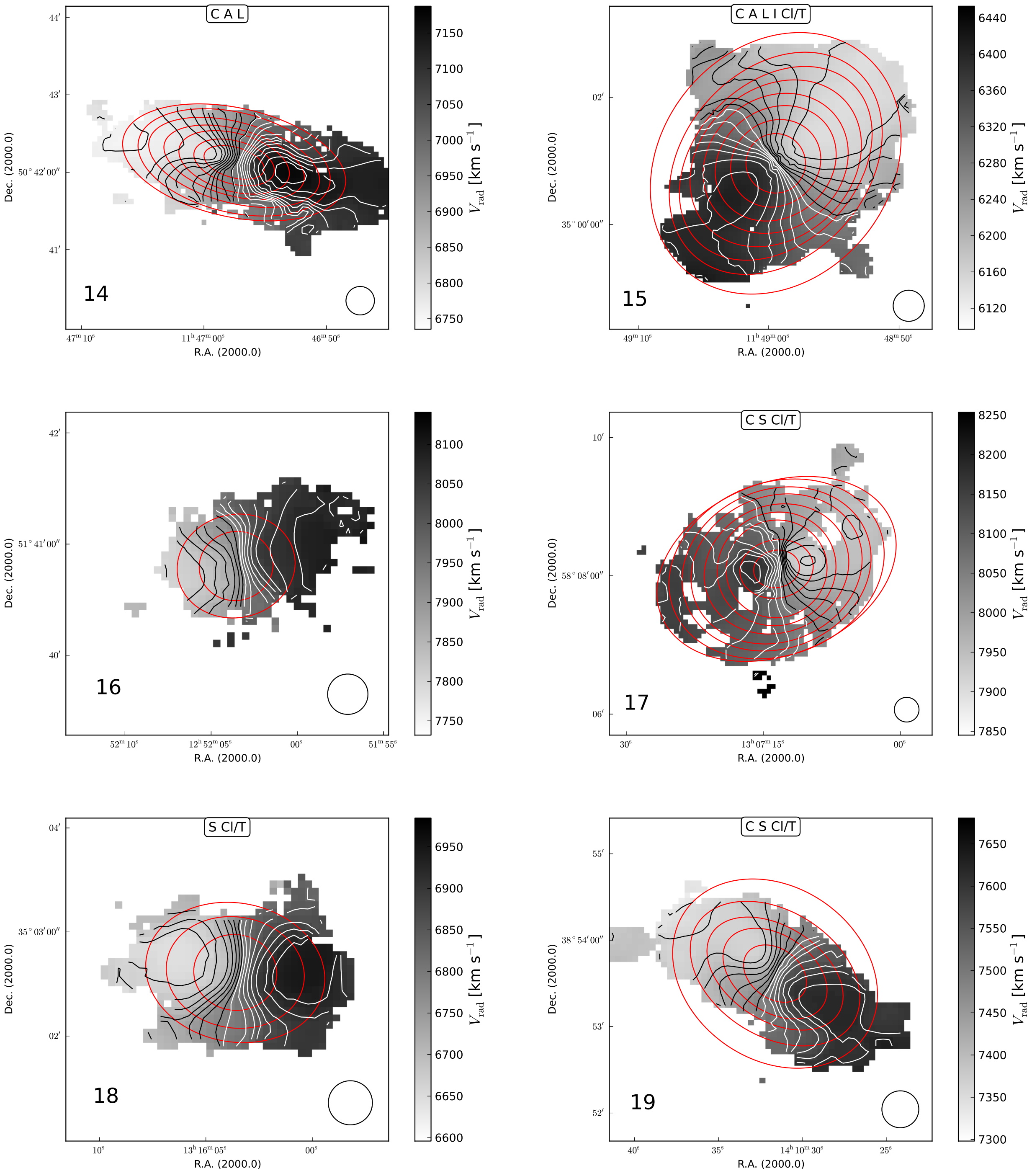

Figure B.1: cont.

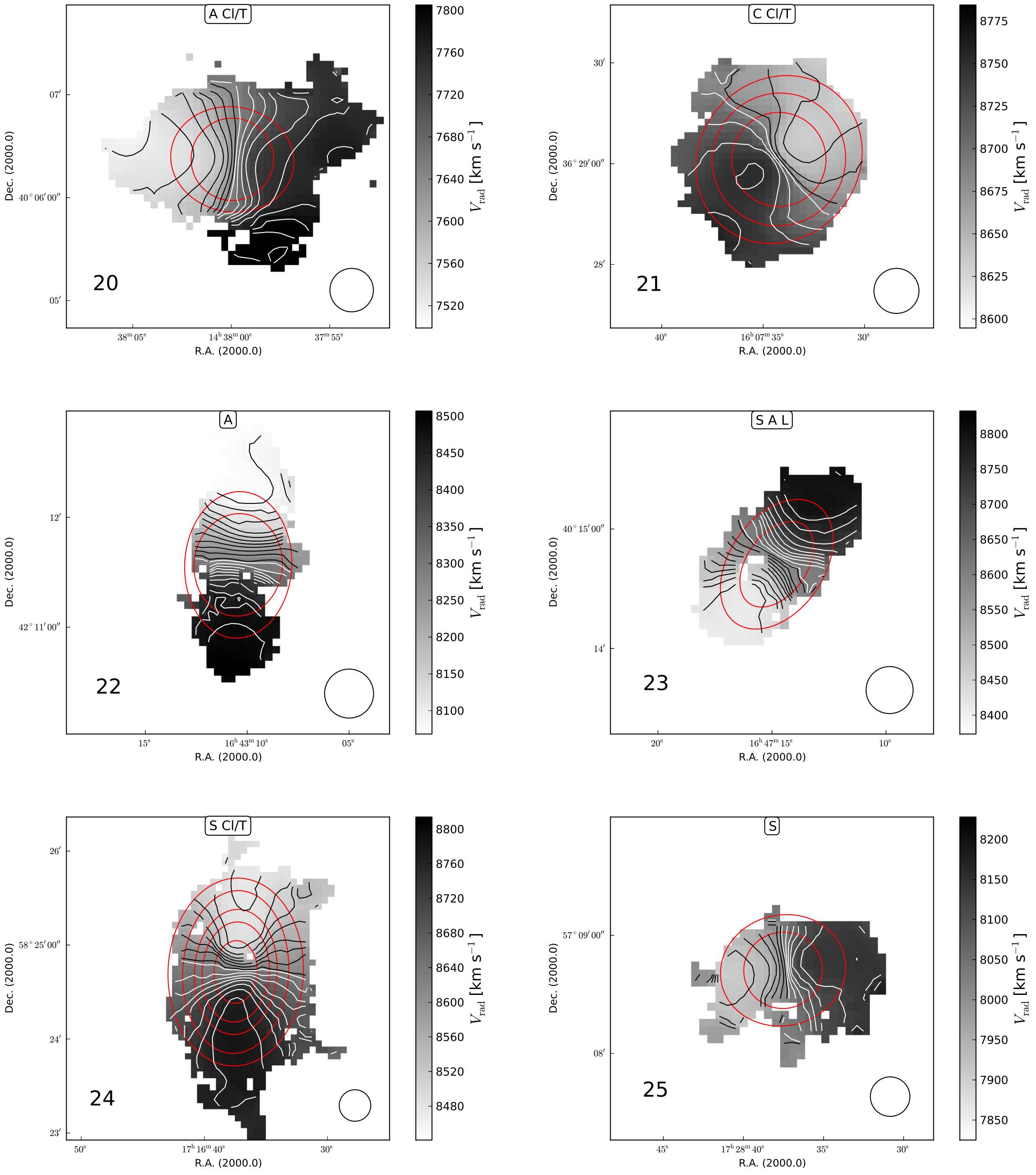

Figure B.1: cont.

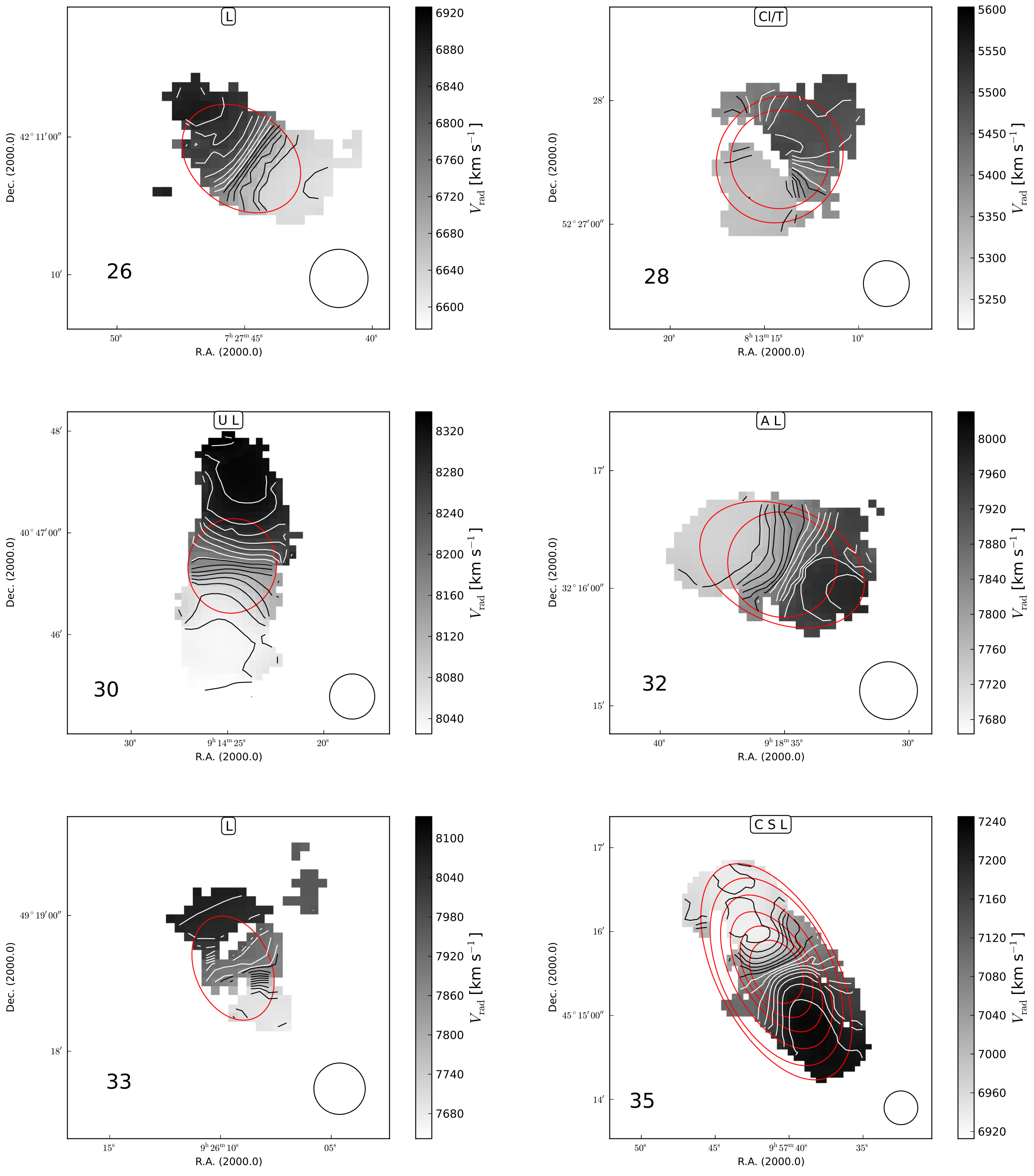

Figure B.1: cont.

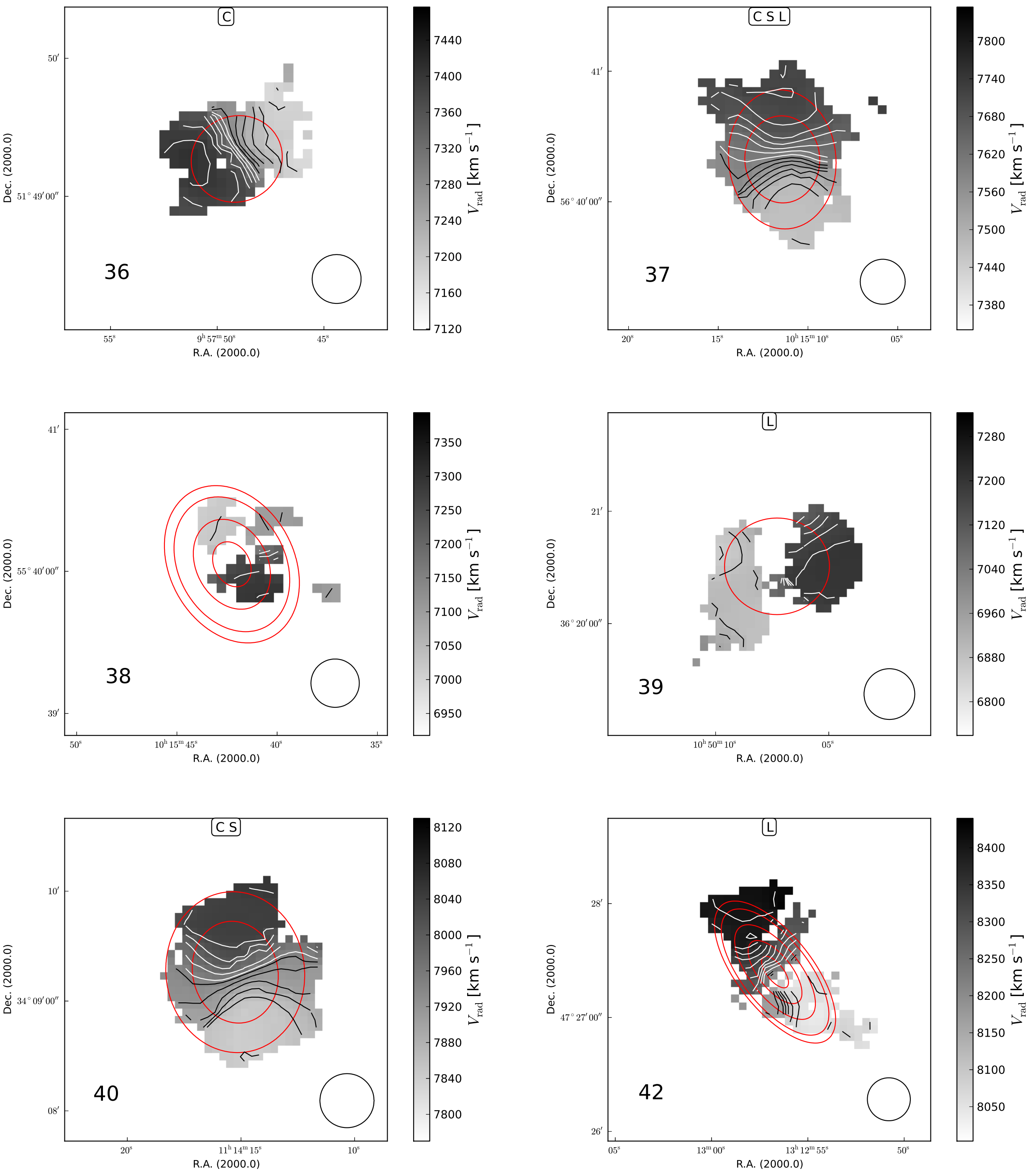

Figure B.1: cont.

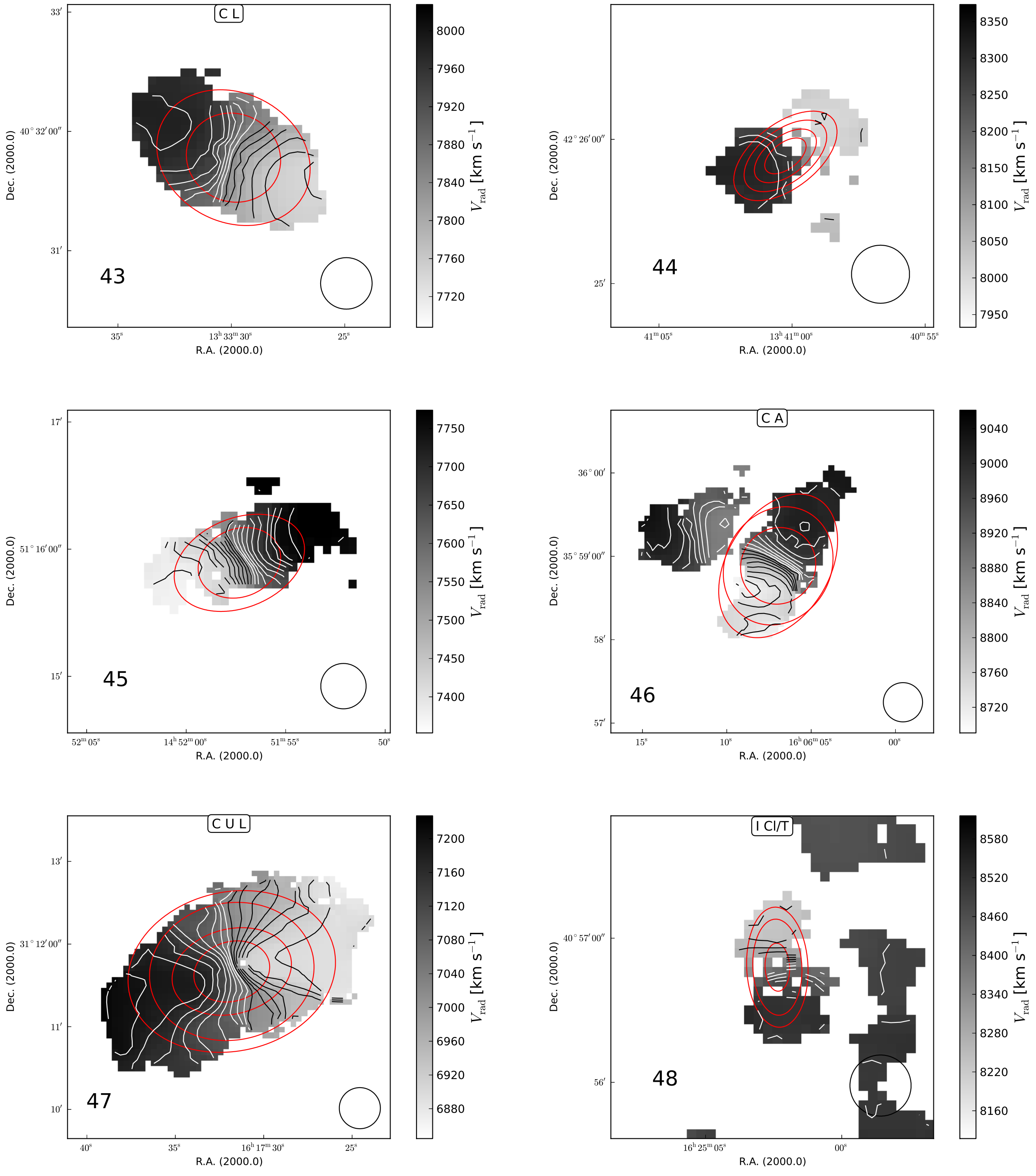

Figure B.1: cont.

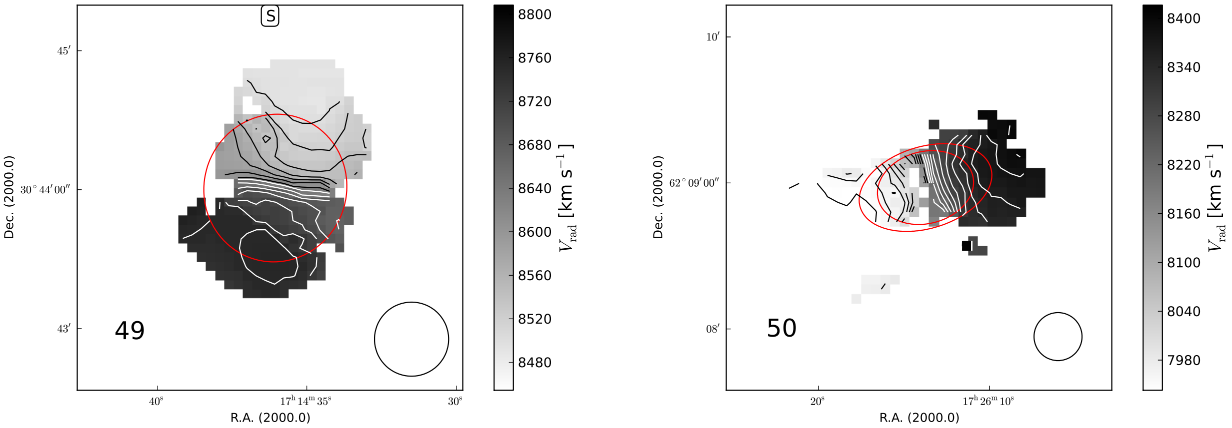

Figure B.1: cont.

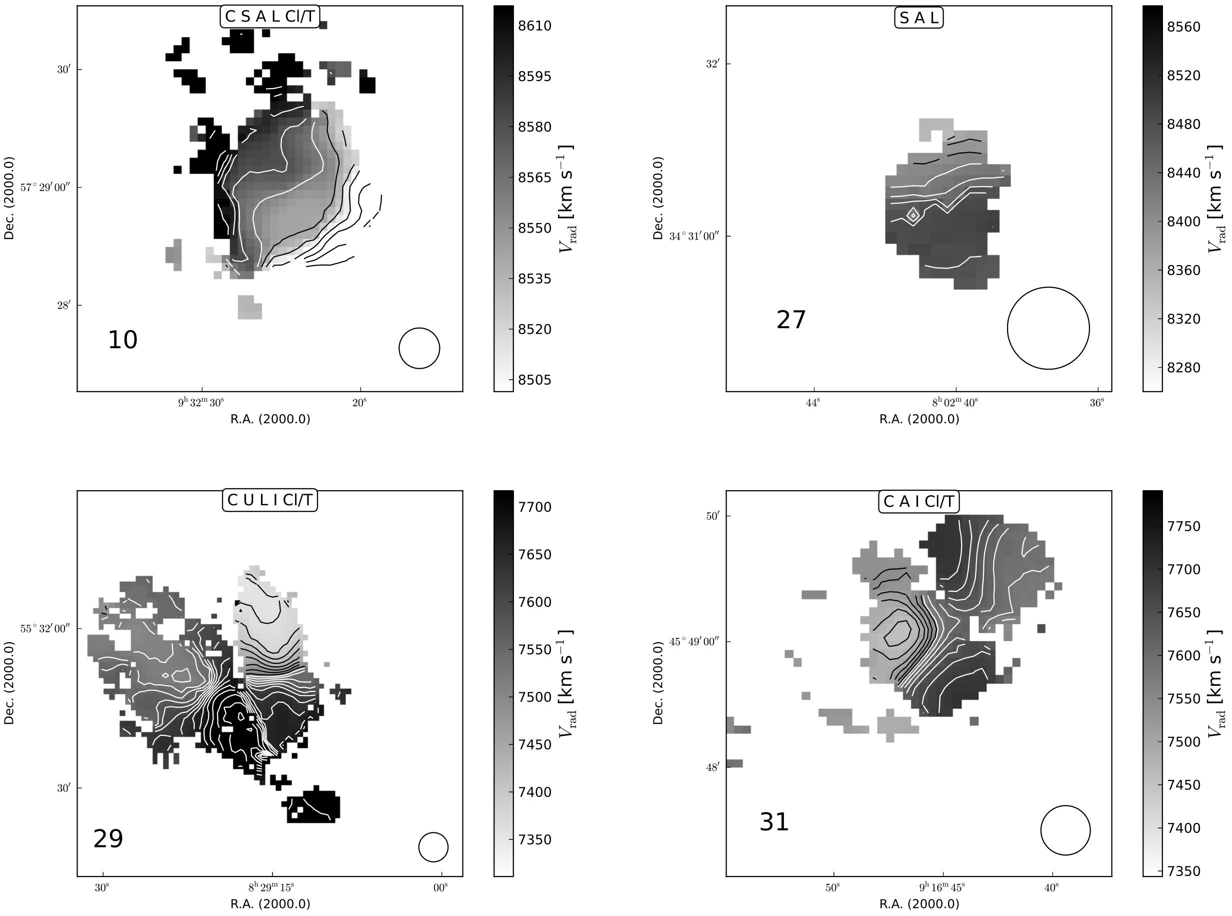

Figure B.2: Velocity fields of the galaxies where no tilted-ring fit has been performed.

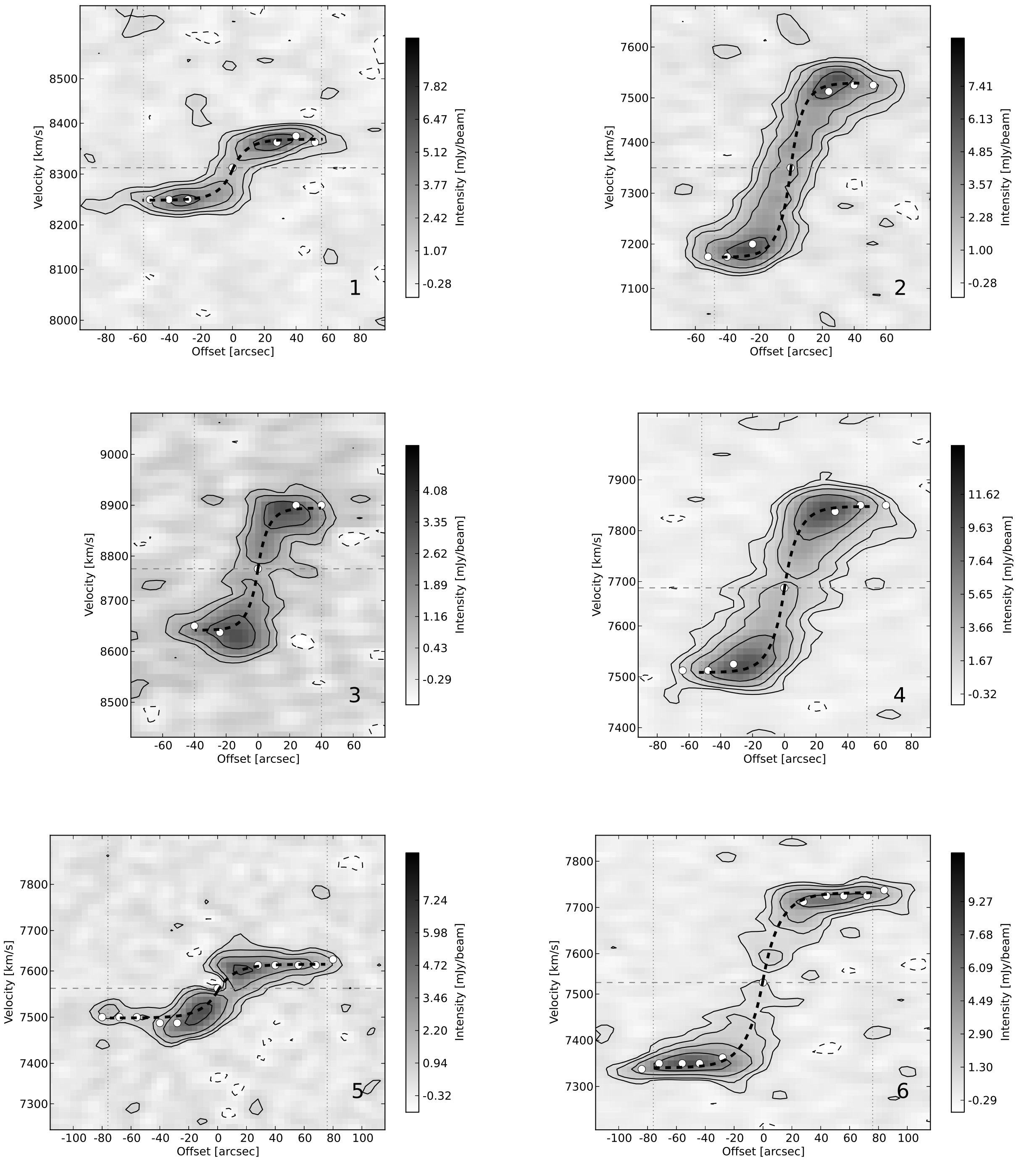

Figure B.3: Position-velocity diagrams with superimposed rotation curves and rotation curve (white points) parameterisations (dashed lines). See the text for a description.

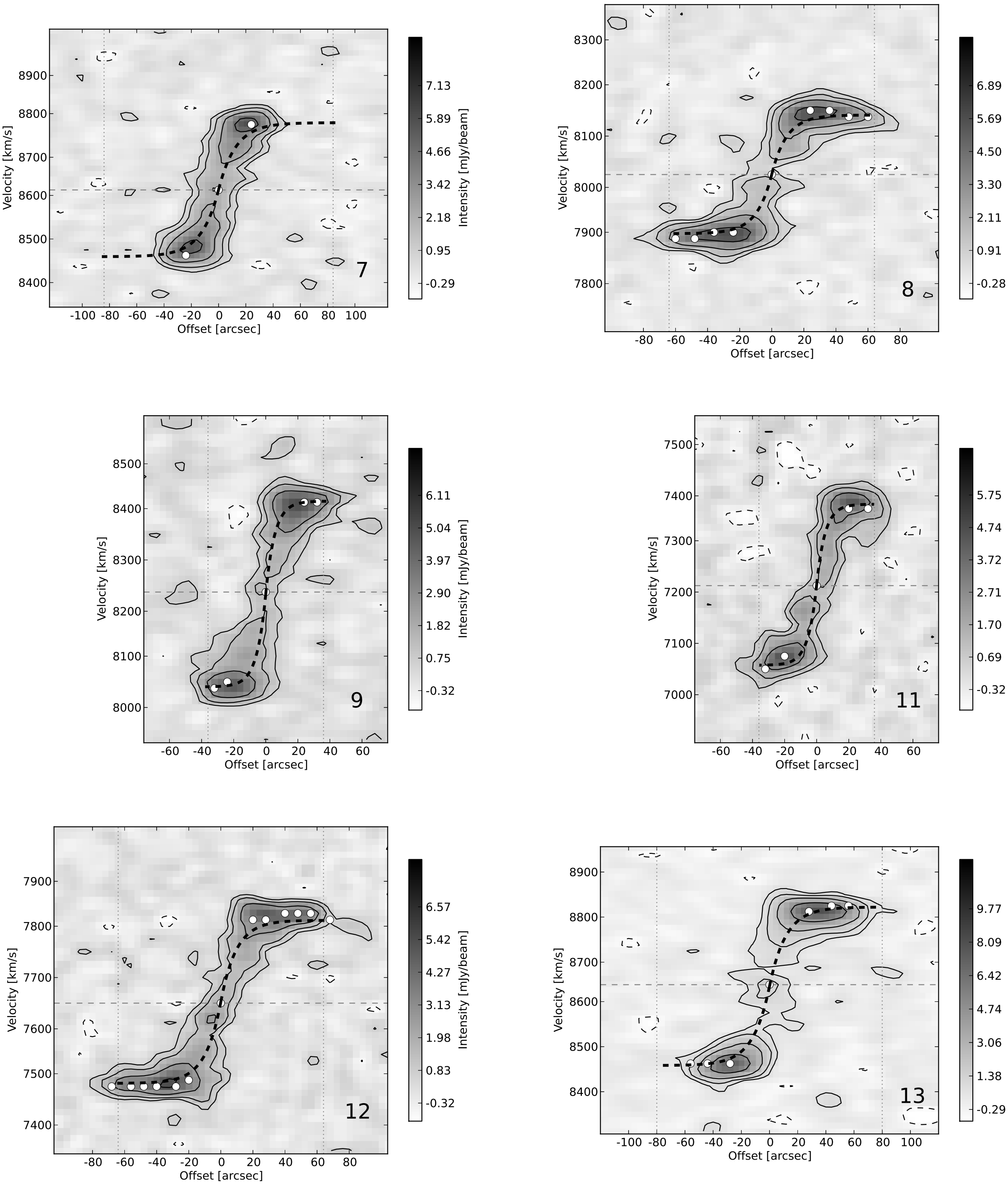

Figure B.3: cont.

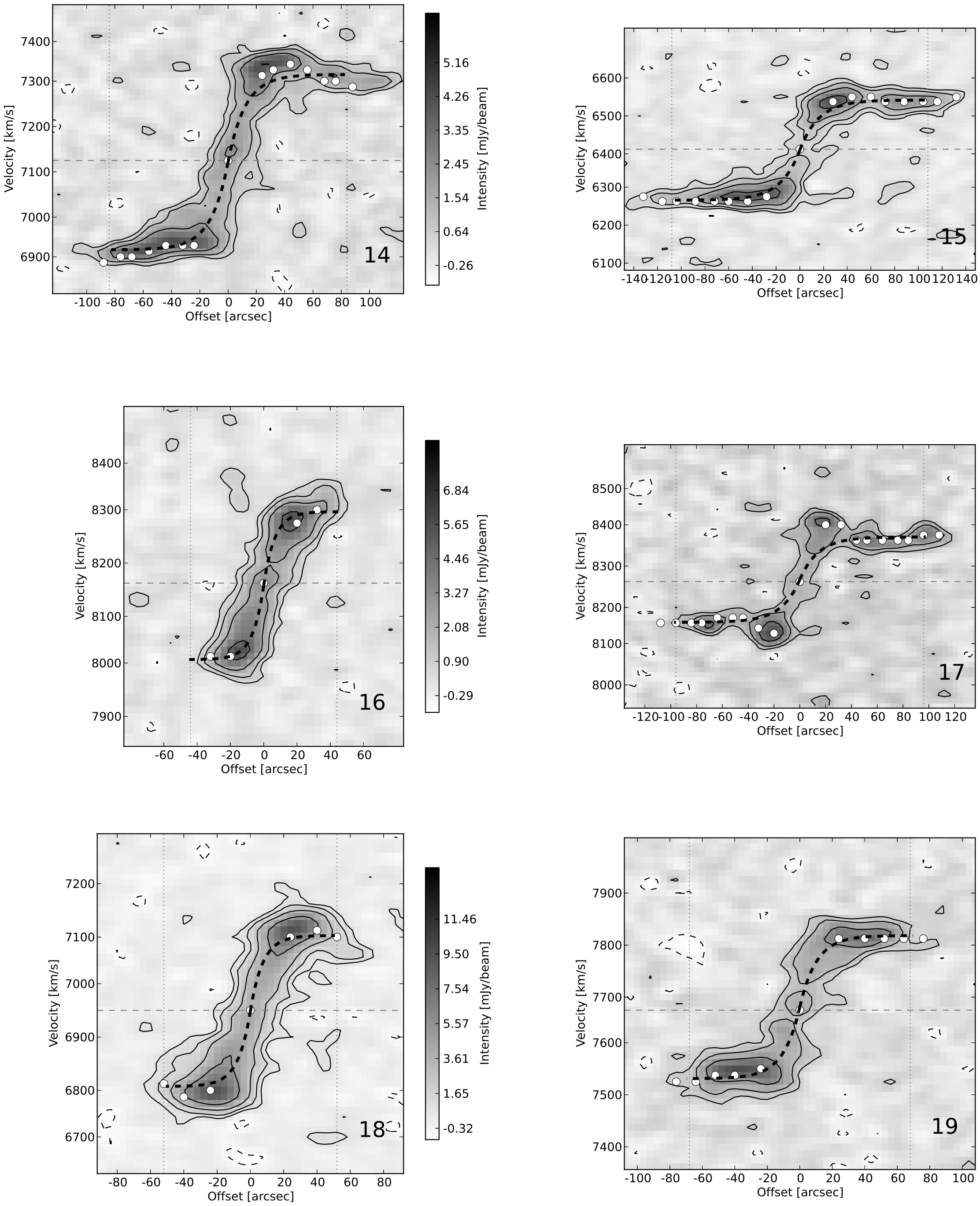

Figure B.3: cont.

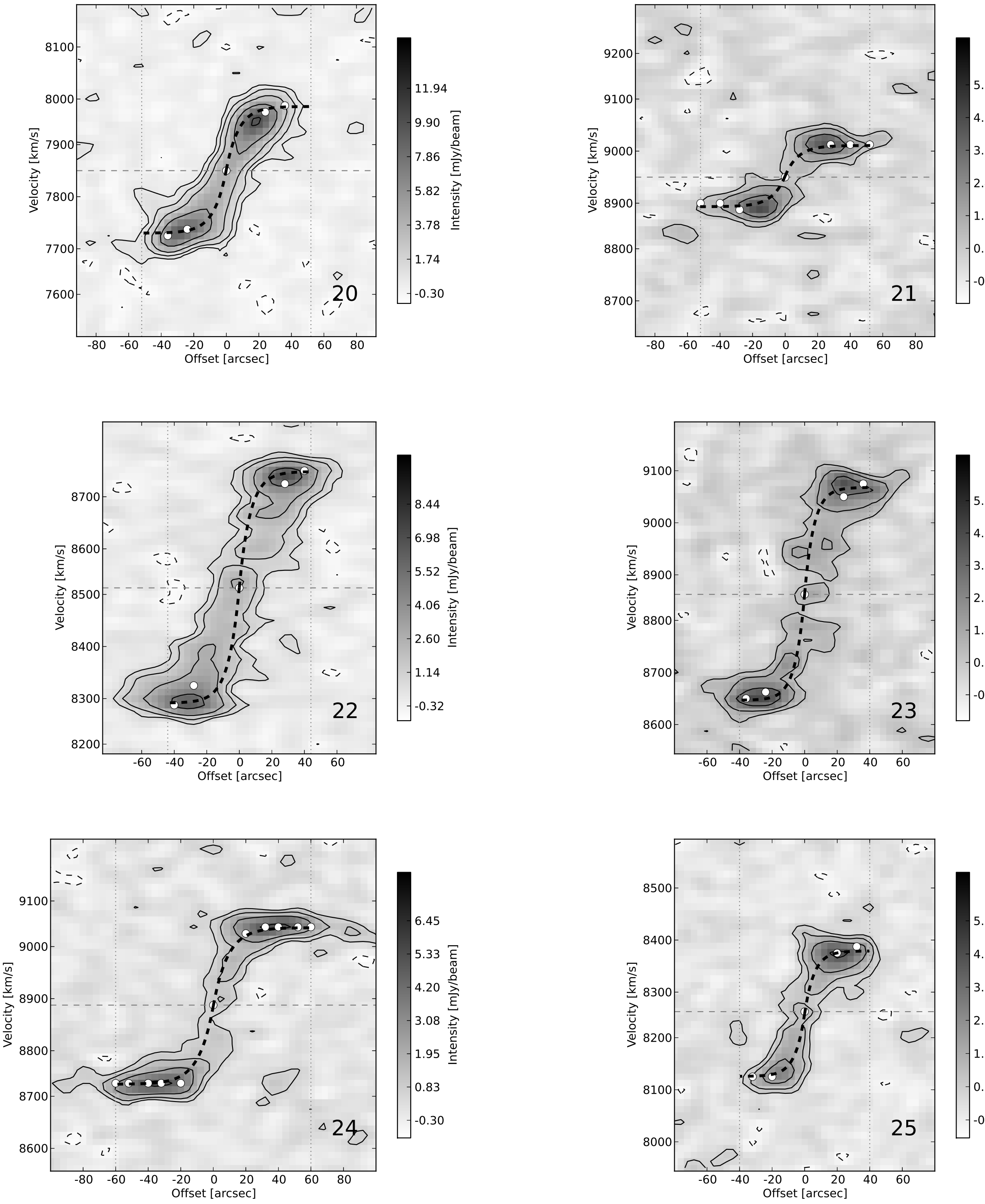

Figure B.3: cont.

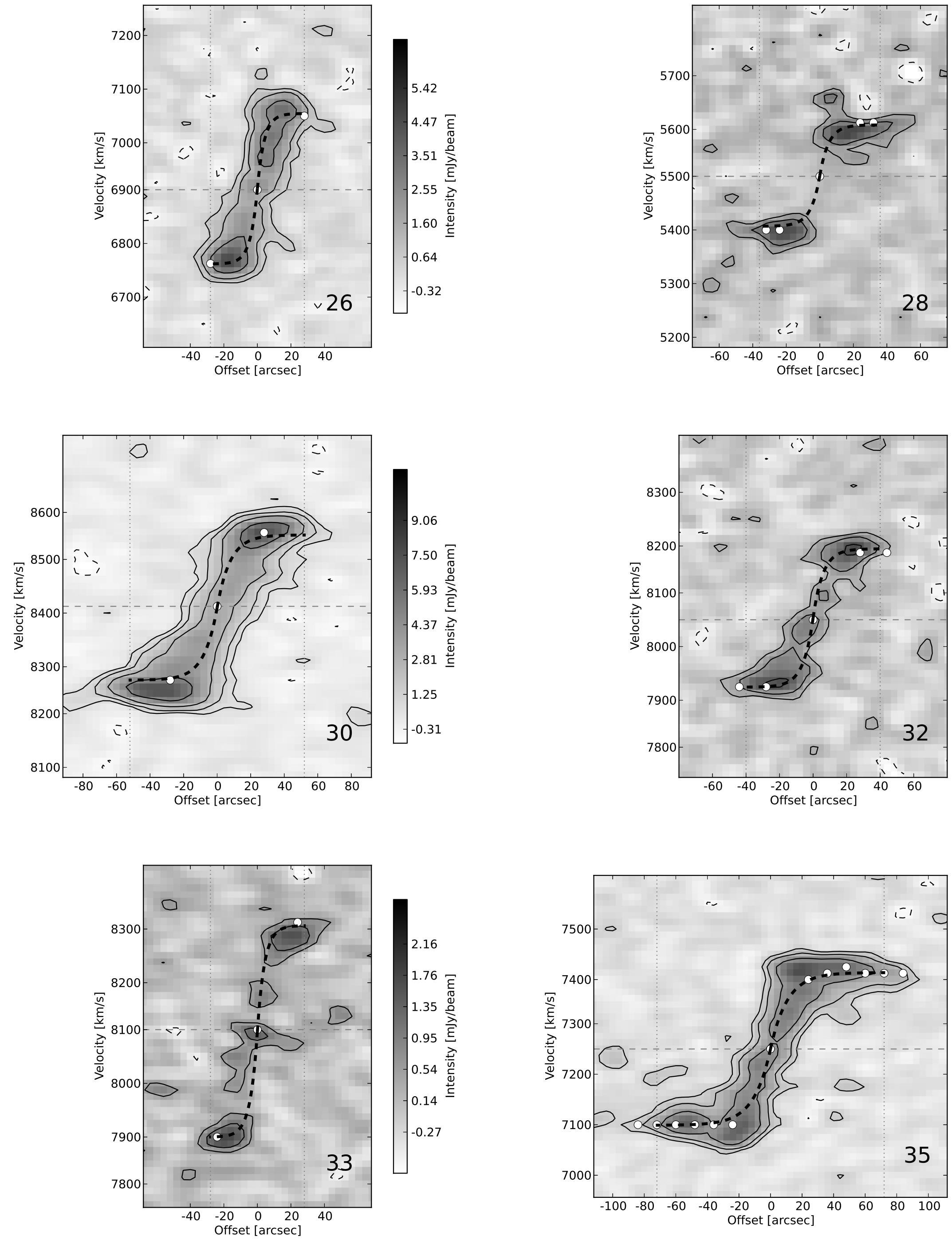

Figure B.3: cont.

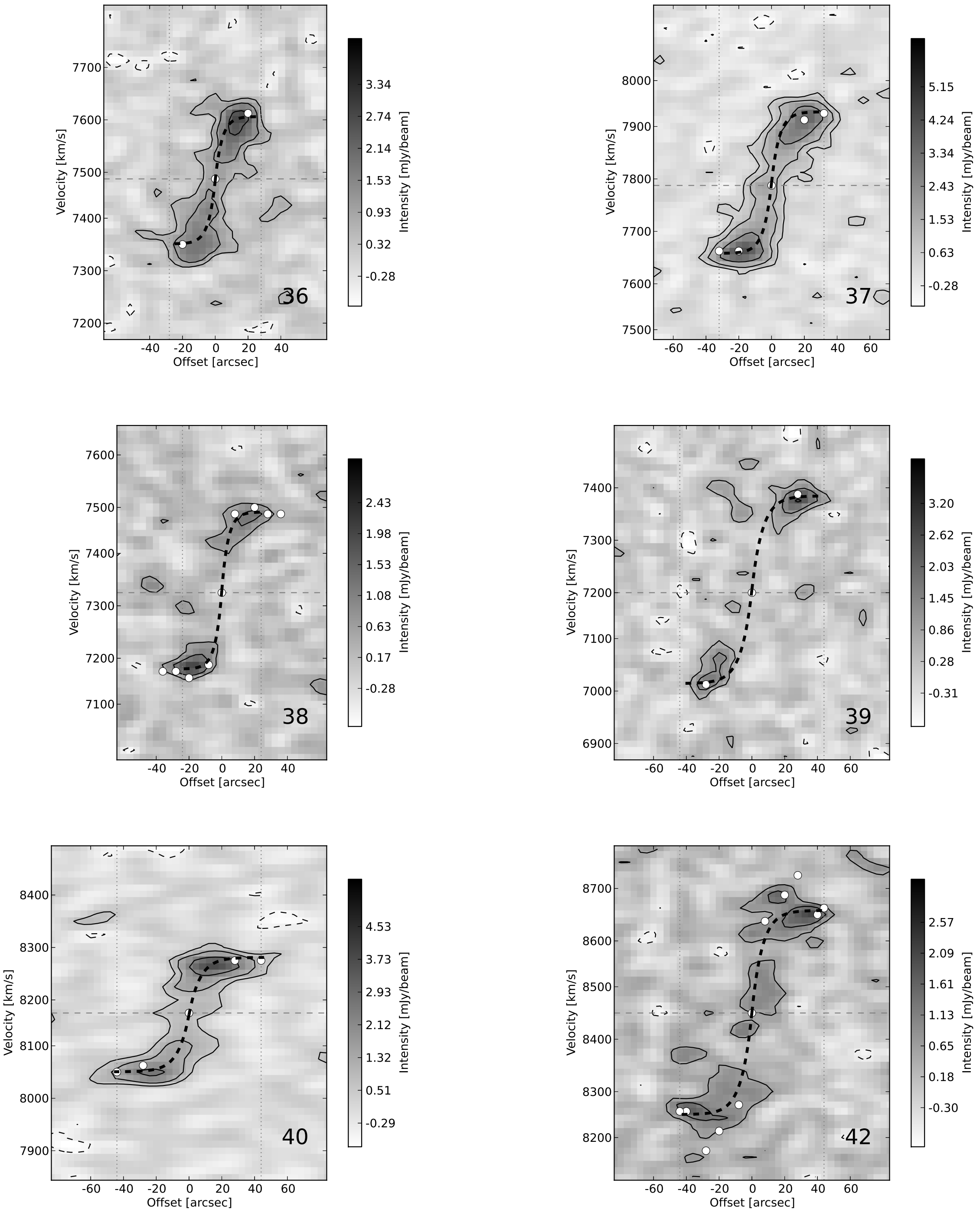

Figure B.3: cont.

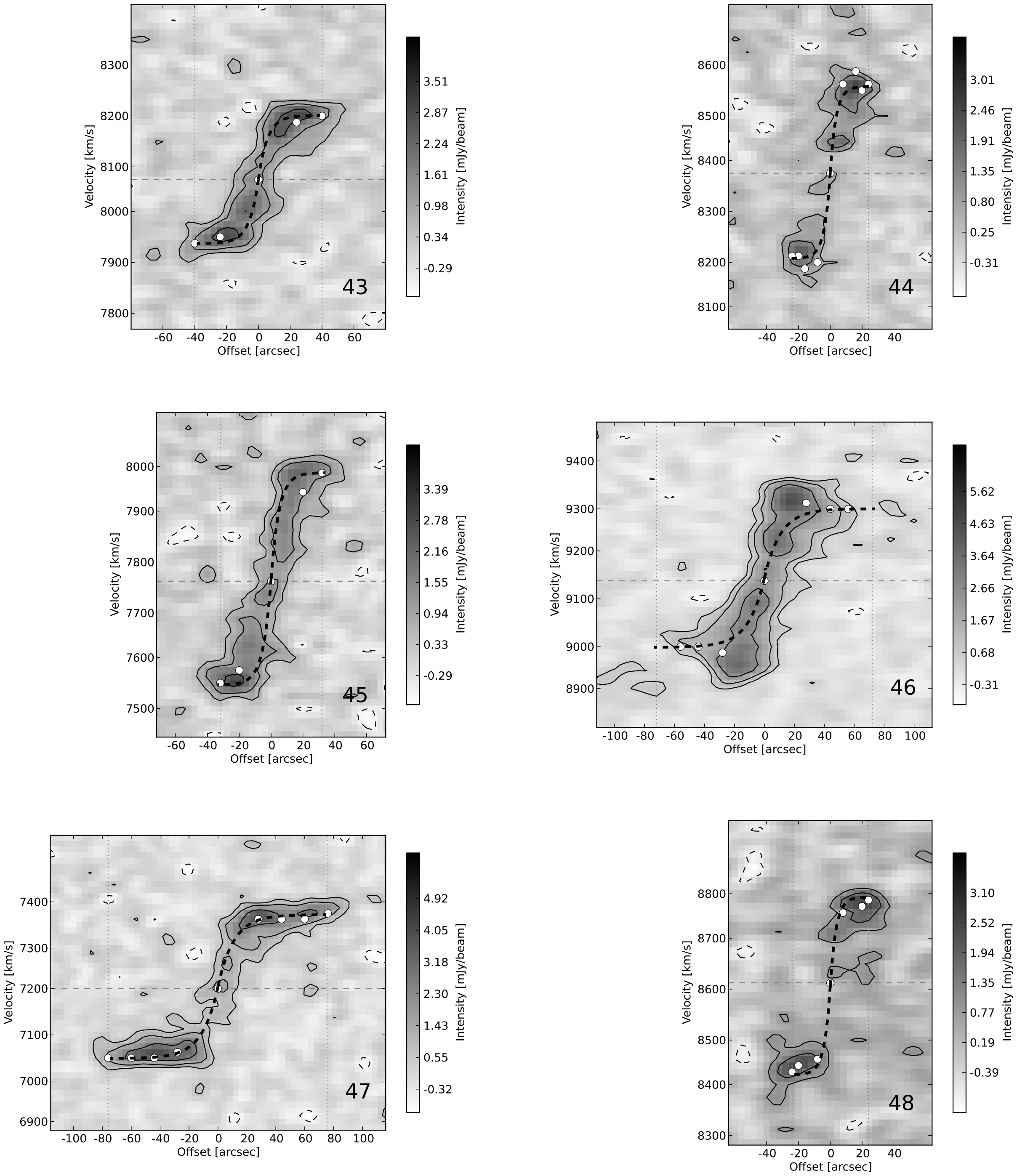

Figure B.3: cont.

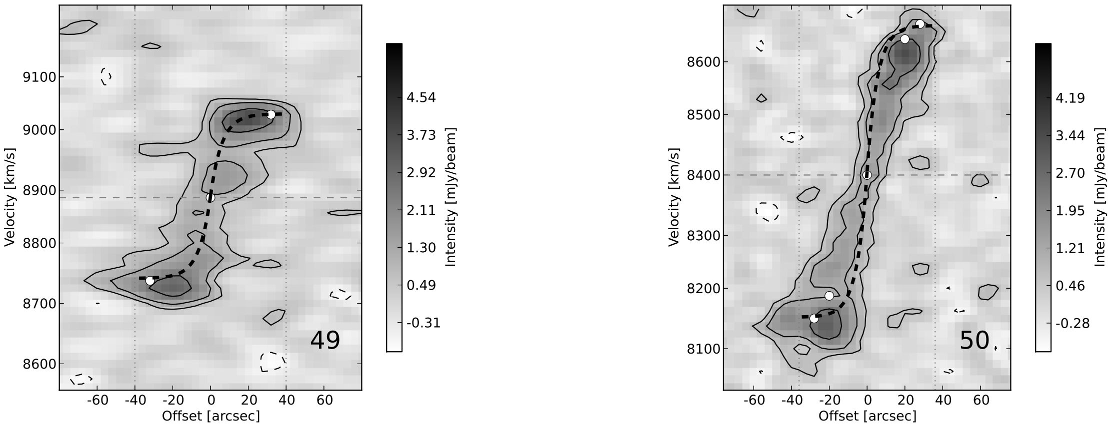

Figure B.3: cont.

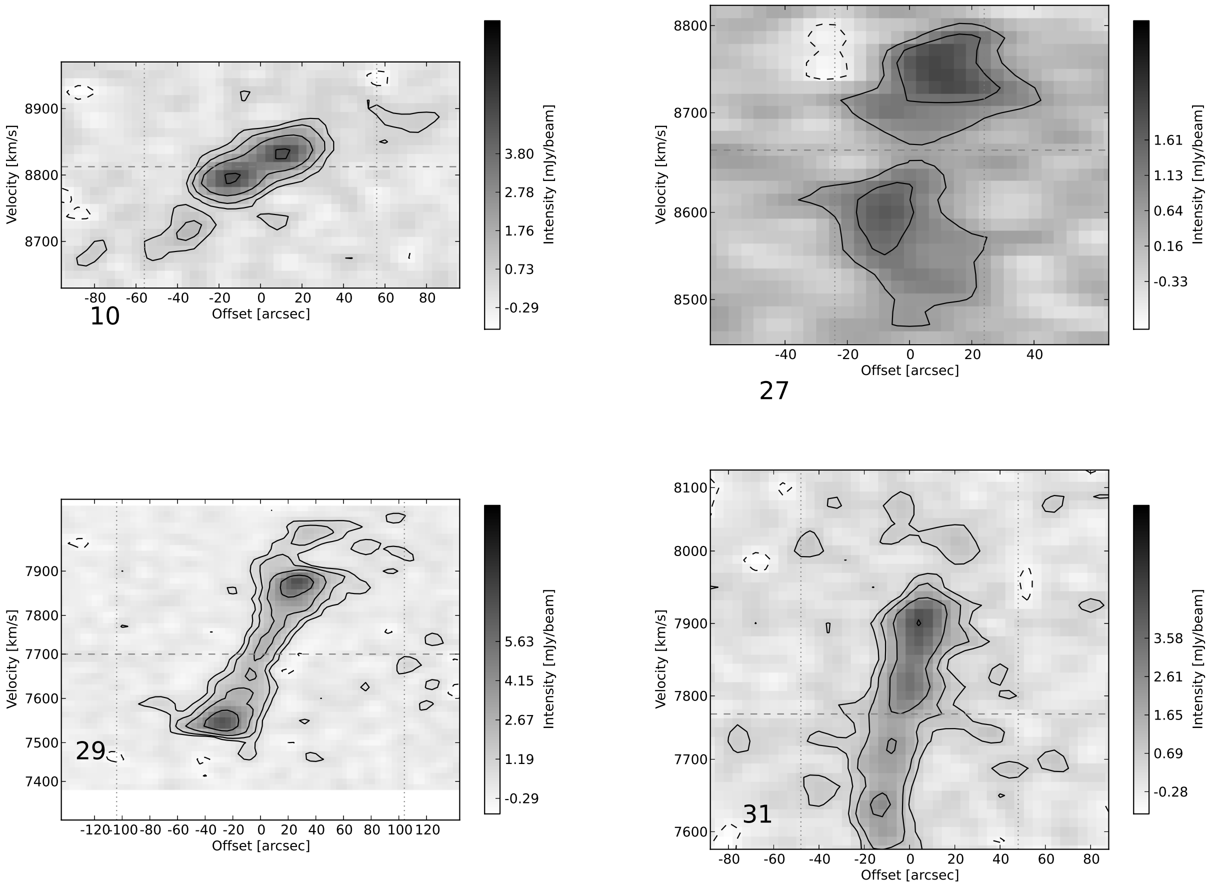

Figure B.4: Position-velocity diagrams of the galaxies where no tilted-ring fit has been performed.

Appendix C

NGC 2403 additional data

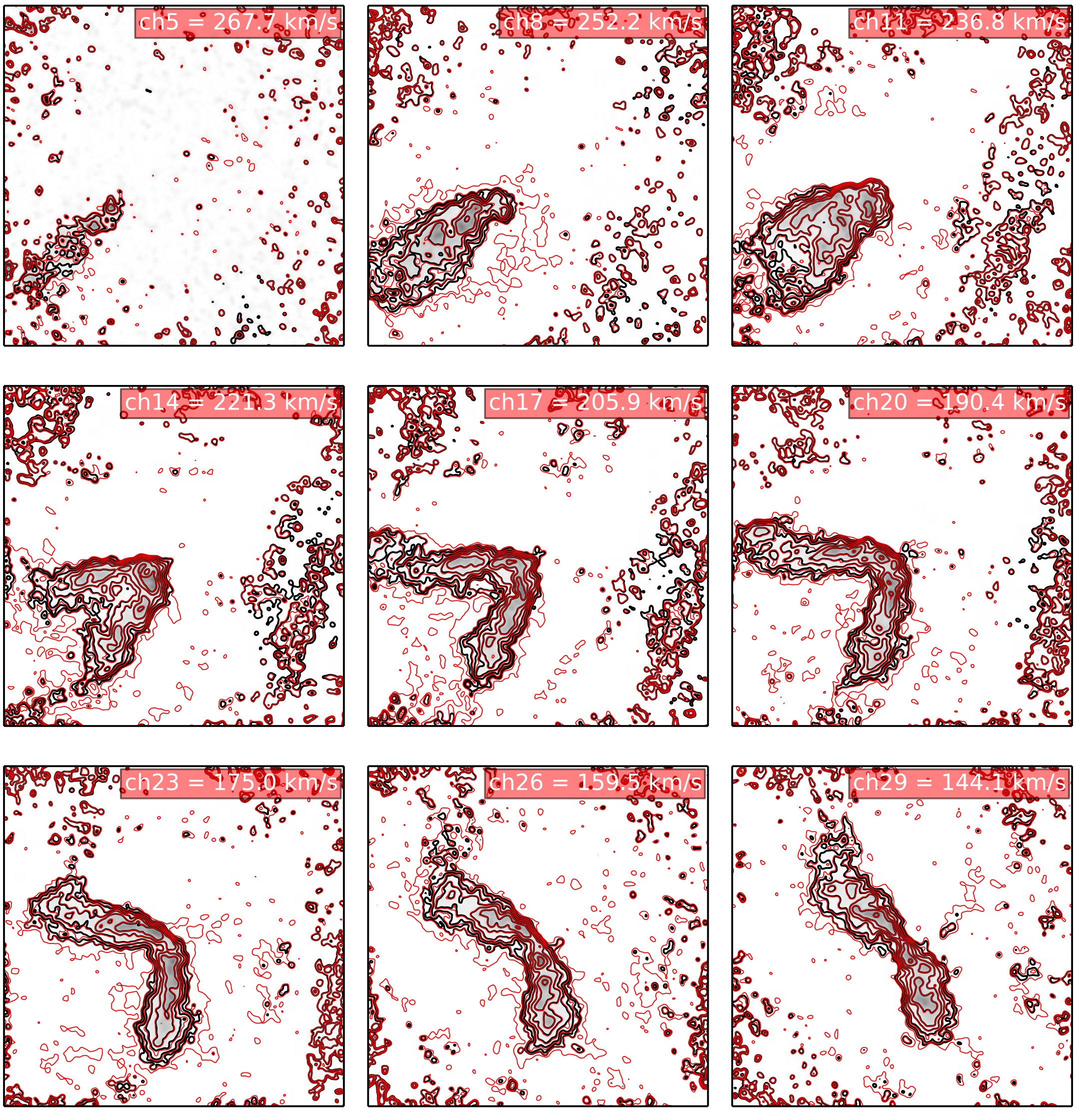

Figure C.1: Selection of velocity channels from the NGC 2403 interferometer data cube overlaid with the combined data cube contours. The black contours represent the interferometer data, the red contours the combined data. The contour levels shown are 1, 2, 4, 8, $16\sigma_{\mathrm{rms}}$, ... of the interferometer data cube.

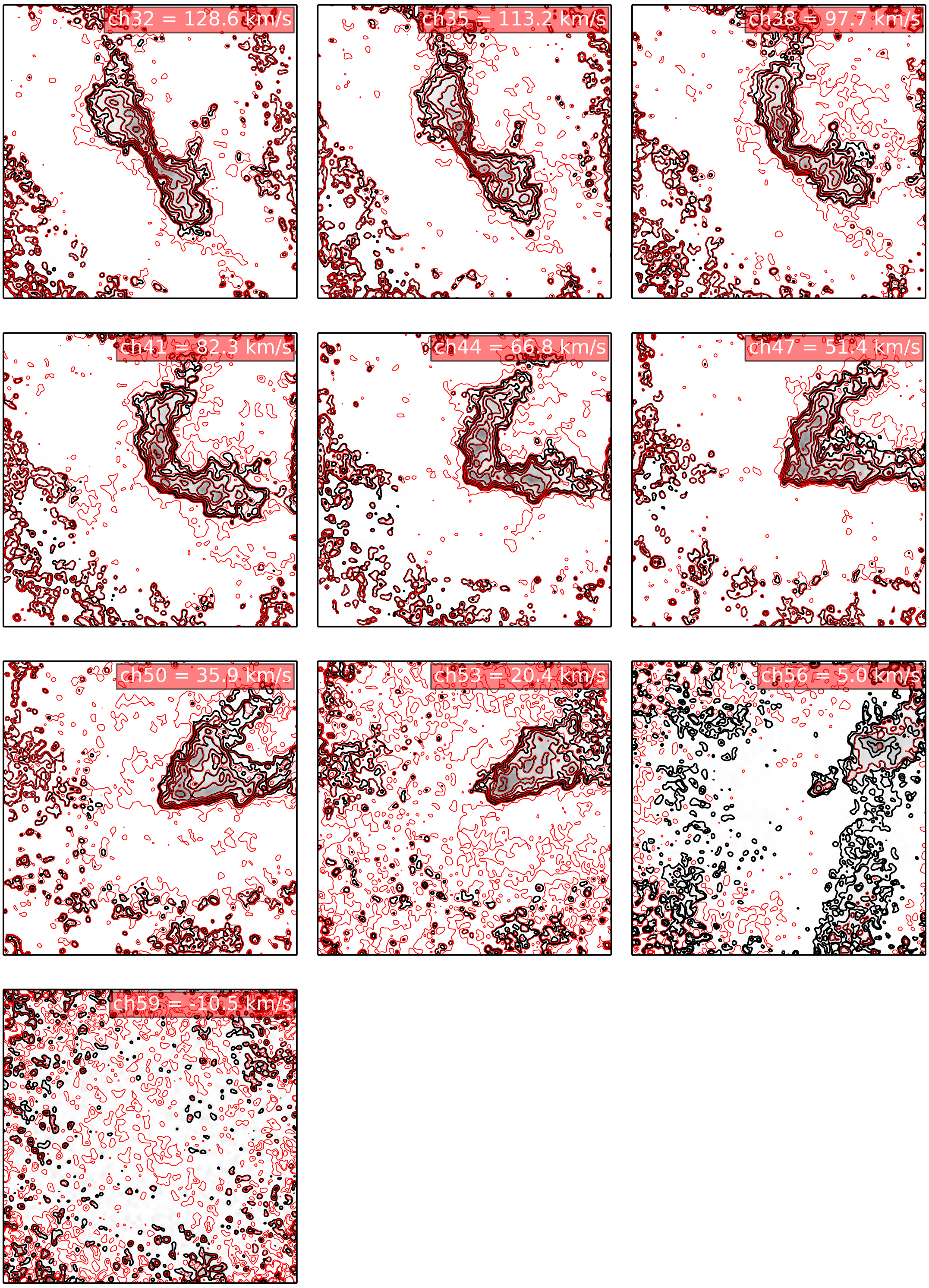

Figure C.1: cont.

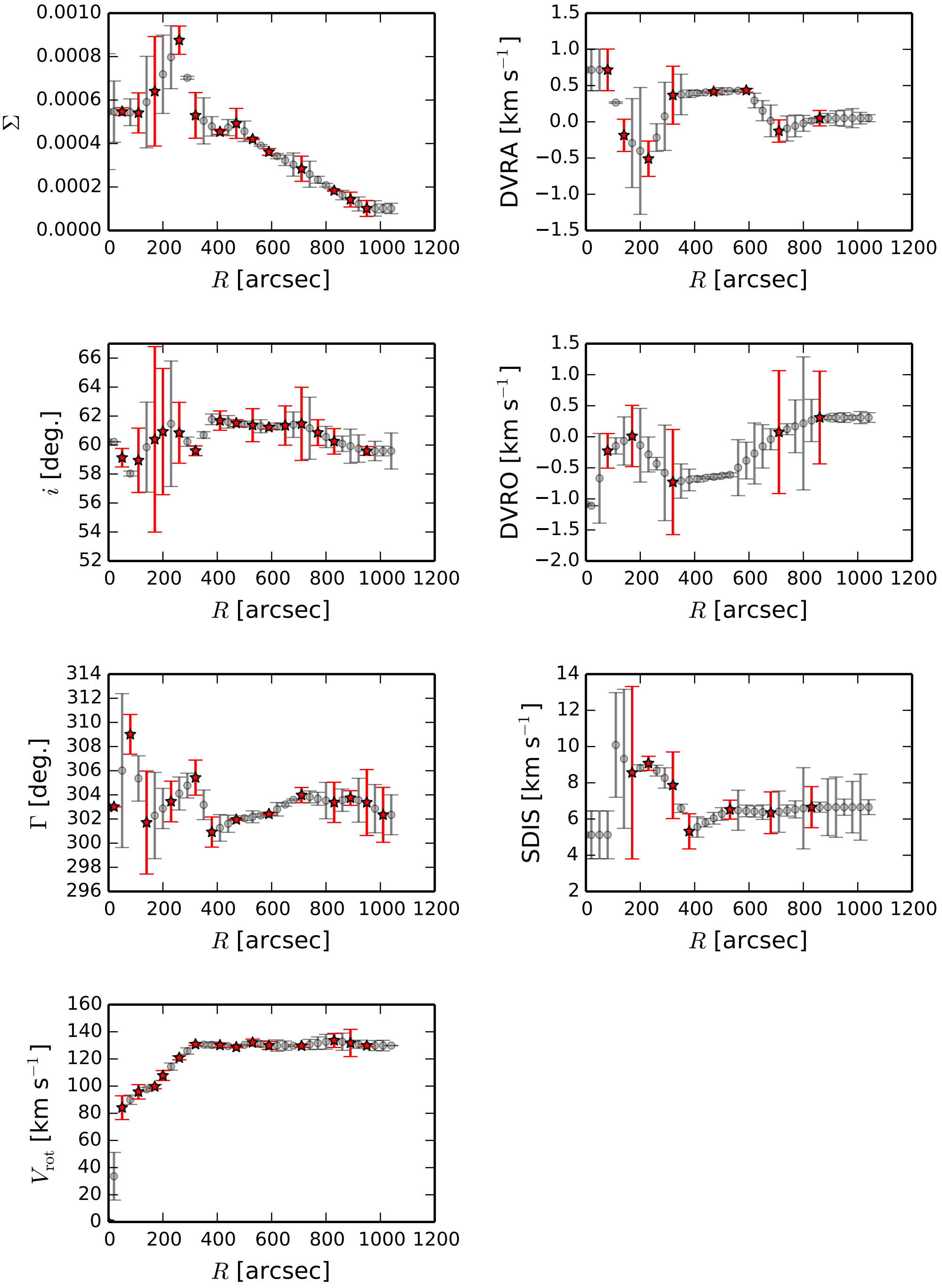

Figure C.2: NGC 2403 best-fitting model including a warp. Note that the points in red are the points fitted in the model. The grey points either result from interpolation between the red points or are fitted together as a group. Σ denotes the surface brightness [Jy km s^{-1} arcsec^{-}2], $DVRA$ [km s^{-1} arcsec^{-1}] the vertical gradient in radial velocity, i the inclination, $DVRO$ [km s^{-1} arcsec^{-1}] the vertical gradient in rotation velocity, Γ the position angle, $SDIS$ the velocity dispersion and $v_{\rm rot}$ the rotation velocity.

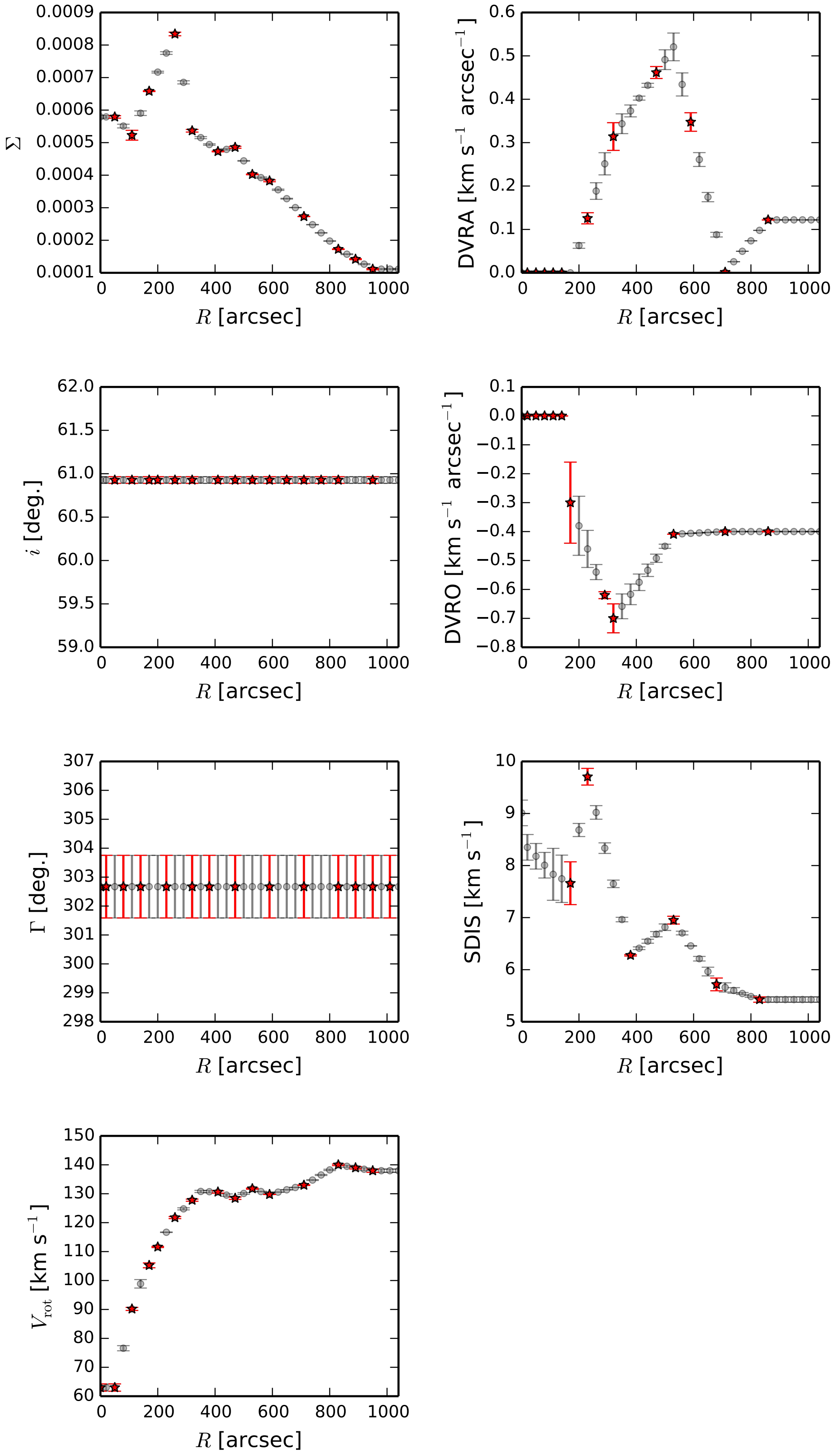

Figure C.3: NGC 2403 best-fitting model with bar streaming instead of a warp in the inner parts of the galaxy. For an explanation of the parameters see Fig. C.2.

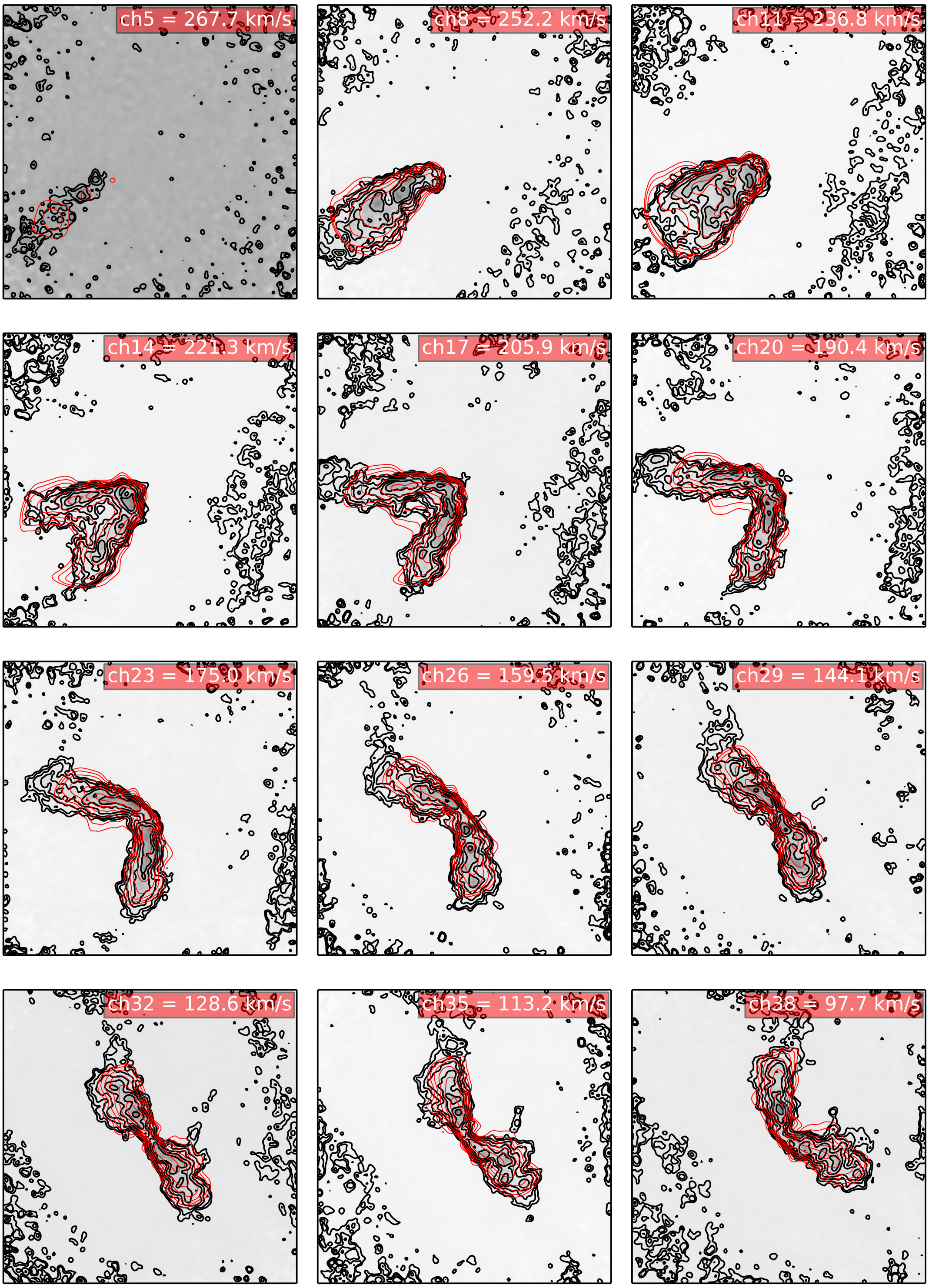

Figure C.4: Selection of velocity channels from the NGC 2403 data cube overlaid with the best fitting model including a warp. The black contours represent the data, the red contours the best-fitting model. The contour levels shown are 1, 2, 4, 8, $16\sigma_{\mathrm{rms}}$, ... of the data cube.

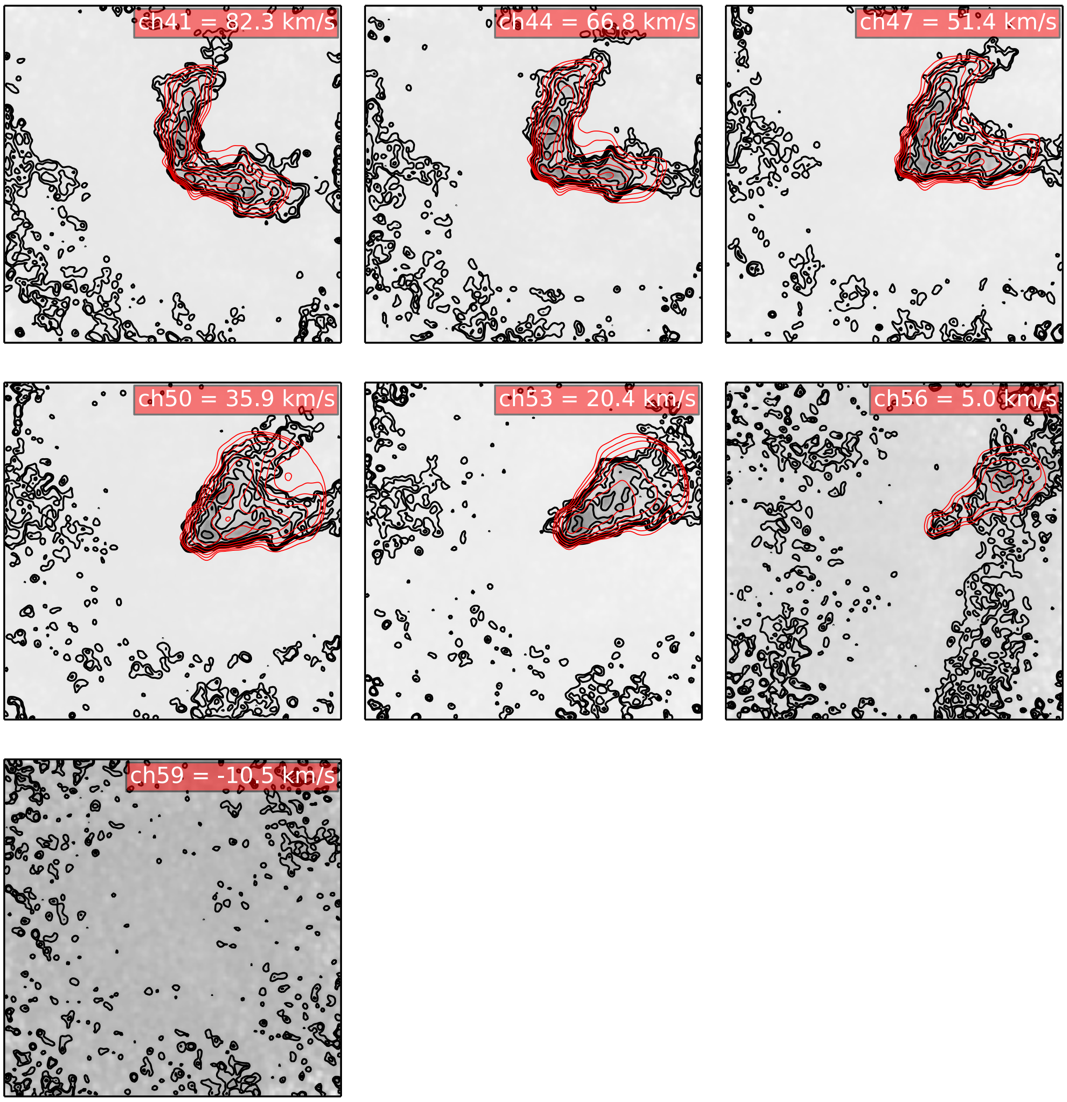

Figure C.4: cont.

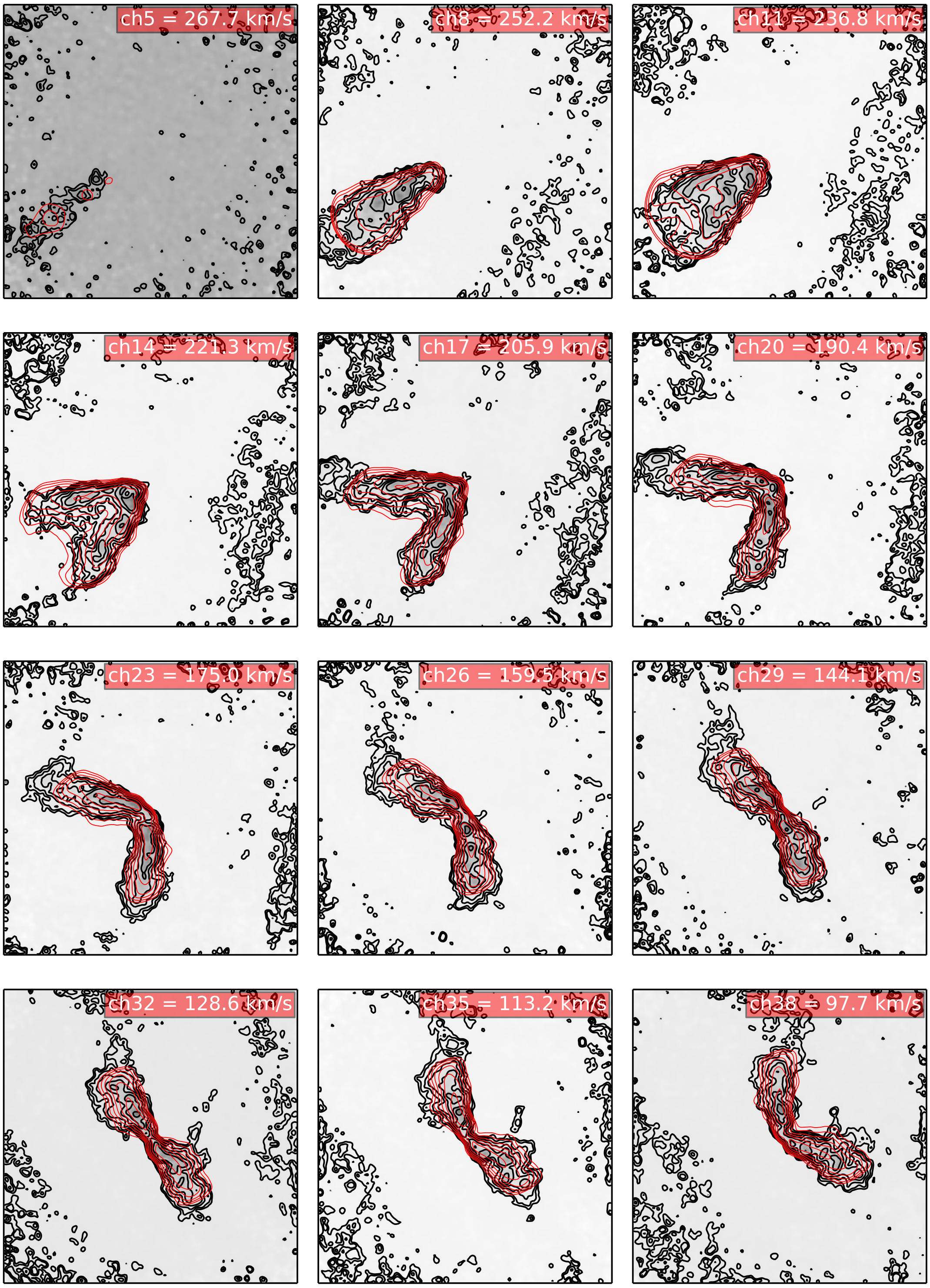

Figure C.5: Selection of velocity channels from the NGC 2403 data cube overlaid with the best fitting model with a flat disk and bar streaming in the inner regions. The black contours represent the data, the red contours the best-fitting model. The contour levels shown are 1, 2, 4, 8, 16σ_{rms}, ... of the data cube.

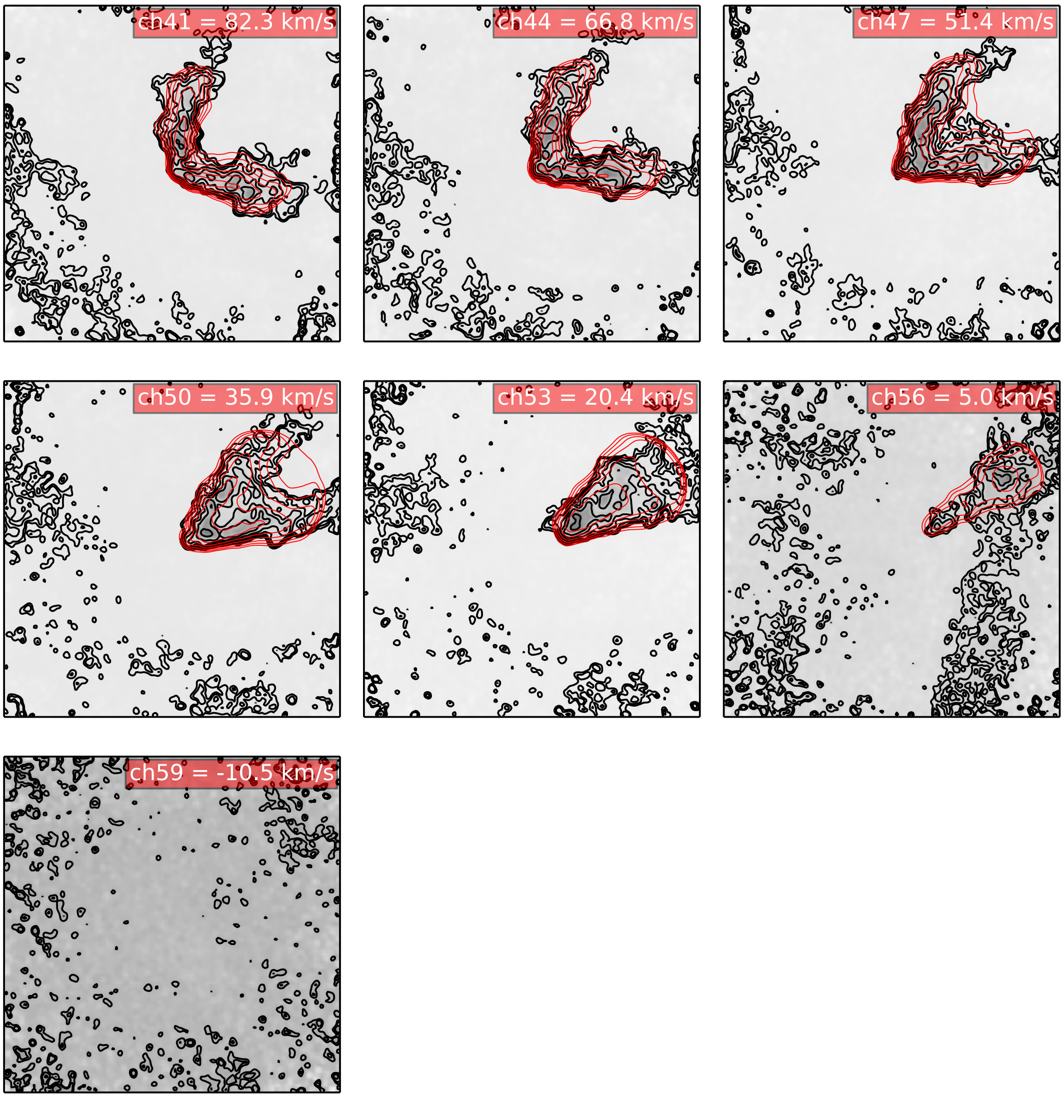

Figure C.5: cont.

Bibliography

Aaronson, M., Huchra, J., & Mould, J. 1979, ApJ, 229, 1

Aaronson, M. & Mould, J. 1983, ApJ, 265, 1

Abazajian, K. N., Adelman-McCarthy, J. K., Agüeros, M. A., et al. 2009, ApJS, 182, 543

Anderson, M. E., Bregman, J. N., & Dai, X. 2013, APJ, 762, 106

Athanassoula, E. 1992, MNRAS, 259, 345

Bacon, R., Copin, Y., Monnet, G., et al. 2001, MNRAS, 326, 23

Bedregal, A. G., Aragón-Salamanca, A., & Merrifield, M. R. 2006, MNRAS, 373, 1125

Begeman, K. G. 1987, PhD thesis, , Kapteyn Institute, (1987)

Begum, A., Chengalur, J. N., Karachentsev, I. D., & Sharina, M. E. 2008, MNRAS, 386, 138

Bell, E. F., McIntosh, D. H., Katz, N., & Weinberg, M. D. 2003, APJS, 149, 289

Bershady, M. A., Martinsson, T. P. K., Verheijen, M. A. W., et al. 2011, ApJ, 739, L47

Bershady, M. A., Verheijen, M. A. W., Swaters, R. A., et al. 2010, ApJ, 716, 198

Bosma, A. 1978, PhD thesis, PhD Thesis, Groningen Univ., (1978)

Bosma, A. 1981, AJ, 86, 1791

Briggs, D. S. 1995, PhD thesis, The New Mexico Insititute of Mining and Technology

Briggs, F. H. 1990, APJ, 352, 15

Broeils, A. H. & Rhee, M.-H. 1997, A&A, 324, 877

Bullock, J. S., Kolatt, T. S., Sigad, Y., et al. 2001, MNRAS, 321, 559

Cappellari, M. 2008, MNRAS, 390, 71

Cappellari, M., Emsellem, E., Krajnović, D., et al. 2011a, MNRAS, 413, 813

Cappellari, M., Emsellem, E., Krajnović, D., et al. 2011b, MNRAS, 416, 1680

Cappellari, M., McDermid, R. M., Alatalo, K., et al. 2012, Nature, 484, 485

Cappellari, M., McDermid, R. M., Alatalo, K., et al. 2013a, MNRAS, 432, 1862

Cappellari, M., Scott, N., Alatalo, K., et al. 2013b, MNRAS, 432, 1709

Catinella, B., Kauffmann, G., Schiminovich, D., et al. 2012, MNRAS, 420, 1959

Catinella, B., Schiminovich, D., Kauffmann, G., et al. 2010, MNRAS, 403, 683

Cortesi, A., Merrifield, M. R., Coccato, L., et al. 2013, MNRAS, 432, 1010

Davis, T. A., Alatalo, K., Bureau, M., et al. 2013, MNRAS, 429, 534

Davis, T. A., Bureau, M., Young, L. M., et al. 2011, MNRAS, 414, 968

de Blok, W. J. G., Walter, F., Brinks, E., et al. 2008, AJ, 136, 2648

de Vaucouleurs, G., de Vaucouleurs, A., Corwin, Jr., H. G., et al. 1991, Third Reference Catalogue of Bright Galaxies. Volume I: Explanations and references. Volume II: Data for galaxies between 0^h and 12^h. Volume III: Data for galaxies between 12^h and 24^h.

de Zeeuw, P. T., Bureau, M., Emsellem, E., et al. 2002, MNRAS, 329, 513

Desmond, H. 2012, ArXiv e-prints

Djorgovski, S. & Davis, M. 1987, ApJ, 313, 59

Dressler, A. 1980, ApJ, 236, 351

Dressler, A., Lynden-Bell, D., Burstein, D., et al. 1987, ApJ, 313, 42

Drissen, L., Roy, J.-R., Moffat, A. F. J., & Shara, M. M. 1999, AJ, 117, 1249

Duffy, A. R., Meyer, M. J., Staveley-Smith, L., et al. 2012, MNRAS, 426, 3385

Eisenstein, D. J. & Loeb, A. 1996, ApJ, 459, 432

Ewen, H. I. & Purcell, E. M. 1951, Nature, 168, 356

Faridani, S. 2014, PhD thesis, Universität Bonn

Fich, M., Blitz, L., & Stark, A. A. 1989, ApJ, 342, 272

Franx, M., van Gorkom, J. H., & de Zeeuw, T. 1994, ApJ, 436, 642

Fraternali, F. & Tomassetti, M. 2012, MNRAS, 426, 2166

Fraternali, F., van Moorsel, G., Sancisi, R., & Oosterloo, T. 2002, AJ, 123, 3124

Freeman, K. C. 1999, in Astronomical Society of the Pacific Conference Series, Vol. 170, The Low Surface Brightness Universe, ed. J. I. Davies, C. Impey, & S. Phillips, 3

García-Ruiz, I., Sancisi, R., & Kuijken, K. 2002, A&A, 394, 769

Giovanelli, R. & Haynes, M. P. 2002, APJ, 571, L107

Giovanelli, R., Haynes, M. P., Herter, T., et al. 1997, AJ, 113, 22

Giovanelli, R., Haynes, M. P., Salzer, J. J., et al. 1995, AJ, 110, 1059

Greisen, E. W. 2003, Information Handling in Astronomy - Historical Vistas, 285, 109

Gupta, A., Mathur, S., Krongold, Y., Nicastro, F., & Galeazzi, M. 2012, ApJ, 756, L8

Gurovich, S., McGaugh, S. S., Freeman, K. C., et al. 2004, PASA, 21, 412

Heald, G., Józsa, G., Serra, P., et al. 2011, AAP, 526, A118

Heesen, V., Brinks, E., Leroy, A. K., et al. 2014, AJ, 147, 103

Högbom, J. A. 1974, A&AS, 15, 417

Holmberg, E. 1958, Meddelanden fran Lunds Astronomiska Observatorium Serie II, 136, 1

Huang, M.-L., Kauffmann, G., Chen, Y.-M., et al. 2013, MNRAS, 431, 2622

Hubble, E. P. 1926, ApJ, 64, 321

Huynh, M. & Lazio, J. 2013, ArXiv e-prints

Jaffé, Y. L., Aragón-Salamanca, A., Ziegler, B., et al. 2014, MNRAS, 440, 3491

Johnston, S., Bailes, M., Bartel, N., et al. 2007, PASA, 24, 174

Jorsater, S. & van Moorsel, G. A. 1995, AJ, 110, 2037

Józsa, G. 2005, PhD thesis

Józsa, G. I. G., Kenn, F., Klein, U., & Oosterloo, T. A. 2007, A&A, 468, 731

Józsa, G. I. G., Oosterloo, T. A., Morganti, R., Klein, U., & Erben, T. 2009, A&A, 494, 489

Kalberla, P. M. W. & Kerp, J. 2009, ARA&A, 47, 27

Karachentsev, I. D., Karachentseva, V., Huchtmeier, W., et al. 2008, Mining the Local Volume, ed. B. S. Koribalski & H. Jerjen, 21

Kauffmann, G., White, S. D. M., & Guiderdoni, B. 1993, MNRAS, 264, 201

Kennicutt, Jr., R. C. 1998, ARA&A, 36, 189

Kerp, J. 2013, in Phases of the ISM, MPIA Summer Conference, Heidelberg, Germany

Kerp, J., Winkel, B., Ben Bekhti, N., Flöer, L., & Kalberla, P. M. W. 2011, Astronomische Nachrichten, 332, 637

Komatsu, E., Dunkley, J., Nolta, M. R., et al. 2009, ApJS, 180, 330

Krajnović, D., Cappellari, M., de Zeeuw, P. T., & Copin, Y. 2006, MNRAS, 366, 787

Kroupa, P. 2001, MNRAS, 322, 231

Li, C., Kauffmann, G., Fu, J., et al. 2012, MNRAS, 424, 1471

Madore, B. F. & Freedman, W. L. 1991, PASP, 103, 933

Malhotra, S., Spergel, D. N., Rhoads, J. E., & Li, J. 1996, ApJ, 473, 687

Maller, A. H. & Bullock, J. S. 2004, MNRAS, 355, 694

Marasco, A., Fraternali, F., & Binney, J. J. 2012, MNRAS, 419, 1107

Maraston, C. 2005, MNRAS, 362, 799

Marinacci, F., Fraternali, F., Binney, J., et al. 2012, in European Physical Journal Web of Conferences, Vol. 19, European Physical Journal Web of Conferences, 8008

Markwardt, C. B. 2009, in Astronomical Society of the Pacific Conference Series, Vol. 411, Astronomical Data Analysis Software and Systems XVIII, ed. D. A. Bohlender, D. Durand, & P. Dowler, 251

Martinsson, T. P. K. 2011, PhD thesis, University of Groningen

Martinsson, T. P. K., Verheijen, M. A. W., Westfall, K. B., et al. 2013, A&A, 557, A131

McGaugh, S. S. 2012, AJ, 143, 40

McGaugh, S. S., Rubin, V. C., & de Blok, W. J. G. 2001, AJ, 122, 2381

McGaugh, S. S., Schombert, J. M., Bothun, G. D., & de Blok, W. J. G. 2000, APJL, 533, L99

McWilliam, A. 1997, ARA&A, 35, 503

Merritt, D. 2000, in Astronomical Society of the Pacific Conference Series, Vol. 197, Dynamics of Galaxies: from the Early Universe to the Present, ed. F. Combes, G. A. Mamon, & V. Charmandaris, 221

Milgrom, M. 1983a, ApJ, 270, 371

Milgrom, M. 1983b, ApJ, 270, 384

Milgrom, M. 1983c, ApJ, 270, 365

Misiriotis, A., Xilouris, E. M., Papamastorakis, J., Boumis, P., & Goudis, C. D. 2006, A&A, 459, 113

Mo, H. J., Mao, S., & White, S. D. M. 1998, MNRAS, 295, 319

Moran, S. M., Heckman, T. M., Kauffmann, G., et al. 2012, APJ, 745, 66

Noordermeer, E. & Verheijen, M. A. W. 2007, MNRAS, 381, 1463

Oosterloo, T., Fraternali, F., & Sancisi, R. 2007, AJ, 134, 1019

Pierce, M. J. & Tully, R. B. 1988, ApJ, 330, 579

Pizagno, J., Prada, F., Weinberg, D. H., et al. 2007, APJ, 134, 945

Putman, M. E., Peek, J. E. G., & Joung, M. R. 2012, ARA&A, 50, 491

Rauch, M. 1998, ARA&A, 36, 267

Regan, M. W., Sheth, K., Teuben, P. J., & Vogel, S. N. 2002, ApJ, 574, 126

Richter, P. 2012, APJ, 750, 165

Roberts, M. S. 1978, AJ, 83, 1026

Robitaille, T. P. & Whitney, B. A. 2010, ApJ, 710, L11

Russell, D. G. 2004, ApJ, 607, 241

Saintonge, A., Kauffmann, G., Kramer, C., et al. 2011, MNRAS, 415, 32

Sakai, S., Mould, J. R., Hughes, S. M. G., et al. 2000, ApJ, 529, 698

Salpeter, E. E. 1955, ApJ, 121, 161

Sancisi, R., Fraternali, F., Oosterloo, T., & van der Hulst, T. 2008, AAPr, 15, 189

Sault, R. J., Teuben, P. J., & Wright, M. C. H. 1995, in Astronomical Society of the Pacific Conference Series, Vol. 77, Astronomical Data Analysis Software and Systems IV, ed. R. A. Shaw, H. E. Payne, & J. J. E. Hayes, 433

Schmidt, P., Józsa, G. I. G., Gentile, G., et al. 2014, A&A, 561, A28

Schoenmakers, R. H. M., Franx, M., & de Zeeuw, P. T. 1997, MNRAS, 292, 349

Schruba, A., Leroy, A. K., Walter, F., et al. 2012, AJ, 143, 138

Serra, P., Oosterloo, T., Morganti, R., et al. 2012, MNRAS, 422, 1835

Shen, S., Wang, C., Chang, R., et al. 2009, ApJ, 705, 1496

Shostak, G. S. & Rogstad, D. H. 1973, A&A, 24, 405

Sicking, F. J. 1997, PhD thesis, PhD Thesis, University of Groningen, (1997)

Skrutskie, M. F., Cutri, R. M., Stiening, R., et al. 2006, AJ, 131, 1163

Steinmetz, M. 2012, Astronomische Nachrichten, 333, 523

Steinmetz, M. & Navarro, J. F. 1999, ApJ, 513, 555

Strauss, M. A. & Willick, J. A. 1995, Phys. Rep., 261, 271

Swaters, R. A., Schoenmakers, R. H. M., nn, R., & van Albada, T. S. 1999, MNRAS, 304, 330

Taylor, G. B., Carilli, C. L., & Perley, R. A., eds. 1999, Astronomical Society of the Pacific Conference Series, Vol. 180, Synthesis Imaging in Radio Astronomy II

Teuben, P. J. 2002, in Astronomical Society of the Pacific Conference Series, Vol. 275, Disks of Galaxies: Kinematics, Dynamics and Peturbations, ed. E. Athanassoula, A. Bosma, & R. Mujica, 217–228

Tonini, C., Maraston, C., Devriendt, J., Thomas, D., & Silk, J. 2009, MNRAS, 396, L36

Tonini, C., Maraston, C., Thomas, D., Devriendt, J., & Silk, J. 2010, MNRAS, 403, 1749

Tosi, M. 1988, A&A, 197, 33

Trachternach, C., de Blok, W. J. G., McGaugh, S. S., van der Hulst, J. M., & Dettmar, R.-J. 2009, A&A, 505, 577

Trachternach, C., de Blok, W. J. G., Walter, F., Brinks, E., & Kennicutt, Jr., R. C. 2008, AJ, 136, 2720

Tully, R. B. & Fisher, J. R. 1977, AAP, 54, 661

Tully, R. B. & Pierce, M. J. 2000, APJ, 533, 744

Tully, R. B., Pierce, M. J., Huang, J.-S., et al. 1998, AJ, 115, 2264

van Albada, T. S., Bahcall, J. N., Begeman, K., & Sancisi, R. 1985, ApJ, 295, 305

van den Bosch, F. C. 2000, ApJ, 530, 177

van der Hulst, J. M., Terlouw, J. P., Begeman, K. G., Zwitser, W., & Roelfsema, P. R. 1992, in Astronomical Society of the Pacific Conference Series, Vol. 25, Astronomical Data Analysis Software and Systems I, ed. D. M. Worrall, C. Biemesderfer, & J. Barnes, 131

van der Marel, R. P. & Franx, M. 1993, APJ, 407, 525

van Eymeren, J., Jütte, E., Jog, C. J., Stein, Y., & Dettmar, R.-J. 2011, AA, 530, A29

Verheijen, M., Oosterloo, T., Heald, G., & van Cappellen, W. 2009, in Panoramic Radio Astronomy: Wide-field 1-2 GHz Research on Galaxy Evolution

Verheijen, M. A. W. 2001, APJ, 563, 694

Walker, M. A. 1999, MNRAS, 308, 551

Walter, F., Brinks, E., de Blok, W. J. G., et al. 2008, AJ, 136, 2563

Wang, H. 2010, PhD thesis

Wang, J., Fu, J., Aumer, M., et al. 2014, MNRAS, 441, 2159

Wang, J., Kauffmann, G., Józsa, G. I. G., et al. 2013, MNRAS, 433, 270

Weijmans, A.-M., Krajnović, D., van de Ven, G., et al. 2008, MNRAS, 383, 1343

Wevers, B. M. H. R., van der Kruit, P. C., & Allen, R. J. 1986, A&AS, 66, 505

White, S. D. M. & Frenk, C. S. 1991, ApJ, 379, 52

White, S. D. M. & Rees, M. J. 1978, MNRAS, 183, 341

Williams, M. J., Bureau, M., & Cappellari, M. 2009, MNRAS, 400, 1665

Williams, M. J., Bureau, M., & Cappellari, M. 2010, MNRAS, 409, 1330

Wong, T., Blitz, L., & Bosma, A. 2004, ApJ, 605, 183

Young, L. M., Bureau, M., Davis, T. A., et al. 2011, MNRAS, 414, 940

Zaritsky, D., Courtois, H., Muñoz-Mateos, J.-C., et al. 2014, ArXiv e-prints

Ziegler, B. L., Bower, R. G., Smail, I., Davies, R. L., & Lee, D. 2001, MNRAS, 325, 1571

Zwaan, M. A., van der Hulst, J. M., de Blok, W. J. G., & McGaugh, S. S. 1995, MNRAS, 273, L35

Acronyms

AIPS Astronomical Image Processing System. 68

ALMA Atacama Large Milimeter Array. 34, 103, 104

ASKAP Australia's Square Kilometer Array Pathfinder. 106

C11 Cappellari et al. 2011a. 15, 16, 23, 35

CO carbon monoxide. 5, 9, 16, 17, 21, 24–26, 28, 29, 31, 32, 34, 83, 103, 104

DVRA vertical gradient in radial velocity. 66, 78–81, 96, 98–100

DVRO vertical gradient in rotation velocity. 66, 79–81, 96, 98–100

EBHIS Effelsberg Bonn H I Survey. 67–69

ETG early-type galaxy. 5, 7–10, 14–16, 21, 24, 26, 27, 29, 30, 32–35, 103, 104

FWHM full width at half maximum. 45, 70, 77, 86, 87, 91

GIPSY Groningen Image Processing System. 18, 19, 21, 71

HALOGAS Hydrogen Accretion in Local Galaxies Survey. 39

H I neutral atomic hydrogen. 5, 7, 9–12, 15–19, 21, 23–34, 37–59, 78, 83, 103–106

HPBW half power beam width. 68, 70

HVC high-velocity cloud. 84

IMF initial-mass function. 12, 27, 28, 30, 32–35, 55

ISM interstellar medium. 61, 85

JAM Jeans Anisotropic Multi-Gaussian Expansion. 27–35

LOSVD line-of-sight velocity distribution. 65, 67, 70, 72

McG12 McGaugh 2012. 27, 28, 32–35

Miriad Multichannel Image Reconstruction, Image Analysis and Display. 16, 17, 41, 86

MW Milky Way. 5, 11, 38, 39, 68, 69, 73–76, 79, 82–84, 87, 92, 101, 103, 105

NV07 Noordermeer & Verheijen 2007. 12, 15, 17, 25–32, 35, 53–56, 58

SDSS Sloan Digital Sky Survey. 8, 37, 39, 40, 48, 54, 58

SFH star formation history. 27–34

SFR star formation rate. 67, 84

SSC short-spacing correction. 5, 8, 61–63, 66–68, 72–77, 79–84, 101, 105, 106

T&P00 Tully & Pierce 2000. 11, 24, 25, 28

TFR Tully-Fisher Relation. 5, 7–18, 21, 23–35, 52, 53, 55, 103, 104

THINGS The H I Nearby Galaxy Survey. 68, 70, 83

TiRiFiC Titled-Ring Fitting Code. 19, 21, 46, 66, 76–78, 80, 92, 93, 95, 96, 98, 101, 102, 106

VLA Very Large Array. 67, 71–75

WBC10 Williams et al. 2010. 24–26, 28, 29

WSRT Westerbork Synthesis Radio Telescope. 9, 16, 17, 19, 21, 31, 37, 39, 40, 55, 67, 103, 104, 106

xv position-velocity. 18, 21, 22, 41–45, 49, 77–81, 87, 88, 90, 113

ZDRA onset height above plane for change in radial velocity. 66, 78, 80, 98

ZDRO onset height above plane for change in rotation velocity. 66, 78